



TEL AVIV UNIVERSITY
RAYMOND AND BEVERLY SACKLER FACULTY OF EXACT SCIENCES
SCHOOL OF PHYSICS AND ASTRONOMY

**Study of hard double parton scattering
in four-jet events in pp collisions at $\sqrt{s} = 7$ TeV
with the ATLAS experiment at the LHC**

Thesis submitted to the senate of Tel Aviv University
towards the degree "Doctor of Philosophy"

by

Orel Gueta

September 2015

CERN-THESIS-2015-359
//2016



Thesis supervisors,
Prof. **Halina Abramowicz** and
Prof. **Aharon Levy**.

The research for this thesis has been carried out in the Particle Physics Department of Tel Aviv University, under the supervision of Prof. **Halina Abramowicz** and Prof. **Aharon Levy**.

Abstract

Inclusive four-jet events produced in proton–proton collisions at a center-of-mass energy of $\sqrt{s} = 7$ TeV have been analysed for the presence of double parton scattering using data corresponding to an integrated luminosity of (37.3 ± 1.3) pb⁻¹, collected with the ATLAS detector at the LHC. The fraction of events arising from double parton scattering has been extracted using an artificial neural network, under the assumption that the four-jet topology originating from double parton scattering can be represented by a random combination of dijet events. The fraction was estimated to be $f_{\text{DPS}} = 0.084^{+0.009}_{-0.012}$ (stat.) $^{+0.062}_{-0.031}$ (syst.) in four-jet events, where each event contains at least four reconstructed jets with transverse momentum, $p_{\text{T}} \geq 20$ GeV, pseudo-rapidity, $|\eta| \leq 4.4$, and the highest- p_{T} jet has $p_{\text{T}} \geq 42.5$ GeV. Combined with the measurements of the dijet and four-jet cross-sections in the appropriate phase-space regions, the effective overlap area between the interacting protons, σ_{eff} , was found to be $\sigma_{\text{eff}} = 16.1^{+2.0}_{-1.5}$ (stat.) $^{+6.1}_{-6.8}$ (syst.) mb. This value is consistent within the quoted uncertainties with previous measurements of σ_{eff} at center-of-mass energies above 1 TeV, using various final states, and it is roughly a quarter of the inelastic cross-section. A sample enriched with double parton scattering events was extracted and some characteristics of these events were studied.

Acknowledgements

I would like to express my immense gratitude to my supervisors, Prof. Halina Abramowicz and Prof. Aharon Levy for teaching me to be an experimental physicist, for showing me that no obstacle is insurmountable and for all of the support and dedication throughout this analysis. I could not have asked for better advisors, both professionally and personally.

I owe a great debt of gratitude to Dr. Iftach Sadeh with whom I have had the pleasure to work on this analysis. Your input, advice and ideas were invaluable and perhaps more importantly, you made the journey fun. I would also like to show special appreciation to Prof. Frank Krauss for his considerable contribution to this study.

I have had the pleasure to work and share an office with Dr. Sergey Kananov, Dr. Oleksandr Borysov, Amir Stern, Itamar Levy and Oron Rosenblat, of the experimental particle physics group at Tel Aviv University. Thank you for allowing me to pick your brains, bounce ideas off of you and for making the breaks enjoyable.

I am especially grateful to Prof. Ricardo Piegaiia, Dr. Gustavo Otero y Garzon, Dr. Javier Tiffenberg, Dr. Laura Gonzalez Silva, Dr. Gaston Romeo, Dr. Yann Guardincerri, Dr. Hernan Reisin, Sabrina Sacerdoti and Pablo Pieroni, from the experimental high energy physics group at the University of Buenos Aires, for welcoming me during my stay in Argentina. You have helped me get started in ATLAS, taught me all about jets and made me feel at home.

I would like to thank to Prof. Allen Caldwell, Dr. Sven Menke, Dr. Teresa Barillari, Dr. Daniele Zanzi and Fabian Spettel for the stimulating discussions on physics related issues and otherwise. You have made my visits to the Max-Planck-Institut für Physik in Munich both productive and enjoyable.

The completion of this thesis would not have been possible without the love, support and encouragement of my parents, sisters and wife. You have made it possible for me to pursue this dream of studying physics, stood by me through it all and gave a meaning to life, thank you.

The research presented here was partly supported by ISF, GIF and I-CORE.

Preface

The analysis presented in this thesis was initiated in collaboration with Dr. Iftach Sadeh whose thesis contains preliminary results. Since those preliminary results, the following advances were made by the author:

- two new Monte Carlo (MC) samples were generated with ALPGEN +HERWIG +JIMMY (AHJ) and SHERPA, including a full simulation of the ATLAS detector. Since the detector simulation is a CPU-intensive process, two special filters had to be developed, one to select four-jet events and the other to select double parton scattering (DPS) events on parton-level. With these filters, it was possible to increase the amount of events available for the analysis by about a factor 10;
- the four-jet event selection was modified from exclusive to inclusive, i.e., events with more than four jets are included in the measurement. Throughout the analysis, when discussing a four-jet (dijet) event, the leading (highest transverse momentum) four (two) jets in the event are considered. The inclusive selection introduced two complications, it made differentiating between DPS and single parton scattering (SPS) events harder and it forced the distinction between two classes of DPS events, complete-DPS (cDPS) and semi-DPS (sDPS). The former are events in which the two dijets of DPS are among the four leading jets. In the latter class of DPS events, out of the four leading jets, three jets originate from one scattering and one from the other;
- a new method was developed to classify double parton scattering events on parton-level by matching partons to jets. This method is different from the one employed in the previous DPS measurement performed in ATLAS since the four-jet final state and the inclusive selection require the classification to be performed at the jet-level, rather than at the event-level. Classifying the events in this manner allowed to select SPS events which contain the low transverse momentum (p_T) activity, while ensuring that none of the four leading jets originate from hard secondary interactions. A more physical description of SPS events is obtained this way;
- the sample representing cDPS was constructed by overlaying dijets from data, rather than from MC, thanks to the development of a new overlaying scheme which allowed to take advantage of the entire sample of dijet events;
- the classification of DPS and SPS events was performed using an artificial neural network (NN). A principal component analysis was utilized to further optimize the selection of variables used as input to the NN. New variables were constructed to improve the classification of cDPS events and additional variables were added for the classification of sDPS events;
- the NN was expanded to include three outputs, corresponding to three probabilities for the event to be a SPS, cDPS or sDPS event. Combining the three probabilities and the constraint that the sum of the probabilities is one, the outputs of the NN for each event were plotted as a single point inside an equilateral triangle (Dalitz plot). Plotting the NN outputs on a Dalitz plot helped visualize the classification power of the NN and the results of the fit used to determine the fractions of cDPS and sDPS events (f_{cDPS} and f_{sDPS} , respectively);
- the methodology of the measurement was validated extensively using the new MC samples. In order to ascertain that the topology of cDPS events is reproducible by overlaying two dijet events, the dijet overlay sample was compared to a cDPS sample extracted from the AHJ MC.

A comparison of the NN output distributions in the two samples verified that the topology of the overlaid dijet events is comparable to that of cDPS events extracted from AHJ;

- ✎ the topology of SPS events extracted from the AHJ sample was tested due to a disagreement observed between the data and AHJ in distributions related to back-to-back topologies of the third and fourth jet in the event (sorted according to jet p_T). Four-jet events were generated in SHERPA with the module adding multi-parton interactions turned off. Thus, four-jet SPS events, simulated using matrix element (ME) calculations in the realm of perturbative quantum chromodynamics, were obtained. A good agreement was observed in the comparison between the distributions of SPS events in both MC generators. This indicated that the topology of SPS events in AHJ, simulated with ME calculations as well, is similar to that in SHERPA. Based on this comparison, the disagreements between the distributions in the data and in AHJ were understood to be due to an excess of DPS events in AHJ;
- ✎ an additional check of the last conclusion was performed by studying the same distributions as above as a function of the NN output. Using the NN output, a sample composed almost entirely from SPS events and a sample enriched with DPS events were selected from the data and MC samples. A good agreement was observed between the distributions in all three SPS samples, while an excess of DPS events in AHJ was observed in the DPS enriched sample. As expected, the distributions in SHERPA underestimated the distributions in the data in the DPS enriched sample;
- ✎ the fit procedure used to estimate f_{cDPS} and f_{sDPS} was validated by fitting the NN output distributions in the inclusive AHJ sample with the corresponding distributions in the SPS, cDPS and sDPS samples. Comparing the fractions obtained from the fit with the parton-level fractions, an excellent agreement was observed, confirming the fit method and further verifying the overlay method to construct complete-DPS events;
- ✎ the availability of MC samples which include a full simulation of the ATLAS detector facilitated a different approach to estimate systematic uncertainties. Additional systematic uncertainties were included, pertaining to various corrections and parameters used in the analysis;
- ✎ a two-dimensional fit to the NN output distributions in data was performed and an estimate of f_{cDPS} and f_{sDPS} in data was obtained. This is the first time the fraction of sDPS events is extracted from data directly;
- ✎ the distributions in data of the main observables used in the analysis are compared to the combination of distributions in the SPS, cDPS and sDPS samples, normalized based on the estimated f_{cDPS} and f_{sDPS} . Systematic uncertainties were included in the distributions and a good description of the data in most regions of phase-space is achieved;
- ✎ combining the f_{cDPS} and f_{sDPS} extracted in data with the measured dijet and four-jet cross-sections, the effective overlap area between the interacting protons, σ_{eff} , was estimated, obtaining a value which is consistent within the quoted uncertainties with previous measurements of σ_{eff} at center-of-mass energies above 1 TeV, using various final states. The measured value of σ_{eff} is roughly a quarter of the inelastic cross-section;
- ✎ some characteristics of DPS events were studied by using the NN output to extract a sample enriched with DPS events (34%) and comparing it to a sample of SPS events (with purity above 99%). Distributions of the proton longitudinal momentum carried by the massless

parton participating in the interaction, x , in this sample were compared to the x distributions in the SPS sample. The comparison indicated that in DPS events the x values of the two interactions taking place are uncorrelated. The average charged particle multiplicity in DPS events in data was estimated to be $\sim 8\%$ higher than in SPS events.

This analysis is intended to be published as an ATLAS paper and submitted to a journal. At the time of the submission of this thesis, the editorial process within the ATLAS collaboration has been initiated.

Contents

1	Introduction	11
2	Theoretical background	15
2.1	The Standard Model of particle physics	15
2.2	Strong interactions	16
2.2.1	Color confinement	17
2.2.2	Running coupling and asymptotic freedom	18
2.2.3	Parton distribution functions	19
2.2.4	QCD factorization	23
2.3	Phenomenological models of pp collisions	24
2.3.1	Parton showers	24
2.3.2	Matching the hard scatter with parton shower	25
2.3.3	Hadronization	26
2.3.4	The underlying event	26
2.4	Double parton scattering phenomenology	27
2.4.1	Four-jet final state	30
3	Experimental setup	32
3.1	The Large Hadron Collider	32
3.2	The ATLAS Detector	32
3.3	Luminosity	35
3.4	Jet algorithms	36
3.5	Inputs to jet reconstruction	39
3.6	Jet energy calibration	39
3.6.1	Pile-up correction	40
3.6.2	Jet origin correction	40
3.6.3	Jet energy scale	40
3.6.4	Jet pseudo-rapidity correction	41
3.7	Jet quality selection	41
3.7.1	Jet reconstruction efficiency	42
3.8	Jet calibration uncertainties	43
3.9	Dataset	43
3.10	Trigger	44
3.10.1	Trigger efficiency	44
3.10.2	Luminosity calculation using a two-trigger selection scheme	45
4	Monte Carlo simulation	53

4.1	Event generators	53
4.1.1	Multi-parton interactions in event generators	53
4.1.2	ALPGEN + HERWIG + JIMMY	54
4.1.3	PYTHIA	55
4.1.4	SHERPA	55
4.2	Simulation of the ATLAS detector	56
5	Event selection	57
6	Methodology	59
6.1	Classes of double parton scattering events	59
6.2	Symmetry factor	59
6.3	Correction due to overlapping jets	61
6.4	The effective cross-section in terms of experimental observables	62
6.5	Measurement of the dijet and four-jet cross-sections	63
6.5.1	Correcting for the selection of single-vertex events	63
6.5.2	Measured cross-sections	63
6.6	Acceptance	64
6.6.1	Acceptance for dijet events	64
6.6.2	Acceptance for four-jet events	65
6.6.3	Jet rapidity distributions	67
6.6.4	Final acceptance calculation	68
6.7	Template samples	68
6.7.1	Event classification in MC	68
6.7.2	Jet to parton matching	69
6.7.3	Single parton scattering sample	71
6.7.4	Double parton scattering sample	71
6.7.5	Semi-DPS sample	73
6.8	Differentiating variables	74
6.8.1	Possible variables	75
6.8.2	Distributions of the variables in the three samples	76
6.9	Principal component analysis	80
6.10	Extraction of the fraction of DPS events using a neural network	83
6.10.1	Training of the neural network	83
6.10.2	Significance of variables to the output of the neural network	84
6.10.3	Output of the neural network	85
6.11	Estimate of the cDPS and sDPS contributions	88
7	Methodology validation	90
7.1	Determination of the fraction of double parton scattering on parton-level	90
7.2	Kinematic properties of jets in AHJ	91
7.2.1	Jet p_T - y distributions in AHJ	91
7.2.2	Variables distributions in data and in AHJ	92
7.2.3	Re-weighting of AHJ	93
7.2.4	Variables distributions after re-weighting AHJ	93
7.2.5	Fractions of DPS after re-weighting AHJ	94

Contents

7.3	Double parton scattering fraction in AHJ	94
7.4	Validation of overlay method	100
7.5	Validation of fit procedure	101
8	Uncertainties	104
8.1	Statistical uncertainty	104
8.2	Systematic uncertainties	105
8.2.1	Uncertainty due to the re-weighting of AHJ	105
8.2.2	Uncertainty due to single-vertex events selection	105
8.2.3	Jet reconstruction efficiency uncertainty	106
8.2.4	Uncertainty on the jet energy scale	106
8.2.5	Jet energy and angular resolution uncertainty	110
8.3	Stability checks	112
9	Results	113
9.1	Determination of σ_{eff}	113
9.2	Characteristics of DPS events	117
9.2.1	Parton kinematics	117
9.2.2	Charged particle multiplicity	121
10	Summary and conclusions	124
	Appendix	125
A	Additional figures	125
A.1	Distributions of the input variables in the three samples	125
A.2	Variables distributions in data compared to fit results	130
A.3	Distributions of x^{obs} in data and AHJ	135
	Bibliography	137

Introduction

The Standard Model of particle physics (SM) [1–4] is one of the greatest achievements of modern physics. It provides a unified picture of the fundamental constituents of matter and combines the three interactions that mediate the dynamics of subatomic particles, the electromagnetic, weak and strong interactions. With the discovery of the Higgs boson at the LHC [5–11], all of the particles in the SM have now been discovered.

The SM contains 26 free parameters (including the parameters of the neutrino sector); it has been tested in numerous measurements and has been shown to successfully describe high energy particle interactions. Data from precision measurements of the Z -pole parameters, performed at LEP and at SLAC [12], may be used to predict the W boson and top quark masses, where the latter prediction is obtained through radiative corrections evaluated in the framework of the SM. Global fits of the electroweak sector of the SM [13] provide predictions for additional electroweak observables. Comparing these indirect constraints to direct measurements provides a stringent test of the SM. The latest prediction of the SM confirmed recently is the existence of the Higgs boson, the last piece of the SM puzzle.

With these successes, the validity of the SM at energies up to the electroweak scale has been firmly established. However, the remaining unanswered questions point to the fact that the SM is not the complete fundamental theory sought after. One of the four fundamental forces in the universe, gravitation, described by general relativity, is not included in the SM. Attempts to unify general relativity with the SM have been unsuccessful thus far. The SM does not provide an explanation for the accelerated expansion of the universe, as observed in cosmological measurements, nor does it contain a viable candidate for dark matter, necessary to account for the orbital velocities of stars in the Milky Way. Measurements of neutrino oscillations imply that neutrinos have non-zero mass, whilst in the “classic” SM they are massless. The observed matter-antimatter asymmetry of the universe is not explained by the SM. These inadequacies of the SM lead to the current view of it as an effective field theory that is valid at low energy scales where measurements have been performed so far, but which arises from a more fundamental theory at higher energy scales.

The research conducted at the Large Hadron Collider (LHC) at CERN is at the forefront of particle physics as well as at the energy frontier. Any study performed at the LHC, be it the investigation of the properties of the Higgs boson or the search for new phenomena beyond the SM, requires a detailed understanding of the strong interactions, described by Quantum Chromodynamics (QCD). This is due to the fact that in proton–proton (pp) collisions at high energy, the rate of strong interactions is orders of magnitude higher than any other interaction.

Strong interactions involve partons (quarks and gluons), yet partons are never visible in their own right. Almost immediately after being produced, gluons and quarks fragment into other quarks and gluons, or quarks decay semi-leptonically into other quarks, which in turn form hadrons, leading to a collimated spray of energetic hadrons referred to as a *jet*. As a result, jet production is the dominant process in pp collisions and jets often accompany the production of other SM particles. The high rate of jet production provides an ideal avenue to probe QCD and parton distribution functions (PDF) [14–16], which describe the longitudinal distribution of the momenta of quarks and gluons

1 Introduction

within a proton. The transverse distribution of the partons within the proton has yet to be measured, though at low energies there is an ongoing program attempting to extract it [17–27].

Most studies of pp collisions consider a single hard interaction occurring between two partons in the colliding protons, where “hard” refers to a minimum momentum transfer in the interaction of the order of a few GeV^2 . However, when two hadrons collide at high energy, there is a possibility that more than one parton in one of the hadrons will interact with partons in the other hadron. The importance of such multi-parton interactions (MPI) has been realized long ago [28,29]. At high energy colliders such as the Tevatron, with a center-of-mass energy, \sqrt{s} , ranging between 1.8 – 1.96 TeV, and the LHC ($\sqrt{s} = 7 - 13$ TeV), MPI are a potential source of multi-jet and/or multi-lepton events and therefore constitute a source of background in particular for rare physics processes. Multi-parton interactions may also provide the option to investigate the transverse structure of the proton [30].

In hadronic collisions, MPI are an inseparable part of a wider phenomenon called the underlying event (UE). The UE is defined as any hadronic activity that cannot be attributed to the particles originating from the hard scattering. In this sense the UE consists of MPI and the hadronization of beam remnants. Most of these interactions are soft, at scales below ~ 1 GeV^2 , and generally do not result in jets with high transverse momenta (p_T). However, the high energy available at the LHC and the high density of partons accessible with low fraction of the proton momenta, enhance the probability of hard MPI relative to past experiments [31]. The expected abundance of MPI phenomena at the LHC and their importance for the full picture of hadronic collisions has led to many phenomenological estimates of the MPI contribution in various final states such as four jets [31–39], four jets including b-jets [31, 40, 41], jets associated with photons or leptons [42], four leptons produced in double Drell-Yan processes [43] as well as in a number of channels with electroweak gauge bosons [44–50].

The existing phenomenology of MPI is based on several simplifying assumptions, since such interactions cannot be completely described by perturbative quantum chromodynamics (pQCD). Recent interest has produced some advances [51–70], however, a systematic treatment within QCD remains to be developed. The simplest case of MPI is that of double parton scattering (DPS). The rate of DPS is characterized by the so-called effective cross-section, σ_{eff} , which is related to the degree of overlap between the interacting hadrons in the plane perpendicular to the direction of motion. In principle, it holds information about the transverse density distributions of partons in the proton and about the correlations between partons.

Measurements of DPS have been performed at energies between 63 GeV and 1.96 TeV in the four-jet and γ + three-jets channels [71–76]. At the LHC, manifestations of DPS have been measured in the W + two-jet final state using 7 TeV data by the ATLAS [77] and CMS [78] collaborations. Estimations of σ_{eff} were performed by the LHCb collaboration in the observation of double charm production involving open charm, using 7 TeV data [79]. In the measurement of four-jet production performed by the CMS collaboration [80], contributions from DPS were found to improve the agreement between distributions extracted from data and Monte Carlo predictions. Table 1.1 summarizes the existing measurements of σ_{eff} .

In this analysis, the DPS rate is studied in the four-jet final state in pp collisions at $\sqrt{s} = 7$ TeV, using a data sample of (37.3 ± 1.3) pb^{-1} with an average number of interactions per bunch crossing, $\langle \mu \rangle = 0.41$, collected at the LHC with the ATLAS experiment during 2010. The four-jet final state may arise due to a single parton-parton collision (SPS), accompanied by additional radiation.

Experiment	\sqrt{s} (GeV)	Final state	σ_{eff}
AFS (pp), 1986 [71]	63	4 jets	~ 5 mb
UA2 ($p\bar{p}$), 1991 [72]	630	4 jets	> 8.3 mb (95% C.L.)
CDF ($p\bar{p}$), 1993 [73]	1800	4 jets	$12.1^{+10.7}_{-5.4}$ mb
CDF ($p\bar{p}$), 1997 [74]	1800	γ + 3-jets	$14.5 \pm 1.7^{+1.7}_{-2.3}$ mb
DØ ($p\bar{p}$), 2010 [75]	1960	γ + 3-jets	$16.4 \pm 0.3 \pm 2.3$ mb
LHCb (pp), 2012 [79]	7000	$D^0 D^0$	$21 \pm 1.5 \pm 2$ mb
LHCb (pp), 2012 [79]	7000	$D^0 \bar{D}^0$	$2.35 \pm 0.05 \pm 0.20$ mb
LHCb (pp), 2012 [79]	7000	$D^0 D^+$	$23.5 \pm 3.5 \pm 2$ mb
LHCb (pp), 2012 [79]	7000	$D^0 D^-$	$3.00 \pm 0.1 \pm 0.25$ mb
LHCb (pp), 2012 [79]	7000	$D^0 D_s^+$	$18 \pm 4 \pm 2$ mb
LHCb (pp), 2012 [79]	7000	$D^0 D_s^-$	$2.80 \pm 0.25 \pm 0.30$ mb
LHCb (pp), 2012 [79]	7000	$D^0 \bar{\Lambda}_c^-$	$4.5 \pm 1.0 \pm 0.5$ mb
LHCb (pp), 2012 [79]	7000	$D^+ D^+$	$33.0 \pm 5.5 \pm 3.5$ mb
LHCb (pp), 2012 [79]	7000	$D^+ D^-$	$3.20 \pm 0.20 \pm 0.35$ mb
LHCb (pp), 2012 [79]	7000	$D^+ D_s^+$	$29.5 \pm 7.5 \pm 3.0$ mb
LHCb (pp), 2012 [79]	7000	$D^+ D_s^-$	$3.5 \pm 0.5 \pm 0.5$ mb
LHCb (pp), 2012 [79]	7000	$D^+ \Lambda_c^+$	$70 \pm 35 \pm 10$ mb
LHCb (pp), 2012 [79]	7000	$D^+ \bar{\Lambda}_c^-$	$7.5 \pm 2.0 \pm 1.0$ mb
LHCb (pp), 2012 [79]	7000	$J/\psi D^0$	$14.9 \pm 0.4 \pm 1.1^{+2.3}_{-3.1}$ mb
LHCb (pp), 2012 [79]	7000	$J/\psi D^+$	$17.6 \pm 0.6 \pm 1.3^{+2.8}_{-3.7}$ mb
LHCb (pp), 2012 [79]	7000	$J/\psi D_s^+$	$12.8 \pm 1.3 \pm 1.1^{+2.0}_{-2.7}$ mb
LHCb (pp), 2012 [79]	7000	$J/\psi \Lambda_c^+$	$18.0 \pm 3.3 \pm 2.1^{+2.8}_{-3.8}$ mb
ATLAS (pp), 2013 [77]	7000	W + 2 jets	$15 \pm 3^{+5}_{-3}$ mb
CMS (pp), 2014 [78]	7000	W + 2 jets	$20.7 \pm 0.8 \pm 6.6$ mb

Table 1.1: Summary of the published measurements of σ_{eff} at various center-of-mass energies (\sqrt{s}) and final states. The first quoted uncertainty is the statistical uncertainty and the second is the systematic uncertainty. In the case of the measurements involving J/ψ mesons in the final state, the third uncertainty is due to the unknown polarization of the prompt J/ψ mesons.

1 Introduction

Alternatively, it can also originate from two separate parton-parton collisions, each producing at least a pair of jets. The latter case is expected to have different characteristics from the former and thus the rate of DPS may be statistically estimated. Presented here is the extraction of the rate of DPS and the corresponding σ_{eff} , using Monte Carlo to represent the topology of four jets arising from SPS and under the assumption that the four-jet topology originating from DPS can be represented by a random combination of dijet events.

Outline of the thesis

Following the short introduction given here, a theoretical overview of QCD and DPS is presented in [Chapter 2](#). The LHC and the ATLAS experiment, together with the trigger and jet reconstruction are described in [Chapter 3](#). A summary of Monte Carlo event generators and detector simulation is given in [Chapter 4](#). The event selection procedure is described in [Chapter 5](#). [Chapter 6](#) details the methodology adopted for the measurement of σ_{eff} and [Chapter 7](#) presents various validations of the methodology. The statistical and systematic uncertainties associated with the measurement are discussed in [Chapter 8](#). Finally, the results and conclusions are presented in [Chapters 9](#) and [10](#), respectively.

Theoretical background

2.1 The Standard Model of particle physics

The SM is a gauge quantum field theory (QFT) describing most elementary particles in nature and the interactions between them [81]. Each of the three forces of relevance to particle physics is described by a QFT corresponding to the exchange of an integer spin force-carrying particle, known as a gauge boson. The photon is the gauge boson responsible for electromagnetic interactions. In the case of the strong interaction, the force-carrying particle is the gluon which, like the photon, is massless. The weak interaction is mediated by three massive bosons, the W^\pm and Z bosons. The unification of the electromagnetic and weak interactions leads to a mixing of the physical photon with the Z boson. Within this unified model, referred to as the Glashow, Salam and Weinberg electroweak model [1–3], the couplings of the photon, the W^\pm and Z bosons are related via a mixing angle. The SM is based in the symmetry group $SU(3)_C \times SU(2)_L \times U(1)_Y$, where the electroweak sector is based in the $SU(2)_L \times U(1)_Y$ group, and the strong sector is based in the $SU(3)_C$ group.

The elementary particles in the SM are half-integer spin fermions, six quarks and six leptons. Both quarks and leptons carry the electroweak charge and hence interact via the electroweak force. Quarks may be classified depending on their electric charge Q ; quarks u , c and t have $Q = 2/3$ and quarks d , s and b have $Q = -1/3$. Quarks interact both via the strong interaction and via electroweak interactions. Electrons (e), muons (μ) and taus (τ) are massive leptons with an electric charge $Q = -1$. Their associated neutrinos, respectively ν_e , ν_μ and ν_τ , do not carry an electric charge. For each particle in the SM, there is an anti-particle with the same mass and quantum numbers, but with opposite electroweak charge (and opposite color charge in the case of quarks). The fundamental particles of the Standard Model, sorted according to family, generation and mass, are listed in Fig. 2.1.

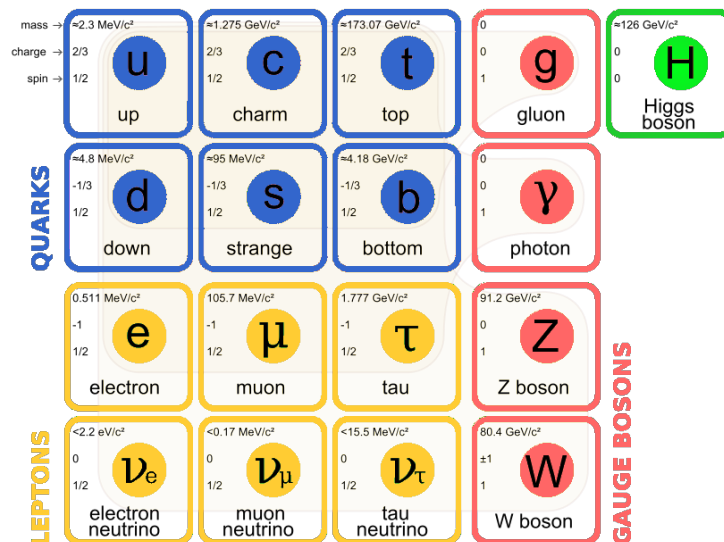


Figure 2.1: The fundamental particles of the Standard Model, sorted according to family, generation and mass.

2 Theoretical background

The SM formalism is based on local gauge invariance and its success in describing the experimental data places the local gauge invariance on a solid experimental basis. However, terms in the Lagrangian corresponding to particle masses break the required local gauge invariance. The Higgs mechanism of spontaneous symmetry breaking [82–87] provides a solution to this issue. Within this mechanism, the fermions and electroweak gauge bosons acquire masses through their interaction with the Higgs field. This field leads to the existence of a massive scalar boson, the Higgs boson, recently discovered at the LHC [5–11].

The existence of the Higgs boson also provides a solution to the violation of the cross-section unitarity in $W^+W^- \rightarrow W^+W^-$ scattering, the Feynman diagrams of which are shown in Fig. 2.2. The unitarity violation may be cancelled by the Feynman diagrams involving the exchange of a scalar particle, the Higgs boson, as shown in Fig. 2.3.

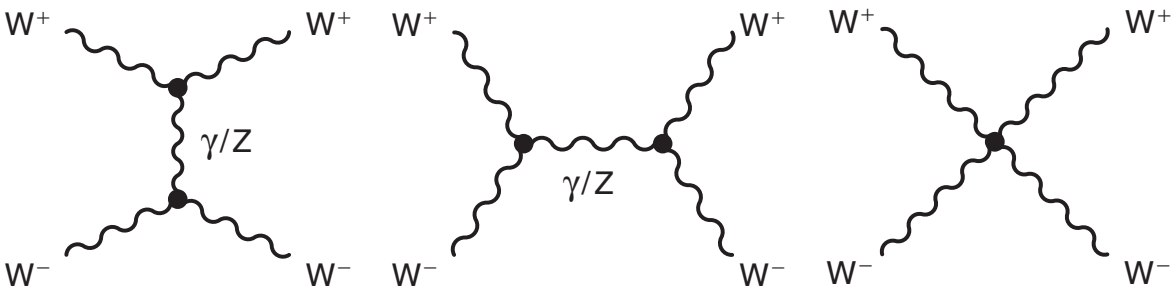


Figure 2.2: The lowest-order Feynman diagrams for $W^+W^- \rightarrow W^+W^-$ scattering.

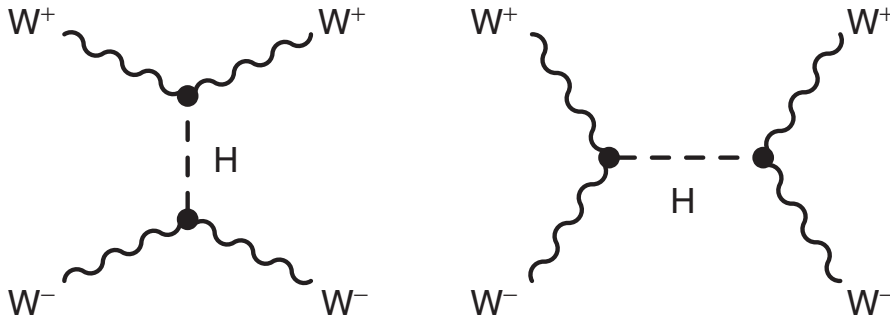


Figure 2.3: Feynman diagrams for Higgs boson exchange in $W^+W^- \rightarrow W^+W^-$ scattering.

2.2 Strong interactions

The QFT describing strong interactions is Quantum Chromodynamics [88]. Its development began in the 1950s, when a large number of particles (hadrons) were discovered. Attempts at sorting the hadrons into groups of similar properties led to the *Eightfold Way* [89–91] framework, invented by Murray Gell-Mann and Yuval Ne’eman, organizing the particles into octet groups. The Eightfold Way was successful in describing the new particles in a symmetry scheme based on the $SU(3)$ group. Subsequently, Gell-Mann [92] and George Zweig [93], went on to propose that the structure of the

groups could be explained by the existence of three smaller particles inside the hadrons. Gell-Mann referred to these smaller particles as quarks, but since they were never observed as free particles, he considered them to be merely convenient mathematical constructs, not real particles. Later deep inelastic scattering (DIS) experiments [94] confirmed the existence of point-like fermions within the hadron. Based on these collision experiments and the scaling observations made by James Bjorken [95], Richard Feynman proposed the parton model [96], suggesting that quarks are real particles composing hadrons. It was also postulated that quarks carried a new quantum number called color [97,98], which could explain certain puzzles such as the apparent symmetry of the wave function of the lightest hadron composed of three quarks (a baryon), the rate for $\pi^0 \rightarrow 2\gamma$ and later on the rate for $e^+e^- \rightarrow \text{hadrons}$. The first circumstantial evidence for the existence of the neutral gluons was found by measuring the total fraction of the proton momentum carried by the quarks. Gluons were later found to be spin 1 bosons by studying the angles between three jets produced in $e^+e^- \rightarrow qqg$ interactions [99, 100]. In QCD, gluons mediate strong interactions between quarks, carrying a combination of color and anti-color charge.

Quantum Chromodynamics was established as a theoretical framework for strong interactions only following the discovery of asymptotic freedom as a consequence of the renormalisability of the theory [101, 102]. A short overview of the features of QCD follows.

2.2.1 Color confinement

Colored particles are never observed directly; they are confined to color singlet states. This is referred to as the *color confinement* hypothesis, believed to originate from gluon–gluon self-interactions. There is currently no analytic proof of the concept of color confinement. However, a qualitative understanding of the likely origin may be obtained by considering the case in which two free quarks are pulled apart. The interaction between the quarks may be thought of in terms of the exchange of virtual gluons. Since gluons carry a color charge, there are attractive interactions between the virtual gluons being exchanged. A schematic illustration of these gluon–gluon interactions is shown in Fig. 2.4. The effect of these interactions is the squeezing of the color field between the quarks into

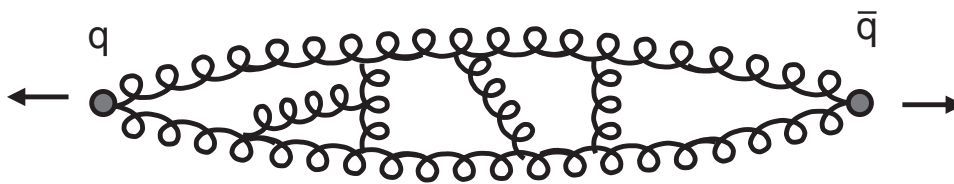


Figure 2.4: Schematic of the effect of gluon–gluon interactions on the long-range strong force.

a tube. At relatively large distances, the energy density in the tube between the quarks containing the gluon field is constant. Therefore, the energy stored in the field is proportional to the separation between the quarks, giving a term in the potential of the form

$$V(\vec{r}) \sim \kappa r, \quad (2.1)$$

where κ is determined experimentally to be $\kappa \sim 1 \text{ GeV/fm}$. The value of κ corresponds to a force of about 10^5 N between two unconfined quarks. As the energy stored in the color field increases linearly with distance, an infinite amount of energy would be required to separate two quarks. As a result,

2 Theoretical background

quarks are confined into bound hadronic states that are colorless combinations of quarks/anti-quarks. Since gluons carry a color charge, they are also confined to colorless hadrons and do not propagate over macroscopic distances (unlike the photon).

A consequence of color confinement is that quarks and gluons do not propagate freely and are observed as jets of colorless particles. The process by which high-energy quarks and gluons produce jets is known as hadronization and it may be described qualitatively as follows:

- i a quark and anti-quark produced in the interaction initially separate at high velocities;
- ii as they separate, the color field is restricted to a tube with high energy density;
- iii as the quarks separate further, the energy stored in the color field is sufficient to form new $q\bar{q}$ pairs, breaking the color field into shorter “strings”;
- iv this process continues, producing more $q\bar{q}$ pairs, until all the quarks and anti-quarks have sufficiently low energy to combine and form colorless hadrons.

The hadronization process results in two collimated spray of energetic hadrons, referred to as jets, one following the initial quark direction and the other the initial anti-quark direction. Hence, in high-energy collisions, quarks and gluons are always observed as jets of hadrons. The process of hadronization is not understood from first principals. However, a number of phenomenological models exist, providing a reasonable description of experimental data.

2.2.2 Running coupling and asymptotic freedom

At low-energy scales, the coupling constant of QCD is relatively large, $\alpha_S \sim O(1)$. Consequently, perturbation theory cannot be applied to QCD at low energies. However, α_S is not constant; its value depends on the energy scale of the interaction. At high energies, α_S becomes sufficiently small ($\alpha_S \sim 0.1$), such that perturbation theory may be used. In this way, QCD divides into a non-perturbative low-energy regime, where first-principles calculations are not currently possible, and a high-energy regime where predictions are calculable using perturbation theory. The running of α_S is closely related to renormalization.

Renormalization in the context of particle physics is a technique used to treat infinite integrals arising in calculations in perturbation theory. In QCD, higher-order corrections to the propagator in the $q\bar{q} \rightarrow q\bar{q}$ interaction would lead to a divergence of the cross-section. These corrections are due to infinite contributions from loop diagrams such as the ones shown in Fig. 2.5. A renormalization procedure is necessary in order to absorb these infinities and allow the theory to give meaningful results, comparable with experimental measurements. This is achieved by effectively subtracting these infinities through counter-terms embedded in so-called bare parameters that are not measurable. The renormalization procedure introduces a correction to the renormalised parameter, depending on the renormalization scale, μ_R , (interpreted as the scale at which the subtraction is made), and on the physical scale at which the measurement is made. The latter is taken as the squared momentum transfer $|q^2|$ (Q^2). The renormalization scale is usually chosen to be of the order of Q^2 . However, the renormalization scale in itself is not a physical quantity. The physical predictions of the theory, calculated to all orders, should in principle be independent of the choice of the renormalization scale. This fact can be exploited in order to calculate the effective variation of α_S with changes in scale. In

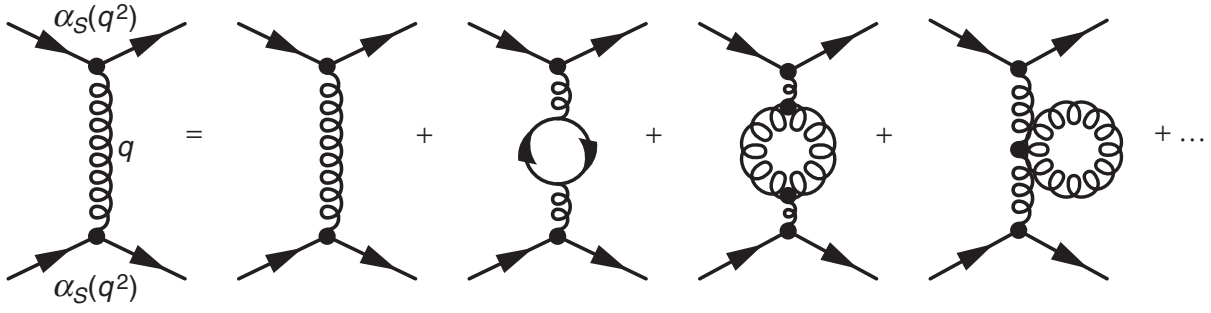


Figure 2.5: Loop diagrams contributing to the propagator in the $qq \rightarrow qq$ interaction at squared momentum transfer q^2 .

the one loop approximation (first order in perturbation theory), the evolution of α_S with the scale Q^2 is given by,

$$\alpha_S(Q^2) = \frac{\alpha_S(\mu_R^2)}{1 + \beta_1 \alpha_S(\mu_R^2) \ln(Q^2/\mu_R^2)} = \frac{1}{\beta_1 \ln(Q^2/\Lambda_{\text{QCD}}^2)}, \quad (2.2)$$

where

$$\Lambda_{\text{QCD}}^2 = \mu_R^2 \exp\left(-\frac{1}{\beta_1 \alpha_S(\mu_R^2)}\right) \quad (2.3)$$

sets the scale of the coupling constant of QCD. The parameter β_1 is the first term in the *beta function* of the strong coupling constant,

$$\beta(\alpha_S) = -\beta_1 \alpha_S^2(\mu^2) \left(1 + \beta_2 \alpha_S(\mu^2)\right) + \mathcal{O}(\alpha_S^4(\mu^2)), \quad (2.4)$$

which encodes the dependence of α_S on the energy scale. The first term, β_1 , is

$$\beta_1 = \frac{11N_c - 2N_f}{12\pi}, \quad (2.5)$$

where N_c and N_f are the number of colors and flavors, respectively. For $N_c = 3$ and $N_f \leq 6$ quarks, β_1 is greater than zero and hence α_S *decreases* with increasing Q^2 . Therefore, the coupling constant is sizeable at low values of Q^2 , leading to confined partons, and as it decreases with increasing Q^2 it leads to *asymptotic freedom* [101, 102]. Consequently, at high Q^2 (small distances), quarks and gluons behave as if they were free and perturbative theory is applicable. The current theoretical and experimental results for the running α_S are shown in Fig. 2.6 [103].

2.2.3 Parton distribution functions

The presence of free quarks within the proton was first observed in DIS experiments performed at the Stanford Linear Accelerator Center (SLAC) [94]. Electrons of energies between 5 GeV and 20 GeV were fired at a liquid hydrogen target. The scattering angle of the electron was measured using a large movable spectrometer, in which the energy of the detected final-state electrons could be selected by using a magnetic field. The differential cross sections, measured over a range of incident electron energies, were used to determine the structure of the proton via the so-called *structure functions*.

2 Theoretical background

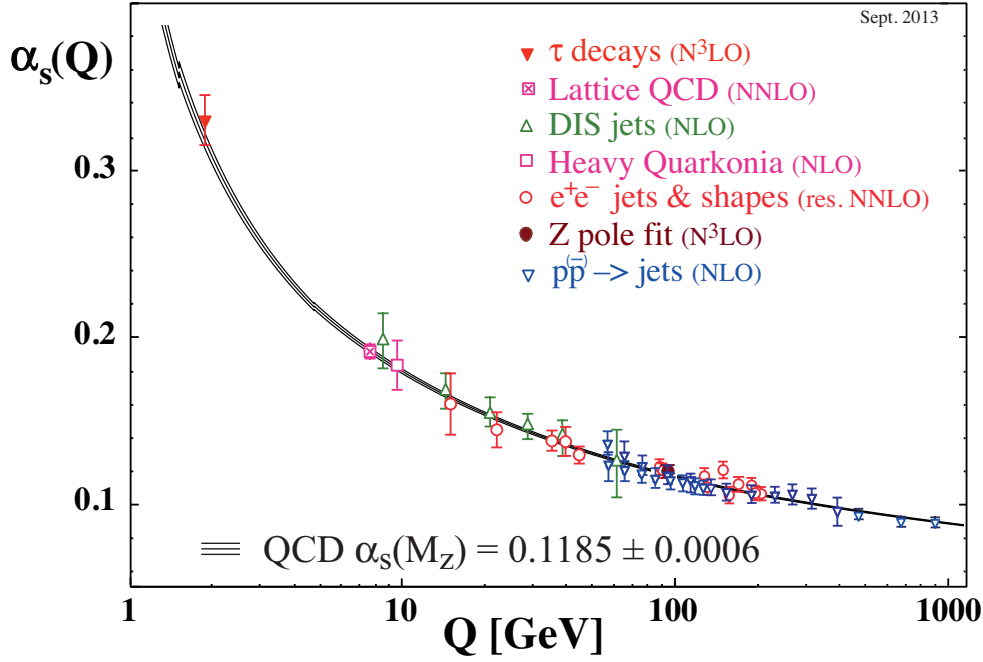


Figure 2.6: Summary of the current measurements of α_s as a function of the energy scale Q (markers) and the theoretical prediction for the dependence of α_s on Q (black line). The respective degree of QCD perturbation theory used in the extraction of α_s is indicated in brackets. (Figure taken from [103].)

The differential cross-section for electron–proton (e^-p) inelastic scattering, under the assumption $Q^2 \gg y^2 m_p^2$, may be written as

$$\frac{d^2\sigma^{e^-p}}{dx dQ^2} \approx \frac{4\pi\alpha}{Q^4} \left(y^2 F_1(x, Q^2) + \frac{1-y}{x} F_2(x, Q^2) \right), \quad (2.6)$$

where α is the fine-structure constant and $F_1(x, Q^2)$ and $F_2(x, Q^2)$ are the structure functions. The latter are parametrized in terms of the momentum transfer, Q^2 , and of x , which represents (at leading-order) the fraction of proton longitudinal momentum carried by the massless struck quark. The parameter y is the fractional energy lost by the electron in the scattering process in the frame where the proton is initially at rest and m_p is the mass of the proton.

The experimental data revealed two striking features of the structure functions. The first observation, known as *Bjorken scaling*, was that both $F_1(x, Q^2)$ and $F_2(x, Q^2)$ are (almost) independent of Q^2 , allowing the structure functions to be written as

$$F_1(x, Q^2) \rightarrow F_1(x) \quad \text{and} \quad F_2(x, Q^2) \rightarrow F_2(x). \quad (2.7)$$

The lack of Q^2 dependence of the structure functions is strongly suggestive of scattering from point-like constituents within the proton. This is equivalent to the onset of $\sin^{-4}(\theta/2)$ behavior for large momentum transfers in the Rutherford experiment, which revealed the “point” charge of the nucleus in the atom, where θ is the scattering angle of the incident α particle.

The second observation was that in the DIS regime, $Q^2 \sim \mathcal{O}(10)$ GeV², the structure functions $F_1(x)$ and $F_2(x)$ are not independent, but satisfy the Callan-Gross relation [104]

$$F_2 = 2xF_1. \quad (2.8)$$

This observation can be explained by assuming that the underlying process in electron–proton inelastic scattering is the elastic scattering of electrons from point-like spin-half constituent particles within the proton, namely the quarks.

The quarks inside the proton interact with each other through the exchange of gluons. The dynamics of this interacting system result in a distribution of quark momenta within the proton. These distributions are expressed in terms of *parton distribution functions*. The structure function F_2 may be written as

$$F_2 = \sum_i^{N_q} e_i^2 x f_i(x), \quad (2.9)$$

where e_i^2 and $f_i(x)$ are respectively the squared electric charge and momentum distribution of the i^{th} quark, and the sum goes over all quarks in the hadron (in total N_q quarks). The $f_i(x)$ functions are the PDFs which can be interpreted (at leading order of perturbation theory) as the probability densities of finding a quark with flavor i , carrying a fraction x of the proton longitudinal momentum.

Since $f_i(x)$ reflects a probability, the following relation is required:

$$\int_0^1 x \sum_i^{N_q} f_i(x) dx = 1. \quad (2.10)$$

This relation is referred to as the *momentum sum rule*. However, in DIS measurements, the measured integral of Eq. (2.10) comes up to be about 0.5. This was the first hint for the presence of gluons within the proton, carrying about half of the momentum of the proton. Conventionally, partons composing a hadron are divided between gluons, *valence quarks* and *sea quarks*. Valence quarks are responsible for the quantum numbers of the hadron, while sea quarks are quark/anti-quark pairs that are generated due to quantum fluctuations.

The interactions among the partons within the proton lead to a deviation from the naive parton model in terms of *scaling violations*. The latter have been observed experimentally, as seen in Fig. 2.7, where measurements at a given value of x are shown to depend on Q^2 . At high (low) values of x , the proton structure function is observed to decrease (increase) with increasing Q^2 . This implies that at high Q^2 the proton is observed to have a greater fraction of low x quarks. Qualitatively, this could be described as follows: at low Q^2 , the wavelength of the virtual photon is too long to resolve the spatial sub-structure of the proton. At higher values of Q^2 , corresponding to shorter-wavelengths of the virtual photon, it is possible to resolve finer detail. In this case, the DIS process is sensitive to the effects of quarks radiating virtual gluons, $q \rightarrow qg$, gluons radiating gluons, $g \rightarrow gg$, and gluons producing quark/anti-quark pairs $g \rightarrow q\bar{q}$. Consequently, more low- x quarks are “seen” in high- Q^2 deep inelastic scattering.

The HERAPDF2.0 PDF parameterization, obtained using measurements of deep inelastic $e^\pm p$ scattering at HERA [105], for gluons (xg), valence up (xu_v) and down (xd_v) quarks and sea (xS) quarks is shown in Fig. 2.8. Because gluons with large momenta are suppressed by the gluon $1/Q^2$ propagator, sea quarks and gluons tend to be produced at low x values, as seen in Fig. 2.8.

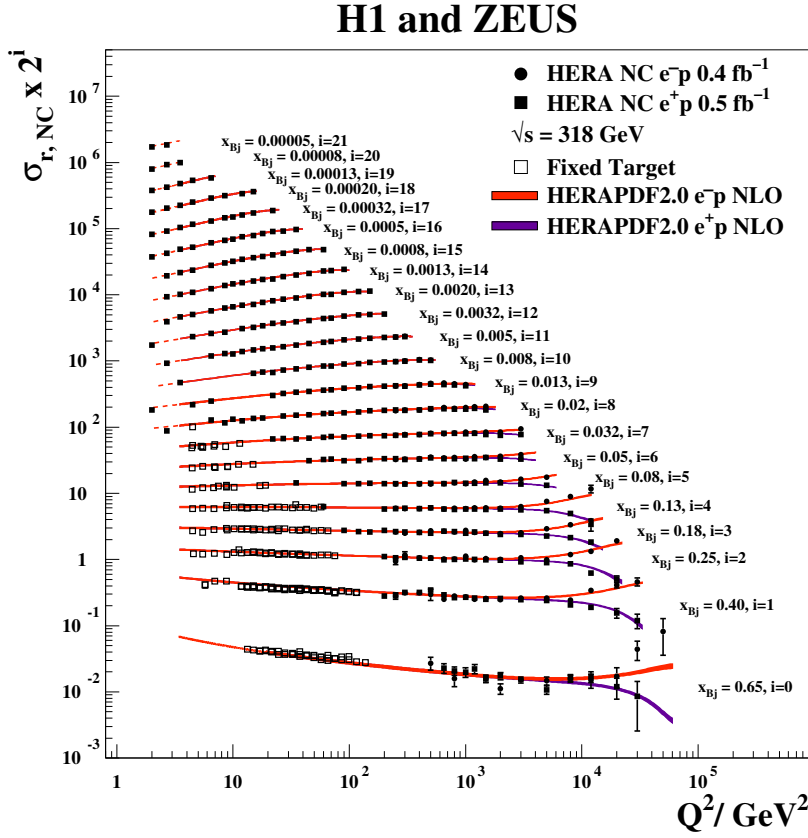


Figure 2.7: The combined HERA data for the inclusive neutral current (NC) $e^\pm p$ reduced cross-sections together with fixed-target measurements and the predictions of the HERAPDF2.0 NLO parameterization [105] as a function of momentum transfer, Q^2 , at fixed values of Bjorken- x . The bands represent the total uncertainties on the predictions. Dashed lines indicate extrapolation into kinematic regions not included in the fit. (Figure taken from [105].)

The DGLAP (Dokshitzer, Gribov, Lipatov, Altarelli and Parisi) formalism [106–108] models the $q \rightarrow qg$, $g \rightarrow gg$, and $g \rightarrow q\bar{q}$ interactions through splitting functions, and uses them to perturbatively evolve the renormalised parton densities that contain the Q^2 dependence. Hence, even though currently it is not possible to calculate the proton PDFs from first principles within the theory of QCD, the Q^2 dependence of the PDFs is calculable. The implication of PDF evolution is that measuring parton distributions at one scale, μ_0 , allows their prediction at any other scale, μ_1 , as long as both μ_0 and μ_1 are large enough for both $\alpha_S(\mu_0)$ and $\alpha_S(\mu_1)$ to be small.

It should be noted that PDFs parameterize the longitudinal momentum distributions of the partons in the proton, but offer no information about the transverse motion or spatial distribution of the partons, which are integrated over. Recent years have seen a growing number of attempts to include the momentum distribution in the plane perpendicular to the direction of motion [109–112]. A number of experiments [17–27] study the nucleon partonic structure through the so-called Semi-Inclusive Deep Inelastic Scattering processes ($\ell N \rightarrow \ell h X$), in which one observes in the final state,

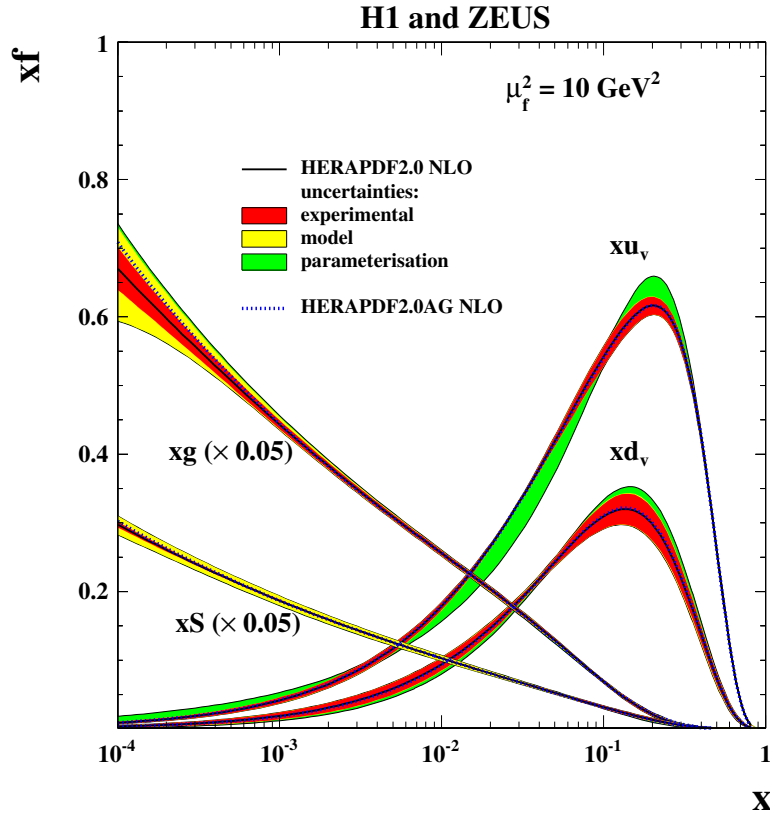


Figure 2.8: The parton distribution functions for gluons (xg), valence up (xu_v) and down (xd_v) quarks and sea (xS) quarks of the HERAPDF2.0 next-to-leading-order (NLO) parameterization [105] at a factorization scale, $\mu_f^2 = 10 \text{ GeV}^2$ (see Section 2.2.4 for definition), as a function of x . The gluon and sea distributions are scaled down by a factor of 20. The experimental, model and parameterization uncertainties are shown. (Figure taken from [105].)

in addition to the lepton, also one hadron, e.g. a pion. In this case, the hadron, which results from the fragmentation of a scattered quark, “remembers” the original motion of the quark, including the transverse motion, and offers new information. Such measurements, and in principle measurements of MPI, may provide the option to expand the concept of PDFs to include correlations between the partons in the transverse plane.

2.2.4 QCD factorization

Calculations in QCD are possible only in the high-energy regime, where perturbation theory applies. However, high energy pp collisions involve processes occurring both at high and low energy scales. The QCD *factorisation theorem* [113, 114] allows the separation of the two components in cross-section calculations. Similarly to renormalization, the factorization procedure is used to absorb singularities produced by massless partons into the (unobserved) bare PDFs. A new scale, μ_F^2 , called the *factorisation scale*, is introduced in addition to the renormalization scale μ_R^2 and the momentum

2 Theoretical background

transfer, Q^2 . Both μ_R^2 and μ_F^2 are typically chosen to be of the order of Q^2 , however physical cross-sections should not be affected by the choice of scales.

Using factorization, the cross-section for the process $ij \rightarrow X$ may be written as

$$d\sigma_{ij \rightarrow X}(x_i, x_j, Q^2) = \sum_{ij} \int dx_i dx_j f_i(x_i, \mu_F^2) f_j(x_j, \mu_F^2) \times d\hat{\sigma}_{ij \rightarrow X}(\alpha_S(\mu_R^2), Q^2/\mu_R^2), \quad (2.11)$$

where $\sigma_{ij \rightarrow X}$ and $\hat{\sigma}_{ij \rightarrow X}$ are the “full” hadronic and partonic cross-sections, respectively, for the $ij \rightarrow X$ interaction. The $\hat{\sigma}_{ij \rightarrow X}$ partonic cross-section is calculable in perturbative QCD. The functions $f_i(x_i, \mu_F^2)$ and $f_j(x_j, \mu_F^2)$ are the PDFs for partons i and j , respectively, and μ_F^2 is the factorization scale. The sum runs over the flavor of the partons in the proton. The factorization theorem implies that the PDFs observed experimentally are universal and process independent. Once they are derived from a particular measurement, they may be used in Eq. (2.11) for other processes. Full cross-section calculations are therefore possible within the QCD framework.

2.3 Phenomenological models of pp collisions

Thus far, pp collisions were described only in the context of two quasi-free partons interacting. While it is possible to calculate and give predictions for cross-sections involving the interaction between two partons, final states of pp collisions at the LHC are more complex and include many particles and non-perturbative effects. Monte Carlo techniques in event generators are most commonly used to simulate the full picture of the collision in order to obtain predictions of experimental observables. Event generators use phenomenological models to describe the low scale aspect of the collision. A description of these models is given in the following sections.

2.3.1 Parton showers

The hard scattering is calculated in pQCD at a fixed order in α_S . Usually leading-order (LO) calculations are used, although in recent years many final states calculations were expanded to next-to-leading-order (NLO). At leading-order, only $2 \rightarrow 2$ diagrams are included, such as the ones shown in Fig. 2.9 for dijet production. The ALPGEN event generator [115] (see Section 4.1.2) is able to provide tree-level matrix elements for hard multi-parton processes ($2 \rightarrow n$).

Once the hard scattering is simulated starting from the matrix element calculation that includes the convolution with the PDF, subsequent radiation is simulated using a series of probabilities for partons to split. This approach is called the parton shower approximation and it serves as approximate higher-order corrections to the hard process. The parton shower algorithm is typically formulated as an evolution in momentum transfer down from the high scales associated with the hard process to the low scales, of order 1 GeV^2 , associated with confinement of the partons into hadrons. In each step (scale), the probabilities $P_{q\bar{q}}$, P_{gq} , P_{qg} and P_{gg} corresponding to the collinear splittings $g \rightarrow q\bar{q}$, $g \rightarrow gq$, $q \rightarrow qg$ and $g \rightarrow gg$, respectively, are estimated. These probabilities are governed by the DGLAP splitting kernels [108] and they are dependent on the flavor and spin of the parton.

For each parton participating in the hard interaction, the probability to be accompanied by a collinear splitting is used iteratively to generate one collinear splitting and then treating the final state of that

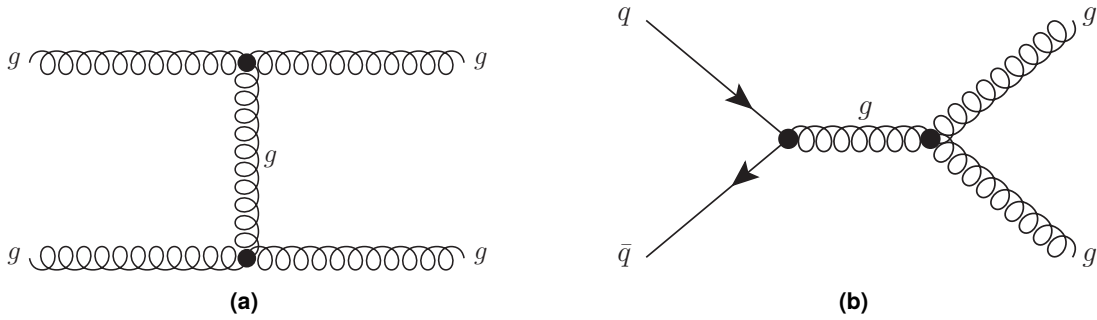


Figure 2.9: Examples for leading-order Feynman diagrams for dijet production in proton–proton collisions at the LHC, for (a) t -channel gluon scattering and (b) quark/anti-quark s -channel annihilation.

splitting as a new hard process, generating an even more collinear splitting from it, and so on. A collinear emission is required to be “resolvable”, i.e., $k_{\perp} > Q_0$, where k_{\perp} is the transverse momentum of the emitted parton and Q_0 is the cut-off scale. The latter is a parameter of the model which cuts both collinear and soft divergences. In order to avoid the scale where $\alpha_S \sim 1$, Q_0 has to be above Λ_{QCD} and it therefore becomes a physical parameter affecting observable distributions.

Virtual (loop) corrections are treated together with emissions below Q_0 (unresolvable) in the parton shower algorithm. The probabilities for unresolvable emissions, also known as *Sudakov form factors* [116], are derived from the splitting probabilities through unitarity. Wide angle soft gluon emission effects are taken into account in the collinear parton shower algorithm by ordering the emissions based on the angle.

Partons may radiate prior to the interaction and lose some of their momentum. This is referred to as initial state radiation. Initial state radiation is treated within the parton shower algorithm in a similar way to final state radiation, albeit with backward evolution (from low- x to high- x).

2.3.2 Matching the hard scatter with parton shower

Emissions in parton showers are limited from below in scale by Q_0 . However, a limit on the upper scale is also necessary in order to avoid double counting. A QCD $2 \rightarrow 2$ scattering accompanied by an emission from one of the external legs that is much harder than the hard scale gives the hard process a strong recoil that boosts one or both of its outgoing partons to a significantly higher transverse momentum. The outcome is a configuration that is indistinguishable from one that arises from a harder process accompanied by a softer emission from one of its external legs. This can be avoided by setting the upper limit of the parton shower evolution to the scale of the hard scattering. This is referred to as matching between the matrix element and parton showers. A number of matching algorithms were developed, such as the MLM matching scheme [117] and the CKKW merging algorithm [118, 119].

2.3.3 Hadronization

The hypothesis of local *parton-hadron duality* states that the momentum and quantum numbers of hadrons follow those of their constituent partons [120]. The two main models of hadronization in event generators, the string model and cluster model, follow this hypothesis. The string model [121] is based on the qualitative description of hadronization given in Section 2.2.1. The cluster model [122, 123] starts by splitting gluons non-perturbatively, $g \rightarrow q\bar{q}$ after the parton shower. Color-singlet $q\bar{q}$ combinations have lower masses and a universal spectrum due to the so-called *preconfinement* property [124] of the shower. These color-singlet combinations are assumed to form clusters, which mostly undergo simple isotropic decay into pairs of hadrons, chosen according to the density of states with appropriate quantum numbers. A schematic illustration of the string model and cluster model is shown in Figs. 2.10(a) and 2.10(b), respectively.

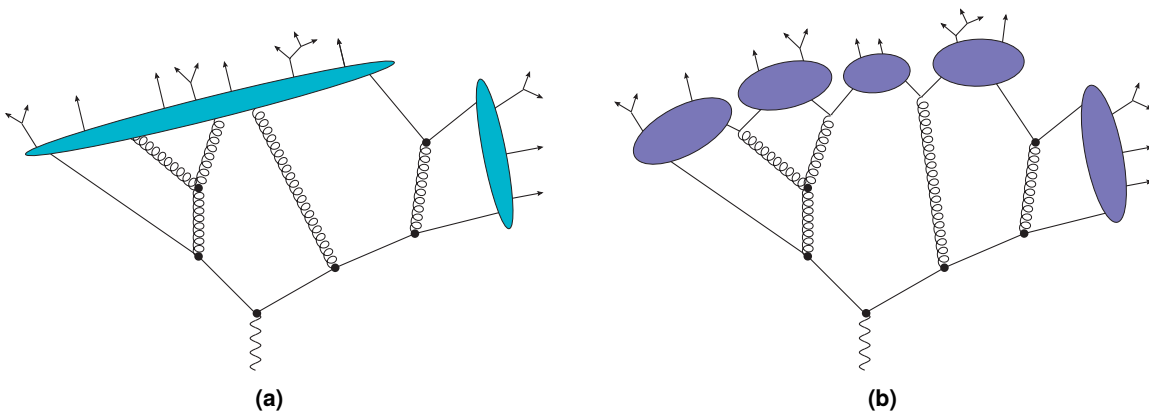


Figure 2.10: Schematic illustration of hadronization in the (a) string and in the (b) cluster models.

2.3.4 The underlying event

In order to perform measurements in pp collisions it is important to have a good understanding not only of the short-distance hard scattering process, but also of the accompanying activity, collectively referred to as the *underlying event* [125]. This includes partons not participating in the hard-scattering process (beam remnants), and additional scatters in the same proton–proton collision, termed multiple parton interactions. Initial and final state gluon radiation also contribute to the UE activity.

The soft interactions contributing to the UE cannot be calculated reliably using pQCD methods and are generally described using various phenomenological models in event generators. These models rely extensively on MPI for the description of the UE. A detailed description of the MPI model implemented in the JIMMY [126, 127] package for the HERWIG event generator is given in Section 4.1.2.

Underlying event models typically contain many parameters whose values and energy dependences are not known *a priori*. Therefore, the model parameters must be tuned to experimental data to obtain insight into the nature of soft QCD processes and to optimise the description of UE contributions for studies of hard-process physics. Since it is impossible to unambiguously separate the UE from the

hard scattering process on an event-by-event basis, measurements of various distributions sensitive to the properties of the UE are performed [128]. The parameters in event generators are then tuned such that their predictions simultaneously describe as many of the distributions as possible.

An additional way to gain insight into the nature of the UE is to study hard MPI. The simplest and most prominent case of hard MPI is that of hard double parton scattering. The latter refers to pp collisions in which two hard interactions occur simultaneously, each resulting in high- p_T particles. An overview of the phenomenology of DPS is given in the next section.

2.4 Double parton scattering phenomenology

The DPS phenomenology is based on the general expression for the differential double parton scattering cross-section in hadronic interactions at a center-of-mass energy \sqrt{s} , $d\hat{\sigma}_{(A,B)}^{\text{DPS}}(s)$,

$$d\hat{\sigma}_{(A,B)}^{\text{DPS}}(s) = \frac{1}{1 + \delta_{AB}} \sum_{i,j,k,l} \int \Gamma_{ij}(x_1, x_2, r_{\perp}; Q_A, Q_B) d\hat{\sigma}_{ik}^{(A)}(x_1, x'_1) d\hat{\sigma}_{jl}^{(B)}(x_2, x'_2) \times \Gamma_{kl}(x'_1, x'_2, r_{\perp}; Q_A, Q_B) dx_1 dx_2 dx'_1 dx'_2 d^2 r_{\perp}. \quad (2.12)$$

The two final states produced in the two hard partonic subprocesses are denoted by A and B and the subscript (A,B) refers to the production of both final states. The term $d\hat{\sigma}_{ik}^{(A)}$ ($d\hat{\sigma}_{jl}^{(B)}$) denotes the differential partonic cross-sections for the production of a system A (B) in the collision of partons i and k (j and l). The $\Gamma_{ij}(x_1, x_2, r_{\perp}; Q_A, Q_B)$ term represents the double parton distribution. It may be loosely interpreted as the inclusive probability distribution function to find a parton i (j) with longitudinal momentum fraction x_1 (x_2) at scale Q_A (Q_B) in the proton, with the two partons separated by a transverse distance r_{\perp} . The scale Q_A (Q_B) is given by the characteristic scale of subprocess A (B). The quantity δ_{AB} is the Kronecker delta used to construct a symmetry factor such that if $A = B$, the double parton scattering cross-section is divided by two. The integration over the momentum fractions x_1 and x_2 is constrained by energy conservation, such that $(x_1 + x_2 \leq 1)$. Summation over all possible parton combinations is performed. A sketch of double parton scattering in the four-jet final state is shown in Fig. 2.11 for illustration.

The expression given in Eq. (2.12) is often simplified by making two assumptions. First, it is assumed that the double parton distribution may be decomposed into a transverse and a longitudinal part,

$$\Gamma_{ij}(x_1, x_2, r_{\perp}; Q_A, Q_B) \simeq F(r_{\perp}) D_{ij}(x_1, x_2; Q_A, Q_B).$$

The longitudinal component, $D_{ij}(x_1, x_2; Q_A, Q_B)$, has a rigorous interpretation in leading-order pQCD as the double parton density function (dPDF). It quantifies the inclusive probability of finding a parton i with momentum fraction x_1 at scale Q_A in conjunction with a parton j with momentum fraction x_2 at scale Q_B in a proton. Predictions of double parton scattering cross-sections and of event signatures require modelling of $D_{ij}(x_1, x_2; Q_A, Q_B)$ and of the transverse component, $F(r_{\perp})$. Correlations in both longitudinal momenta and transverse positions may have to be taken into account in these functions.

Distribution of partons in the transverse region cannot be calculated using pQCD. Existing models typically use Gaussian or exponential forms (or their combination) to describe $F(r_{\perp})$ [129, 130].

2 Theoretical background

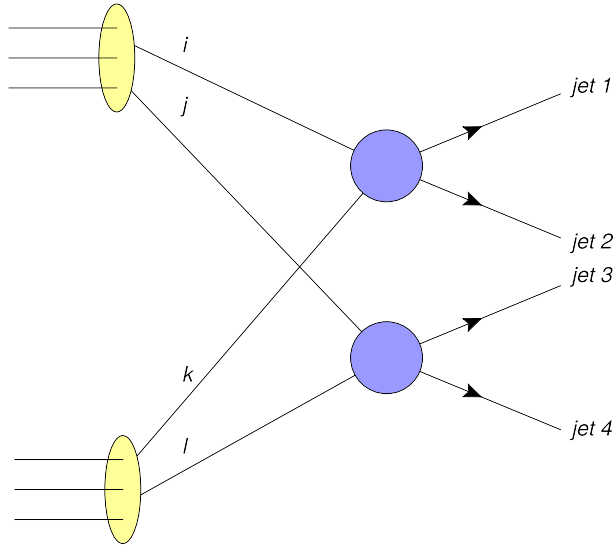


Figure 2.11: Sketch of a double parton scattering process in the four-jet final state, in which the active partons originating from one proton are i and j and from the other are k and l . Each interaction results in two outgoing partons (jets) such that $i + k \rightarrow \text{jet 1} + \text{jet 2}$ and $j + l \rightarrow \text{jet 3} + \text{jet 4}$.

Therefore the transverse component is effectively encoded through a phenomenological parameter with the units of an area or a cross-section, $\sigma_{\text{eff}}(s)$,

$$\sigma_{\text{eff}}(s) = \left[\int d^2r_{\perp} (F(r_{\perp}))^2 \right]^{-1}.$$

In this formalism, σ_{eff} is a universal scaling parameter, independent of the exact partonic process and the phase-space region considered, and rather a property of the colliding hadrons. Naively, it may be related to the geometrical size of the proton or, more accurately, to the transverse size of the region where hard interactions are localized. This leads to an estimate of $\sigma_{\text{eff}} \approx \pi R_p^2 \approx 50 \text{ mb}$, where R_p is the proton radius. Alternatively, σ_{eff} may be connected to the inelastic cross-section, which would lead to $\sigma_{\text{eff}} \approx \sigma_{\text{inel}} \approx 70 \text{ mb}$ at $\sqrt{s} = 7 \text{ TeV}$ [131, 132]. For hard interactions, assuming uncorrelated scatterings, σ_{eff} can be estimated from the gluon form factor of the proton [133] and comes out to be $\sim 30 \text{ mb}$. Connecting it, on the other hand, with the total or inelastic proton–proton cross-section would render it dependent on the center-of-mass energy of the hadronic collisions.

Using the above, the DPS cross-section reduces to

$$\begin{aligned} d\hat{\sigma}_{(A,B)}^{\text{DPS}}(s) &= \frac{1}{1 + \delta_{AB}} \frac{1}{\sigma_{\text{eff}}(s)} \sum_{i,j,k,l} \int D_{ij}(x_1, x_2; Q_A, Q_B) d\hat{\sigma}_{ik}^{(A)}(x_1, x'_1) \\ &\quad \times d\hat{\sigma}_{jl}^{(B)}(x_2, x'_2) D_{kl}(x'_1, x'_2; Q_A, Q_B) dx_1 dx_2 dx'_1 dx'_2. \end{aligned} \quad (2.13)$$

In the absence of a rigorous formalism, it is typically assumed that $D_{ij}(x_1, x_2; Q_A, Q_B)$ may be written as a product of single parton distribution functions (PDFs),

$$D_{ij}(x_1, x_2; Q_A, Q_B) \simeq D_i(x_1; Q_A) D_j(x_2; Q_B) (1 - x_1 - x_2) \Theta(1 - x_1 - x_2). \quad (2.14)$$

In general, this factorization ansatz is not expected to hold because of energy, momentum and spin conservation. It was also proved that even if such an ansatz works at some scale, the DGLAP evolution equation for the dPDFs will break this simple relation [53, 59]. However, at sufficiently low x values the corrections are assumed to be small, thus the equation above will provide a good approximation. This is in accordance with some experimental results [74], which also suggest that this factorization holds up to moderately low x .

Finally, using the assumptions above, the DPS cross-section can be expressed in the simple form

$$d\hat{\sigma}_{(A,B)}^{\text{DPS}} = \frac{1}{1 + \delta_{AB}} \frac{d\hat{\sigma}_A \cdot d\hat{\sigma}_B}{\sigma_{\text{eff}}}, \quad (2.15)$$

where the assumed dependence of σ_{eff} on s was dropped for simplicity.

As seen in Table 1.1, the measured values of σ_{eff} typically range from about 5 mb at the lowest energy to about 20 mb at LHC energies. Although some of the LHCb results [79] indicate much higher and much lower values, the origin of this spread is not yet understood. The difference between the measured value of σ_{eff} and the phenomenological estimates indicates the existence of correlation effects in the dPDFs of the proton. With the factorization ansatz of Eq. (2.14), the unknown correlations are absorbed into σ_{eff} , which then may become dependant on the process. This might explain the observed departure of the measured value of σ_{eff} from the simple expectations.

Further attempts to reconcile the difference between the expected value of σ_{eff} of 50-70 mb with the measured value of 10-20 mb introduce non-trivial correlations [51, 53], in particular in the impact parameter space [54]. One argument, suggested in Refs. [34, 58, 62, 63, 65] may resolve the discrepancy; it goes as follows: in DPS, two partons from one proton collide with two partons from the other proton. The two partons from a given proton can originate from the non-perturbative hadron wave-function or, alternatively, emerge from perturbative splitting of a single parton from the hadron. The former represents a double-(2→2) interaction, and the latter a (3→4) interaction. The (3→4) process could provide an enhancement in the DPS cross-section by increasing the effective local parton density, leading to σ_{eff} lower than expected.

In Monte Carlo (MC) generators, MPI, which of course also encompass double parton scattering, are a fundamental part of the simulation of the UE. Within MPI models used in MC, the value of σ_{eff} is closely related to the matter distribution in the proton. The parameters of MPI models are set by tuning to UE measurements performed in data. Having fixed the parameters of a given MPI model, an unambiguous prediction of σ_{eff} can be extracted. Values of σ_{eff} for different set of parameters and models are typically in the range 20 to 40 mb, depending on the assumed $F(r_{\perp})$, mostly above the measured values.

In a recent study [134] it was shown that by including the average measured value of σ_{eff} as a constraint in the tuning process of the parameters of the MPI model in the HERWIG++ MC event generator, it is possible to obtain a set of parameters that yields a good description of the UE properties with $\sigma_{\text{eff}} = 14.8$ mb. Similarly, the CMS collaboration [135] performed a study in which distributions sensitive to DPS contributions were included in the tuning of the PYTHIA UE parameters. A set of parameters corresponding to a value of $\sigma_{\text{eff}} \sim 20$ mb was obtained. It was therefore concluded that it is possible to describe the DPS cross-section and underlying event final states in the HERWIG and PYTHIA MPI models, without additional dynamics. The parameters obtained in the fit correspond to a larger local parton density, as advocated by the proponents of the (3→4)

2 Theoretical background

process enhancing the DPS cross-section. This was further tested by reweighting events generated with PYTHIA based on the kinematics of the MPI in the event to introduce the contribution expected by the $(3 \rightarrow 4)$ process, obtaining simultaneously a good description of soft UE observables and hard MPI observables [136].

2.4.1 Four-jet final state

The dominant mechanism for the production of events containing four high- p_T jets at the LHC in leading order is double gluon bremsstrahlung. This process is described quantitatively by pQCD. A few Feynman diagrams depicting such events are shown in Fig. 2.12. The topology is characterized

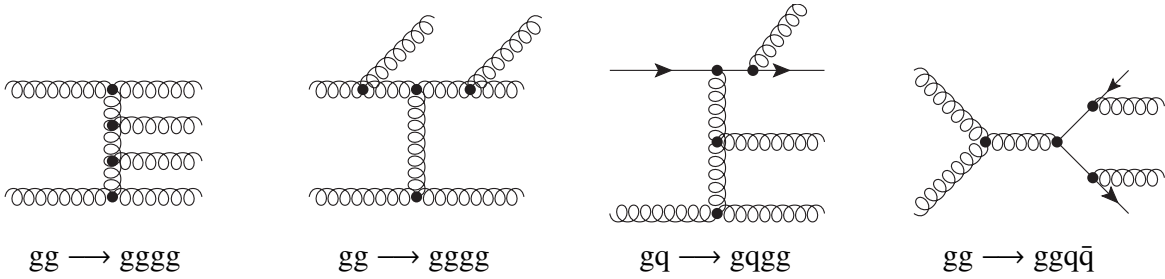


Figure 2.12: Four of the Feynman diagrams which contribute to the leading-order matrix element expression for the double gluon bremsstrahlung process.

by two partons in the initial state and four in the final state, denoted as $(2 \rightarrow 4)$. Alternatively, the final state of four high- p_T jets could also be produced through the DPS mechanism involving two pairs of parton-parton interactions, each leading to two jets, in the same proton-proton collision. The process of DPS is denoted in the following as $(2 \rightarrow 2)^{\times 2}$.

The two pairs of parton-parton interactions in $(2 \rightarrow 2)^{\times 2}$ events would produce two pairs of jets that, in first approximation, balance each other. On the other hand, the extra partons in $(2 \rightarrow 4)$ interactions originate from radiation and would not, in most cases, result in two pairs of balanced jets. On an event-by-event basis, it is impossible to determine whether a $(2 \rightarrow 4)$ or a $(2 \rightarrow 2)^{\times 2}$ interaction took place. However, the topological features of the jets may help establish the frequency of the two processes. In this analysis, these topological features are exploited in order to estimate the rate of DPS in the data.

The topology of the four jets originating from the $(3 \rightarrow 4)$ interaction is expected to be slightly different from the topology in the $(2 \rightarrow 2)^{\times 2}$ process. In particular, since one of the two pairs of interacting partons emerges from a perturbative splitting, the two partons are expected to have high transverse momentum. The high transverse momentum would cause each of the two dijet systems to be boosted and therefore less balanced. However, with the typical jet energy resolution, for jets with $p_T \sim 20$ GeV, the expected difference in topologies is hard to observe. Therefore, in this analysis, no attempt is made to differentiate between the two processes.

2.4.1.1 The effective cross-section in the four-jet final state

After integrating the differential cross-sections in Eq. (2.15) over the phase-space defined by the selection cuts of the A and B final states, the expression for the DPS cross-section in the four-jet final state may be re-written as

$$\sigma_{\text{DPS}} = \frac{1}{1 + \delta_{\text{AB}}} \frac{\sigma_{2j}^{\text{A}} \sigma_{2j}^{\text{B}}}{\sigma_{\text{eff}}}, \quad (2.16)$$

where σ_{2j}^{A} (σ_{2j}^{B}) is the measured cross-section for dijet events in the phase-space region labeled A (B). The double parton scattering cross-section may be expressed as

$$\sigma_{\text{DPS}} = f_{\text{DPS}} \cdot \sigma_{4j}, \quad (2.17)$$

where σ_{4j} is the measured cross-section for four-jet events in the phase-space A + B. The term f_{DPS} is the fraction of DPS events in the four-jet final state. Combining Eqs. (2.16) and (2.17), the expression for σ_{eff} in the four-jet final state becomes,

$$\sigma_{\text{eff}} = \frac{1}{1 + \delta_{\text{AB}}} \frac{1}{f_{\text{DPS}}} \frac{\sigma_{2j}^{\text{A}} \sigma_{2j}^{\text{B}}}{\sigma_{4j}}, \quad (2.18)$$

2.4.1.2 Cross-section definition

The dijet and four-jet final states may be defined inclusively or exclusively. That is, exclusive selection of n -jet events would accept only events with *exactly* n jets in the event. For the purpose of differentiating DPS from SPS in various final states, the exclusive states are easier to handle. However, it was pointed out in Refs. [137, 138] that an exclusive selection leads to a σ_{eff} that is process-dependent. In the following, when discussing a four-jet (dijet) event selection, the selection cuts require *at least* four jets (two jets) in the event. No restrictions are applied on additional jets in the events. However, when measuring the cross-section of four-jet (dijet) events, the leading (highest- p_{T}) four (two) jets in the event are considered, rather than all different combinations of four jets (dijets). This definition of the cross-section is referred to as an “inclusive” cross-section in the following.

Experimental setup

3.1 The Large Hadron Collider

The Large Hadron Collider is a proton–proton collider located at the Franco-Swiss border near Geneva, Switzerland. It lies in a tunnel 27 km in circumference at an average depth of a 100 meters. The tunnel houses 1232 superconducting bending dipole magnets, cooled using liquid helium to an operating temperature of 1.9 K, producing a magnetic field of about 8 T. The use of dipole magnets allows to keep protons traveling clockwise and counter-clockwise on orbit at the same time. In total, 392 quadrupole magnets are used to keep the beams focused and to collide them at the four interaction points (IP) of the LHC experiments. The design center-of-mass energy of the LHC is $\sqrt{s} = 14$ TeV.

Protons are produced by ionizing hydrogen atoms in an electric field. They are injected into RF cavities and accelerated to 750 keV. The beam is then transmitted to the LINAC 2, a linear accelerator, which increases the energy to 50 MeV. The protons are accelerated to 1.4 GeV by the Proton Synchrotron Booster and then further to 26 GeV by the Proton Synchrotron. Next, the Super Proton Synchrotron accelerates the protons to 450 GeV, the minimum energy required to maintain a stable beam in the LHC. Finally, the LHC accelerates them to the operating energy.

During the first two years of operation (2010-2011), the LHC operated at $\sqrt{s} = 7$ TeV, with 3.5 TeV per proton beam, delivering 5.51 fb^{-1} total integrated luminosity with a peak luminosity of $3.65 \times 10^{33} \text{ cm}^{-2}\text{s}^{-1}$ [139]. During 2012, the LHC operated at $\sqrt{s} = 8$ TeV, with 4 TeV per proton beam, delivering 22.8 fb^{-1} total integrated luminosity with a peak luminosity of $7.73 \times 10^{33} \text{ cm}^{-2}\text{s}^{-1}$ [139]. In June of 2015 the LHC started Run-2 after a two-year shutdown for maintenance and upgrades. Currently the LHC is operating at $\sqrt{s} = 13$ TeV, with with 6.5 TeV per proton beam.

At the design luminosity of $10^{34} \text{ cm}^{-2}\text{s}^{-1}$, the beam will consist of 2808 bunches of 10^{11} protons each, 25 ns apart. The dataset used in this measurement was collected during 2010, where the number of bunches increased gradually throughout the data taking period from 50 to 368, with a minimum separation of 150 ns between bunches. A total of 48.1 pb^{-1} integrated luminosity was delivered in 2010, with a peak luminosity of $2.1 \times 10^{32} \text{ cm}^{-2}\text{s}^{-1}$ [139].

3.2 The ATLAS Detector

The ATLAS (A Toroidal Lhc ApparatuS) detector [140] at the LHC covers nearly the entire solid angle around the collision point. It consists of an inner tracking detector surrounded by a thin superconducting solenoid, electromagnetic and hadronic calorimeters, and a muon spectrometer

incorporating three large superconducting toroid magnets. The inner-detector system (ID) is immersed in a 2 T axial magnetic field and provides charged particle tracking in the range $|\eta| < 2.5$ ¹. Figure 3.1(a) shows a schematic view of the ATLAS detector and its sub-systems.

The inner detector

The high-granularity silicon pixel detector (Pixel) covers the vertex region and typically provides three measurements per track, the first hit being normally in the innermost layer. It is followed by the silicon microstrip tracker (SCT) which usually provides four two-dimensional measurement points per track. These silicon detectors are complemented by the transition radiation tracker (TRT), which enables radially extended track reconstruction up to $|\eta| = 2.0$. The TRT also provides electron identification information based on the fraction of hits (typically 30 in total) above a higher energy deposit threshold corresponding to transition radiation.

The calorimeter

The ATLAS calorimeter, shown schematically in Fig. 3.1(b), is the principal tool used in the analysis. The calorimeter system covers the pseudo-rapidity range $|\eta| < 4.9$. Within the region $|\eta| < 3.2$, electromagnetic calorimetry is provided by barrel and endcap high-granularity lead/liquid-argon (LAr) electromagnetic calorimeters, with an additional thin LAr presampler covering $|\eta| < 1.8$, to correct for energy loss in material upstream of the calorimeters. Hadronic calorimetry is provided by the steel/scintillating-tile calorimeter, segmented into three barrel structures within $|\eta| < 1.7$, and two copper/LAr hadronic endcap calorimeters (HEC). The solid angle coverage is completed with forward copper/LAr and tungsten/LAr calorimeter modules (FCal) optimized for electromagnetic and hadronic measurements, respectively.

The muon spectrometer

The muon spectrometer comprises separate trigger and high-precision tracking chambers measuring the deflection of muons in a magnetic field generated by superconducting air-core toroids. The precision chamber system covers the region $|\eta| < 2.7$ with three layers of monitored drift tubes, complemented by cathode strip chambers in the forward region, where the background is highest. The muon trigger system covers the range $|\eta| < 2.4$ with resistive plate chambers in the barrel, and thin gap chambers in the endcap regions.

The trigger system

A three-level trigger system is used to select interesting events [141]. The Level-1 trigger is implemented in hardware and uses a subset of detector information to reduce the event rate to a design value of at most 75 kHz. This is followed by two software-based trigger levels which together reduce

¹ ATLAS uses a right-handed coordinate system with its origin at the nominal interaction point in the center of the detector and the z -axis along the beam pipe. The x -axis points from the IP to the center of the LHC ring, and the y -axis points upwards. Cylindrical coordinates (r, ϕ) are used in the transverse plane, ϕ being the azimuthal angle around the z -axis. The pseudo-rapidity is defined in terms of the polar angle θ as $\eta = -\ln \tan(\theta/2)$. Angular distance is measured in units of $\Delta R \equiv \sqrt{(\Delta\eta)^2 + (\Delta\phi)^2}$. When dealing with massive jets and particles, the rapidity $y = \frac{1}{2} \ln \left(\frac{E+p_z}{E-p_z} \right)$ is used, where E is the jet energy and p_z is the z -component of the jet momentum.

3 Experimental setup

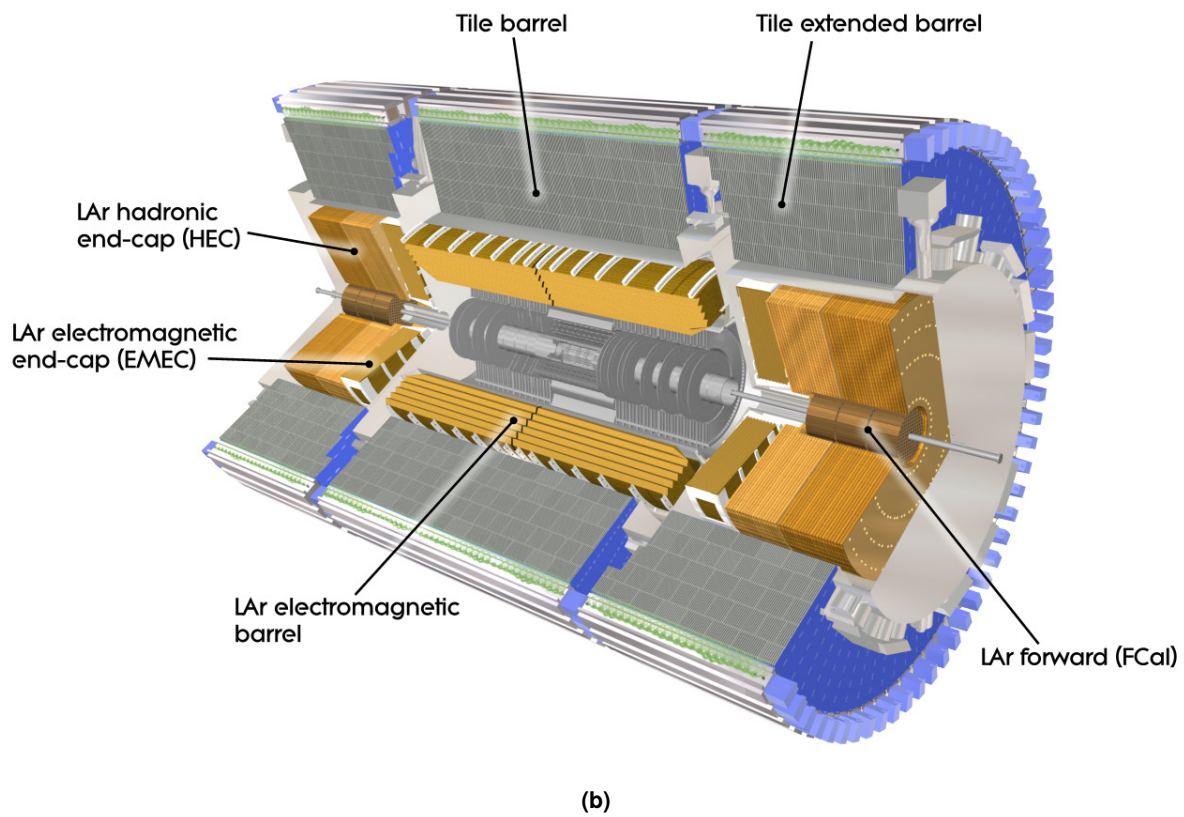
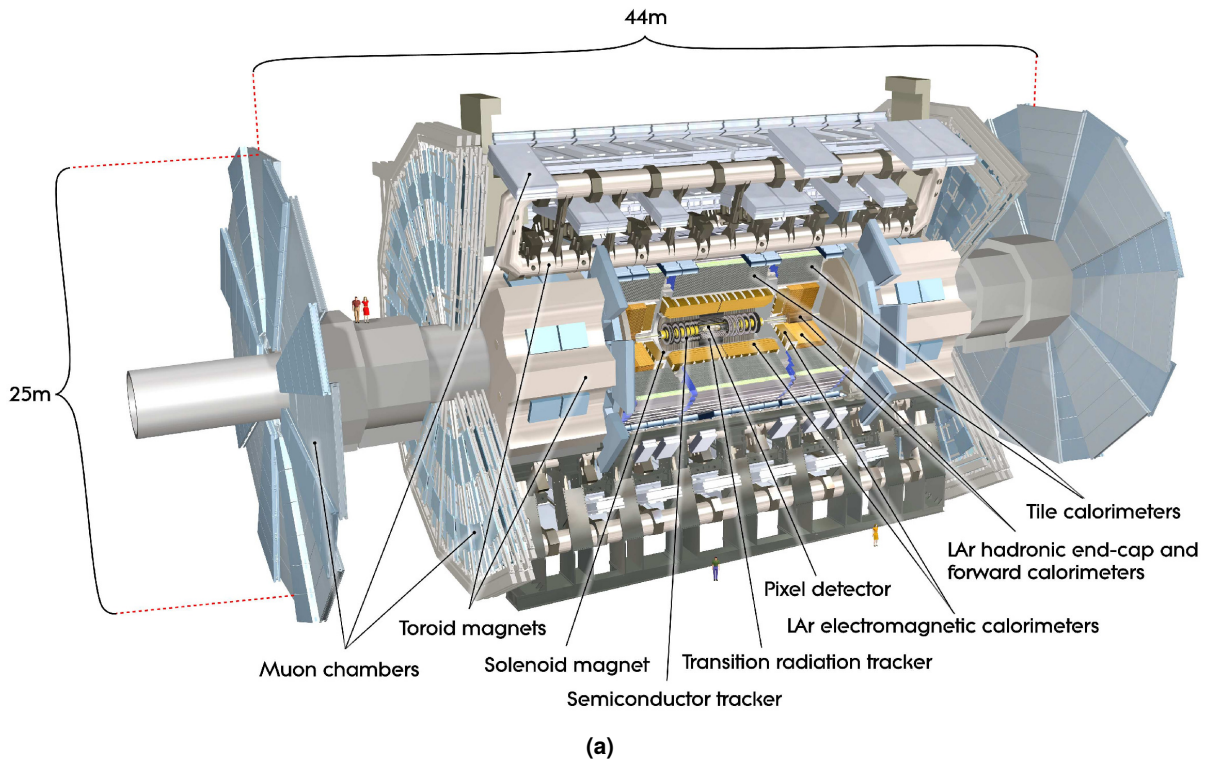


Figure 3.1: Schematic view of the (a) ATLAS detector and of the (b) ATLAS calorimeter system.

the event rate to about 200 Hz. An additional trigger system used in ATLAS relies on the minimum-bias trigger scintillators. The various triggers used in the analysis are described in further detail in [Section 3.10](#).

3.3 Luminosity

The accurate measurement of the delivered luminosity is a key component of the ATLAS physics program. For cross-section measurements of SM processes the uncertainty on the delivered luminosity is often one of the dominant systematic uncertainties. The instantaneous luminosity of proton–proton collisions can be calculated as

$$L = \frac{R_{\text{inel}}}{\sigma_{\text{inel}}}, \quad (3.1)$$

where R_{inel} is the rate of inelastic proton–proton interactions and σ_{inel} is the inelastic cross-section. Any detector sensitive to inelastic proton–proton interactions can be used as a source for relative luminosity measurement and several ATLAS devices are utilized for this purpose, as described in [\[142\]](#). However, these detectors must be calibrated using an absolute measurement of the luminosity.

The recorded luminosity can be written as

$$L = \frac{\mu_{\text{vis}} n_b f_{\text{rev}}}{\sigma_{\text{vis}}}, \quad (3.2)$$

where μ_{vis} is the visible number of interactions per bunch crossing in the detector, n_b is the number of bunch pairs colliding in ATLAS, f_{rev} is the LHC revolution frequency (11245.5 Hz) and σ_{vis} is the visible cross-section, to be determined via calibration for each detector.

The calibration is done using dedicated beam separation scans, also known as “van der Meer” scans [\[143\]](#), where the two beams are stepped through each other in the horizontal and vertical planes to measure their overlap function. The delivered luminosity is measured using beam parameters

$$L = \frac{n_b f_{\text{rev}} n_1 n_2}{2\pi \Sigma_x \Sigma_y}, \quad (3.3)$$

where n_1 and n_2 are the number of protons per bunch in beam 1 and beam 2, respectively, forming the bunch charge product, and Σ_x and Σ_y characterize the horizontal and vertical profiles of the colliding beams.

By comparing the delivered luminosity to the peak interaction rate $\mu_{\text{vis}}^{\text{Max}}$ observed by a given detector during the van der Meer scan, σ_{vis} is determined as

$$\sigma_{\text{vis}} = \mu_{\text{vis}}^{\text{Max}} \frac{2\pi \Sigma_x \Sigma_y}{n_1 n_2}. \quad (3.4)$$

Two primary detectors were used to make bunch-by-bunch luminosity measurements during the 2010 running period: LUCID and BCM. The LUCID detector is a Cerenkov detector specifically designed for measuring the luminosity in ATLAS. Sixteen mechanically polished aluminum tubes filled with C_4F_{10} gas surround the beampipe on each side of the IP at a distance of 17 m, covering the pseudo-rapidity range $5.6 < |\eta| < 6.0$.

3 Experimental setup

The beam conditions monitor (BCM) consists of four small diamond sensors on each side of the ATLAS IP arranged around the beam-pipe in a cross pattern. The BCM is a fast device primarily designed to monitor background levels and issue a beam-abort request in case beam losses start to risk damage to ATLAS detectors.

In total, $(37.3 \pm 1.3) \text{ pb}^{-1}$ of data taken during 2010 are used in this analysis. The systematic uncertainty on the integrated luminosity for 2010 proton–proton data is 3.5% [144].

3.4 Jet algorithms

As mentioned, quarks and gluons manifest themselves as groups of collimated particles in the final state called jets. The reconstruction of a jet requires a procedure that associates particles or energy deposits to a single jet (jet algorithm) and a recombination scheme that specifies how to combine the four-momenta of the jet constituents. Since partons are not physically observable objects, there is no unique jet definition. However, because measurements are performed at the hadron-level and theoretical expectations at the parton-level, a precise definition of jets is required.

The “Snowmass Accord” [145] was the first attempt to standardize jet definitions across different experiments and between theory and experiment. It defined the following properties a jet definition must satisfy:

- ⇒ **infrared safety** - in order to calculate cross-sections in perturbation theory, the jet definition must be insensitive to the presence of infinitely soft gluons. The presence or absence of additional soft particles between two particles belonging to the same jet should not affect the recombination of these two particles into a jet. Generally, any soft particles not coming from the fragmentation of a hard scattered parton should not affect the number of produced jets;
- ⇒ **collinear safety** - a jet should be reconstructed independently whether the transverse momentum is carried by one particle or if that particle is split into two collinear particles;
- ⇒ **order independence** - the algorithm should be applicable at parton- hadron- or detector-level, and lead to the same origin of the jet.

An illustration of infrared and collinear sensitivity in jet-finding is given in Fig. 3.2.

The Snowmass Accord defined a jet as a direction that maximizes the amount of transverse energy flowing through a cone centered on its direction. First implementations of this definition often included a “seed” particle in order to shorten computation time and a split/merge stage in order to deal with overlapping jets. However, it was found that the precise definition of the seeds makes the merging/splitting step infrared-unsafe.

Other jet algorithms have been proposed over the years such as sequential recombination algorithms (cluster algorithms), which are based on event shape analysis [146]. These algorithms are based upon pair-wise clustering of the input constituents and define a distance measure between constituents, as well as some condition upon which clustering into a jet should be terminated.

The most common clustering algorithms are the anti- k_t [147], k_t [148] and Cambridge/Aachen [149, 150] algorithms. The algorithms begin by calculating the distance d_{ij} between constituents i and j ,

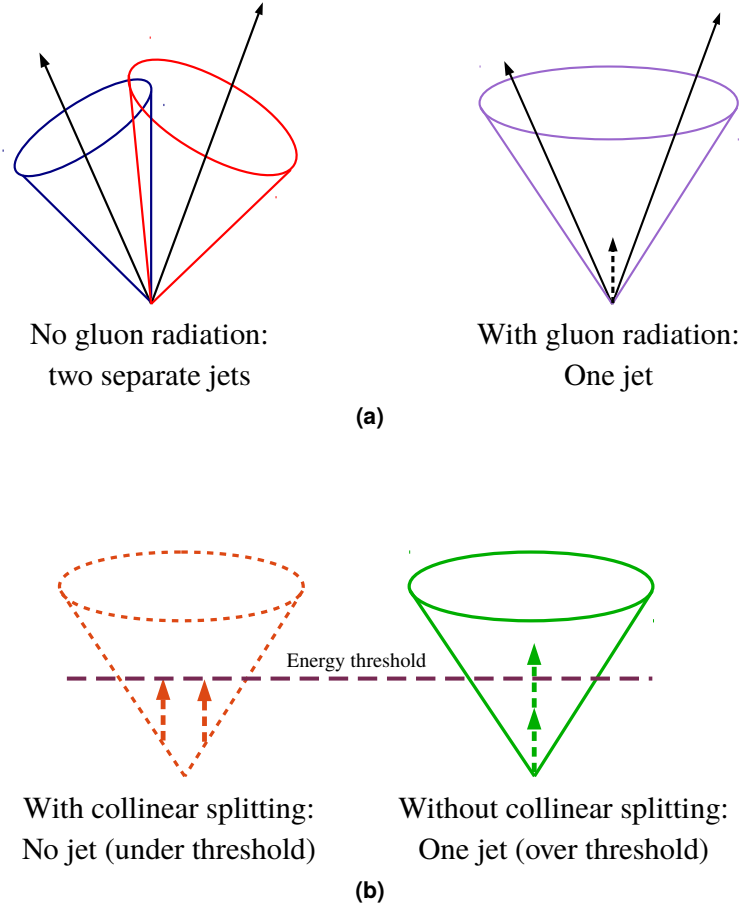


Figure 3.2: An illustration of (a) infrared and (b) collinear sensitivity in jet reconstruction.

as well as the distance d_{iB} between constituent i and the beam (B). These distances, calculated for all sets of constituents $\langle i, j \rangle$, are defined as

$$d_{iB} = k_{T,i}^{2p}, \quad (3.5)$$

$$d_{ij} = \min(k_{T,i}^{2p}, k_{T,j}^{2p}) \frac{(\Delta R)_{ij}^2}{R^2}, \quad (3.6)$$

where

$$(\Delta R)_{ij}^2 = (y_i - y_j)^2 + (\phi_i - \phi_j)^2.$$

The variables R and p are constants of the algorithm and $k_{T,i}$, y_i and ϕ_i are respectively the transverse momentum, the rapidity and the azimuth of the i^{th} constituent.

For each constituent i , the minimal distance ($\min d_{ij}$) is found and compared to d_{iB} . If $(\min d_{ij}) < d_{iB}$, the constituents i and j are combined and the distances are re-calculated. In case $d_{iB} < (\min d_{ij})$, constituent i is removed from the list of constituents and is classified as a jet. This process is repeated until all of the constituents are clustered into jets. The final four-momentum

3 Experimental setup

of the jet is obtained from summing the four-momenta of its constituents in the four-vector recombination scheme [146]. This scheme conserves energy and momentum, and allows a meaningful definition for the jet mass.

The variable R sets the resolution at which jets are resolved from each other and the beam. The type of clustering algorithm is defined by the p variable, where a choice of $p = 1$ results in k_t jets, the special case in which $p = 0$ produces Cambridge/Aachen jets and $p = -1$ leads to anti- k_t jets.

In the analysis presented here, the anti- k_t jet algorithm, implemented in the FASTJET package [151], is used to cluster jets with a distance parameter $R = 0.6$. The anti- k_t algorithm has the advantage of producing fairly circular jets while still being collinear and infrared safe. A pseudo-event display of a dijet event is shown in Fig. 3.3, demonstrating two circular jets with $p_T \sim 20$ GeV reconstructed using the anti- k_t algorithm.

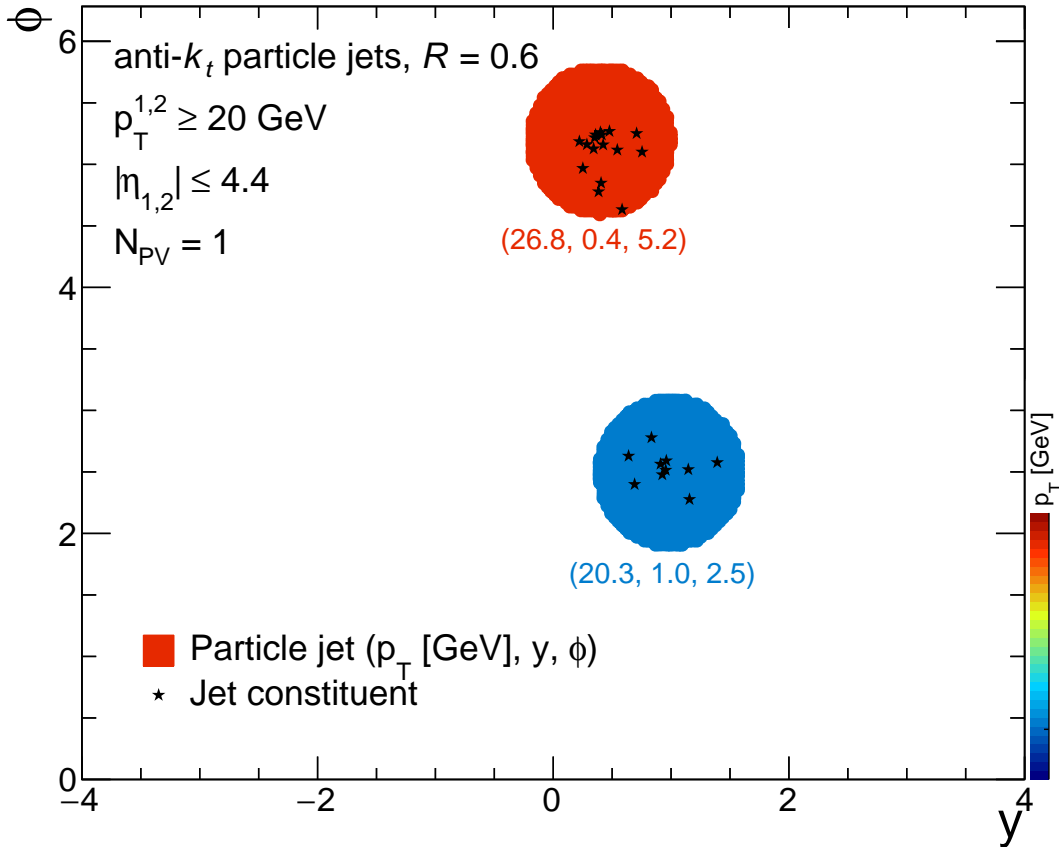


Figure 3.3: Pseudo event display of the distribution of the two highest- p_T particle jets in the event (filled areas, see definition in Section 3.5) and their constituents (black stars) in the $\phi - y$ plane, where ϕ is the jet azimuthal angle and y its rapidity. Each jet area color corresponds to the jet transverse momentum (p_T) and the jet p_T , in GeV, y and ϕ are displayed next to it.

3.5 Inputs to jet reconstruction

Two jet collections are used in the measurement, calorimeter jets and particle jets, termed based on the input used in the jet algorithm.

Calorimeter jets

At the detector level, the input objects to the jet algorithm are three-dimensional topological calorimeter clusters (*topo-clusters*) [152, 153] built from calorimeter cells. Each topo-cluster is built from a *seed* cell, whose signal-to-noise (S/N) ratio is above a threshold of $S/N = 4$. Cells adjacent to the seed (or the cluster being formed) that have a $S/N \geq 2$ are added to the topo-cluster iteratively until no more neighboring cells with $S/N \geq 2$ are found. Finally, all calorimeter cells adjacent to the formed topo-cluster are added, regardless of their S/N .

The topo-cluster algorithm also includes a splitting step in order to optimize the separation of showers from different close-by particles. All cells in a topo-cluster are searched for local maxima in terms of energy content with a threshold of 500 MeV. This means that the selected calorimeter cell has to be more energetic than any of its neighbors. The local maxima are then used as seeds for a new iteration of topological clustering, which splits the original cluster into smaller topo-clusters.

When used as input to the jet reconstruction, only topo-clusters with a positive energy are used and each topo-cluster is considered as a massless particle with energy equal to the sum of energies of all the included calorimeter cells and a direction calculated from the weighted averages of the pseudo-rapidities and azimuthal angles of its constituent cells. The weight used in the average is the absolute cell energy and the direction is relative to the nominal ATLAS coordinate system. This clustering algorithm is designed to suppress calorimeter noise and to follow the shower development in the calorimeter. Calorimeter jets are built from cells calibrated at the electromagnetic (EM) scale².

Particle jets

Jets from Monte Carlo simulations are referred to as *particle jets*. These jets are built from particles with a lifetime longer than 10 ps in the Monte Carlo event record, excluding muons and neutrinos. Particle jets are not passed through the simulation of the ATLAS detector. The definition of a particle jet requires that the transverse momentum of the anti- k_t jet is at least 10 GeV. The variables pertaining to the particle jets are subsequently denoted by the subscript *truth*.

3.6 Jet energy calibration

The jet energy calibration relates the jet energy measured with the ATLAS calorimeter to the true energy of the corresponding jet of stable particles entering the detector. Four calibration steps are applied to the jets, as detailed below. A full description of the jet energy calibration is given in Ref. [154].

² The electromagnetic scale is the basic calorimeter signal scale for the ATLAS calorimeters. It has been established using test-beam measurements for electrons and muons to give the correct response for the energy deposited by electromagnetic showers, while it does not correct for the lower hadron response.

3.6.1 Pile-up correction

Jets calibrated at the EM scale are affected by additional energy due to multiple proton–proton interactions within the same bunch crossing (*pile-up*). An average correction is applied on the reconstructed jets in order to subtract this additional energy. The correction is derived from minimum bias data, where the average additional transverse energy, E_T , per calorimeter tower is measured as a function of η , the number of reconstructed primary vertices, N_{PV} , and bunch spacing. The effect of additional proton–proton interactions from different bunch crossings that can be caused by trains of consecutive bunches (*out-of-time pile-up*) was found to be small in the 2010 dataset [154]. Events with more than one primary vertex are rejected (see Chapter 5). Hence, the pile-up correction applied to jets in this study arises only from out-of-time pile-up and is therefore minimal. Further details on the pile-up correction are given in Ref. [154].

3.6.2 Jet origin correction

The geometrical center of the ATLAS detector is used as a reference to calculate the direction of the topo-clusters utilized in the jet reconstruction. Once the primary vertex, defined as the vertex with the highest $\sum p_T^{\text{track}}$ (see Chapter 5), is selected, the four-momentum of each topo-cluster is re-calculated using this vertex and the jet four-momentum is then re-defined as the four-vector sum of the topo-clusters. This correction depends mainly on the z position of the primary vertex. It improves the angular resolution and results in a small improvement ($< 1\%$) in the jet p_T response, $\mathcal{R}_{EM}^{p_T}$, defined as

$$\mathcal{R}_{EM}^{p_T} = p_T^{\text{EM}} / p_T^{\text{truth}}, \quad (3.7)$$

where p_T^{EM} is the jet p_T at the EM scale and p_T^{truth} is the p_T of the particle jet matched to it.

3.6.3 Jet energy scale

The final stage of the jet calibration is the EM+JES calibration. This calibration corrects for the following detector effects that affect the jet energy measurement:

- **calorimeter non-compensation** - the response of the calorimeter is different for particles of the same energy producing electromagnetic or hadronic showers;
- **inactive material** - energy losses in inactive regions of the detector;
- **leakage** - showers not fully contained in the depth of the calorimeters;
- **out of cone** - energy deposits of the particle jet which are missed in the reconstructed jet;
- **reconstruction efficiency** - signal loss in calorimeter clustering and jet reconstruction due to cell noise thresholds.

The calibration function, $\mathcal{F}_{EM}^{\text{calib}}$, is dependent on the measured energy and jet position and is applied as follows:

$$E^{\text{calib}} = E_{EM}^{\text{det}} \times \mathcal{F}_{EM}^{\text{calib}}(E_{EM}^{\text{det}}, \eta). \quad (3.8)$$

Here $E_{\text{EM}}^{\text{det}}$ is the calorimeter energy measured at the EM scale and E^{calib} is the hadron-level calibrated jet energy. The calibration function $\mathcal{F}_{\text{EM}}^{\text{calib}}$ was derived from Monte Carlo simulated events using the detector-level jet energy response,

$$\mathcal{R}_{\text{EM}} = E_{\text{EM}}^{\text{det}}/E_{\text{truth}} . \quad (3.9)$$

The variable E_{truth} is the energy of the particle jet matched to the detector-level jet. The calibration function was derived by fitting the response distribution as a function of jet energy in bins of pseudo-rapidity. The final jet energy scale that relates the measured calorimeter jet energy to the true jet energy was then calculated as the inverse of the fitted function.

3.6.4 Jet pseudo-rapidity correction

In poorly instrumented regions of the detector, a bias in the reconstructed η of jets is observed. In these regions, topo-clusters are reconstructed with a lower energy with respect to better instrumented regions (see Fig. 10 in [154]). This causes the jet direction to be biased towards the better instrumented calorimeter regions. An η -dependent correction is applied to jets in order to correct for this bias.

The η -correction is derived as the average difference between the η of the origin-corrected reconstructed jets and their matched particle jets. It is parameterized as a function of the jet energy and pseudo-rapidity and is very small ($\Delta\eta = \eta_{\text{truth}} - \eta_{\text{origin}} < 0.01$) for most regions of the calorimeter. In the HEC-FCal transition regions this correction is up to seven times larger ($\Delta\eta = 0.07$ for low p_{T} jets).

3.7 Jet quality selection

Jets with high p_{T} ($p_{\text{T}} \geq 20$ GeV) produced in pp collisions must be distinguished from background jets not originating from hard scattering events. The main sources of background are,

- large calorimeter noise;
- beam-gas events, where one proton of the beam collides with the residual gas within the beam pipe;
- beam-halo events, e.g., caused by interactions in the tertiary collimators in the beam-line far away from the ATLAS detector;
- cosmic ray muons overlapping in-time with collision events.

These backgrounds are divided into two categories, calorimeter noise and non-collision interactions.

3 Experimental setup

Calorimeter noise

Two types of calorimeter noise are addressed, sporadic noise bursts and coherent noise. Sporadic noise bursts in the HEC commonly result in a single noisy calorimeter cell, which contributes almost all of the energy of a jet. Such jets are therefore rejected if they have high HEC energy fractions. The signal shape quality, may also be used for rejection, being a measure of the pulse shape of a calorimeter cell compared to nominal conditions. Due to the capacitive coupling between channels, neighboring calorimeter cells around the noise burst have an apparent negative energy, denoted by E_{neg} . A high value of E_{neg} is therefore used to distinguish jets which originate in noise bursts. On rare occasions, coherent noise in the electromagnetic calorimeter develops. Fake jets arising from this background are characterized by a large EM energy fraction, f_{EM} , which is the ratio of the energy deposited in the EM calorimeter to the total energy. Similar to the case of noise bursts in the HEC, a large fraction of calorimeter cells exhibit a poor signal shape quality.

Non-collision backgrounds

Cosmic rays or non-collision interactions are likely to induce events where jet candidates are not in-time with the beam collision. A cut on the jet-time may therefore be applied to reject such jets. Jet-time is reconstructed from the energy deposition in the calorimeter by weighting the reconstructed time of calorimeter cells forming the jet with the square of the cell energy. The calorimeter time is defined with respect to the event time recorded by the trigger. A cut on f_{EM} is applied to make sure that jets have some energy deposited in the calorimeter layer closest to the interaction region, as expected for a jet originating from the nominal interaction point. Since real jets are expected to have tracks, the f_{EM} cut may be applied together with a cut on the scalar sum of the p_{T} of the tracks associated with the jet, divided by the jet p_{T} . A cut on the maximum energy fraction in any single calorimeter layer is applied to further reject non-collision background.

3.7.1 Jet reconstruction efficiency

A quality criterion is applied to jets, denoted as Medium selection, incorporating the requirements on the conditions defined above. The exact conditions are specified in detail in Ref. [154]. The quality selection introduces inefficiencies to the jet reconstruction which is corrected for on a jet-by-jet basis. For jet $p_{\text{T}} > 60$ GeV, the reconstruction efficiency is above 99% across all rapidities. For lower jet p_{T} , the reconstruction efficiencies range between 96-98% within $|y| < 2.1$ and above 99% at $|y| \geq 2.1$.

The uncertainty on the jet reconstruction efficiency is evaluated using track jets which are used to portray “truth jets” [155]. Track jets are built by applying the anti- k_{t} algorithm to the reconstructed tracks in an event [156]. The efficiency to reconstruct a calorimeter jet given a track jet nearby is studied in both data and MC in the region covered by the tracking detector, $|y| < 2.1$. The comparison of the measured efficiencies in data and in MC is used to infer the degree to which the calorimeter jet reconstruction efficiency may be mis-modeled in the MC. The disagreement was found to be 2% for calorimeter jets with p_{T} of 20 GeV and less than 1% for those with $p_{\text{T}} > 30$ GeV. This disagreement for jets with $|y| < 2.1$ is taken as a systematic uncertainty for all jets in the rapidity range $|y| \leq 4.4$. This is expected to be a conservative estimate in the forward region where the jets have higher energy for a given p_{T} .

3.8 Jet calibration uncertainties

The systematic uncertainty associated with the jet energy scale (JES) is one of the dominant sources of uncertainties. The sources for the JES uncertainty have been evaluated in part using pp collision data and in part using systematic variations of MC simulations. The sources of uncertainty considered in this measurement are the following (values for jets with $20 \leq p_T < 30$ GeV and $0.3 \leq |\eta| < 0.8$ are given in parenthesis):

- **single hadron response** - uncertainty associated with the response of a single particle entering the calorimeter (1.8%). Discrepancies may arise due to the limited knowledge of the exact detector geometry; due to the presence of additional inactive material; and due to the modelling of the exact way particles interact in the detector;
- **cluster thresholds** - uncertainty associated with the thresholds for reconstructing topo-clusters (2.0%). The clustering algorithm is based on the signal-to-noise ratio of calorimeter cells. Discrepancies between the simulated noise and the real noise, or changes in time of the noise in data, can lead to differences in the cluster shapes and to the presence of fake topo-clusters;
- **Perugia 2010 and Alpgen+Herwig+Jimmy** - uncertainty associated with the modelling of fragmentation and the underlying event, or with other choices in the event modelling of the MC generator (2.1%). The response predicted by the nominal PYTHIA generator are compared to the PYTHIA Perugia 2010 tune and to ALPGEN, coupled to HERWIG and JIMMY;
- **intercalibration** - uncertainty associated with the calorimeter response for forward jets ($|\eta| \geq 0.8$), obtained using the dijet balance *in-situ* technique (3.5% for jets with $20 \leq p_T < 30$ GeV and $2.1 \leq |\eta| < 2.8$);
- **relative non-closure** - uncertainty associated with the non-closure of the energy of jets in MC following the JES calibration (1.9%).

The total uncertainty for jets calibrated using the EM+JES calibration described above is roughly 2% for jets with $40 \leq p_T < 2000$ GeV in the central region of the detector, increasing up to roughly 4% for jets with lower or higher p_T . A full description of the jet calibration uncertainty can be found in Ref. [154].

3.9 Dataset

The measurement presented here utilizes the full ATLAS 2010 data sample from proton–proton collisions at $\sqrt{s} = 7$ TeV, with a few exceptions. For the low- p_T region (events where the highest- p_T jet has $20 \leq p_T < 60$ GeV), only data runs taken up to the beginning of June are considered. In that period the instantaneous luminosity of the accelerator was low enough that pile-up contributions were negligible and the majority of the bandwidth was allocated to the Minimum Bias trigger (MBTS) that is used to collect low- p_T events. The first data taking period was not used for forward jets (jets in the η region $|\eta| > 2.8$), since the forward jet trigger was not yet commissioned.

For all data events considered in the following, good operation status was required for the first-level trigger, solenoid magnet, inner detectors (Pixel, SCT, and TRT), calorimeters (barrel, endcap, and forward), luminosity, as well as tracking, jet, and missing energy reconstruction performance. In

3 Experimental setup

addition, stable operation was required for the high-level trigger during the periods when it was used for event rejection.

3.10 Trigger

Three different triggers are used for the measurement: the MBTS, the central ($|\eta| < 3.2$) and the forward jet triggers ($3.1 < |\eta| < 4.9$).

The MBTS (denoted by L1_MBTS_1 at Level 1 and by EF_MBTS for the Event Filter) requires at least one hit in the minimum bias scintillators located in front of the endcap cryostats, covering $2.08 < |\eta| < 3.75$, and is the primary trigger used to select minimum-bias events in ATLAS. It has been demonstrated [157] to have negligible inefficiency for the events of interest for this analysis and is used to select events with low- p_T jets.

The central and forward jet triggers independently select data using several jet transverse energy thresholds, each requiring the presence of a jet with sufficient transverse energy at the EM scale, E_T^{EM} . The jet triggers are composed of three consecutive levels; Level 1 (L1), Level 2 (L2) and Event Filter (EF). For each L1 threshold, there is a corresponding L2 threshold that is generally set 15 GeV above the L1 threshold³. Each such L1+L2 combination is referred to as a L2 trigger chain. The jet trigger names follow a convention such that the names begin with the trigger-level, followed by a “regional” identifier and end with a number. Two regional identifiers are used, the letter J denotes central triggers and the combination FJ denotes forward triggers. The number stands for the trigger threshold, e.g. L1_J5 is a Level 1 central trigger with a threshold, $E_T^{EM} > 5$ GeV.

In 2010, only L1 information was used to select events in the first 3 pb^{-1} of data taken, while both the L1 and L2 stages were used for the rest of the data sample. The jet trigger did not reject events at the EF stage in 2010, so the L2 and EF trigger-levels were equivalent. In the early part of Period A, before run 152777, a mis-timing in the L1 central jet trigger hardware caused large inefficiencies, so all jets before this run are triggered using L1_MBTS_1. A limited number of runs from period E (sub-periods E1-E4) are excluded, due to a problem with the configuration of the trigger. The trigger strategy used in this analysis is equivalent to the trigger strategy developed and used in the measurement of the dijet cross-section using 2010 data [155]⁴.

3.10.1 Trigger efficiency

The per-jet trigger efficiency is determined from the probability that a single jet passes a given trigger threshold, regardless of what the other jets in the event do. In order to determine the efficiency of the jet triggers, the off-line reconstructed jets are matched to central or forward trigger jets based on the rapidity of the reconstructed jet. However, in the transition region, $2.8 < |\eta| < 3.6$, there is an ambiguity whether to associate a reconstructed jet to a central or to a forward trigger object. In this region, central L1 trigger objects may be reconstructed as forward jets, and vice versa. Since the rapidity resolution of trigger objects is insufficient to unambiguously assign a reconstructed jet

³ The exception is the lowest threshold, for which the difference between L1 and L2 is 10 GeV.

⁴ It was tested by repeating the measurement of the dijet cross-section, as described in [158].

to a central or forward trigger jet, the reconstructed jet are matched to a trigger object by the shortest distance,

$$\Delta R = \sqrt{(\phi_{\text{trig}} - \phi_{\text{jet}})^2 + (\eta_{\text{trig}} - \eta_{\text{jet}})^2}, \quad (3.10)$$

using the pseudo-rapidity and azimuth of the trigger object, η_{trig} and ϕ_{trig} , and of the reconstructed jet, η_{jet} and ϕ_{jet} . When available, the matching is performed between reconstructed jets and L2 objects. Since L2 objects are seeded by L1 trigger jets, the matching to a L2 trigger jet provides a direct association of the reconstructed jet to central or forward L1 trigger jet.

When the L2 trigger was not available and matching to L1 trigger jets in FCal was necessary, the ΔR matching (see Eq. (3.10)) was not possible because no η information was available for forward L1 jet triggers. In that case, a different matching scheme was used, by utilizing the distance $\Delta\phi$ between the reconstructed jet and L1 trigger jet. A detailed explanation of this matching procedure is given in Section 6.2.2 of [159].

Figures 3.4 and 3.5 show the efficiencies for L1 and L2 trigger chains with various thresholds as a function of the reconstructed jet p_T for anti- k_t jets with $R = 0.6$. The efficiency curves are shown for various regions of the detector. The first region is the central region, $|y| < 2.8$, where the central trigger system is used (Figs. 3.4(a) and 3.4(b)). It can be seen that the per-jet L1 and L2 trigger efficiencies are fully efficient in this region. The second is the crack region between the barrel and endcap calorimeters, $1.3 \leq |y| < 1.6$ (Figs. 3.4(c) and 3.4(d)); there, the per-jet L1 and L2 trigger efficiencies are never fully efficient due to calorimeter inhomogeneities. The third is the transition region between the central and the forward trigger systems, $2.8 \leq |y| < 3.6$ (Figs. 3.5(a) and 3.5(b)); in this region, trigger selection is performed by matching jets to either the central or the forward triggers, as described above, and the trigger efficiencies are above 97%. The fourth is the forward region, $3.6 \leq |y| \leq 4.4$, where the forward jet trigger is used (Figs. 3.5(c) and 3.5(d)); due to an inactive FCal trigger tower that spans a width of $\Delta\phi = \pi/4$ in the y region $|y| \geq 3.1$, the forward jet triggers are not fully efficient in this region.

As the instantaneous luminosity increased throughout data-taking, it was necessary to prescale triggers with lower E_T thresholds. For each bin of jet- p_T considered, a dedicated trigger threshold is chosen such that the efficiency is as close as possible to 100% and the prescale is as small as possible. Table 3.1 presents the various triggers used in the analysis as a function of jet p_T and y , for different periods of data taken throughout 2010. The corresponding per-jet trigger efficiencies are shown in Table 3.2, where the efficiencies in the ‘‘crack’’ region are given in place of the efficiencies integrated over the entire central region. The uncertainty on the per-jet trigger efficiency ranges between 1 and 2%, depending on the trigger region and threshold, and is propagated as a systematic uncertainty.

3.10.2 Luminosity calculation using a two-trigger selection scheme

In order to maximize the amount of accepted events collected by the trigger, a *two-trigger* strategy is used, following the prescription employed in Ref. [155]. An event is accepted if at least one of the two leading jets can be matched in p_T and y to a triggering jet. The event is then assigned to one of two luminosity classes, $\mathcal{L}_{\text{single}}^{\text{jet}}$ or $\mathcal{L}_{\text{double}}^{\text{jet}}$. The former, a *single-trigger* luminosity class, is for events where the two jets are assigned to the same trigger. The latter, a *double-trigger* luminosity class, is for events in which each jet is assigned to a different trigger. It is worth noting that also jets that did not fire the trigger are assigned a trigger based on their p_T and η for the sake of the luminosity calculation.

3 Experimental setup

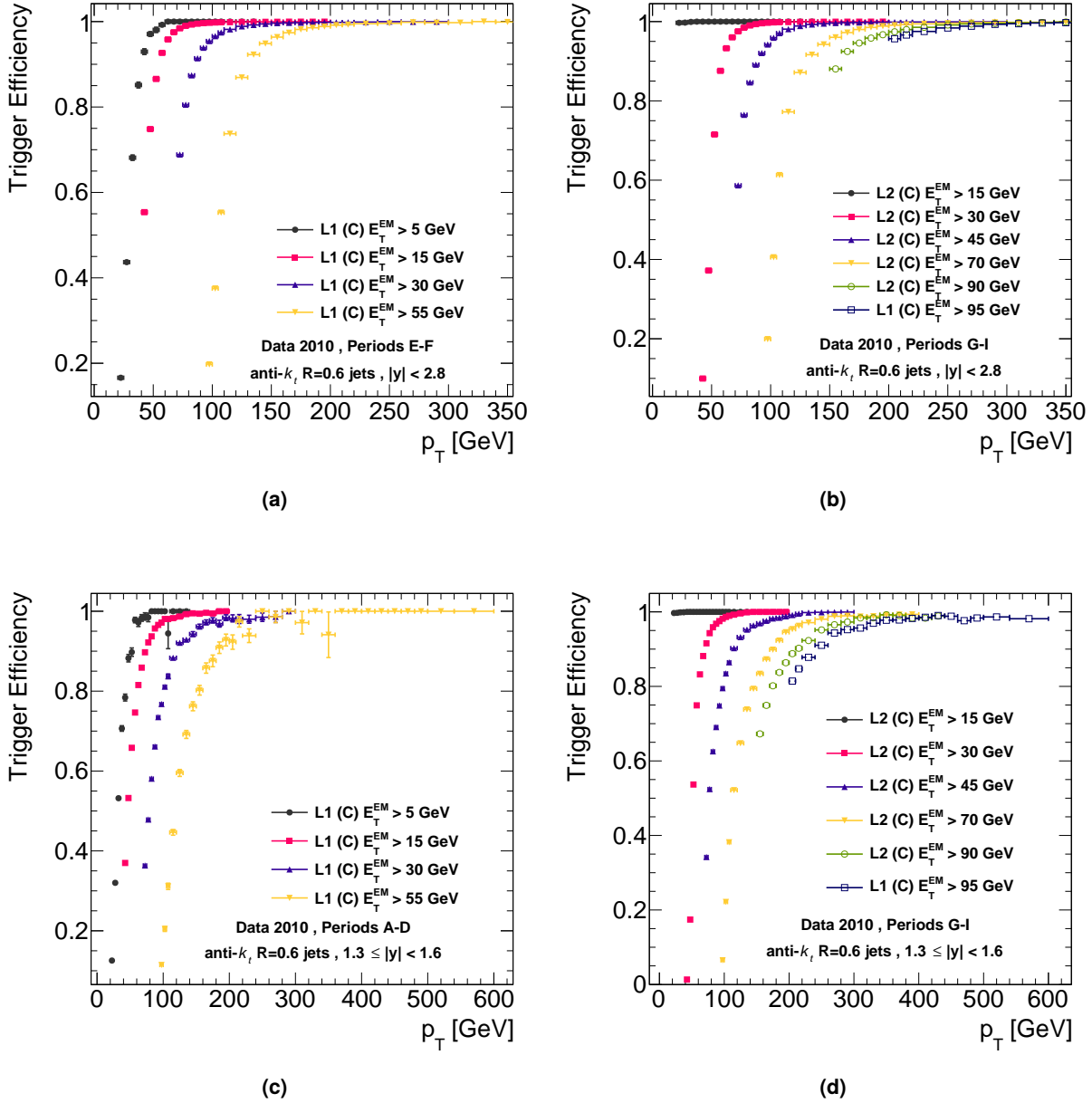


Figure 3.4: Trigger efficiency as a function of the reconstructed jet transverse momentum, p_T , for jets within rapidity $|y| < 2.8$, (a) and (b), and for jets in the crack region between the barrel and endcap calorimeters, (c) and (d). Various triggers (L1 and L2) and different data taking periods are shown, as indicated in the figures. The jets are associated with central triggers, denoted by (C). Trigger thresholds are denoted by E_T^{EM} , the minimal transverse energy at the electromagnetic scale of a jet which is required to fire the trigger.

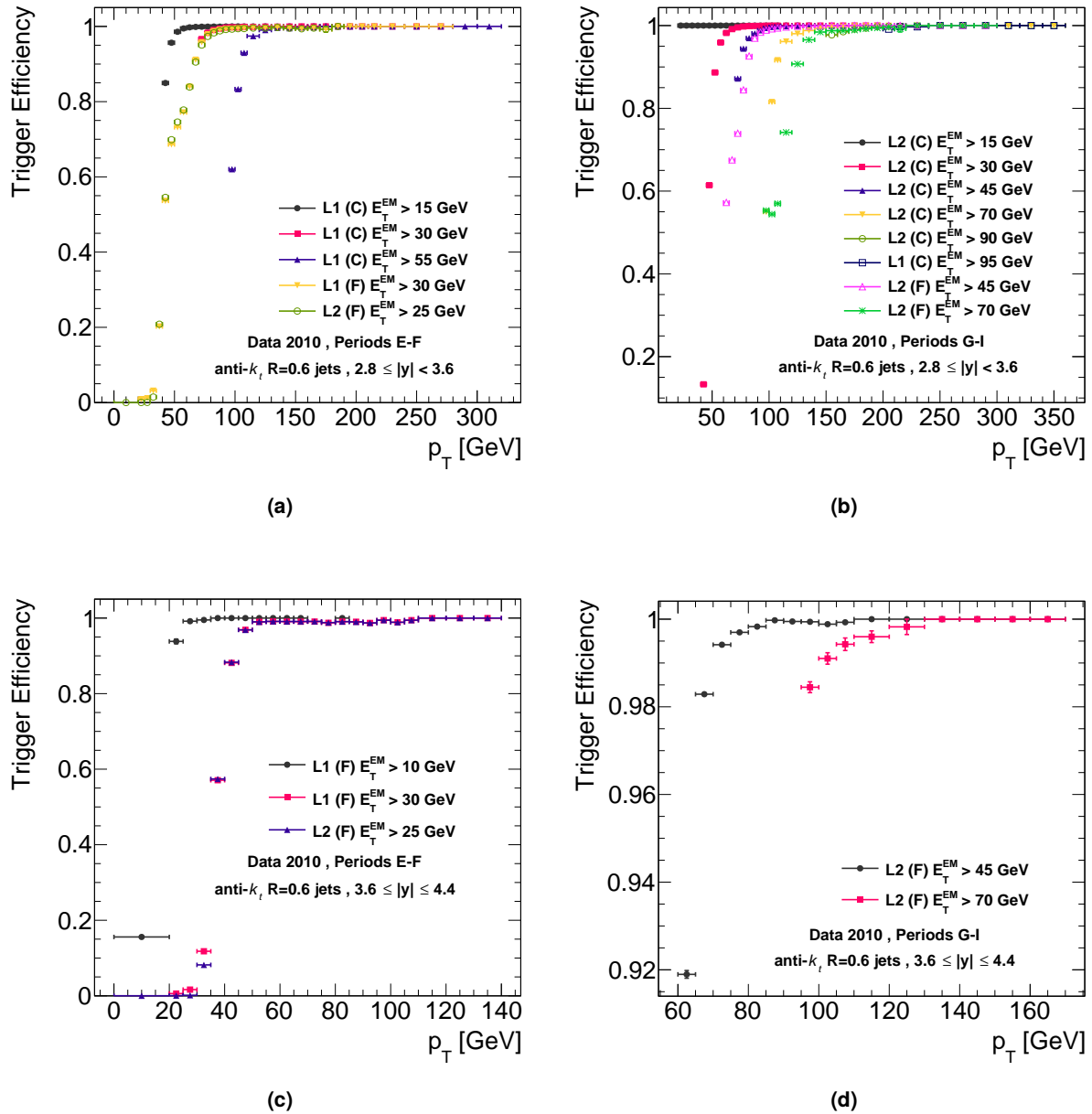


Figure 3.5: Trigger efficiency as a function of the reconstructed jet transverse momentum, p_T , for various triggers (L1 and L2) and for different data taking periods, as indicated in the figures. The trigger objects are associated with jets within rapidity $2.8 < |y| < 3.6$ ((a) and (b)) and within rapidity $3.6 < |y| < 4.4$ ((c) and (d)), belonging to either the central (C) or the forward (F) jet trigger systems. Trigger thresholds are denoted by E_T^{EM} , the minimal transverse energy at the electromagnetic scale of a jet which is required to fire the trigger.

3 Experimental setup

p_T [GeV]	Trigger name			
	Period A (Run < 152777)	Periods A-D (Run \geq 152777)	Periods E-F (excl. E1-E4)	Periods G-I
$ y < 3.6$				
20 < p_T \leq 42.5	L1_MBTS	L1_MBTS	L1_MBTS	EF_MBTS
42.5 < p_T \leq 70	L1_MBTS	L1_J5	L1_J5	L2_J15
70 < p_T \leq 97.5	L1_MBTS	L1_J15	L1_J15	L2_J30
97.5 < p_T \leq 152.5	L1_MBTS	L1_J30	L1_J30	L2_J45
152.5 < p_T \leq 197.5	L1_MBTS	L1_J55	L1_J55	L2_J70
197.5 < p_T \leq 217.5	L1_MBTS	L1_J55	L1_J55	L2_J90
217.5 < p_T	L1_MBTS	L1_J55	L1_J55	L1_j95
$2.8 \leq y < 3.6$				
20 < p_T \leq 42.5	L1_MBTS	L1_MBTS	L1_MBTS	EF_MBTS
42.5 < p_T \leq 62.5	L1_MBTS	L1_MBTS	L1_FJ10	EF_MBTS
62.5 < p_T \leq 72.5	L1_MBTS	L1_MBTS	L1_FJ10	L2_FJ25
72.5 < p_T \leq 95	L1_MBTS	L1_MBTS	L1_FJ30	L2_FJ25
95 < p_T \leq 160	L1_MBTS	L1_MBTS	L1_FJ30	L2_FJ45
160 < p_T	L1_MBTS	L1_MBTS	L1_FJ30	L2_FJ70
$3.6 \leq y \leq 4.4$				
20 < p_T \leq 42.5	L1_MBTS	L1_MBTS	L1_FJ10	EF_MBTS
42.5 < p_T \leq 50	L1_MBTS	L1_MBTS	L1_FJ10	L2_FJ25
50 < p_T \leq 67.5	L1_MBTS	L1_MBTS	L1_FJ30	L2_FJ25
67.5 < p_T \leq 100	L1_MBTS	L1_MBTS	L1_FJ30	L2_FJ45
100 < p_T	L1_MBTS	L1_MBTS	L1_FJ30	L2_FJ70

Table 3.1: Trigger chains as a function of the reconstructed jet transverse momentum, p_T , and rapidity, y , ranges in various data-taking periods, as indicated in the table. In the naming scheme (for details see text), the number that follows the trigger name stands for the threshold in transverse energy at the EM scale, E_T^{EM} .

p_T [GeV]	Per-jet trigger efficiency			
	Period A (Run < 152777)	Periods A-D (Run \geq 152777)	Periods E-F (excl. E1-E4)	Periods G-I
Crack region, $1.3 \leq y < 1.6$				
20 < $p_T \leq$ 42.5	1	1	1	1
42.5 < $p_T \leq$ 70	1	0.89	0.89	0.96
70 < $p_T \leq$ 97.5	1	0.88	0.88	0.87
97.5 < $p_T \leq$ 152.5	1	0.81	0.81	0.83
152.5 < $p_T \leq$ 197.5	1	0.83	0.83	0.82
197.5 < $p_T \leq$ 217.5	1	0.83	0.83	0.80
217.5 < p_T	1	0.83	0.83	0.81
Forward region, $2.8 \leq y < 3.6$				
20 < $p_T \leq$ 42.5	1	1	1	1
42.5 < $p_T \leq$ 62.5	1	1	1	1
62.5 < $p_T \leq$ 72.5	1	1	1	0.99
72.5 < $p_T \leq$ 95	1	1	0.97	0.99
95 < $p_T \leq$ 160	1	1	0.97	0.99
160 < p_T	1	1	0.97	1
Forward region, $3.6 \leq y \leq 4.4$				
20 < $p_T \leq$ 42.5	1	1	0.95	1
42.5 < $p_T \leq$ 50	1	1	0.95	0.99
50 < $p_T \leq$ 67.5	1	1	0.95	0.99
67.5 < $p_T \leq$ 100	1	1	0.95	0.97
100 < p_T	1	1	0.95	0.97

Table 3.2: The plateau per-jet trigger efficiency as a function of the jet transverse momentum, p_T , and rapidity, y , ranges in various data taking periods, as indicated in the table. The uncertainty on the per-jet trigger efficiency ranges between 1 and 2%, depending on the trigger region and threshold.

3 Experimental setup

In order to account for different prescale combinations of the two jets, the *Inclusive method for fully efficient combinations* [160] is used. In this scheme, the integrated luminosity of each trigger is calculated over the entire event sample, taking into account the trigger prescale in each period. In the same manner, the integrated luminosity of all possible combinations of two prescaled triggers firing simultaneously is calculated over the entire sample.

Let \mathcal{L}_{LB} denote the integrated luminosity in a luminosity-block (LB), and let P_{LB} denote the prescale of a given jet trigger within this LB. The effective luminosity of a single trigger for the entire dataset can then be written as

$$\mathcal{L}_{\text{single}}^{\text{jet}} = \sum_{\text{LB}} \frac{\mathcal{L}_{\text{LB}}}{P_{\text{LB}}}, \quad (3.11)$$

where the summation is over all luminosity-blocks. The effective luminosity for a pair of triggers takes into account the probability that two triggers with prescales, P_{LB}^0 and P_{LB}^1 , fired simultaneously in a given event; it is defined by

$$\mathcal{L}_{\text{double}}^{\text{jet}} = \sum_{\text{LB}} \frac{\mathcal{L}_{\text{LB}}}{P_{\text{LB}}^0 P_{\text{LB}}^1 / (P_{\text{LB}}^0 + P_{\text{LB}}^1 - 1)}. \quad (3.12)$$

The resulting matrix of integrated luminosities for each trigger combination is then used as a weight for each event. Tables 3.3 and 3.4 show the integrated single- and double-trigger luminosities for the different trigger-bins used in the analysis.

The combined trigger efficiency of the two leading jets is computed in a similar manner as in Eq. (3.12), using the corresponding per-jet trigger efficiencies (given in Table 3.2) and the single-jet reconstruction efficiency (see Section 3.7.1). Together these yield the probability for an event to have fired a given trigger (or trigger combination), and for a jet (or pair of jets) to have been reconstructed and matched to the trigger(s). The inverse of the combined trigger and reconstruction efficiency factor is multiplied by the luminosity of the selected luminosity class, producing the final luminosity weight for each event.

2010 Period A , Run < 152777	
Trigger name	L1_MBTS
L1_MBTS	$1.81 \cdot 10^{-4}$

2010 Periods A-D (Run \geq 152777)					
Trigger name	L1_MBTS	L1_J5	L1_J15	L1_J30	L1_J55
L1_MBTS	$5.52 \cdot 10^{-4}$	$2.48 \cdot 10^{-2}$	$2.57 \cdot 10^{-1}$	$2.57 \cdot 10^{-1}$	$2.57 \cdot 10^{-1}$
L1_J5		$2.48 \cdot 10^{-2}$	$2.57 \cdot 10^{-1}$	$2.57 \cdot 10^{-1}$	$2.57 \cdot 10^{-1}$
L1_J15			$2.57 \cdot 10^{-1}$	$2.57 \cdot 10^{-1}$	$2.57 \cdot 10^{-1}$
L1_J30				$2.57 \cdot 10^{-1}$	$2.57 \cdot 10^{-1}$
L1_J55					$2.57 \cdot 10^{-1}$

2010 Periods E-F (excl. E1-E4)							
Trigger name	L1_MBTS	L1_J5	L1_J15	L1_J30	L1_J55	L1_FJ10	L1_FJ30
L1_MBTS	$7.78 \cdot 10^{-5}$	$2.41 \cdot 10^{-3}$	$2.36 \cdot 10^{-2}$	$1.08 \cdot 10^0$	$2.13 \cdot 10^0$	$1.52 \cdot 10^{-2}$	$2.13 \cdot 10^0$
L1_J5		$2.34 \cdot 10^{-3}$	$2.58 \cdot 10^{-2}$	$1.08 \cdot 10^0$	$2.13 \cdot 10^0$	$1.75 \cdot 10^{-2}$	$2.13 \cdot 10^0$
L1_J15			$2.36 \cdot 10^{-2}$	$1.08 \cdot 10^0$	$2.13 \cdot 10^0$	$3.80 \cdot 10^{-2}$	$2.13 \cdot 10^0$
L1_J30				$1.08 \cdot 10^0$	$2.13 \cdot 10^0$	$1.08 \cdot 10^0$	$2.13 \cdot 10^0$
L1_J55					$2.13 \cdot 10^0$	$2.13 \cdot 10^0$	$2.13 \cdot 10^0$
L1_FJ10						$1.51 \cdot 10^{-2}$	$2.13 \cdot 10^0$
L1_FJ30							$2.13 \cdot 10^0$

Table 3.3: Integrated luminosity in pb^{-1} for different trigger combinations used in several data-taking periods in 2010, up to period F. The uncertainty on the luminosity is 3.5%.

3 Experimental setup

2010 Periods G-I							
Trigger name	EF_MBTS	L2_J15	L2_J30	L2_J45	L2_J70	L2_J90	L1_J95
EF_MBTS	$9.66 \cdot 10^{-5}$	$2.37 \cdot 10^{-3}$	$4.94 \cdot 10^{-2}$	$2.40 \cdot 10^{-1}$	$6.15 \cdot 10^0$	$5.89 \cdot 10^0$	$3.38 \cdot 10^1$
L2_J15		$2.29 \cdot 10^{-3}$	$5.14 \cdot 10^{-2}$	$2.44 \cdot 10^{-1}$	$6.15 \cdot 10^0$	$5.89 \cdot 10^0$	$3.38 \cdot 10^1$
L2_J30			$4.93 \cdot 10^{-2}$	$2.63 \cdot 10^{-1}$	$6.17 \cdot 10^0$	$5.91 \cdot 10^0$	$3.38 \cdot 10^1$
L2_J45				$2.41 \cdot 10^{-1}$	$6.21 \cdot 10^0$	$5.95 \cdot 10^0$	$3.38 \cdot 10^1$
L2_J70					$6.15 \cdot 10^0$	$7.58 \cdot 10^0$	$3.38 \cdot 10^1$
L2_J90						$5.89 \cdot 10^0$	$3.38 \cdot 10^1$
L1_J95							$3.38 \cdot 10^1$

2010 Periods G-I			
Trigger name	L2_FJ25	L2_FJ45	L2_FJ70
EF_MBTS	$1.55 \cdot 10^{-1}$	$3.66 \cdot 10^0$	$3.38 \cdot 10^1$
L2_J15	$1.58 \cdot 10^{-1}$	$3.66 \cdot 10^0$	$3.38 \cdot 10^1$
L2_J30	$1.79 \cdot 10^{-1}$	$3.68 \cdot 10^0$	$3.38 \cdot 10^1$
L2_J45	$3.24 \cdot 10^{-1}$	$3.74 \cdot 10^0$	$3.38 \cdot 10^1$
L2_J70	$6.20 \cdot 10^0$	$7.48 \cdot 10^0$	$3.38 \cdot 10^1$
L2_J90	$5.94 \cdot 10^0$	$7.29 \cdot 10^0$	$3.38 \cdot 10^1$
L1_J95	$3.38 \cdot 10^1$	$3.38 \cdot 10^1$	$3.38 \cdot 10^1$
L2_FJ25	$1.55 \cdot 10^{-1}$	$3.73 \cdot 10^0$	$3.38 \cdot 10^1$
L2_FJ45		$3.66 \cdot 10^0$	$3.38 \cdot 10^1$
L2_FJ70			$3.38 \cdot 10^1$

Table 3.4: Integrated luminosity in pb^{-1} for the different trigger combinations used during data-taking periods G-I in 2010. The uncertainty on the luminosity is 3.5%.

Monte Carlo simulation

The final states of pp interactions at the LHC are very complex and typically involve many particles and different scales. Monte Carlo techniques are most commonly used to simulate these interactions in order to obtain predictions of experimental observables. For comparison of distributions obtained using MC with distributions in data, a detailed simulation of the interactions of particles with the ATLAS detector is required.

A description of the MC generators and of the ATLAS detector simulation used in the analysis is presented in the following.

4.1 Event generators

A pp collision at the LHC is composed of interactions at different scales of the momentum transfer involved. Factorization is used to separate the processes occurring in the interaction according to that scale. At the highest scales the constituent partons of the incoming protons interact to produce a relatively small number of energetic outgoing particles. The matrix elements of these hard subprocesses are perturbatively computable. Soft interactions at the very lowest scales, of the order of 1 GeV^2 , cannot yet be calculated from first principles and have to be modelled. The hard and soft regimes are distinct but connected by an evolutionary process that can be calculated in principle from perturbative QCD.

Event generators simulate the full picture of pp collisions using MC techniques. An overview of MC event generators for LHC physics can be found in [161]. A short summary of multi-parton interactions in event generators, a subject of interest to this study, is presented in the following, and a brief description of the different event generators utilized in this analysis is given.

4.1.1 Multi-parton interactions in event generators

The inclusion of MPI in event generators is important not only for the purpose of achieving a better description of observables in data, e.g., particle multiplicity. A first model for this phenomenon in the framework of MC was presented in [162]. Adding MPI resolves a fundamental theoretical issue, namely the fact that the inclusive dijet cross-section (σ_{2j}), calculated assuming one parton-parton scatter per proton-proton collision, exceeds the total cross-section (σ_{tot}) as extrapolated using non-perturbative fits. Naively, this violates the unitarity of perturbative QCD cross-sections, but this problem can be resolved by assuming more than one parton scatter per hadron collision. The logic is as follows: the total cross-section is an inclusive number, quantifying the intrinsic likelihood of an interaction to occur when two protons collide. When measuring σ_{tot} , a collision between two protons would count as one interaction, regardless of how many parton-parton interactions occur. Thus, an event with n parton-parton interactions will be counted n times when measuring σ_{2j} , but only once when measuring σ_{tot} . Under the assumption that all parton-parton interactions are independent, σ_{2j} may be expressed as

$$\sigma_{2j}(p_{\perp, \text{min}}) = \langle n \rangle (p_{\perp, \text{min}}) \sigma_{\text{tot}}, \quad (4.1)$$

4 Monte Carlo simulation

where $\langle n \rangle(p_{\perp, \min})$ is the average number of parton-parton interactions producing partons with transverse momentum above $p_{\perp, \min}$ per proton–proton collision. The problem is therefore restated such that instead of the inclusive jet cross-section diverging as $p_{\perp, \min} \rightarrow 0$, the number of interactions per collision diverges. The latter divergence is regularized within event generators by introducing a cutoff value of $p_{\perp, \min}$, motivated by color screening (see section 7.3.1 in [161]). The cutoff parameter is tuned to data and is usually of the order of a few GeV.

4.1.2 ALPGEN + HERWIG + JIMMY

The ALPGEN package is a tree level matrix element generator for hard multi-parton processes ($2 \rightarrow n$) in hadronic collisions [115]. Matching of parton showers with matrix element partons from ALPGEN is done using the MLM matching scheme [117]. Here, ALPGEN has been interfaced to the HERWIG [163, 164] general-purpose event generator which uses angular-ordered parton showers. It also employs a cluster model for jet hadronization based on non-perturbative gluon splitting [122]. Simulation of multiple parton interactions is done in the JIMMY [126, 127] package, interfaced to the HERWIG generator. Further details on the multi-parton interactions model implemented in JIMMY is given below.

The sample utilized in this analysis was generated with ALPGEN 2.14 using the CTEQ6L1 PDF set, interfaced to JIMMY and HERWIG 6.520 using the AUET2 [165] set of underlying event parameters (tune). The MPI parameters in the AUET2 tune were set with the early ATLAS data. The MLM matching scale, the energy scale in which matching of matrix elements to parton showers begins, was set to 15 GeV. The implication of this choice is that partons with $p_T \geq 15$ GeV in the final state, originate from matrix elements, and not from the parton shower.

Five separate ALPGEN samples were generated, each corresponding to a fixed order matrix element ($2 \rightarrow n$, with $n = 2, 3, \dots, 6$). The samples were then combined based on the respective matrix element cross-section as calculated in ALPGEN. To increase the amount of DPS events in the final sample, a filter was applied during the generation of the $2 \rightarrow 2$ matrix element sample. The so-called DPS filter selected events containing at least two partons with $p_T \geq 15$ GeV originating from a secondary interaction.

The main SPS sample used in the analysis is extracted from the ALPGEN + HERWIG + JIMMY MC combination (AHJ) by matching jets to partons, as described in Section 6.7.2. A sample of DPS events is also extracted from AHJ in order to study their topology and validate the measurement methodology.

Multi-parton interactions model in JIMMY

The JIMMY model for MPI assumes some distribution of the matter inside the hadron in impact parameter (\mathbf{b}) space, which is independent of the momentum fraction, x . The MPI rate of interactions of type A, accompanying the “trigger” interaction, B, is then calculated using the cross section for the hard sub-process, the PDF and the area overlap function, $\Gamma(\mathbf{b})$. The starting point for the MPI model is the assertion that, at fixed impact parameter, \mathbf{b} , different scatters are independent, so their number obeys Poisson statistics.

The cross-section for events in which there are n scatters of type A is given by

$$\sigma_n = \int d^2\mathbf{b} \frac{(\Gamma(\mathbf{b})\sigma_A)^n}{n!} e^{-\Gamma(\mathbf{b})\sigma_A}, \quad (4.2)$$

where σ_A is the parton-parton cross-section and $\Gamma(\mathbf{b})$ is the matter density distribution, obeying

$$\int d^2\mathbf{b} \Gamma(\mathbf{b}) = 1. \quad (4.3)$$

The probability distribution for n is then

$$P_n \approx \frac{\int d^2\mathbf{b} n \frac{(\Gamma(\mathbf{b})\sigma_A)^n}{n!} e^{-\Gamma(\mathbf{b})\sigma_A}}{\sigma_A}. \quad (4.4)$$

Equation (4.4) is an approximation made under the assumption that the “trigger” interaction of type B has a small cross-section compared to the cross-section of the interaction of type A, $\sigma_B \ll \sigma_A$. With this assumption, P_n becomes independent of σ_B . The Monte Carlo implementation of MPI in JIMMY generates n scatters of type A, according to Eq. (4.4), for each event of type B. Further corrections to the generation process are introduced when B is a subset of A, as is the case for the present analysis. For a more comprehensive derivation of the MPI model in pp interactions implemented in JIMMY, see [166].

4.1.3 PYTHIA

The PYTHIA [167] event generator simulates non-diffractive pp collisions using a $2 \rightarrow 2$ matrix element at leading order to model the hard subprocess. It uses p_T -ordered parton showers to model additional radiation in the leading-logarithmic approximation. Multiple parton interactions are modelled based on the original ideas of [162], but further refined [129, 168]. The hadronization of partons is achieved with the Lund string model [121].

The model implemented in PYTHIA for the generation of MPI is similar to the one implemented in JIMMY, although with a few differences [161]. The “turn-off curve” for interactions with p_T below the cutoff value $p_{\perp, \min}$ is a smooth one in PYTHIA, while JIMMY employs a step function, $\Theta(p_{\perp} - p_{\perp, \min})$. The form of the matter distribution in the proton in PYTHIA is a simple parametric form such as a Gaussian, double Gaussians or exponentials [162], while the form implemented in JIMMY is based on the electromagnetic form factor [169]. A detailed description of multiple interactions in PYTHIA is given in [129].

Samples generated with PYTHIA 6.425 are used in this analysis mainly in the geometrical acceptance calculation (see Section 6.6). The samples were generated utilizing the modified leading-order PDF set MRST LO* [15] with the AMBT1 set of underlying event parameters, tuned to describe the distributions measured by ATLAS in minimum bias collisions [170].

4.1.4 SHERPA

SHERPA is a general-purpose tool for the simulation of particle collisions at high-energy colliders, using tree-level matrix-element generators for the calculation of hard scattering processes [171, 172].

4 Monte Carlo simulation

The emission of additional QCD partons off the initial and final states is performed using a p_T -ordered parton shower model. Combining leading order matrix elements and parton showers is done with special care in SHERPA [173], based on the CKKW merging algorithm [118, 119]. A simple model of multiple interactions, based on the model described in [162], is used to account for underlying events in hadron–hadron collisions. The fragmentation of partons into primary hadrons is described using a phenomenological cluster-hadronization model [123].

The sample used for the analysis was generated within SHERPA 1.4.2 with the CT10 PDF set and the default SHERPA underlying event tune. The CKKW matching scale was set to 15 GeV, similarly to the AHJ sample described above. Events were generated without multi-parton interactions by setting the internal flag, `MI_HANDLER=None`. The resulting sample is compared to the SPS sample extracted from the AHJ sample for validation purposes (see Section 7.3).

4.2 Simulation of the ATLAS detector

Four-vectors of stable particles in the events generated are passed through the full ATLAS detector simulation. The GEANT software toolkit [174] within the ATLAS simulation framework [175] propagates the particles through the ATLAS detector and simulates their interactions with the detector material. The energy deposited by particles in the active detector material is converted into detector signals with the same format as the ATLAS detector read-out. The simulated detector signals are in turn reconstructed with the same reconstruction software as used for the data. Finally, simulated events are reconstructed and jets are calibrated in the same manner as in the data.

The resulting MC events are used to construct detector-level distributions directly comparable with the data and to study the performance of the detector by estimating reconstruction efficiencies, geometrical coverage and the performance of the triggers.

Event selection

To reject events initiated by cosmic-ray muons and other non-collision backgrounds, events in this analysis are required to have at least one primary hard scattering vertex. A primary hard scattering vertex is required to be consistent with the beam-spot and to have at least five tracks, each complying with the following criteria:

- track transverse momentum, $p_T^{\text{track}} > 150 \text{ MeV}$;
- combined number of hits in the Pixel and SCT detectors associated with the track, $N_{\text{Pixel}} + N_{\text{SCT}} \geq 7$;
- transverse (d_0) and longitudinal (z_0) impact parameters, measured with respect to the vertex to which the tracks are extrapolated, $|d_0| < 1.0 \text{ mm}$ and $|z_0| \cdot \sin \theta < 1.5 \text{ mm}$, where θ is the polar angle of the track;
- quality of track fit, $(\chi^2/\text{NDF})_{\text{track}} < 3.5$.

As mentioned in [Section 3.6.2](#), the primary vertex associated to the event of interest (hard scattering vertex) is the one with the highest associated transverse track momentum $\sum p_T^{\text{track}}$.

The rate of hard double parton scattering is measured in events which have at least four jets in the final state – an event set referred to as *inclusive* four-jet events. For the purpose of measuring σ_{eff} in the four-jet final state, inclusive dijet events are selected in a similar manner as four-jet events, having at least two jets in the final state. Both dijet and four-jet events are selected using the two-trigger selection scheme described in [Section 3.10](#).

Jets are required to have $p_T \geq 20 \text{ GeV}$ and $|\eta| \leq 4.4$. In each event selected, jets are ordered in descending order of their transverse momenta. That is, denoting by p_T^i the transverse momentum of the i^{th} jet in an event, the p_T of jets in e.g., a four-jet event, fulfil the condition,

$$p_T^1 > p_T^2 > p_T^3 > p_T^4 .$$

Once the jets are sorted in descending order of p_T , the jet with the highest- p_T , p_T^1 , is referred to as the leading jet.

The leading jet in four-jet events is required to have $p_T \geq 42.5 \text{ GeV}$. Restricting the p_T of the leading jet to be higher than the minimal threshold for reconstruction, creates a scale separation between the jets in the event. This sets a different scale for the interactions in DPS events, which is helpful when attempting to identify these events. The restriction on the leading jet is also motivated by the trigger strategy of the analysis. It amounts to the requirement that at least one jet in the event fires a jet trigger (see [Section 3.10](#)). Four-jet events in which the two leading jets are associated with the MBTS trigger are rejected due to the argument below. Such events constitute a very small fraction of the overall sample, but they dominate completely the phase-space region in which both leading jets have transverse momenta in the range $20 < p_T < 42.5 \text{ GeV}$. Since they are associated with very high luminosity weights (see [Section 3.10.2](#)), they tend to introduce large statistical fluctuations into the measurement. Consequently, the requirement that at least one jet in the event is associated with a jet trigger is enforced.

5 Event selection

The expression for the DPS cross-section for the final state (A,B), given in Eq. (2.15), involves two cross-sections for the final states A and B. The transverse momentum requirement applied on the leading jet in four-jet events therefore splits the final states A and B into two classes of dijet events. In one class of dijet events, the cut on the transverse momentum of the leading jet must be equivalent to the cut on the leading jet in four-jet events, $p_T \geq 42.5$ GeV. The other type of dijet events corresponds to the sub-leading pair of jets in the four-jet event, with a requirement $p_T \geq 20$ GeV. In the following, the cross-section for dijets selected with $p_T \geq 20$ GeV is denoted by σ_{2j}^A and the cross-section for dijets with $p_T^1 \geq 42.5$ GeV is denoted by σ_{2j}^B .

Pile-up may potentially introduce a bias to the measurement by adding extra jets, by changing the p_T of the jets or by causing splitting of the jets. In order to avoid these issues, the 2010 data taking periods with a low average number of interactions per beam crossing are used, $\langle \mu \rangle = 0.41$. The average number of reconstructed vertices in the data sample collected with the triggers described in Section 3.10 is 1.4. To further reduce the effects of pile-up, only single-vertex events are selected.

To summarize, the measurement is performed using three samples, two distinct samples of dijet events and a sample of four-jet events, selected using the following requirements:

$$\begin{aligned}
 (\text{dijet A}) \quad N_{\text{PV}} = 1, \quad N_{\text{jet}} = 2, \quad p_T^{1,2} \geq 20 \text{ GeV}, \quad |\eta_{1,2}| \leq 4.4, \\
 (\text{dijet B}) \quad N_{\text{PV}} = 1, \quad N_{\text{jet}} = 2, \quad p_T^1 \geq 42.5 \text{ GeV}, \quad p_T^2 \geq 20 \text{ GeV}, \quad |\eta_{1,2}| \leq 4.4, \\
 (\text{four-jet}) \quad N_{\text{PV}} = 1, \quad N_{\text{jet}} = 4, \quad p_T^1 \geq 42.5 \text{ GeV}, \quad p_T^{2-4} \geq 20 \text{ GeV}, \quad |\eta_{1-4}| \leq 4.4,
 \end{aligned} \tag{5.1}$$

where N_{PV} is the number of reconstructed vertices in the event and N_{jet} is the minimum number of reconstructed anti- k_t , $R = 0.6$, jets in the event.

Methodology

The expression for σ_{eff} , defined in Eq. (2.18),

$$\sigma_{\text{eff}} = \frac{1}{1 + \delta_{\text{AB}}} \frac{\sigma_{2j}^{\text{A}} \sigma_{2j}^{\text{B}}}{\sigma_{\text{DPS}}} = \frac{1}{1 + \delta_{\text{AB}}} \frac{1}{f_{\text{DPS}}} \frac{\sigma_{2j}^{\text{A}} \sigma_{2j}^{\text{B}}}{\sigma_{4j}}, \quad (6.1)$$

guides the analysis, where the double parton scattering cross-section,

$$\sigma_{\text{DPS}} = f_{\text{DPS}} \cdot \sigma_{4j},$$

is extracted using the measured cross-section of four-jet events, σ_{4j} . The latter includes all events with a four-jet final state, i.e., both $(2 \rightarrow 4)$ and $(2 \rightarrow 2)^{\times 2}$ topologies. The cornerstone of the measurement of σ_{eff} is the extraction of f_{DPS} [77] and the measurement of the ratio of inclusive dijet and four-jet cross-sections.

6.1 Classes of double parton scattering events

Among events with at least four jets, DPS contributes two classes of events. The first class consists of events in which the two dijets of DPS are among the four leading jets, referred to as complete-DPS (cDPS) events. In the second class of events, out of the four leading jets, three jets originate from one scattering and one from the other. A schematic sketch of the latter class of DPS events, named semi-DPS (sDPS), is shown in Fig. 6.1.

In the following, the distinction between the two classes of double parton scattering events is taken into account by modifying Eq. (6.1) to read

$$\sigma_{\text{eff}} = \frac{1}{1 + \delta_{\text{AB}}} \frac{1}{f_{\text{cDPS}} + f_{\text{sDPS}}} \frac{\sigma_{2j}^{\text{A}} \sigma_{2j}^{\text{B}}}{\sigma_{4j}}, \quad (6.2)$$

where f_{cDPS} and f_{sDPS} are the fractions of complete-DPS events and semi-DPS events, respectively, and their values in AHJ are $f_{\text{cDPS}} = 0.1$ and $f_{\text{sDPS}} = 0.05$ (see Chapter 7). The cross-sections in Eq. (6.2) do not require any modification since they are all inclusive cross-sections. That is, the three-jet cross-section accounting for the production of a sDPS event is already included in the dijet cross-sections.

6.2 Symmetry factor

As explained in Section 2.4, the symmetry factor in the expression for the double parton scattering cross-section is set to two if the two cross-sections under consideration are identical, or to one otherwise. The two cross-sections, σ_{2j}^{A} and σ_{2j}^{B} , selected in the A and B phase-space regions defined in Eq. (5.1), overlap in the region where the leading jet has $p_{\text{T}} \geq 42.5$ GeV. This is taken into account by a symmetry factor proportional to the size of the overlap, as described in this section.

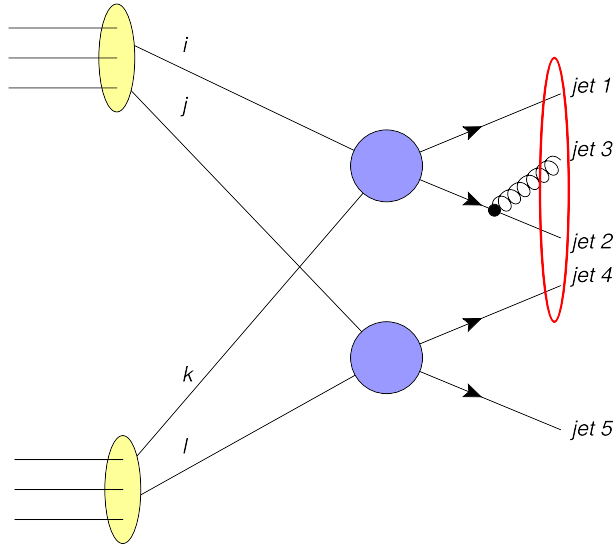


Figure 6.1: Schematic sketch of a semi-DPS event, in which one interaction contributes three partons (jets) to the four-jet final state and the other interaction contributes one parton (jet). The four leading (highest- p_T) partons in the schematic event are circled by the red ellipse, marking the partons selected in the event topology reconstruction.

The expression for the DPS cross-section, defined in Eq. (2.16), is re-written as the sum of two exclusive contributions,

$$\sigma_{\text{DPS}} = \sigma_{2j}(20 \leq p_T^1 < 42.5) \cdot \sigma_{2j}(p_T^1 \geq 42.5) + \frac{1}{2} \left(\sigma_{2j}(p_T^1 \geq 42.5) \right)^2, \quad (6.3)$$

where the definition $\sigma_{2j}(p_T^1 \geq 42.5) \equiv \sigma_{2j}^{\text{B}}$ is used and $\sigma_{2j}(20 \leq p_T^1 < 42.5)$ refers to the dijet cross-section for events selected in the phase-space region labeled A in Eq. (5.1), with an additional requirement that the leading jet has $20 \leq p_T < 42.5$ GeV. The first term on the right-hand side of Eq. (6.3) relates two mutually exclusive cross-sections and therefore the symmetry factor in this term is set to one. The second term contains two equivalent cross-sections, thus its symmetry factor is set to half. For simplicity, the factor $(\sigma_{\text{eff}})^{-1}$ is dropped in this discussion.

The cross-sections in Eq. (6.3) may be expressed in terms of the σ_{2j}^{A} cross-section and the fractional overlap, γ ,

$$\sigma_{2j}(p_T^1 \geq 42.5) = \gamma \sigma_{2j}^{\text{A}} \equiv \gamma \sigma_{2j}(p_T^1 \geq 20), \quad (6.4)$$

$$\sigma_{2j}(20 \leq p_T^1 < 42.5) = (1 - \gamma) \sigma_{2j}^{\text{A}} \equiv (1 - \gamma) \sigma_{2j}(p_T^1 \geq 20), \quad (6.5)$$

where $\sigma_{2j}(p_T^1 \geq 20) \equiv \sigma_{2j}^{\text{A}}$. Introducing these relations into Eq. (6.3) yields

$$\sigma_{\text{DPS}} = \sigma_{2j}(p_T^1 \geq 42.5) \cdot \left((1 - \gamma) \sigma_{2j}(p_T^1 \geq 20) + \frac{1}{2} \gamma \sigma_{2j}(p_T^1 \geq 20) \right) \quad (6.6)$$

$$= \left(1 - \frac{\gamma}{2} \right) \sigma_{2j}(p_T^1 \geq 20) \cdot \sigma_{2j}(p_T^1 \geq 42.5) \quad (6.7)$$

$$= \left(1 - \frac{\gamma}{2} \right) \sigma_{2j}^{\text{A}} \cdot \sigma_{2j}^{\text{B}}. \quad (6.8)$$

Hence, the symmetry factor in Eq. (6.2) comes out to be

$$\frac{1}{1 + \delta_{AB}} = 1 - \frac{\gamma}{2}, \quad (6.9)$$

where

$$\gamma = \frac{\sigma_{2j}^B}{\sigma_{2j}^A}. \quad (6.10)$$

The fractional overlap may be extracted from the measured cross-sections in data (see Section 6.5),

$$\gamma_{\text{data}} = \frac{\sigma_{2j}^B(\text{data})}{\sigma_{2j}^A(\text{data})} = 0.1293 \pm 0.0007 \text{ (stat.)}, \quad (6.11)$$

where each cross-section is corrected for the fiducial acceptance (see Section 6.6). The fractional overlap may also be estimated in PYTHIA. Two dijet samples are selected by applying the cuts defined in Eq. (5.1) on particle jets in PYTHIA. The ratio between the calculated cross-sections is then used to estimate γ ,

$$\gamma_{\text{PYTHIA}} = \frac{\sigma_{2j}^B(\text{PYTHIA})}{\sigma_{2j}^A(\text{PYTHIA})} = 0.1333 \pm 0.0011 \text{ (stat.)}. \quad (6.12)$$

A good agreement is observed between the values of γ obtained in data and in MC. In order to estimate the effect of the difference between γ_{data} and γ_{PYTHIA} on the measured value of σ_{eff} , the latter is calculated for each value of γ . The relative difference between the two results is of the order of 0.2%, a negligible difference compared to the statistical uncertainty on σ_{eff} . Thus, no systematic uncertainty is associated with the value of γ .

6.3 Correction due to overlapping jets

Two anti- k_t jets with a radius parameter of 0.6 occupy a non-negligible area in the $\eta - \phi$ plane. It is therefore conceivable that one of the jets from the secondary interaction would overlap with a jet from the primary interaction. In such an occurrence, the anti- k_t algorithm would merge the two jets and the event would not be counted as a four-jet event. The probability for this to occur is related to the combined area of the two jets from the primary interaction with respect to the total fiducial area in the $\eta - \phi$ plane. In the case of hard jets, the anti- k_t algorithm produces circular jets with a radius R (see Fig. 3.3). Therefore, an estimate for the probability of a jet originating from DPS overlapping with one of the jets from the primary interaction may be calculated from,

$$P(\text{overlap}) = \frac{2 \cdot \pi R^2}{\int_{-4.4}^{4.4} d\eta \cdot \int_0^{2\pi} d\phi} = \frac{2 \cdot \pi R^2}{8.8 \cdot 2\pi} = 0.041. \quad (6.13)$$

The fiducial volume in the $\eta - \phi$ plane is defined by the cuts in Eq. (5.1). This probability is used as a geometrical correction to the measured DPS cross-section. The fraction of three-jet events failing the four-jet cut due to merging of a jet from the secondary interaction with a jet from the primary interaction was also determined directly from AHJ to be 0.0428 ± 0.0005 . In order to evaluate the effect of the difference between these two estimates on the measured value of σ_{eff} , the latter is

calculated for each value of $P(\text{overlap})$. The relative difference between the two results is of the order of 0.2%, a negligible difference compared to the statistical uncertainty on σ_{eff} . Thus, no systematic uncertainty is associated with this geometrical correction.

6.4 The effective cross-section in terms of experimental observables

The general expression for the measured dijet and four-jet cross-sections may be written as

$$\sigma_{nj} = \frac{N_{nj}}{\mathcal{A}_{nj}\epsilon_{nj}\mathcal{L}_{nj}}, \quad (6.14)$$

where the subscript, nj , denotes either dijet ($2j$) or four-jet ($4j$) topologies. For each nj channel, N_{nj} is the number of measured events, \mathcal{A}_{nj} is the geometrical acceptance of these events, ϵ_{nj} is the efficiency for reconstructing the event¹ and \mathcal{L}_{nj} is the corresponding luminosity.

Using the identity given in Eq. (6.14) and incorporating the symmetry factor defined in Eq. (6.9), the expression for σ_{eff} may be re-written using measurable observables as

$$\sigma_{\text{eff}} = \left(1 - \frac{\gamma}{2}\right) \frac{1}{f_{\text{cDPS}} + f_{\text{sDPS}}} \frac{N_{2j}^A N_{2j}^B}{N_{4j}} \frac{\mathcal{L}_{4j}}{\mathcal{L}_{2j}^A \mathcal{L}_{2j}^B} \frac{\epsilon_{4j}}{\epsilon_{2j}^A \epsilon_{2j}^B} \frac{\mathcal{A}_{4j}}{\mathcal{A}_{2j}^A \mathcal{A}_{2j}^B}. \quad (6.15)$$

This expression may be simplified by defining

$$\mathcal{S}_{nj} = N_{nj}/(\epsilon_{nj}\mathcal{L}_{nj})$$

as the *observed* cross-section at the detector-level and by defining the *acceptance ratio*,

$$\alpha_{2j}^{4j} = \frac{\mathcal{A}_{4j}}{\mathcal{A}_{2j}^A \mathcal{A}_{2j}^B}.$$

Following these definitions, Eq. (6.15) reduces to

$$\sigma_{\text{eff}} = \left(1 - \frac{\gamma}{2}\right) \frac{\alpha_{2j}^{4j}}{f_{\text{cDPS}} + f_{\text{sDPS}}} \frac{\mathcal{S}_{2j}^A \mathcal{S}_{2j}^B}{\mathcal{S}_{4j}}. \quad (6.16)$$

Equation (6.16) is the fundamental expression used to extract σ_{eff} , where the acceptance ratio α_{2j}^{4j} , cross-sections \mathcal{S}_{nj} , and the fractions f_{cDPS} and f_{sDPS} , are the observables necessary for the determination of σ_{eff} . The following sections detail the strategy adopted for the measurement of each of these observables.

¹ In the 2010 data there is need to differentiate between the acceptance and the efficiency, as the non-geometrical inefficiencies of the detector (e.g. faulty electronic channels) were not properly simulated as part of the MC10 campaign.

6.5 Measurement of the dijet and four-jet cross-sections

The dijet and four-jet cross-sections, \mathcal{S}_{nj} , are estimated in data by counting the number of dijet and four-jet events passing the cuts detailed in Eq. (5.1). Events are weighted by the appropriate luminosity factors and are corrected for trigger efficiency. In addition, jet reconstruction efficiency corrections are applied for each jet, depending on its p_T and η . For a given event, the total reconstruction efficiency correction depends on whether it contributes to the dijet or the four-jet sample.

6.5.1 Correcting for the selection of single-vertex events

As mentioned in Chapter 5, only events with one primary vertex are analyzed. In order to compensate for the loss of events with $N_{PV} > 1$, a correction based on the average number of interactions per bunch crossing, $\langle\mu\rangle$, is applied.

The measured cross-section may be expressed as

$$\sigma = \sigma(N_{PV} = 1) \cdot \frac{N_{\text{evt}}}{N_{\text{evt}}(N_{PV} = 1)}, \quad (6.17)$$

where $\sigma(N_{PV} = 1)$ is the measured cross-section after selecting events with $N_{PV} = 1$, $N_{\text{evt}}(N_{PV} = 1)$ is the number of single-vertex events and N_{evt} is the number of events for all N_{PV} values. The fraction on the right-hand side of Eq. (6.17) may be expressed as

$$\frac{N_{\text{evt}}}{N_{\text{evt}}(N_{PV} = 1)} = \frac{1 - P(N_{PV} = 0)}{P(N_{PV} = 1)}, \quad (6.18)$$

where $P(N_{PV} = 1)$ is the probability that one interaction occurred in the bunch crossing and the probability to have any number of interactions is expressed as $1 - P(N_{PV} = 0)$. The probability follows the Poisson distribution with an average rate $\langle\mu\rangle$. Therefore, $P(N_{PV} = 0)$ and $P(N_{PV} = 1)$ may be estimated using $\langle\mu\rangle$,

$$P(N_{PV} = 0) = e^{-\langle\mu\rangle}, \quad P(N_{PV} = 1) = \langle\mu\rangle e^{-\langle\mu\rangle}. \quad (6.19)$$

The correction is then applied by assigning to each single-vertex event a weight,

$$w = \frac{1 - P(N_{PV} = 0)}{P(N_{PV} = 1)} = \frac{1 - e^{-\langle\mu\rangle}}{\langle\mu\rangle e^{-\langle\mu\rangle}} = 1.236, \quad (6.20)$$

where the value of μ is averaged over the entire data sample, yielding $\langle\mu\rangle = 0.41$. Various methods are used to measure μ and the maximal difference between the values obtained using the different methods is taken as the uncertainty, $\Delta\mu = \pm 0.5\%$ [144]. This uncertainty is propagated to σ_{eff} as described in Section 8.2.2.

6.5.2 Measured cross-sections

The numbers of events in the selected dijet and four-jet samples are

$$N_{2j}^A = 2,241,633, \quad N_{2j}^B = 2,036,798 \quad \text{and} \quad N_{4j} = 488,693. \quad (6.21)$$

The combination of these numbers with the corresponding luminosity and efficiency factors (see [Sections 3.7.1](#) and [3.10](#)) and the correction applied for selecting single-vertex events yields the following observed cross-sections:

$$\begin{aligned}
S_{2j}^A &= 1.9534 \cdot 10^8 \pm 4.9 \cdot 10^5 \text{ (stat.) } \begin{matrix} +5.73 \\ -6.01 \end{matrix} \cdot 10^6 \text{ (syst.) pb} \quad , \\
S_{2j}^B &= 2.6206 \cdot 10^7 \pm 3.4 \cdot 10^4 \text{ (stat.) } \begin{matrix} +5.64 \\ -5.84 \end{matrix} \cdot 10^5 \text{ (syst.) pb} \quad , \\
S_{4j} &= 3.109 \cdot 10^6 \pm 1.1 \cdot 10^4 \text{ (stat.) } \begin{matrix} +1.53 \\ -1.64 \end{matrix} \cdot 10^5 \text{ (syst.) pb} \quad ,
\end{aligned}
\tag{6.22}$$

where the first uncertainty is statistical (stat.) and the second systematic (syst.). The systematic uncertainties on the observed cross-sections are related to the systematic uncertainty on the jet reconstruction efficiency (see [Section 3.7.1](#)). The methodology for the measurement of σ_{eff} was chosen such that these uncertainties cancel almost entirely (see [Eq. \(6.16\)](#)), as discussed in [Section 8.2.3](#).

6.6 Acceptance

The second component of the measurement is the acceptance ratio, α_{2j}^{4j} . The acceptance of each class of events is individually estimated using the PYTHIA MC sample. The same restrictions on the phase-space of calorimeter jets, defined in [Eq. \(5.1\)](#), are applied on particle jets. The definition of the acceptance is given by

$$\mathcal{A}_{nj}^{\text{A,B}} = \frac{N_{nj}^{\text{A,B cal}}}{N_{nj}^{\text{A,B truth}}} \quad ,
\tag{6.23}$$

where $N_{nj}^{\text{A,B cal}}$ ($N_{nj}^{\text{A,B truth}}$) is the number of n -jet events passing the (A or B) selection cuts using detector (particle) jets.

The acceptance is sensitive to the migration of events into and out of the phase-space of the measurement. Due to the very steep jet p_T spectrum in dijet and four-jet events, it is crucial to achieve the best agreement possible between the jet p_T spectra in data and MC before calculating the acceptance. Moreover, because the migration towards higher momenta is more probable than in the opposite direction, it is important to have good control over the p_T distribution below the threshold used for the analysis. Therefore, for the following studies, the threshold was lowered to 10 GeV. The fiducial $|y|$ range was also increased to 4.5, in order to take into account possible migration in y .

6.6.1 Acceptance for dijet events

In the following comparisons of jet p_T spectra between data and MC ([Figs. 6.2](#) and [6.3](#)), the leading jet p_T distribution in data, in the range $50 < p_T < 70$ GeV, is used to set the normalization of the distributions in the MC.

A comparison between the p_T spectra of the two leading jets in dijet events in data and in PYTHIA is shown in [Fig. 6.2\(a\)](#). It can be seen that in the range $10 \leq p_T < 20$ GeV, the MC distributions underestimates the data by a factor of 1.7 for the leading jet and by a factor of 1.4 for the sub-leading jet. In the range $20 \leq p_T < 80$ GeV, the data and MC agree to within a few percent. As p_T increases however, a growing discrepancy is observed, increasing up to 30% at $p_T = 500$ GeV.

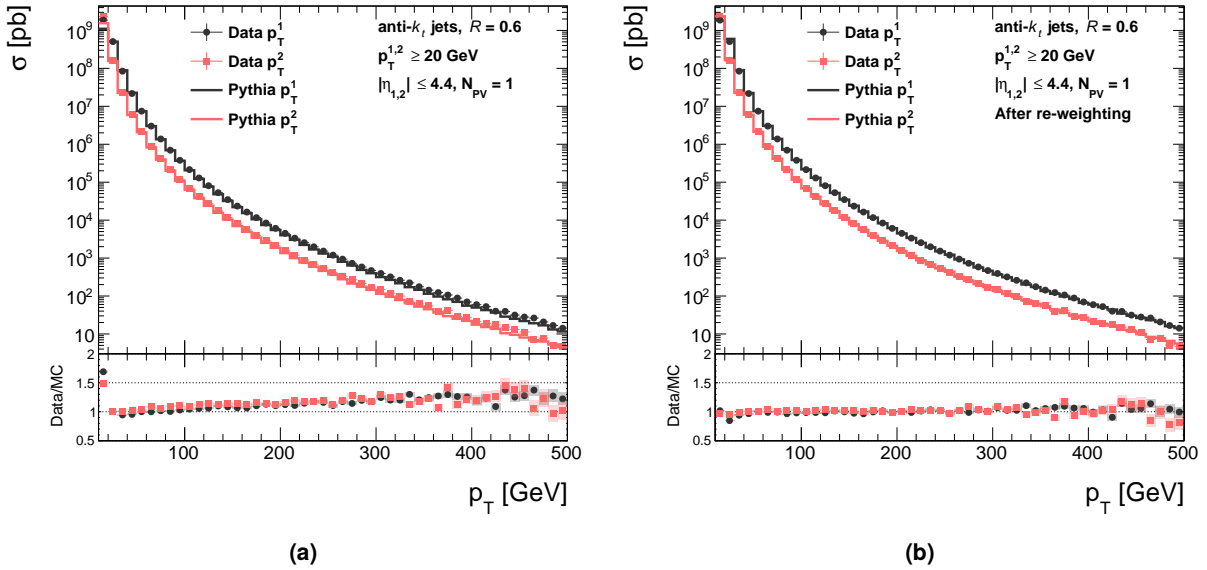


Figure 6.2: Transverse momentum, p_T , spectra of the two highest- p_T jets, denoted as $p_T^{1,2}$ in the figures, in data and in MC, (a) before and (b) after re-weighting of the MC (see text for details). The leading jet p_T distribution in data, in the range $50 < p_T < 70$ GeV, is used to set the normalization of the distributions in the MC. The ratio of data to MC is shown in the bottom panels, where statistical uncertainties are shown as the shaded areas, visible only at $p_T \geq 400$ GeV.

To reach a better agreement, the events in the MC are re-weighted, based on two dimensional p_T - y distributions. Normalized p_T - y distributions of the leading jet in data and in MC are constructed, where, at this stage, detector-level jets are used in the MC. As a first guess, the weights are estimated from the ratio of the two distributions. The resulting distribution is then parametrized by a smooth function for each y bin, producing a two-dimensional re-weighting function which is continuous in one dimension (p_T) and discrete in the other (y). The weight correction is applied to each event in the MC based on the leading particle jet p_T and y .

The p_T distributions of the two leading jets after re-weighting the events in MC are compared to data in Fig. 6.2(b). The agreement between the distributions in data and MC after the correction is within 5% across the p_T spectrum, apart from the range $20 \leq p_T < 30$ GeV where the disagreement rises to $\sim 15\%$. This level of agreement between the data and the MC is sufficient for the purpose of calculating the acceptance.

6.6.2 Acceptance for four-jet events

The calculation of the acceptance for four-jet events is performed by selecting a subset of the dijet sample. As mentioned in Section 4.1.3, PYTHIA uses a $2 \rightarrow 2$ matrix element at leading order to generate events. Extra jets beyond the two leading ones are generated as part of the parton shower. Therefore, in order to obtain a good representation of the topology of four-jet events in data, the four-jet events in PYTHIA are re-weighted to the data. The four-jet acceptance calculation

6 Methodology

cannot be performed with the AHJ MC sample due to the DPS filter applied during generation (see Section 4.1.2).

A comparison between the p_T distributions of the four leading jets in data and in PYTHIA is shown in Fig. 6.3(a). In the range $30 \leq p_T < 200$ GeV, the agreement between the leading jet distributions is within statistical uncertainties. At $p_T \geq 200$ GeV, the distribution in the MC is steeper than in the data, which leads to an observed difference of about 10% at $p_T = 500$ GeV. The same is true for the second jet, where a good agreement is observed in the range $10 \leq p_T < 120$ GeV, while at $p_T \geq 120$ GeV a discrepancy of about 15% is observed. In the case of the third and fourth jet, a good agreement is seen in the range $10 \leq p_T < 30$ GeV, while the MC underestimates the data by about 20% at $p_T \geq 30$ GeV.

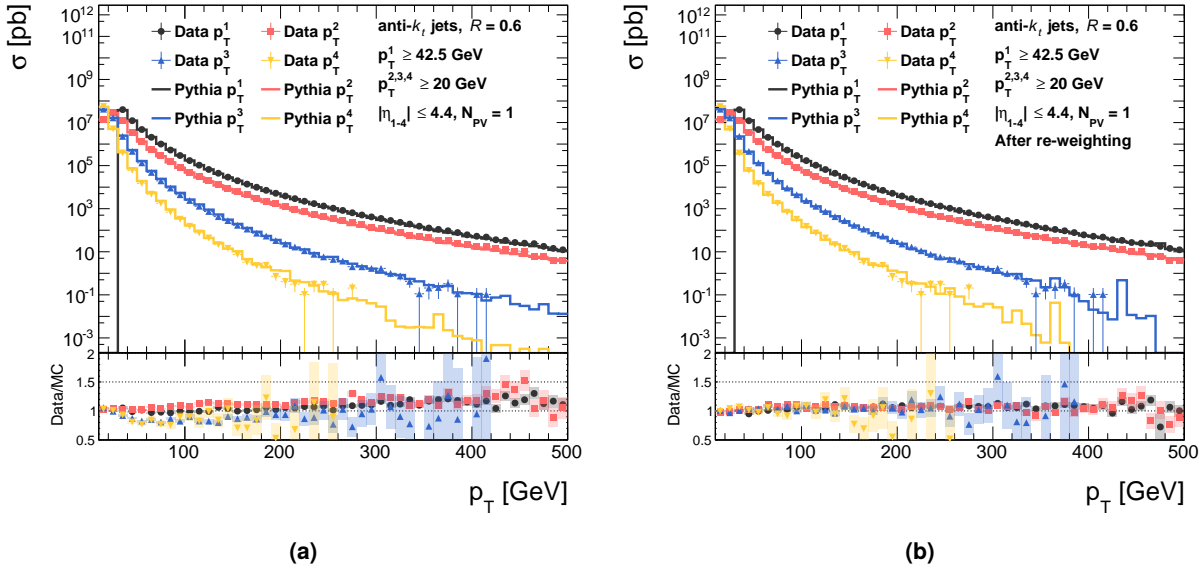


Figure 6.3: Transverse momentum, p_T , spectra of the four highest- p_T jets, denoted as p_T^{1-4} in the figures, in data and in MC, (a) before and (b) after re-weighting of the MC (see text for details). The leading jet p_T distribution in data, in the range $50 < p_T < 70$ GeV, is used to set the normalization of the distributions in the MC. The ratio of data to MC is shown in the bottom panels, where statistical uncertainties are shown as the shaded areas.

As a first attempt to re-weight the MC, the re-weighting factors are calculated from six-dimensional distributions, constructed from the p_T and y of the three measured leading jets. Similar to the dijet case, the weights are estimated by taking the ratio of the normalized distribution in data to the corresponding distribution in the MC. Interpolation between p_T bins is used to extract a smooth function from the ratio distribution. Like in the dijet case, this smooth function is applied based on the p_T and y of the three leading particle jets.

The p_T distributions of the four leading jets in data and in MC, after applying the correction, are compared in Fig. 6.3(b). In spite of this approximate “unfolding”, a good agreement between data and MC across the entire p_T range, for all four jets, is observed. A deviation of the order of 10% is

seen for leading jets with $p_T \geq 150$ GeV. However, such a difference at this range of p_T has no effect on the acceptance. It is therefore concluded that the correction applied to the MC, based on the three leading jets, is adequate for the acceptance calculation.

6.6.3 Jet rapidity distributions

A comparison between the y distributions of the two (four) leading jets in dijet (four-jet) events in data and in PYTHIA, after re-weighting, is shown in Fig. 6.4(a) (Fig. 6.4(b)). The leading jet y distributions in data, in the range $-1 < y < 1$, are used to set the normalization of the distributions in the MC.

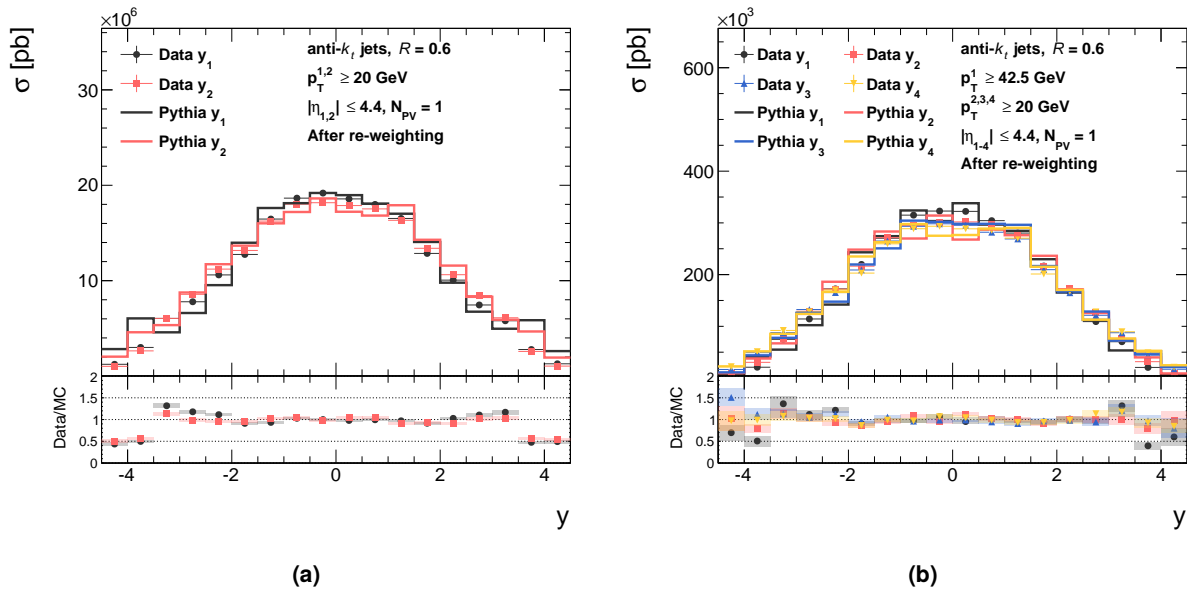


Figure 6.4: Rapidity, y , distribution of the (a) two (y_{1-2}) and (b) four (y_{1-4}) jets with highest transverse momentum, p_T , in data and in PYTHIA, after re-weighting the latter (see text for details). The leading jet y distribution in data, in the range $-1 < y < 1$, is used to set the normalization of the distributions in the MC. The ratio of data to MC is shown in the bottom panels, where statistical uncertainties are shown as the shaded areas.

In the range $-2 < y < 2$, the y distributions in data and in MC agree to within 10%, both in dijet and in four-jet events. For dijet events, in the range $-3.5 < y < -2.0$ ($2.0 < y < 3.5$), the leading jet distribution in the MC underestimates the data by about 20% (15%). The sub-leading jet distribution in data is well described by the MC in these ranges. At the far edges of the detector, $|y| > 3.5$, the MC overestimates the data by a factor of 2. In the case of four-jet events, a similar tendency is observed for the leading jet, while the distributions of the other jets display better agreement with data.

Disagreements between the data and the MC within the fiducial y range of the measurement do not affect the acceptance calculation. The effect on the acceptance calculation due to the disagreements seen in the ranges $|y| > 4$ is minimal. There are relatively few events that migrate into and out of the fiducial $|y|$ range of the measurement.

6.6.4 Final acceptance calculation

The values of the acceptance factors, as obtained from the re-weighted MC using Eq. (6.23), are

$$\mathcal{A}_{2j}^A = 1.113 \pm 0.004 \text{ (stat.)}, \quad \mathcal{A}_{2j}^B = 1.073 \pm 0.004 \text{ (stat.)} \quad \text{and} \quad \mathcal{A}_{4j} = 1.125 \pm 0.011 \text{ (stat.)} .$$

The factors are all above one, reflecting the higher probability for migration towards higher momenta, due to the very steep jet p_T spectrum in dijet and four-jet events. The corresponding value of the acceptance ratio is

$$\alpha_{2j}^{4j} = 0.94 \pm 0.01 \text{ (stat.)} . \tag{6.24}$$

In order to determine whether the statistical uncertainty on α_{2j}^{4j} should be propagated as a systematic uncertainty, α_{2j}^{4j} was re-calculated after modifying the re-weighting functions used in Sections 6.6.1 and 6.6.2. Two re-weighting functions were obtained from a confidence interval of one standard deviation around the nominal function. One function corresponds to the upper edge and one to the lower edge of the confidence interval. The process of re-weighting PYTHIA and calculating α_{2j}^{4j} was then repeated for each function. The resulting values of α_{2j}^{4j} deviate from the nominal value by 1%. A deviation identical to the statistical uncertainty quoted in Eq. (6.24). Ergo, the statistical uncertainties in the distributions used for re-weighting are translated to a systematic uncertainty on the re-weighting functions. In order to account for this, the statistical uncertainty on α_{2j}^{4j} is propagated as a systematic uncertainty in the following.

6.7 Template samples

The main challenge in the measurement of σ_{eff} is to estimate the double parton scattering contribution to the four-jet data sample. It is impossible to extract complete-DPS and semi-DPS candidate events on an event by event basis. Therefore, the usual approach is to use the expected distributions of a variable sensitive to cDPS and sDPS in the data and fit to it the expected templates for the SPS, cDPS and sDPS contributions. For this purpose, it is essential to first extract the SPS, cDPS and sDPS samples. The second step is to find or build a variable sensitive to the cDPS and sDPS contributions. The following sections describe these steps in detail.

6.7.1 Event classification in MC

In the AHJ combination of MC generators, the user can identify the origin of outgoing partons from the pp collision in the event record. The outgoing partons can be assigned to the *primary* interaction from the ALPGEN ME generator or to a *secondary* interaction, generated in JIMMY. The former are referred to as primary-scatter partons and the latter are referred to as secondary-scatter partons. Once the outgoing partons are classified, the jets in the event may be matched to outgoing partons and the event can be classified as a SPS, cDPS or sDPS event.

6.7.2 Jet to parton matching

The matching of jets to partons relies on the principle of *local parton hadron duality* [176–178] and is done in the $\eta - \phi$ plane by calculating

$$\Delta R_{\text{parton-jet}} = \sqrt{(\eta_{\text{parton}} - \eta_{\text{jet}})^2 + (\phi_{\text{parton}} - \phi_{\text{jet}})^2}, \quad (6.25)$$

between outgoing partons and jets reconstructed using the anti- k_t algorithm with a distance parameter $R = 0.6$. The distribution of the distance $\Delta R_{\text{parton-jet}}$ between primary-scatter partons and the closest jet is shown in Fig. 6.5(a). For 95% of the primary-scatter partons, the parton is within the radius of the jet, $\Delta R_{\text{parton-jet}} \leq 0.6$. A drop in the slope of the distribution is seen around $\Delta R_{\text{parton-jet}} \approx 1.1$. This indicates that the distance between a jet and the parton from which it originated may extend up to $\Delta R_{\text{parton-jet}} = 1.0$. Larger distances seen in Fig. 6.5(a) correspond to cases in which the jet does not originate from the parton. Therefore, a cut on the maximal distance $\Delta R_{\text{parton-jet}} \leq 1.0$ is applied when matching jets and partons.

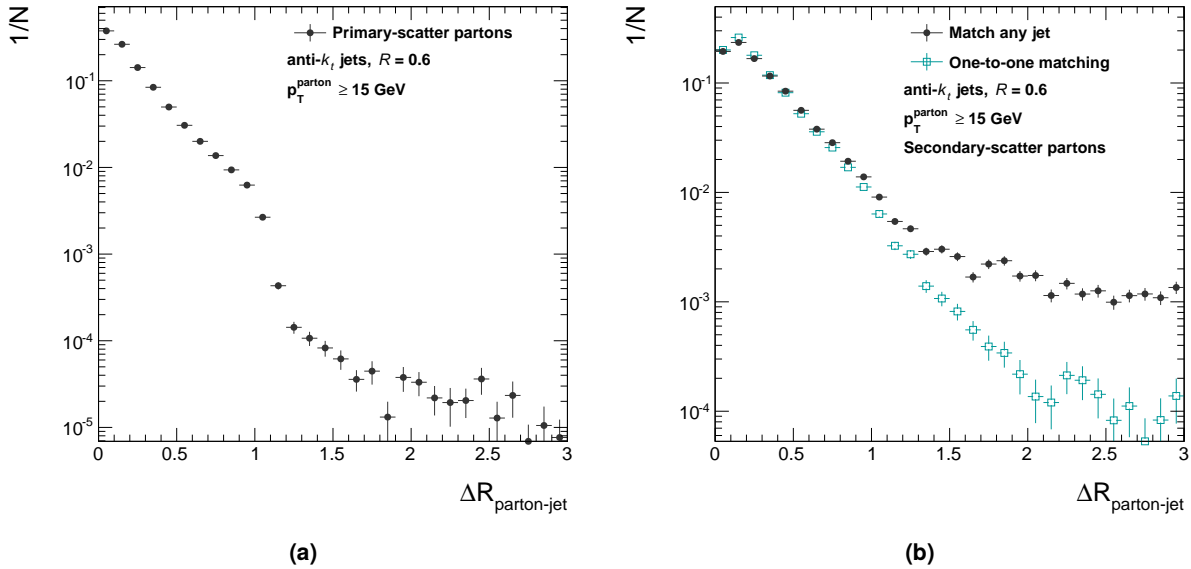


Figure 6.5: (a) Normalized distributions of the distance $\Delta R_{\text{parton-jet}}$, defined in Eq. (6.25), between primary-scatter partons and the closest jet. (b) Normalized distributions of the distance $\Delta R_{\text{parton-jet}}$ between secondary-scatter partons and the closest jet before (black dots) and after (blue empty squares) requiring a one-to-one match (see text for definition). The transverse momentum, p_T , of primary-scatter and secondary-scatter partons (see Section 6.7.1 for definition) is limited from below, $p_T^{\text{parton}} \geq 15$ GeV.

The distribution of the distance $\Delta R_{\text{parton-jet}}$ between secondary-scatter partons and the closest jet is shown as black dots in Fig. 6.5(b). For 90% of the secondary-scatter partons, the parton is within the radius of the jet. It can be seen that the distribution for secondary-scatter partons peaks at $\Delta R_{\text{parton-jet}} = 0.1$, unlike the distribution for primary-scatter partons which peaks at $\Delta R_{\text{parton-jet}} = 0.0$. This is expected since secondary-scatter partons typically have lower p_T and hence produce lower p_T jets. The plateau observed at $\Delta R_{\text{parton-jet}} \geq 1.0$ corresponds to cases in which the jet closest to

the secondary-scatter parton originates from a primary-scatter parton. In order to avoid such cases, the distance $\Delta R_{\text{parton-jet}}$ is required to be the shortest out of all combinations of jets and partons in the event. This produces a one-to-one matching between partons and jets. The distribution of the distance $\Delta R_{\text{parton-jet}}$ for secondary-scatter partons after requiring a one-to-one match is shown as blue empty squares in Fig. 6.5(b).

Due to the abundance of low- p_T secondary-scatter partons in a typical MC event, a scenario in which a jet with $p_T \geq 20$ GeV matches a low- p_T (~ 5 GeV) secondary-scatter parton is not rare. In such a case, the energy of the secondary-scatter parton is likely combined with radiation from the primary-scatter parton in the jet reconstruction procedure, producing a jet with $p_T \geq 20$ GeV. Classifying this jet as originating from a secondary-scatter parton would be wrong. Therefore, an additional requirement is applied to the partons when performing the jet-to-parton matching,

$$p_T^{\text{parton}} \geq 15 \text{ GeV} . \quad (6.26)$$

This cut on the minimum p_T of the parton is aimed to ensure that the jet was initiated by the matched parton.

The choice of the value 15 GeV as the minimum p_T of matched partons was guided by the matching scale between radiation generated as part of the ME and radiation generated as part of the parton shower in the AHJ combination of generators (see Section 4.1.2). To check that this value is appropriate for jets with $p_T^{\text{jet}} \geq 20$ GeV, the p_T^{parton} distribution of primary-scatter partons matching jets in the range $20 \leq p_T^{\text{jet}} \leq 25$ GeV, shown in Fig. 6.6, was studied. It can be seen that most of the

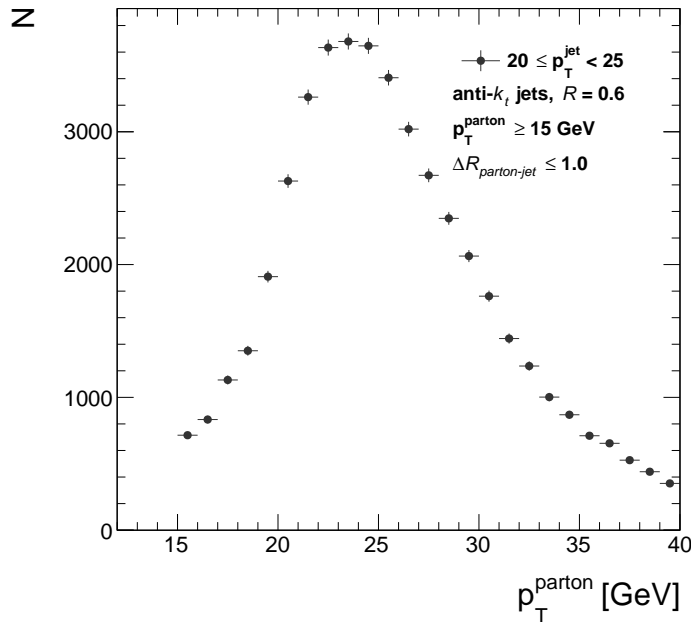


Figure 6.6: The transverse momentum, p_T , distribution of primary-scatter partons matching jets in the range $20 \leq p_T^{\text{jet}} \leq 25$ GeV. A parton and a jet are considered matched if $\Delta R_{\text{parton-jet}} \leq 1.0$. The p_T of a primary-scatter parton (see Section 6.7.1 for definition) is limited from below, $p_T^{\text{parton}} \geq 15$ GeV.

jets are initiated by outgoing partons of comparable transverse momentum. The distribution exhibits a tail towards high p_T^{parton} values from partons which lost some of their transverse momentum to radiation. A shorter tail towards lower values of p_T^{parton} is cut off by the $p_T^{\text{parton}} \geq 15$ GeV requirement applied on the matched partons. Assuming a Gaussian distribution, the estimated fraction of matches lost due to this threshold is about 4% for jets in the range $20 \leq p_T^{\text{jet}} \leq 25$ GeV and about 0.2% for all jets. Since unmatched jets are classified as originating from the primary interaction and since the majority of jets are initiated by the primary interaction, the fraction of jets whose origin is wrongly classified is even smaller.

The matching efficiency is tested in four-jet events which contain at least four primary-scatter partons. In 99.6% of these events, all four jets match primary-scatter partons. This leads to the conclusion that for partons with $p_T^{\text{parton}} \geq 15$ GeV, the matching procedure is fully efficient. Jets not matched to an outgoing parton with $p_T^{\text{parton}} \geq 15$ GeV (primary or secondary) are most likely initiated by a parton from the shower stage of the simulation (HERWIG), dressed with energy from the underlying event. This cannot be checked, since the event record does not contain the necessary information about partons generated in the shower. The stability of the measurement with respect to the jet-to-parton matching is discussed in [Section 8.3](#)

6.7.3 Single parton scattering sample

The SPS sample has to be extracted from MC event generators which use MPI (and therefore double parton scattering) to generate the underlying activity accompanying the hard interaction. For a good description of pQCD and to ascertain the measurement of *hard* double parton scattering, the SPS sample should contain all of the soft MPI and underlying activity, without any hard secondary interactions. By matching partons to jets, as described in the previous section, events from the inclusive AHJ sample in which none of the leading four jets are matched to a secondary-scatter parton are selected for the SPS sample. This ensures that none of the jets in the SPS events originate from hard secondary interactions, while all of the soft MPI and underlying activity is retained in these events.

A pseudo event display of the four leading particle jets in an event classified as a SPS event is shown in [Fig. 6.7](#). In this event, all four jets were matched to primary-scatter partons, shown as black squares in the figure. As was mentioned in [Section 6.7.2](#), this is the case in almost all events with at least four primary-scatter partons.

6.7.4 Double parton scattering sample

In the picture of double parton scattering advocated here, the two dijet productions are decorrelated. Therefore, a four-jet cDPS event may be constructed from two overlaid dijet events. To reduce any dependence of the measurement on the modelling of dijet production in MC, cDPS events are built from dijet events in data.

The first step in constructing the overlaid dijets sample consists of selecting dijet events from the data sample. The selection criteria are similar to the dijet selection cuts given in [Eq. \(5.1\)](#), i.e., two jets in the event, each with $p_T \geq 20$ GeV and $|y| \leq 4.4$. The one crucial difference is an extra cut applied on additional jets in the event. In order to avoid double counting with the sDPS final state, events with

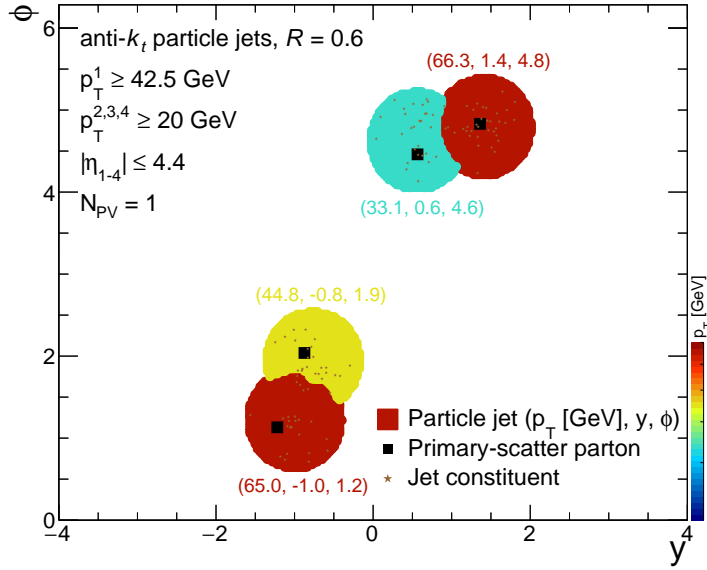


Figure 6.7: Pseudo event display of the distribution of the four leading particle jets (filled areas), jet constituents (brown stars) and primary-scatter partons (full black squares) in the $\phi - y$ plane in an event classified as SPS, where ϕ is the jet azimuthal angle and y its rapidity. Each jet area color corresponds to the jet transverse momentum (p_T) and the jet p_T , in GeV, y and ϕ are displayed next to it. Primary-scatter partons are defined in Section 6.7.1.

an additional jet with $p_T \geq 20$ GeV are rejected. Double counting would occur in case an event with three jets is overlaid with a dijet event, since such a final state is included in the sDPS sample.

Once a list of dijet events is assembled, pairs of events are overlaid into four-jet events. The conditions which must be fulfilled in order for a given pair of events to be overlaid are the following:

- none of the four jets overlap, i.e., $\Delta R_{\text{jet-jet}} > 0.6$ for anti- k_t jets with a distance parameter of 0.6;
- the vertices of the two overlaid events are no more than 10 mm apart in the z direction;
- at least one of the four jets has $p_T \geq 42.5$ GeV;
- only single-vertex events are used.

The first condition ensures none of the jets would have been merged if the four-jet event was reconstructed as a real event; the second condition avoids possible bias, due to events where two jet pairs originate from far-away vertices; the last two conditions are imposed in order to match the conditions and phase-space cuts in the four-jet sample.

After a pair of dijet events are overlaid into a four-jet event, the jets are re-ordered based on their p_T . As a result, the sub-leading jet in the four-jet overlay event may have originally been either the sub-leading jet in the first dijet pair, or the leading jet in the second dijet pair. This reflects the possible scenarios of four-jet cDPS events in data and the limitation of pairing the jets based on their p_T . The ordering in p_T of the four reconstructed jets does not necessarily correspond to the two

highest- p_T jets originating from one interaction and the second pair from the other interaction. This and other limitations are discussed further in [Section 6.8](#).

For various studies performed using AHJ, it is necessary to extract a cDPS sample from the AHJ sample in the same manner in which the SPS sample is extracted. Events in AHJ are classified as cDPS events if two of the four leading jets are matched to primary-scatter partons and the other two are matched to secondary-scatter partons.

A pseudo event display of a cDPS event extracted from the AHJ sample is shown in [Fig. 6.8](#). It can be seen that two jets were matched to primary-scatter partons, marked with black squares in the figure, and two jets were matched to secondary-scatter partons, marked with yellow circles. The event shown in [Fig. 6.8](#) displays the typical topology of cDPS events. The jets in each pair are of almost equivalent p_T and the distance between them in azimuth is close to π .

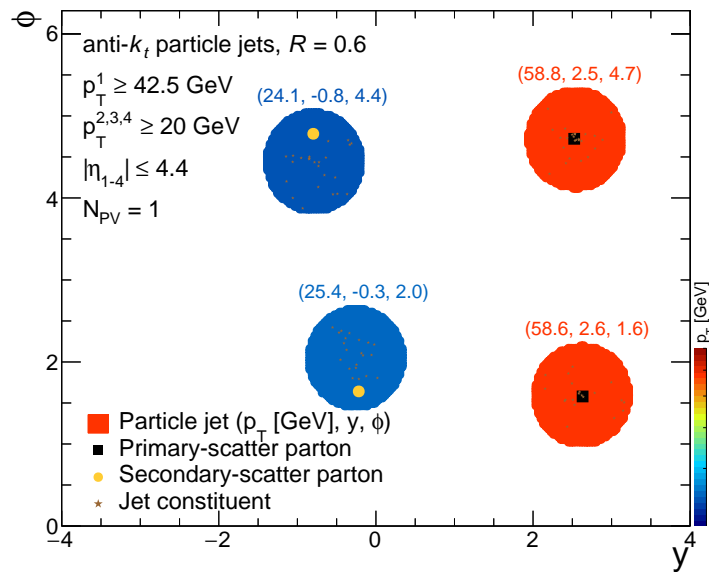


Figure 6.8: Pseudo event display of the distribution of the four leading particle jets (filled areas), jet constituents (brown stars), primary-scatter partons (full black squares) and secondary-scatter partons (full yellow circles) in the ϕ – y plane in an event classified as complete-DPS, where ϕ is the jet azimuthal angle and y its rapidity. Each jet area color corresponds to the jet transverse momentum (p_T) and the jet p_T , in GeV, y and ϕ are displayed next to it. Primary-scatter and secondary-scatter partons are defined in [Section 6.7.1](#).

The topology of cDPS events constructed by overlaying two dijet events is compared to the topology of cDPS events extracted from the AHJ sample. A description of the comparison is given in [Chapter 7](#), where the measurement methodology is validated in MC. The required distance between jets in the overlay procedure, $\Delta R_{\text{jet-jet}} > 0.6$, and its effect on the measurement is discussed in [Section 8.3](#).

6.7.5 Semi-DPS sample

The semi-DPS sample is extracted from the AHJ sample by matching outgoing partons to jets. Events in which three of the leading jets are matched to primary-scatter partons and the fourth jet is matched to a secondary-scatter parton are classified as sDPS events. In principal, a sDPS event

may be constructed by overlaying three-jet events and dijet events, similar to the way cDPS events are built for the complete-DPS sample. However, the data cannot be used for this purpose since it is impossible to know *a-priori* whether the three-jet event was the result of one or two partonic interactions. Thus, a sDPS sample extracted from AHJ is used.

A pseudo event display of a sDPS event extracted from the AHJ sample is shown in Fig. 6.9. Three of the four leading jets were matched to primary-scatter partons, marked with black squares in the figure, and the fourth jet was matched to a secondary-scatter parton, marked with a yellow circle. An additional secondary-scatter parton, not matched to any of the four leading jets, is also seen in the event.

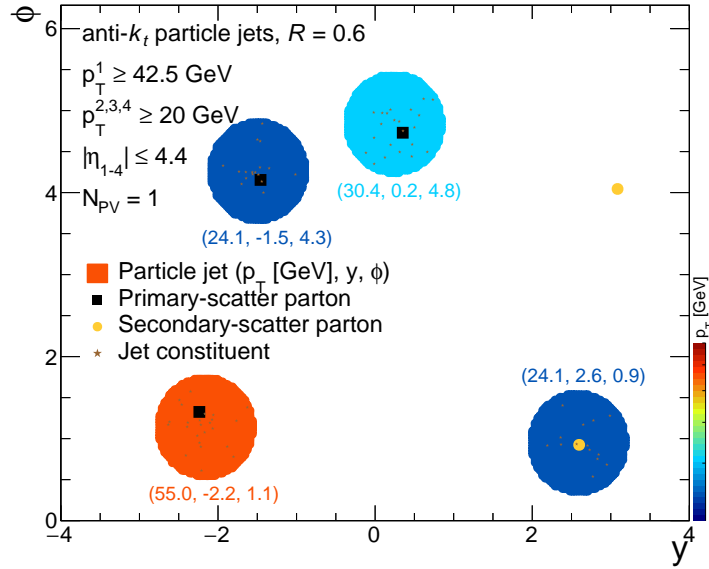


Figure 6.9: Pseudo event display of the distribution of the four leading particle jets (filled areas), jet constituents (brown stars), primary-scatter partons (full black squares) and secondary-scatter partons (full yellow circles) in the $\phi - y$ plane in an event classified as semi-DPS, where ϕ is the jet azimuthal angle and y its rapidity. Each jet area color corresponds to the jet transverse momentum (p_T) and the jet p_T , in GeV, y and ϕ are displayed next to it. Primary-scatter and secondary-scatter partons are defined in Section 6.7.1.

6.8 Differentiating variables

To determine f_{cDPS} and f_{sDPS} it is necessary to find a variable that is able to differentiate between four jets produced in a SPS or in a DPS interaction. In a DPS, two dijet interactions occur and should result in pair-wise p_T balanced jets. On the other hand, in a SPS interaction, extra jets are the result of radiation, so the pair-wise p_T balancing happens rather accidentally. Therefore, the topology of the four jets is expected to be different for DPS events and SPS events.

Correlations are expected between all four jets in the final state of a SPS interaction. These correlations have several characteristics that could be used to construct variables. For example, one would expect the third and fourth jets (assumed here to be higher-order radiative corrections to the hard scattering)

to be close-by in the $\phi - y$ plane to the two leading jets. No pair-wise balance in p_T and no pair-wise back-to-back symmetry in azimuth are expected.

In a DPS event, under the assumption of uncorrelated $(2 \rightarrow 2)^{\times 2}$ QCD interactions, different topologies should be prominent. For instance, one would expect that there would be pair-wise balance in p_T between the two pairs corresponding to the two interactions. Each pair should be back-to-back in the transverse plane, and the azimuthal angle between the planes of interactions should have a random distribution. A random distribution is also expected for the Δy between the two pairs of jets.

The topology of three of the jets in sDPS events would resemble the topology of the jets in SPS interactions. In the majority of the events, the third or fourth jet is expected to be collinear in azimuth with one of the leading jets. In addition, the jet initiated by radiation is expected to be closer, in the $\phi - y$ plane, to the plane defined by the leading interaction. The jet produced in the second interaction would most likely not be correlated with the other three jets in the event, neither in azimuth nor in the rapidity space.

The simplest differentiating variables would involve choosing the two pairs among the four jets and then requiring the jets in each pair to balance in p_T or have large azimuthal separation. However, there are various ways to select two pairs of jets in a four-jet event. One could order the jets in p_T and define the leading pair (the two jets with the highest p_T) and the sub-leading pair (remaining two jets). A more sophisticated method, used in Ref. [74], chooses the pairs that minimize the pair-wise p_T balance. Once the pairs are selected, a variable may be constructed based on one pair of jets, the two pairs of jets or a multi-dimensional combination of pairs and kinematic properties.

However, such an approach is always limited by the need to select the pairs in each event based on *a priori* assumptions. In addition, the use of one kinematic property, for example jet p_T , could lead to large uncertainties stemming from the jet energy scale uncertainty. In the case of a multi-dimensional combination between kinematic properties like p_T balance and the azimuthal angle separation, the strong correlation between the variables is not taken into account.

For the topology of sDPS events, in which only one of the jets is expected to be uncorrelated with the rest, pairing of the four jets into two pairs would not serve the goal of differentiating this topology from the others. In this case, one would need to build a variable which tests the correlation of each jet with the three other jets in the event. That is, the differentiating variable would be constructed differently whether the event is a cDPS or sDPS candidate event. Such a complication presents further limitations on the approach of using a single differentiating variable constructed from the kinematic properties of the jets.

These limitations were studied and a conclusion was reached that no single variable could encompass all of the information in the topology of four-jet events in an uncorrelated manner. Therefore, a different approach was adopted, the use of an artificial neural network (NN). Various variables may be given as input to the NN (see Section 6.10), a study of possible ones is described in the following.

6.8.1 Possible variables

In constructing possible variables, three guiding principals were followed:

1. use pair-wise relations that have the potential to differentiate SPS and cDPS topologies;

6 Methodology

2. include angular relations between all jets in light of the expected topology of sDPS events;
3. attempt to construct variables least sensitive to systematic uncertainties.

The first two guidelines entail in them the different characteristics of SPS and cDPS events discussed in [Section 6.8](#). The third guideline led to the usage of ratios of p_T in order to avoid large dependencies on the JES systematic uncertainties. The variables studied as potential input variables for the NN are,

$$\Delta_{ij}^{p_T} = \frac{|\vec{p}_T^i + \vec{p}_T^j|}{p_T^i + p_T^j}; \quad \Delta\phi_{ij} = |\phi_i - \phi_j|; \quad \Delta y_{ij} = |y_i - y_j|;$$

$$\frac{p_T^2}{p_T^1}, \quad \frac{p_T^3}{p_T^1}, \quad \frac{p_T^4}{p_T^1}; \quad (6.27)$$

$$|\phi_{1+2} - \phi_{3+4}|; \quad |\phi_{1+3} - \phi_{2+4}|; \quad |\phi_{1+4} - \phi_{2+3}|;$$

where p_T^i , \vec{p}_T^i , y_i and ϕ_i stand for the scalar and vectorial transverse momentum, rapidity and azimuthal angle of jet i , respectively, with $i = 1, 2, 3, 4$. The variables with the sub-script ij are calculated for all possible combinations, $ij = 12, 34, 13, 23, 14, 24$. The term ϕ_{i+j} denotes the azimuthal angle of the vectorial sum of jets i and j .

6.8.2 Distributions of the variables in the three samples

The distributions of all² variables are shown in [Appendix A.1](#), where for each variable, three normalized distributions in the SPS, cDPS and sDPS samples are compared. The variables for which the three distributions exhibit the largest differences, are discussed in more detail in the following.

A discussion on the variables in an attempt to relate the distributions to the expected event topology has to be made while taking into account the strong correlation between the variables. The variables constructed from the p_T of two jets, $\Delta_{ij}^{p_T}$, are correlated to the angular difference between the jets, $\Delta\phi_{ij}$, in a non-linear way. Only a combination of the two contains all the information on the relation between jets i and j . Therefore, in the discussion below, the distributions of $\Delta_{ij}^{p_T}$ and $\Delta\phi_{ij}$ will be analyzed together in an attempt to describe the topology of the jets in the different samples.

In most cDPS events the two leading jets originate from one interaction and jets 3 and 4 originate from the other. However, in about 15% of the cDPS events, that is not the case. In the following, the pairing notation $\{\langle i, j \rangle \langle k, l \rangle\}$ is used to describe a cDPS event in which jets i and j originate from one interaction and jets k and l originate from the other.

Transverse momenta and azimuthal angle variables

Normalized distributions of the $\Delta_{12}^{p_T}$ and $\Delta_{34}^{p_T}$ variables in the SPS, cDPS and sDPS samples are shown in [Fig. 6.10](#). The corresponding distributions of the $\Delta\phi_{ij}$ variables are shown in [Fig. 6.11](#). In the

² The distributions of the $\frac{p_T^i}{p_T^1}$ variables are not shown since their differentiating power was found to be negligible (see [Section 6.10](#)).

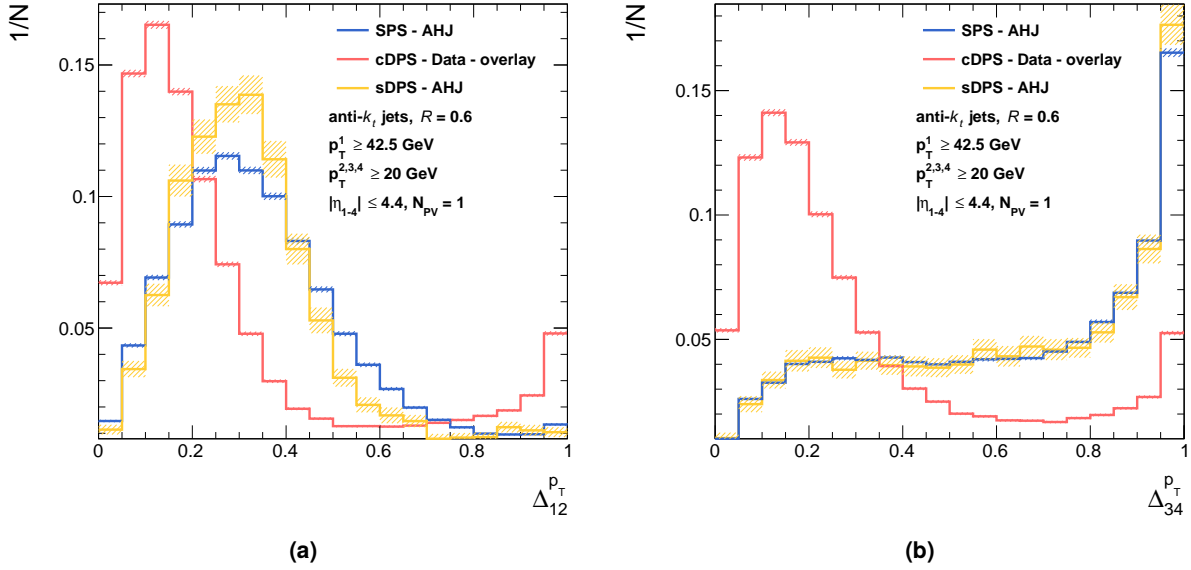


Figure 6.10: Normalized distributions of the variables, (a) $\Delta_{12}^{p_T}$ and (b) $\Delta_{34}^{p_T}$, defined in Eq. (6.27), in the SPS (blue histogram, AHJ), cDPS (red histogram, overlaid dijets from data) and sDPS (yellow histogram, AHJ) samples, selected in the phase-space defined in the legend.

cDPS sample, the $\Delta_{12}^{p_T}$ and $\Delta_{34}^{p_T}$ distributions peak at low values, indicating that both the leading and the sub-leading jet pairs are balanced in p_T . The small peak around unity is likely due to events in which the correct pairing of the jets is $\{(1, 3)\langle 2, 4\rangle\}$. In the SPS sample, the leading jet-pair exhibits a wider peak at higher values of $\Delta_{12}^{p_T}$ compared to that in the cDPS sample. This is due to the fact that the two leading jets cannot balance well in p_T , as the second pair of jets carries some of the momentum of the same hard scatter. A narrower peak around the same values of $\Delta_{12}^{p_T}$ is seen in the sDPS sample. The smaller width of the peak is attributed to the fact that in sDPS events only one of the leading jets is likely to lose significant transverse momentum through radiation. Therefore, the range available for the ratio of transverse momenta between the two leading jets is smaller in the sDPS sample, compared to the SPS sample.

The balance between the dijet pairs seen in the $\Delta_{12}^{p_T}$ and $\Delta_{34}^{p_T}$ distributions in the cDPS sample is also seen in the $\Delta\phi_{12}$ and $\Delta\phi_{34}$ distributions, shown in Fig. 6.11. In the SPS and sDPS samples, the two leading jets are only approximately back-to-back, resulting in a wider peak around π in $\Delta\phi_{12}$, compared to the cDPS sample.

The distribution of $\Delta_{34}^{p_T}$ in both SPS and sDPS samples is driven by the $\Delta\phi_{34}$ distribution shown in Fig. 6.11(b). As expected, the $\Delta\phi_{34}$ distribution is almost uniform. Due to the steeply falling jet p_T spectrum, in the majority of the events $p_T^3 \approx p_T^4 \approx 20$ GeV. Introducing the approximation $p_T^3 \approx p_T^4 \approx p_T$ into $\Delta_{34}^{p_T}$, the expression for $\Delta_{34}^{p_T}$ becomes

$$\Delta_{34}^{p_T} = \frac{|\vec{p}_T^3 + \vec{p}_T^4|}{p_T^3 + p_T^4} \approx \frac{\sqrt{2p_T + 2p_T \cos(\Delta\phi_{34})}}{2p_T} = \frac{\sqrt{1 + \cos(\Delta\phi_{34})}}{\sqrt{2}}. \quad (6.28)$$

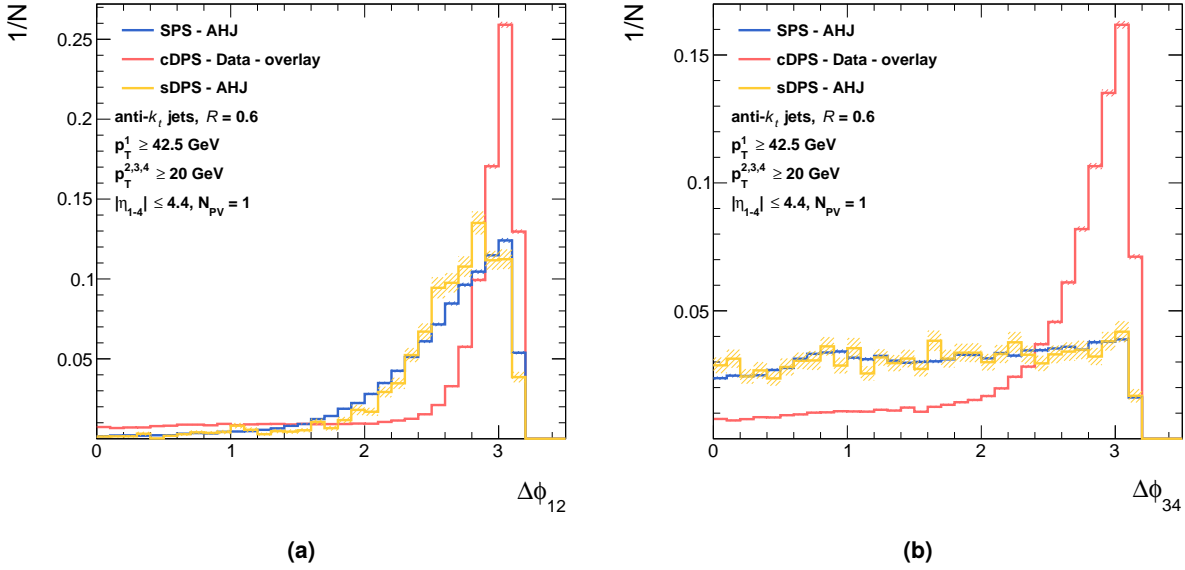


Figure 6.11: Normalized distributions of the variables, (a) $\Delta\phi_{12}$ and (b) $\Delta\phi_{34}$, defined in Eq. (6.27), in the SPS (blue histogram, AHJ), cDPS (red histogram, overlaid dijets from data) and sDPS (yellow histogram, AHJ) samples, selected in the phase-space defined in the legend.

As seen in Fig. 6.10(b), the shape of the distribution of $\Delta\phi_{34}^{PT}$ in the SPS and sDPS samples follows the shape of the function on the right hand side of Eq. (6.28).

In the $\Delta\phi_{34}$ distributions in all three samples, a dip is seen at $\Delta\phi_{34} < 0.6$. This is a direct consequence of the jet reconstruction algorithm in the SPS and sDPS samples and of the overlay requirements in the cDPS sample. In the jet reconstruction algorithm, the distance parameter, $R = 0.6$, dictates how close jets can be to each other before they are merged into one jet. Therefore, jets close to each other in ϕ must be far away in y , a limitation causing the dip seen in the distributions. The dip is less pronounced in the sDPS case since, as expected, the Δy_{34} distribution in this sample is wider (see Fig. 6.12(a)).

Rapidity based variables

The set of variables quantifying the distance between jets in rapidity, Δy_{ij} , is particularly important for the sDPS topology. As seen in the $\Delta\phi_{ij}$ distributions, the azimuthal distance between jets in the SPS sample may be large and in general have a similar distribution as in the sDPS sample. However, in SPS interactions leading to the four-jet final state, the radiated jets are expected to span the rapidity area between the radiating jets. Hence, on average, smaller distances between non-leading jets are expected in the SPS sample compared to the sDPS sample.

Normalized distributions of the Δy_{34} variable in the SPS, cDPS and sDPS samples are shown in Fig. 6.12(a). The distributions in the SPS and cDPS samples are similar, apart from at $\Delta y_{34} < 2$ where a peak structure is observed in the SPS sample, most likely due to events in which jets 3 and 4 are radiated off the same jet.

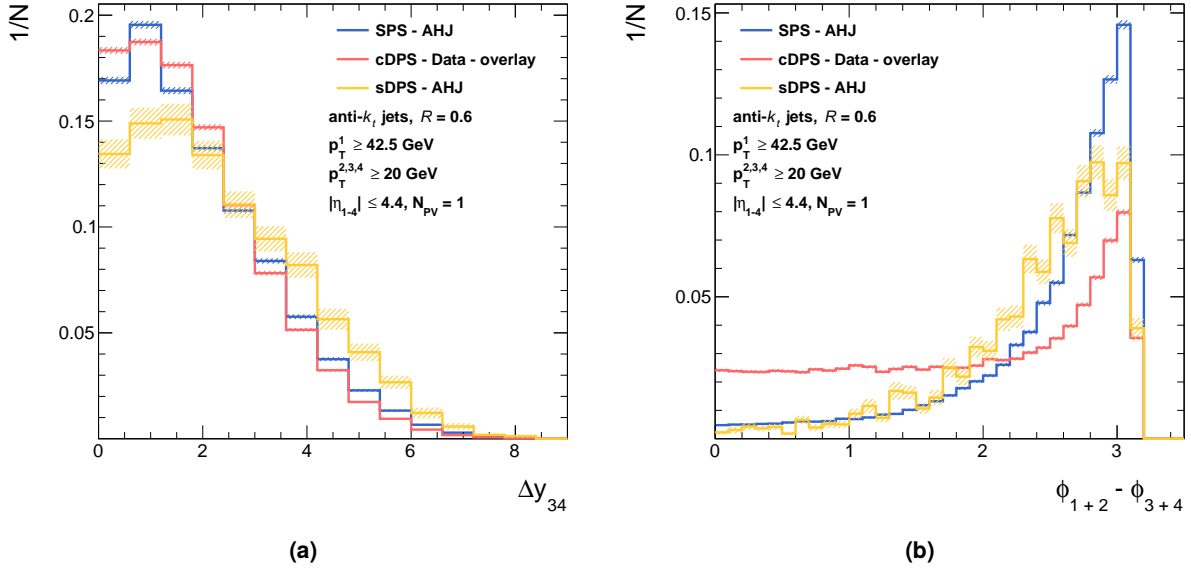


Figure 6.12: Normalized distributions of the variables, (a) Δy_{34} and (b) $\phi_{1+2} - \phi_{3+4}$, defined in Eq. (6.27), in the SPS (blue histogram, AHJ), cDPS (red histogram, overlaid dijets from data) and sDPS (yellow histogram, AHJ) samples, selected in the phase-space defined in the legend.

The distribution of the Δy_{34} variable in the sDPS sample is wider than in the other two samples, as expected from the sDPS topology. In 95% of the sDPS events, jets 3 and 4 are initiated by two different interactions. Therefore, their position in the $\phi - y$ plane is expected to be uncorrelated. This translates into a larger distance, on average, between them, as seen in figure Fig. 6.12(a).

Dijet planes based variables

The $\phi_{i+j} - \phi_{k+l}$ variables represent the azimuthal angle between the planes defined by the two dijet pairs. Normalized distributions of the $\phi_{1+2} - \phi_{3+4}$ variable in the SPS, cDPS and sDPS samples are shown in Fig. 6.12(b).

Since in the cDPS sample, the two dijet events are randomly overlaid, the angle between the planes defined by the leading dijet pair and sub-leading dijet pair is expected to have a uniform distribution. This is clearly seen in the plateau of the distribution of $\phi_{1+2} - \phi_{3+4}$ in the cDPS sample. The enhancement at π represents events in which the pairing of the jets may be either $\{\langle 1, 3 \rangle \langle 2, 4 \rangle\}$ or $\{\langle 1, 4 \rangle \langle 2, 3 \rangle\}$.

The peak at π seen in the SPS sample in the $\phi_{1+2} - \phi_{3+4}$ distribution is a direct result of momentum conservation. The four jets in the event should, up to extra jets in the event, balance in the transverse plane. Therefore, the two jets constructed by vectorially adding the pairs of jets in the event are forced to be back-to-back, as clearly indicated by the peak at π . A wider peak around π is evident in the sDPS sample, indicating that the four leading jets in the event do not balance as well in the transverse plane, compared with SPS interactions. The notion of sDPS events, as portrayed in this

analysis, dictates the existence of (at least) five jets in the final state. Thus, the four leading jets in sDPS events are not expected to fully balance each other in p_T .

Conclusions based on the distributions of the variables

The study of the various distributions of the variables in the three samples may be summed up as follows:

- **strong correlations between all the variables are observed** - The $\Delta_{ij}^{p_T}$ and $\Delta\phi_{ij}$ variables are correlated in a non-linear way, while geometrical constraints correlate the Δy_{ij} and $\Delta\phi_{ij}$ variables. Transverse momentum conservation relate the $\phi_{i+j} - \phi_{k+l}$ variables with the $\Delta_{ij}^{p_T}$ and $\Delta\phi_{ij}$ variables;
- **a clear separation between all three samples is not observed in any of the variables** - The variables in which a large discrepancy is observed between the SPS and cDPS distributions, e.g., $\Delta_{34}^{p_T}$, do not provide any differentiating power between SPS and sDPS;
- **all variables are important** - In cDPS events, where the pairing of the jets is different from $\{(1, 2)\langle 3, 4\rangle\}$, variables relating the other possible pairs, e.g., $\Delta\phi_{13}$, may hint as to which is the correct pairing.

These conclusions lead to the decision to use a multivariate technique in the form of an NN.

6.9 Principal component analysis

The capability of each of the variables defined in Eq. (6.27) to differentiate between SPS, cDPS and sDPS events was tested with the help of principal component analysis (PCA) [179]. The principal components (PC) are calculated using all the variables listed in Eq. (6.27) in a sample constructed by joining the three individual samples. The transformation of the variables to PC is defined in such a way that the first principal component has the largest possible variance, i.e., it accounts for the largest spread in the sample. Each subsequent component in turn has the highest variance possible under the constraint that it is linearly uncorrelated with the preceding components.

A comparison between the variances of the PC in SPS, cDPS and sDPS events is shown in Fig. 6.13. The relative difference between the variances of each principal component,

$$\Omega_{\text{SPS}}^i = \frac{|\sigma_i - \sigma_{\text{SPS}}|}{\sigma_{\text{SPS}}}, \quad (6.29)$$

is calculated separately for the cDPS and sDPS samples and shown in the bottom panel of Fig. 6.13. The term σ_i in Eq. (6.29) denotes the variance for a given principal component in the sample i . A large value of Ω_{SPS}^i for a given principal component corresponds to a higher capability of this component to differentiate between the three classes of events.

The variance values of the first two PC in Fig. 6.13 are of similar magnitude. About 44% of the variance of the combined sample is accounted for in the first two PC. A gradual drop in variance is seen for the subsequent components, until the 19th component, where a large drop in variance is observed. To account for $\sim 95\%$ of the variance in the sample, the first 12 components are necessary.

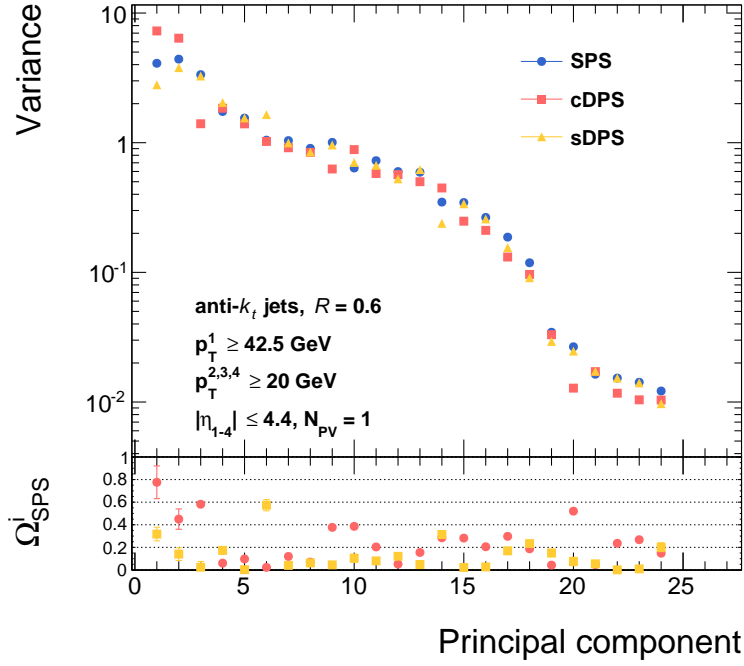


Figure 6.13: Variance values for the principal components calculated in the combined sample of SPS, cDPS and sDPS, selected in the phase-space defined in the legend, shown separately for each sample, as indicated. The relative difference between the variances of each principal component, defined in Eq. (6.29), is shown in the lower panel.

A large value of $\Omega_{\text{SPS}}^{\text{cDPS}}$ is observed for the first three PC. The sixth principal component displays the largest value of $\Omega_{\text{SPS}}^{\text{sDPS}}$, suggesting it is capable to differentiate between sDPS and SPS.

Each group of variables was tested by comparing the difference in variance of the PC with and without the group included in the PCA. For this comparison, the difference in variance,

$$\omega_{\text{SPS}}^i = |\sigma_i - \sigma_{\text{SPS}}|, \quad (6.30)$$

is used, where i refers to either cDPS or sDPS. The PCA is repeated five times, each time after removing one group of variables from the full list of variables. Thus, six sets of PC are obtained, one calculated using all the variables and five calculated with one group missing. The values of ω_{SPS}^i for each principal component in each set are shown in Figs. 6.14(a) and 6.14(b) in the cDPS and sDPS samples, respectively. A drop in the value of ω_{SPS}^i for a given principal component after removing a group of variables is interpreted as a loss of differentiating power, while taking into account that the new set of PC is not identical to the original one.

Separation between SPS and cDPS

Comparing the $\omega_{\text{SPS}}^{\text{cDPS}}$ values obtained using all variables to the values obtained after removing the Δ_{ij}^{pT} or $\Delta\phi_{ij}$ variables, a significant decrease is observed in the differentiating power between SPS and cDPS. On the other hand, removing the Δy_{ij} variables has a negligible effect. The drop in

6 Methodology

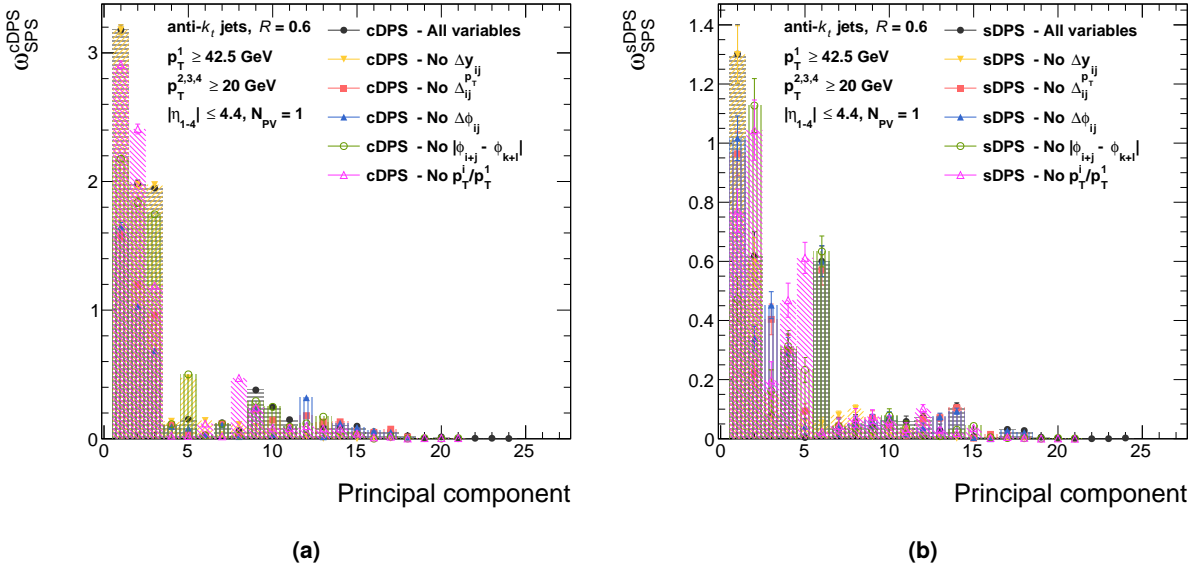


Figure 6.14: Values of (a) $\omega_{\text{SPS}}^{\text{cDPS}}$ and (b) $\omega_{\text{SPS}}^{\text{sDPS}}$, defined in Eq. (6.30), for each principal component calculated in the combined sample of SPS, cDPS and sDPS, selected in the phase-space defined in the legend, using all the variables listed in Eq. (6.27) and after removing each group of variables as indicated in the legend.

$\omega_{\text{SPS}}^{\text{cDPS}}$ value after removing the $|\phi_{i+j} - \phi_{k+l}|$ variables is significant in the first principal component, suggesting it is partially constructed from these variables.

The p_T^i/p_T^1 variables have a small effect on the differentiating power between SPS and cDPS. The visible decrease in the $\omega_{\text{SPS}}^{\text{cDPS}}$ value for the first principal component is compensated by a rise in the $\omega_{\text{SPS}}^{\text{cDPS}}$ value for the second principal component.

Separation between SPS and sDPS

The conclusions reached in the cDPS case on the differentiating power of the Δ_{ij}^{pT} , $\Delta\phi_{ij}$ and $|\phi_{i+j} - \phi_{k+l}|$ variables apply also in the sDPS case. The difference occurs for the Δy_{ij} variables in the sDPS case. As mentioned, when performing the PCA with all the variables, the sixth principal component has potential to separate between SPS and sDPS. Removing the Δy_{ij} variables leads to a significant drop in the $\omega_{\text{SPS}}^{\text{sDPS}}$ value for the sixth principal component, without a visible rise in any other principal component. This suggests that the Δy_{ij} variables are mapped to the sixth principal component and contribute significantly to the differentiating power between sDPS and SPS, as expected.

A similar drop for the sixth principal component is seen when removing the p_T^i/p_T^1 variables. However, an almost identical rise in the value of $\omega_{\text{SPS}}^{\text{sDPS}}$ is observed for the fifth principal component. It is therefore likely that removing the p_T^i/p_T^1 variables leads to the Δy_{ij} variables being mapped to the fifth principal component. Hence, the observed drop is misleading and the p_T^i/p_T^1 variables are not capable of separating sDPS and SPS.

Conclusions based on PCA

The PCA is a useful tool used to reduce the amount of variables required to classify events. Here it demonstrated that the Δy_{ij} variables do not contribute to the separation between SPS and cDPS, while playing an important role in classifying sDPS events. The p_T^i/p_T^1 variables show the least classification power out of all the variables, therefore they were removed from the list of variables given as input to the NN.

6.10 Extraction of the fraction of DPS events using a neural network

It has been shown that artificial neural network computing is a powerful method of solving complex problems, such as pattern recognition [180], regression [181] and classification [182]. The advantage of using an NN to construct a differentiating variable is that it allows the use of as many input variables as can be constructed from the four-jet topology, while taking into account the correlation between the variables on an event by event basis. For each event, the NN receives information describing the topology of the four jets in the event and returns three probabilities for the event to be SPS, cDPS or sDPS. Essentially, the NN folds the N dimensions of the N input variables into two dimensions, while fully taking into account the correlations between the input variables. The two dimensions take the form of three NN output variables, ξ_{SPS} , ξ_{cDPS} and ξ_{sDPS} , with the constraint, $\xi_{\text{SPS}} + \xi_{\text{cDPS}} + \xi_{\text{sDPS}} = 1$.

6.10.1 Training of the neural network

Once the three input samples for the NN are prepared, events from each sample are divided into two (statistically independent) sub-samples, the *training sample* and the *test sample*. As the names imply, the former is used to train the NN, and the latter to test the robustness of the result. The samples are weighted such that the same effective number of events from the SPS, cDPS and sDPS samples is used for the training of the NN. In all subsequent figures, only the test SPS, cDPS and sDPS samples are shown.

The NN is a feed-forward multilayer perceptron, implemented in the Root analysis framework [183]. The Broyden-Fletcher-Goldfarb-Shanno [184–187] supervised learning algorithm is used in the training, utilizing back-propagation to update the weights based on a set of examples.

Studies [188, 189] have shown that given enough hidden neurons in one layer, the NN can approximate any continuous function. However, in practice, this requires a very large number of hidden neurons in the one layer. On the other hand, if two hidden layers are used, a more modest number of hidden neurons is needed to reach the same numerical accuracy [190]. Therefore, in order to achieve high numerical accuracy and shorter convergence time, the final structure of the NN used here consists of two hidden layers.

The input layer has 21 neurons, corresponding to the variables selected as input variables to the NN, the first and second hidden layers have 30 and nine neurons, respectively, and the output of the network consists of three neurons. A sigmoid function is used as the activation function of hidden neurons and a linear activation function is used in neurons in the input layer. These choices represent

6 Methodology

the product of an optimization study on the performance of the NN and balance the complexity of the network with the computation time of the training.

The PCA described in Section 6.9 transforms a set of *linearly* correlated variables into a set of uncorrelated PC. However, as demonstrated in Section 6.8.2, the variables defined in Eq. (6.27) are correlated in a non-linear way. Since the NN is capable of resolving non-linear correlations between the input variables [188], the PC computed in Section 6.9 are not used as input. Instead, the original variables are given as input to the NN.

For the training process, three flags are used to mark each event as belonging to one of the samples; e.g., an event from the cDPS sample is marked as

$$\xi_{\text{SPS}} = 0, \quad \xi_{\text{cDPS}} = 1, \quad \xi_{\text{sDPS}} = 0.$$

Each output of the NN, ξ_i , is normalized to values in the range [0, 1] by using a softmax function at the output layer. The input variables are normalized as well, in order not to cause a numeric bias towards variables with larger values.

During the training phase of the NN, weights between the various neurons are modified, changing the output of the network. The result is quantified by an error function, E_{NN} , which measures the agreement of the response of the network with the desired result. Figure 6.15(a) shows the value of E_{NN} as a function of the number of training cycles (epochs) of the network. The training should be stopped when the value of E_{NN} begins to rise for the test sample while it continues to fall for the training sample. Here, training was stopped after 1300 epochs, as E_{NN} converged to a stable value for the training sample and there was a slight indication of a rise in the value of E_{NN} for the test sample.

6.10.2 Significance of variables to the output of the neural network

The chosen structure of the NN and the final set of weights after completion of the training are illustrated in Fig. 6.15(b). The circles represent neurons, where each column stands for a layer of the network, and the width of a connecting line between neurons is proportional to the magnitude of the respective weight. The larger the weight of a given neuron, the more significant the contribution of the corresponding variable.

A more quantitative presentation of the significance of each input variable is given in Fig. 6.16. For each event in the test samples, small variations, $\pm\varepsilon$, are made to the value of each input variable and the difference between the corresponding NN output values, $\Delta\xi_{\text{NN}}$, is recorded. The small variation for each variable was chosen to be 10% of the RMS of the variable distribution, $\varepsilon = 0.1 \times \text{RMS}$, where the RMS is calculated after normalizing the variables to the range [0, 1]. The difference $\Delta\xi_{\text{NN}}$ is calculated as

$$\Delta\xi_{\text{NN}} = \sqrt{(\xi_{\text{SPS}}^{+\varepsilon} - \xi_{\text{SPS}}^{-\varepsilon})^2 + (\xi_{\text{cDPS}}^{+\varepsilon} - \xi_{\text{cDPS}}^{-\varepsilon})^2 + (\xi_{\text{sDPS}}^{+\varepsilon} - \xi_{\text{sDPS}}^{-\varepsilon})^2}, \quad (6.31)$$

where $\xi_i^{\pm\varepsilon}$ signifies the value of ξ_i after the variation $\pm\varepsilon$ is made to one of the input variables. After repeating the calculation of $\Delta\xi_{\text{NN}}$ for each input variable and for all the events in the test samples, the resulting distributions are compared, as shown in Fig. 6.16. High values of $\Delta\xi_{\text{NN}}$ are interpreted

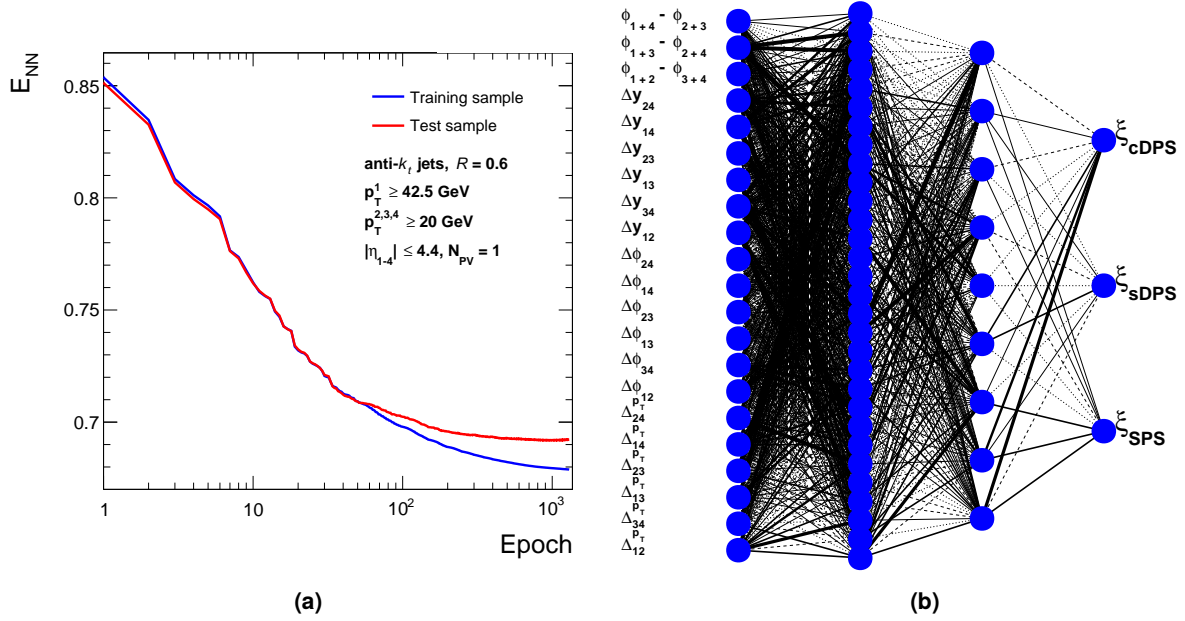


Figure 6.15: (a) Dependence of the value of the error function of the NN, E_{NN} , on the number of training cycles (epochs) of the network, for the NN training and test samples, as indicated in the figure. (b) Schematic depiction of the structure of the NN, where neurons are denoted by blue circles, layers are denoted by columns of circles, and lines represent the weights which connect neuron pairs, where the thickness of a line is proportional to the relative magnitude of the corresponding weight. Each input variable, denoted next to each input neuron and defined in Eq. (6.27), corresponds to a neuron in the first layer of the network. The outputs of the NN are denoted by ξ_i .

as high significance of the corresponding input variable to the NN output. This serves as a test for which variables are useful for classification.

As the topology of double parton scattering would lead us to expect, the most significant variables are the variables representing the “back-to-back”-ness of the sub-leading dijet pair, Δ_{34}^{PT} and $\Delta\phi_{34}$. The variable representing the angle between the planes of the leading dijet pair and the sub-leading dijet pair, $\phi_{1+2} - \phi_{3+4}$, exhibits strong significance as well.

6.10.3 Output of the neural network

Since the NN outputs are three probabilities, their sum is normalized to one, $\xi_{SPS} + \xi_{cDPS} + \xi_{sDPS} = 1$. With this normalization, the three outputs of the NN for each event may be plotted as a single point inside an equilateral triangle (Dalitz plot). A point in the triangle expresses the three probabilities as three distances from each of the sides of the triangle. The vertices would therefore be populated according to the probability to belong to one of the samples. Events assigned high probabilities are pushed into the vertices. Plotting the NN outputs on a Dalitz plot this way helps visualize the classification power of the NN. Figure 6.17 shows an illustration of the Dalitz plot, where the horizontal axis corresponds to $\frac{1}{\sqrt{3}}\xi_{sDPS} + \frac{2}{\sqrt{3}}\xi_{cDPS}$ and the vertical axis to the value of ξ_{sDPS} . The corners of the triangle are then divided to the three classes of events as illustrated in Fig. 6.17.

6 Methodology

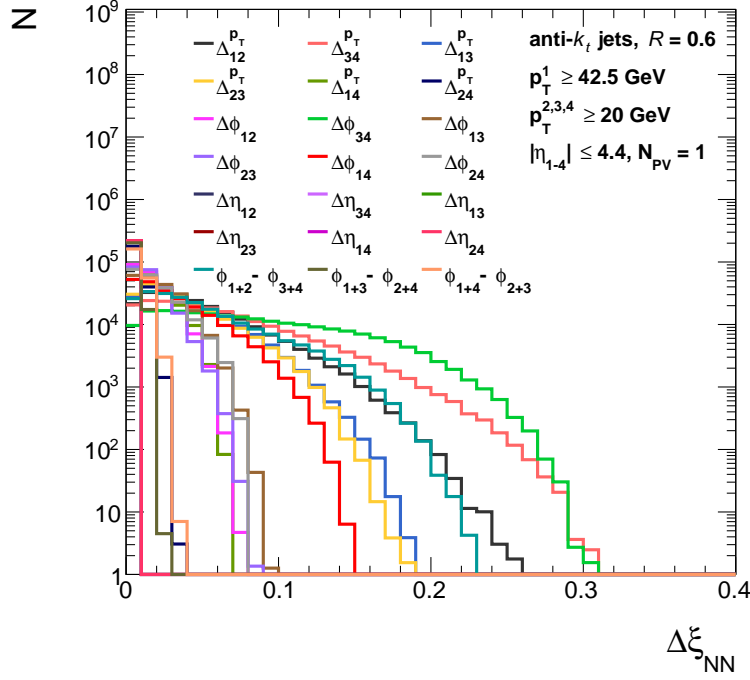


Figure 6.16: Distributions of the difference in the output of the NN, $\Delta\xi_{\text{NN}}$, for all events in the test sample, selected in the phase-space defined in the legend, as calculated by making small variations, $\pm\varepsilon$, to each input variable to the NN (see text for details). Input variables are defined in Eq. (6.27) and their corresponding distributions are indicated in the legend.

The separation power of the NN may be judged by examining the distributions of the three test samples in the Dalitz plot, as shown in Fig. 6.18. The distributions are drawn in three-dimensions, where the number of events in each bin is proportional to the area of the box drawn. The dashed horizontal lines in Fig. 6.18 mark the slices the triangle is divided to for visualization of the distributions, as discussed in Section 6.11.

Three clusters are visible in Fig. 6.18. The clearest peak is seen in the bottom right corner, of events from the cDPS sample. However, a contribution from SPS events in the same corner is also visible. The bottom left corner is mostly populated by SPS events, where a sharp peak is visible in the corner. A lower ridge of SPS events extending towards the sDPS corner is observed as well. A visible peak of sDPS events is seen, though it is not concentrated in the top corner. The peak is concentrated around $\xi_{\text{sDPS}} \sim 0.8$ and along the side connecting the SPS and sDPS corners.

The peak structure seen in Fig. 6.18 suggests that the NN is able to classify cDPS events with some overlap of SPS events. The latter confirms the assumption that some SPS interactions result in a topology similar to the one seen in cDPS events. Ergo, a cut based classification would lead to an impure sample of cDPS events. Classification of sDPS events is a harder task, as seen from the peak structure in Fig. 6.18. The topologies of SPS and sDPS events overlap even more, so the classification power of the NN is lower than in the cDPS case.

Based on the results seen above, it is clear that classification of cDPS and sDPS events on an event by event basis is impossible. However, the peak structure suggests that estimation of the different

6.10 Extraction of the fraction of DPS events using a neural network

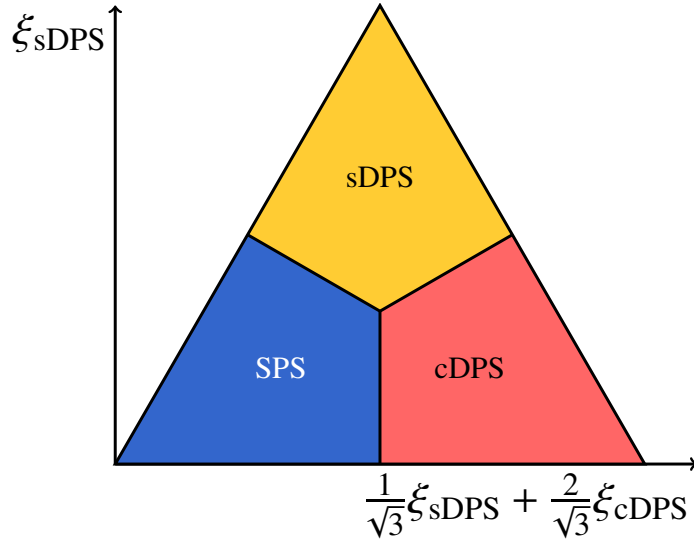


Figure 6.17: Illustration of the Dalitz plot constructed from the three NN outputs, ξ_{SPS} , ξ_{cDPS} , and ξ_{sDPS} , and the constraint, $\xi_{\text{SPS}} + \xi_{\text{cDPS}} + \xi_{\text{sDPS}} = 1$. The vertical and horizontal axes are defined in the figure. Each event is translated to a point in the triangle by applying the NN and mapping the outputs to the two-dimensional Dalitz plot. The distance of the point from the three triangle sides may be used to classify the event as coming from SPS, cDPS or sDPS. The colored areas illustrate the zones closest to the corresponding vertex.

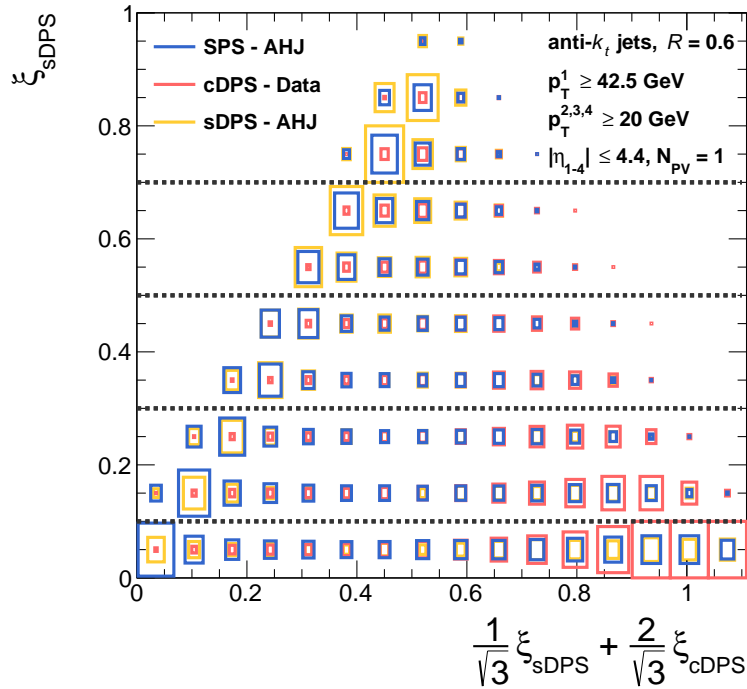


Figure 6.18: Normalized distributions of the NN outputs, mapped to a two-dimensional Dalitz plot as described in the text, in the SPS (blue), cDPS (red) and sDPS (yellow) test samples selected in the phase-space defined in the legend. For each sample, the relative number of events in each bin is proportional to the area of the box drawn. The dashed horizontal lines show the five slices used to visualize the fit results.

contributions may be performed.

6.11 Estimate of the cDPS and sDPS contributions

To estimate the cDPS and sDPS fractions in four-jet events, the two-dimensional Dalitz distribution in data (\mathcal{D}) is fitted to a weighted sum of the SPS (\mathcal{M}_{SPS}), cDPS ($\mathcal{M}_{\text{cDPS}}$) and sDPS ($\mathcal{M}_{\text{sDPS}}$) distributions, each normalized to the measured four-jet cross-section in data, with the fractions as free parameters. The optimal fractions are obtained using a fit of the form,

$$\mathcal{D} = (1 - f_{\text{cDPS}} - f_{\text{sDPS}}) \cdot \mathcal{M}_{\text{SPS}} + f_{\text{cDPS}} \cdot \mathcal{M}_{\text{cDPS}} + f_{\text{sDPS}} \cdot \mathcal{M}_{\text{sDPS}}, \quad (6.32)$$

where a χ^2 minimization is performed, as implemented in the MINUIT package in ROOT [183], taking into account statistical uncertainties of all the samples in each bin.

In order to visualize the results of the fit, the triangle shown in Fig. 6.18 is divided into five slices,

1. $0.0 \leq \xi_{\text{sDPS}} < 0.1$,
2. $0.1 \leq \xi_{\text{sDPS}} < 0.3$,
3. $0.3 \leq \xi_{\text{sDPS}} < 0.5$,
4. $0.5 \leq \xi_{\text{sDPS}} < 0.7$,
5. $0.7 \leq \xi_{\text{sDPS}} \leq 1.0$,

as illustrated by the dashed horizontal lines in Fig. 6.18. The fit is performed in two dimensions, but the fit results and NN output distributions are shown in the one-dimensional slices.

The fit to the NN output distribution in four-jet events in data is shown in Figs. 6.19, the results of which will be discussed in detail in Section 9.1. The distributions for four-jet events in data are compared to a combination of the SPS, cDPS and sDPS fractional contributions, based on the results from the fit. A validation of the methodology proposed here is given in the next section.

6.11 Estimate of the cDPS and sDPS contributions

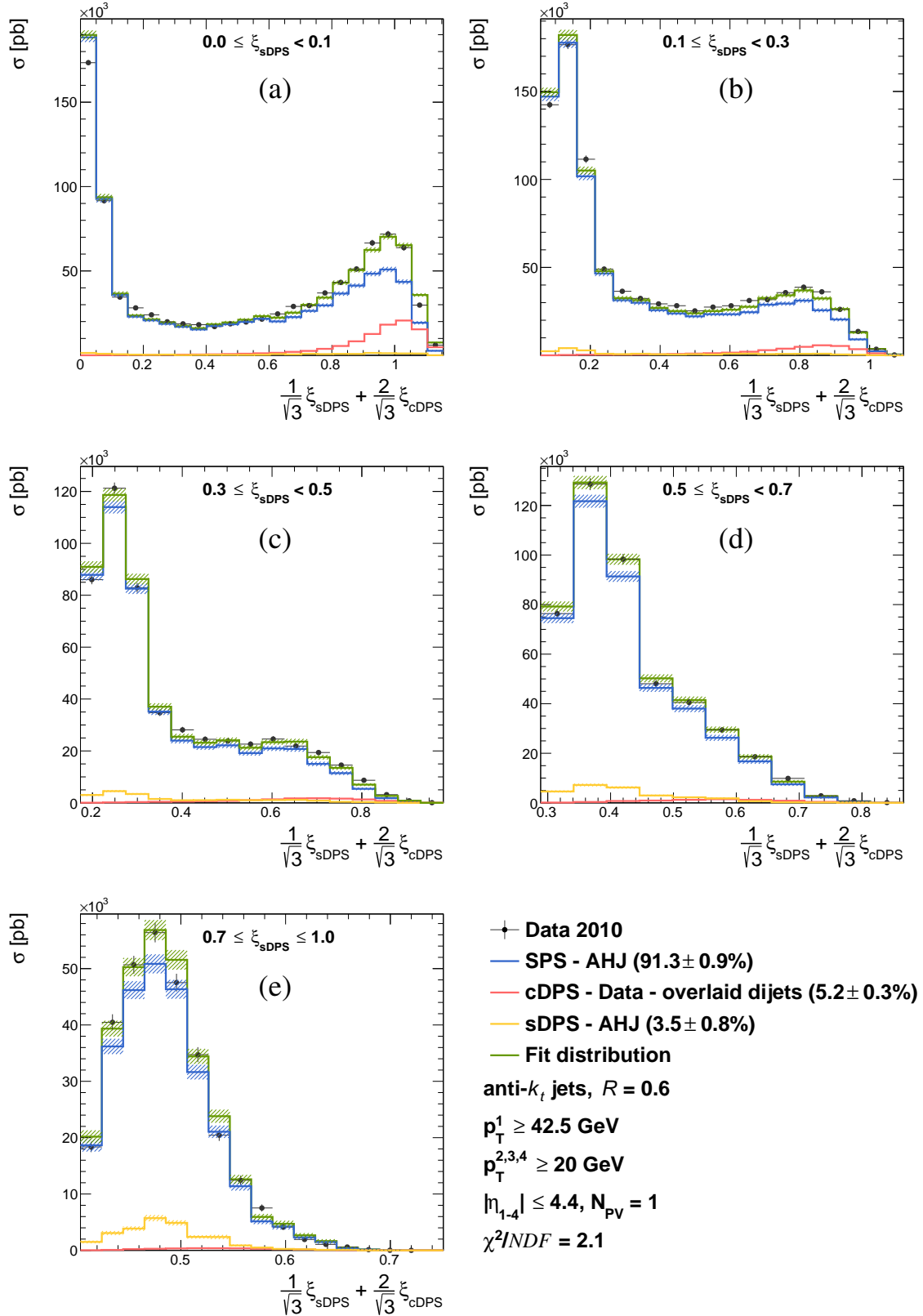


Figure 6.19: Distributions of the NN outputs, $\frac{1}{\sqrt{3}}\xi_{\text{sDPS}} + \frac{2}{\sqrt{3}}\xi_{\text{cDPS}}$, in the ξ_{sDPS} ranges indicated in the figures, for four-jet events in data (dots), selected in the phase space defined in the legend, compared to the result of fitting a combination of the SPS (blue histogram), cDPS (red histogram) and sDPS (yellow histogram) contributions, the sum of which is shown as the green histogram. The fractions ξ_{sDPS} obtained and the quality criteria of the fit, χ^2/NDF , are indicated in the legend.

Methodology validation

The measurement methodology requires extensive validation. For this purpose, the inclusive AHJ sample is used to mimic the data and the NN is applied to the AHJ events. Fitting the NN output distributions of the SPS, cDPS and sDPS samples to the NN output distribution of the inclusive AHJ sample allows to estimate the fractions of double parton scattering in the inclusive AHJ sample, $f_{\text{cDPS}}^{(\text{MC})}$ and $f_{\text{sDPS}}^{(\text{MC})}$. The cDPS and sDPS fractions on parton-level in the AHJ sample, $f_{\text{cDPS}}^{(\text{P})}$ and $f_{\text{sDPS}}^{(\text{P})}$, can be extracted directly from the event record. A comparison of $f_{\text{cDPS}}^{(\text{P})}$ and $f_{\text{sDPS}}^{(\text{P})}$ with the values obtained from the fit to the inclusive AHJ sample, $f_{\text{cDPS}}^{(\text{MC})}$ and $f_{\text{sDPS}}^{(\text{MC})}$, serves as validation for the measurement methodology.

7.1 Determination of the fraction of double parton scattering on parton-level

To determine the parton-level cDPS and sDPS fractions in the AHJ sample, the cuts defined in Eq. (5.1) were applied to the sample. Namely, only events passing the following cuts at the reconstructed level are retained:

- exactly one reconstructed vertex, $N_{\text{PV}} = 1$;
- the four leading jets in the event are within $|\eta| \leq 4.4$;
- the transverse momentum of the leading jet obeys $p_T^1 \geq 42.5$ GeV;
- the transverse momenta of the three sub-leading jets obey, $p_T^{2,3,4} \geq 20$ GeV.

Thus, a four-jet AHJ sample equivalent to the four-jet data sample is selected. The next step is to classify the events as SPS, cDPS and sDPS events on parton-level.

The process of selecting SPS, cDPS and sDPS events from the AHJ sample based on partonic information is described in Section 6.7.1. Briefly, outgoing partons from the interactions are matched to the four leading jets in the event. In case the four jets match two primary-scatter partons and two secondary-scatter partons, the event is classified as a cDPS event. Events where three primary-scatter partons match three jets and one secondary-scatter parton matches one jet are classified as sDPS events. In case none of the four jets matches a secondary-scatter parton, the event is classified as coming from a SPS interaction.

Once the events are classified on parton-level to three classes, $f_{\text{cDPS}}^{(\text{P})}$ and $f_{\text{sDPS}}^{(\text{P})}$ are defined as

$$f_{\text{cDPS}}^{(\text{P})} = \frac{N_{\text{P}}(\text{cDPS})}{N_{\text{P}}(\text{SPS}) + N_{\text{P}}(\text{cDPS}) + N_{\text{P}}(\text{sDPS})}, \quad f_{\text{sDPS}}^{(\text{P})} = \frac{N_{\text{P}}(\text{sDPS})}{N_{\text{P}}(\text{SPS}) + N_{\text{P}}(\text{cDPS}) + N_{\text{P}}(\text{sDPS})}, \quad (7.1)$$

where $N_{\text{P}}(\text{SPS})$, $N_{\text{P}}(\text{cDPS})$ and $N_{\text{P}}(\text{sDPS})$ are the number of SPS, cDPS and sDPS events in the AHJ sample, respectively. The fractions come out to be

$$f_{\text{cDPS}}^{(\text{P})} = 0.103 \pm 0.001 \text{ (stat.)}, \quad f_{\text{sDPS}}^{(\text{P})} = 0.052 \pm 0.001 \text{ (stat.)}. \quad (7.2)$$

7.2 Kinematic properties of jets in AHJ

7.2.1 Jet p_T - y distributions in AHJ

The inclusive AHJ sample is used as pseudo-data in the validation process. In comparisons of kinematic properties of the jets, between the data and the AHJ sample, some discrepancies were found. Figure 7.1 shows a comparison between the data and the AHJ sample of the p_T and y distributions of the four leading jets. In subsequent figures comparing p_T (y) distributions, the leading jet p_T (y) distribution in data, in the range $50 < p_T < 70$ GeV ($-1.0 < y < 1.0$), is used to set the normalization of the distributions in the MC.

In the range $20 < p_T < 30$ GeV, the MC underestimates the data by 45%, 15% and 5% for the second, third and fourth jet, respectively. Above 30 GeV, the MC overestimates the data by about 5% for the second jet and by 15% for the third and fourth jet. The leading jet p_T distributions in data and MC agree within 5% in the range $42.5 \leq p_T < 100$ GeV. Above 100 GeV, the distribution in the MC starts falling less steeply than in the data, overestimating the data by about 20%.

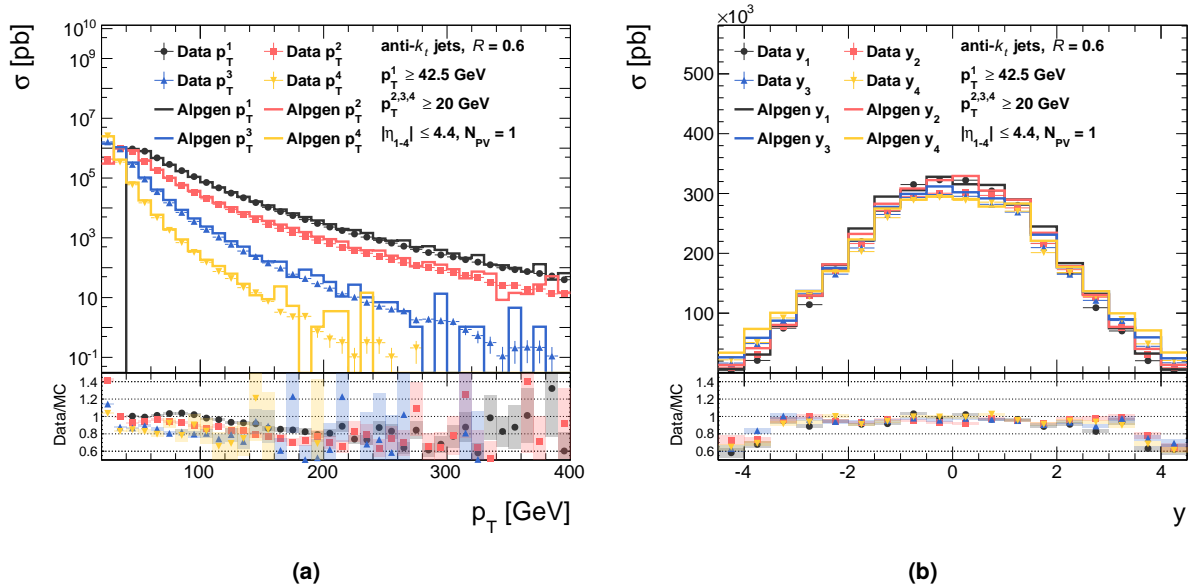


Figure 7.1: Distributions of the (a) transverse momentum, p_T , and (b) rapidity, y , of the four highest- p_T jets, denoted as p_T^{1-4} and y_{1-4} in the figures, in data and in AHJ. The leading jet p_T (y) distribution in data, in the range $50 < p_T < 70$ GeV ($-1.0 < y < 1.0$), is used to set the normalization of the distributions in the MC. The ratio of data to MC is shown in the bottom panels, where statistical uncertainties are shown as the shaded areas.

A disagreement is also seen in the y distributions shown in Fig. 7.1(b). The MC exhibits more jets at high rapidity, $|y| > 3.5$. The difference is largest for the leading jet, reaching 40% in both extremes of the rapidity range.

7.2.2 Variables distributions in data and in AHJ

These differences between data and MC in the basic kinematic properties of the jets are exhibited as differences in the distributions of the NN input variables as well. Two representative comparisons between data and MC are shown in Fig. 7.2. Distributions in the MC are rescaled to the cross-section measured in data. The distributions of the $\Delta_{12}^{p_T}$ input variable in data and MC are compared in Fig. 7.2(a), where in addition to the inclusive MC distribution, the SPS, cDPS and sDPS distributions composing the inclusive AHJ sample are shown with their respective fractions. The two leading jets in MC appear to be more balanced than in the data, as reflected by a shift of the peak to lower values. This is consistent with the observation that in data the sub-leading jet is of lower p_T than in the MC. Considering the minimum p_T cut on the leading jet, $p_T \geq 42.5$ GeV, a sub-leading jet of lower p_T would lead to less balanced leading dijets.

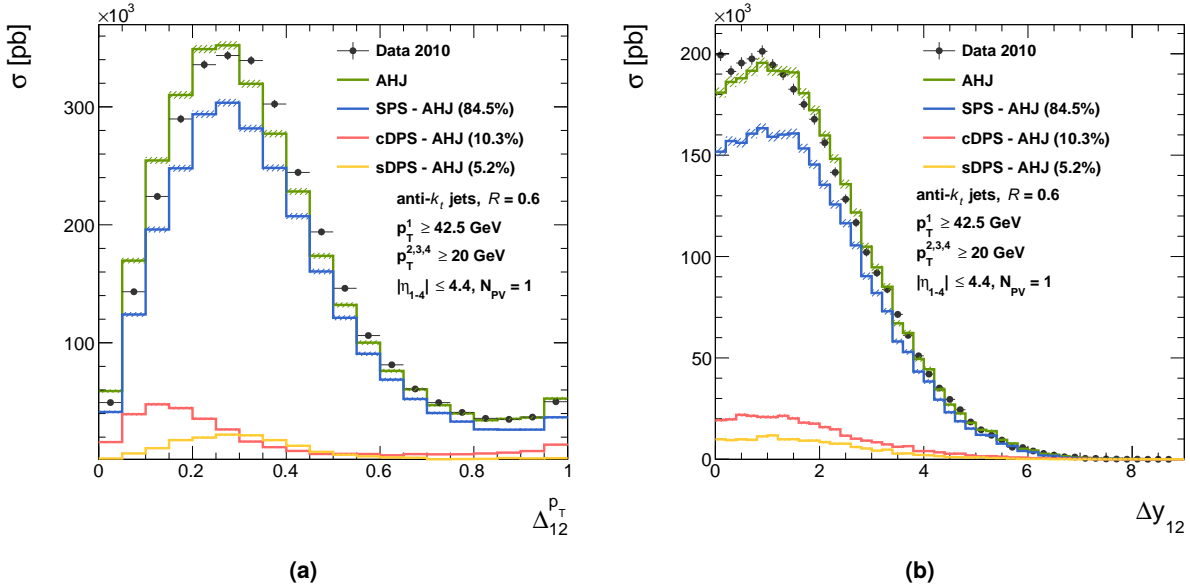


Figure 7.2: Comparison between the distributions of the variables (a) $\Delta_{12}^{p_T}$ and (b) Δy_{12} , defined in Eq. (6.27), in four-jet events in data (dots), selected in the phase space defined in the figure, and in the AHJ MC (green histogram). Also shown are the SPS (blue histogram), cDPS (red histogram) and sDPS (yellow histogram) contributions with their respective fractions indicated in the legend. The distributions of the MC are rescaled to the cross-section measured in data.

A comparison between the distributions of the Δy_{12} input variable in data and MC is shown in Fig. 7.2(b), where similarly the various contributions to the AHJ sample are shown. The distance Δy between the leading jets in the MC is larger, on average, than in data, producing the wider distribution seen in the figure. This observation is consistent with the jet y distributions shown in Fig. 7.1(b). More jets in high y regions in the MC translates to a larger distance between the jets, particularly for the leading jet, for which the largest difference is seen between data and MC.

7.2.3 Re-weighting of AHJ

To correct for the discrepancies in the kinematic properties of four-jet events between data and AHJ, a re-weighting of AHJ is required. Since the migration of events into and out of the phase-space of the measurement is taken into account in the acceptance calculation (see Section 6.6), the re-weighting is applied in the same phase-space as the one defined for the measurement. In addition, the re-weighting factors are calculated using reconstructed jets, rather than particle jets.

To reach a good description of the topology of four-jet events in data, the re-weighting is performed based on eight-dimensional distributions, constructed from the p_T and y of the four leading jets. Normalized, eight-dimensional p_T - y distributions are constructed in data and in AHJ and the ratio between them produces a discrete, bin-by-bin, re-weighting function. The weight correction is then applied to each event in AHJ based on the p_T and y of the four leading jets.

Since jets in cDPS and sDPS events are expected to populate more the low p_T end of the spectrum than the high p_T one, there is a risk that the re-weighting would change their relative fractions by a significant amount. That is, based on the discrepancies seen in Fig. 7.1(a), events in AHJ with jets in the range $20 < p_T^{2,3,4} < 30$ GeV will be given about 20% higher weight and events with jets in the range $30 < p_T^{3,4} < 60$ GeV will be given about 15% lower weight. Modifying the fractions of cDPS and sDPS in AHJ could have an effect on the measurement in data. Therefore, the fractions are re-calculated after the re-weighting in order to ascertain that they were not modified by a significant amount.

The p_T distributions of the four jets in data and MC after the correction are shown in Fig. 7.3(a). At low p_T , $p_T \leq 40$ GeV, the distributions in data and MC agree to within 5%, while as p_T increases the agreement deteriorates to be within 10%, until reaching a range in which it is not possible to make a statistically significant comparison.

The y distributions of the four jets in data and MC after re-weighting the MC are shown in Fig. 7.3(b). The distributions in data and MC agree to within 5% across the entire range.

7.2.4 Variables distributions after re-weighting AHJ

A comparison of the distributions of the $\Delta_{12}^{p_T}$ and Δy_{12} variables in data and MC after re-weighting is shown in Fig. 7.4. The distributions in the MC are rescaled to the cross-section measured in data. Distributions of SPS, cDPS and sDPS events in the AHJ sample are shown as well, normalized to their respective contribution to the AHJ sample.

The shift in the peak position in the $\Delta_{12}^{p_T}$ distribution in the MC with respect to the data (see Fig. 7.4(a)) has been reduced significantly, leading to an overall better agreement with data. The width of the Δy_{12} distribution in MC was reduced as a result of the re-weighting (see Fig. 7.4(b)). The MC agrees with the data across the Δy_{12} range, except for the lowest bin, $\Delta y_{12} < 0.2$, where the MC underestimates the data by about 5%, beyond the statistical uncertainty which is of the order of 2% in this bin. This discrepancy was studied further, examining the shape of the events in this bin in an attempt to understand the source of the difference. However, no obvious candidates of background processes or mis-modelling of the MC were found. Therefore, the disagreement is considered to be the result of a statistical fluctuation.

7 Methodology validation

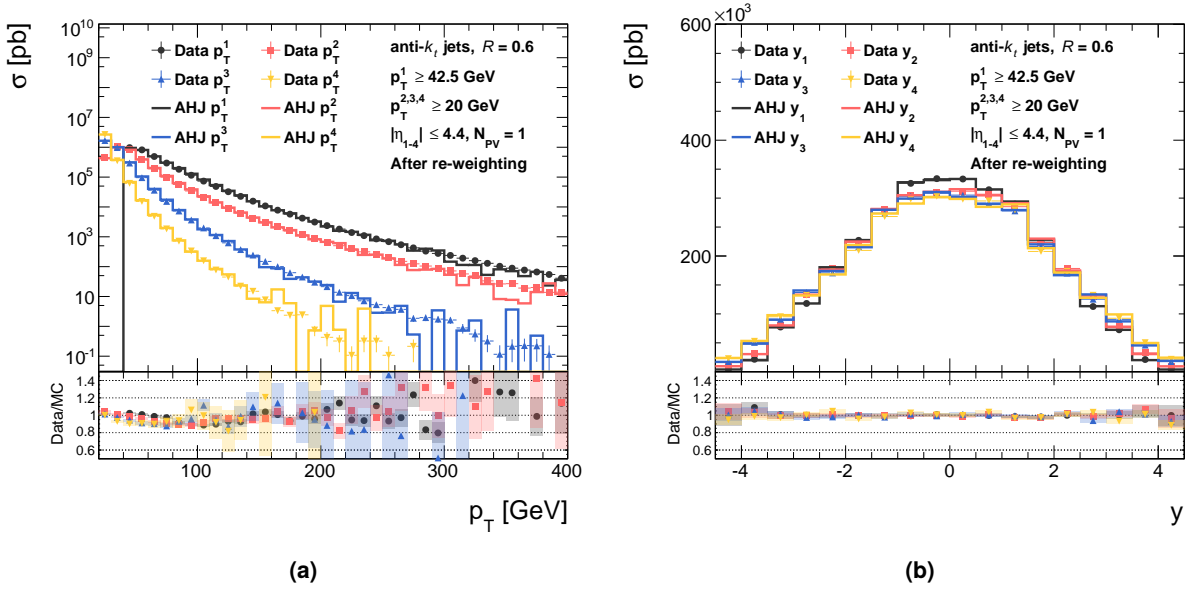


Figure 7.3: Distributions of the (a) transverse momentum, p_T , and (b) rapidity, y , of the four highest- p_T jets, denoted as p_T^{1-4} and y_{1-4} in the figures, in data and in AHJ, after re-weighting the latter. The leading jet p_T (y) distribution in data, in the range $50 < p_T < 70$ GeV ($-1.0 < y < 1.0$), is used to set the normalization of the distributions in the MC. The ratio of data to MC is shown in the bottom panels, where statistical uncertainties are shown as the shaded areas.

The improvement in the description of the data, obtained by re-weighting of the MC sample, is seen in all distributions of the input variables, with the exception discussed in Section 7.3. In the following, all of the distributions extracted from the AHJ sample are taken from the re-weighted sample. The systematic uncertainty associated with the re-weighting of AHJ is discussed in Section 8.2.1.

7.2.5 Fractions of DPS after re-weighting AHJ

The fractions, $f_{\text{cDPS}}^{(P)}$ and $f_{\text{sDPS}}^{(P)}$, after the re-weighting are re-calculated and come out to be

$$f_{\text{cDPS}}^{(P)} = 0.094 \pm 0.001 \text{ (stat.)}, \quad f_{\text{sDPS}}^{(P)} = 0.048 \pm 0.001 \text{ (stat.)}. \quad (7.3)$$

A relatively small change is observed, compared to the average value of the correction ($\sim 20\%$), confirming that the re-weighting is safe to perform. The small change in the fractions, together with the fact that the majority of the AHJ sample is composed of SPS events (85%), leads to the conclusion that re-weighting AHJ essentially re-weights the SPS sample.

7.3 Double parton scattering fraction in AHJ

A discrepancy is found in the $\Delta_{34}^{P_T}$ and $\Delta\phi_{34}$ distributions between the data and MC before and after re-weighting. Comparisons of the $\Delta_{34}^{P_T}$ and $\Delta\phi_{34}$ distributions in data and in the re-weighted AHJ

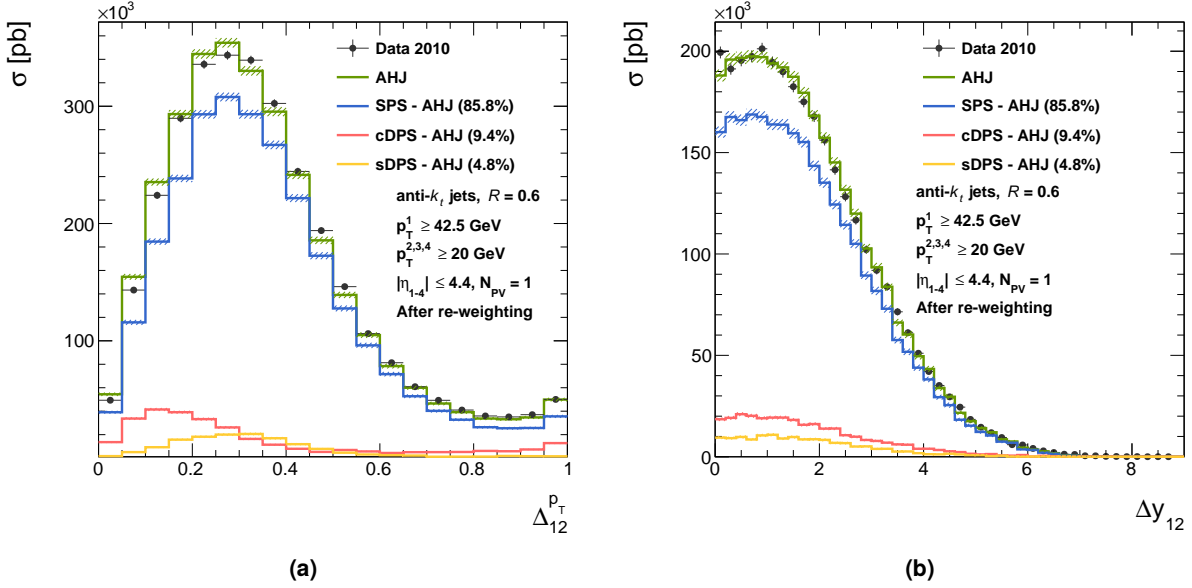


Figure 7.4: Comparison between the distributions of the variables (a) $\Delta_{12}^{p_T}$ and (b) Δy_{12} , defined in Eq. (6.27), in four-jet events in data (dots), selected in the phase space defined in the figure, and in the AHJ MC after re-weighting (green histogram). Also shown are the SPS (blue histogram), cDPS (red histogram) and sDPS (yellow histogram) contributions with their respective fractions indicated in the legend. The distributions of the MC are rescaled to the cross-section measured in data.

sample are shown in Fig. 7.5. The distributions of the MC are rescaled to the cross-section measured in data. Also shown are the SPS (85.8%), cDPS (9.4%) and sDPS (4.8%) contributions to the AHJ, scaled to their respective fractions. The MC overestimates the data at low values of $\Delta_{34}^{p_T}$ by about 14%, summed over the first four bins in Fig. 7.5(a). A similar and related overestimation is seen in the $\Delta\phi_{34}$ distributions, shown in Fig. 7.5(b), where the area below the peak at π is about 13% larger in the MC than in data. These excesses suggest that there are more sub-leading jets (jets 3 and 4) which are back-to-back in the MC than in the data.

The improvement in the discrepancies seen in the distributions of the variables after re-weighting (see Section 7.2.4) is not observed for the $\Delta_{34}^{p_T}$ and $\Delta\phi_{34}$ distributions. The re-weighting does not affect these variables since they are driven by the topology of jets 3 and 4 in the ϕ plane, rather than their p_T and y .

Two hypotheses were considered as possible sources of the abundance of back-to-back jets in the MC with respect to the data,

1. a mis-modelling of SPS interactions in AHJ;
2. a larger fraction of DPS in AHJ compared to data.

It is crucial to test which of the two options is correct, since a mis-modelling of SPS in AHJ which leads to more back-to-back jets would have a very large effect on the measurement. In case the

7 Methodology validation

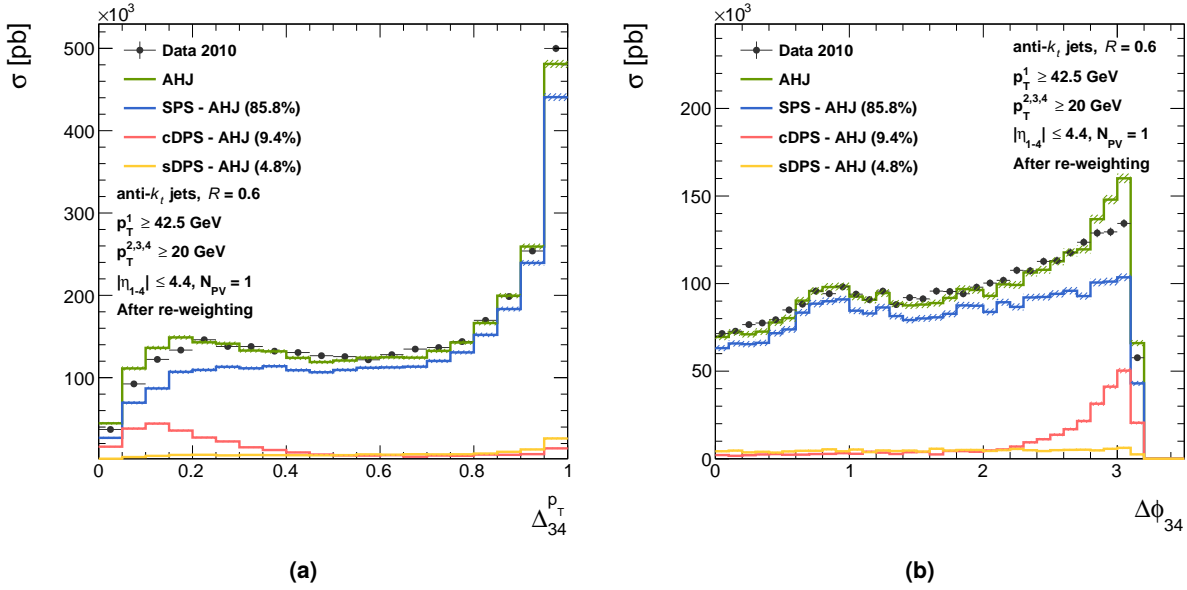


Figure 7.5: Comparison between the distributions of the variables (a) $\Delta_{34}^{p_T}$ and (b) $\Delta\phi_{34}$, defined in Eq. (6.27), in four-jet events in data (dots), selected in the phase space defined in the figure, and in the AHJ MC (green histogram). Also shown are the SPS (blue histogram), cDPS (red histogram) and sDPS (yellow histogram) contributions with their respective fractions indicated in the legend. The distributions of the MC are rescaled to the cross-section measured in data.

fraction of DPS in AHJ turns out to be the culprit, it will have no consequence on the measurement, since the fractions in AHJ do not play a role in the estimation of the fractions in data.

To test the first hypothesis, the distributions in the SPS sample extracted from AHJ were compared to the distributions of a SPS sample from a different MC. Since it is impossible to select SPS events in data, a comparison to a different MC sample is the only option available. For this purpose, a multi-jet QCD sample was generated with the SHERPA generator.

Similarly to AHJ, albeit with a different matching scheme, the CKKW matching scale of SHERPA is set to 15 GeV. This implies that partons with p_T above 15 GeV in the final state, necessarily originate from matrix elements, and not from the parton shower. Most jets passing the $p_T \geq 20$ GeV cut are therefore associated with the hard interaction (cf. Section 6.7.2).

The SHERPA generator does not allow access in the event record to the partons participating in the main and accompanying interactions. Therefore, it is impossible to extract a SPS sample from an inclusive four-jet QCD sample generated with SHERPA as is done in the AHJ case. Subsequently, a different approach was taken. In the generation process, the module adding multi-parton interactions to the main interactions was turned off (see Chapter 4).

Turning off completely the MPI module in SHERPA removes all soft and hard interactions accompanying the main interactions. This is equivalent to rejecting all events with secondary-scatter partons with $p_T \geq 3.5$ GeV in the AHJ sample. Hence, the two SPS samples from AHJ and SHERPA are not exactly equivalent. However, considering the identical matching scale between the AHJ and SHERPA

samples and the fact that in most SPS events extracted from the AHJ sample, the jets were matched to partons originating from the matrix elements, the two SPS samples should be similar. To phrase it differently, the four jets in both SPS samples most likely originate from SPS interactions, despite the different approaches taken in extracting the samples. One caveat is the inclusion of soft secondary interactions in the AHJ SPS sample which could potentially decorrelate the jets somewhat due to color reconnection, extra energy flow in the event and so on.

To test the topology of the sub-leading dijet in SPS events extracted from the AHJ sample, distributions of the $\Delta_{34}^{p_T}$ and $\Delta\phi_{34}$ variables in both samples are compared. The same selection process described in Chapter 5 is applied to the SHERPA sample to select four-jet events. Once four-jet events are extracted from the SHERPA sample, the topology of the sub-leading dijet may be studied. Normalized distributions of the $\Delta_{34}^{p_T}$ and $\Delta\phi_{34}$ variables in the SPS samples from AHJ and SHERPA are shown in Fig. 7.6.

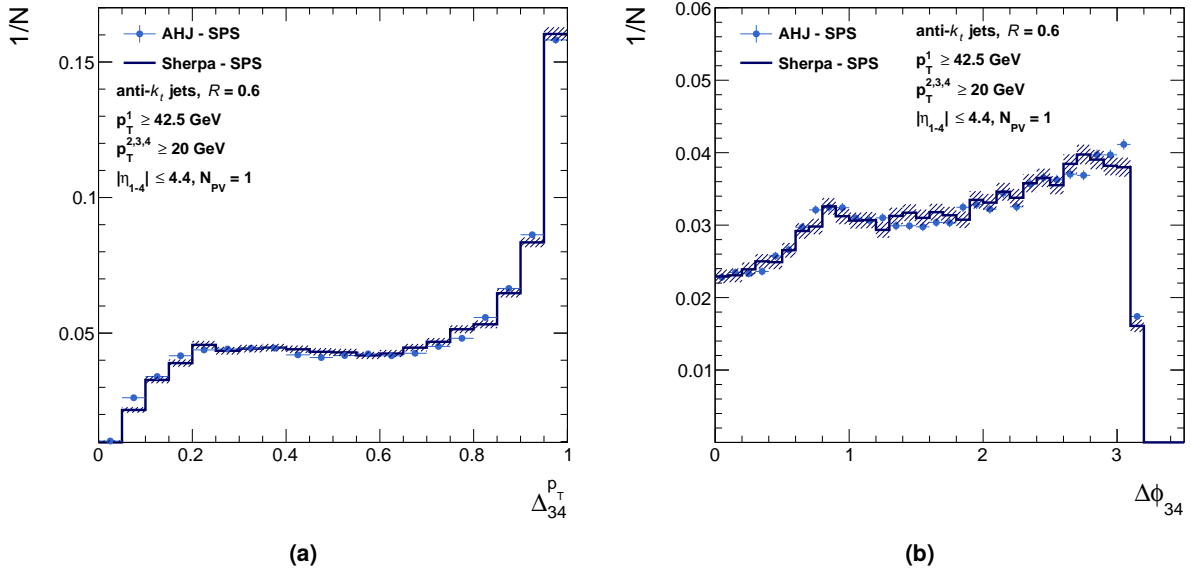


Figure 7.6: Normalized distributions of the variables (a) $\Delta_{34}^{p_T}$ and (b) $\Delta\phi_{34}$, defined in Eq. (6.27), in four-jet SPS events extracted from the AHJ sample (dots, light blue), selected in the phase space defined in the figure, and in SPS events generated with the SHERPA generator (dark blue histogram).

A good agreement in the shapes of the distributions is observed for both variables. Some small discrepancies, of the order of a few percent, are observed in a few isolated bins in both distributions, but these discrepancies are far smaller than the ones observed between the distributions in AHJ and in data. In addition, the bins in which the differences between the distributions are observed are not in values specifically related to back-to-back topologies.

To test the effect of the re-weighting on the $\Delta_{34}^{p_T}$ and $\Delta\phi_{34}$ distributions, an additional comparison between SHERPA and AHJ is performed after re-weighting the SHERPA sample. A similar re-weighting procedure to the one described in Section 7.2.3, using eight-dimensional p_T - y distributions, is applied to the SHERPA sample. In this case, since the SHERPA sample contains only SPS events, it cannot be

7 Methodology validation

re-weighted based on distributions in data. Therefore, the reference distributions used to calculate the correction factors are taken from the SPS sample of AHJ after re-weighting the latter to data.

Normalized distributions of the $\Delta_{34}^{p_T}$ and $\Delta\phi_{34}$ variables in the re-weighted SHERPA sample are compared to the corresponding distributions in AHJ in Fig. 7.7. The same good agreement is observed between the distributions after the re-weighting. It can be seen that the change in the shapes of the distributions in the SHERPA sample as a result of the re-weighting is minimal. This serves as a confirmation that these distributions are not sensitive to a p_T - y based re-weighting of events.

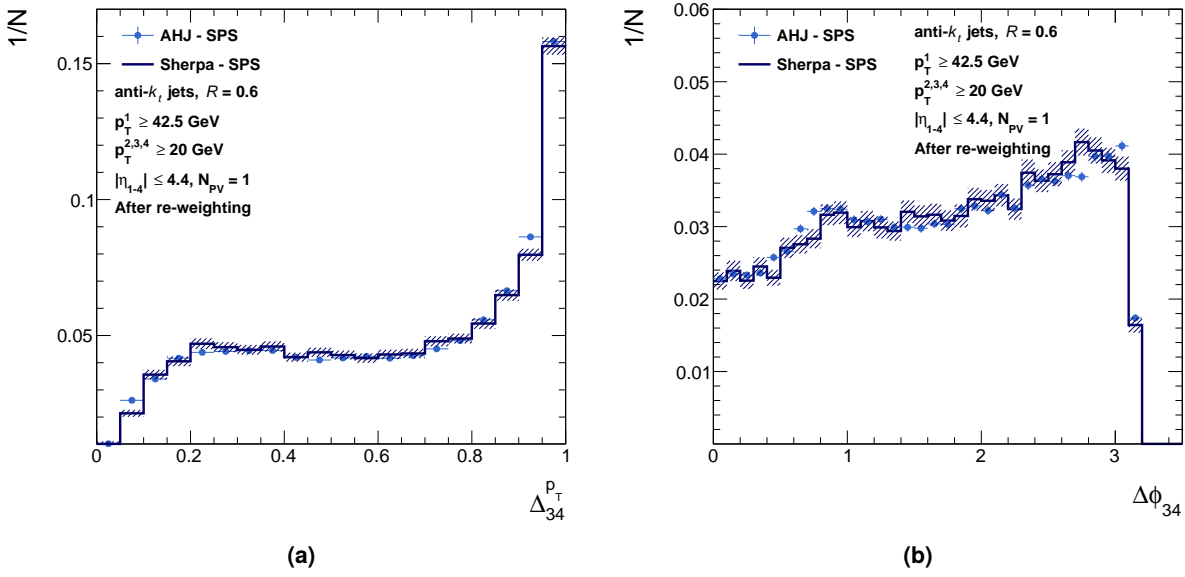


Figure 7.7: Normalized distributions of the variables (a) $\Delta_{34}^{p_T}$ and (b) $\Delta\phi_{34}$, defined in Eq. (6.27), in four-jet SPS events extracted from the AHJ sample (dots, light blue), selected in the phase space defined in the figure, and in SPS events generated with the SHERPA generator (dark blue histogram) after re-weighting.

The topology of SPS events in AHJ and SHERPA is tested further by comparing to that of SPS events extracted from data. Using the NN output, an almost pure sample ($\sim 99.7\%$) of SPS events may be selected from the data by applying the following cuts:

$$\frac{1}{\sqrt{3}}\xi_{sDPS} + \frac{2}{\sqrt{3}}\xi_{cDPS} \leq 0.2, \quad \xi_{sDPS} \leq 0.1. \quad (7.4)$$

These cuts are applied to events in data, AHJ and SHERPA and the resulting $\Delta_{34}^{p_T}$ and $\Delta\phi_{34}$ distributions are compared in Figs. 7.8(a) and (b). The distributions in the MC are normalized to the cross-section measured in the data. A good agreement is observed between all three distributions, indicating that the SPS topology is adequately modelled in the MC generators.

Additional comparisons of the distributions of the $\Delta_{34}^{p_T}$ and $\Delta\phi_{34}$ variables are shown in Fig. 7.8, selected in the ranges,

- $0.2 < \frac{1}{\sqrt{3}}\xi_{sDPS} + \frac{2}{\sqrt{3}}\xi_{cDPS} \leq 0.8$, $\xi_{sDPS} \leq 0.1$ in (c) and (d);

7.3 Double parton scattering fraction in AHJ

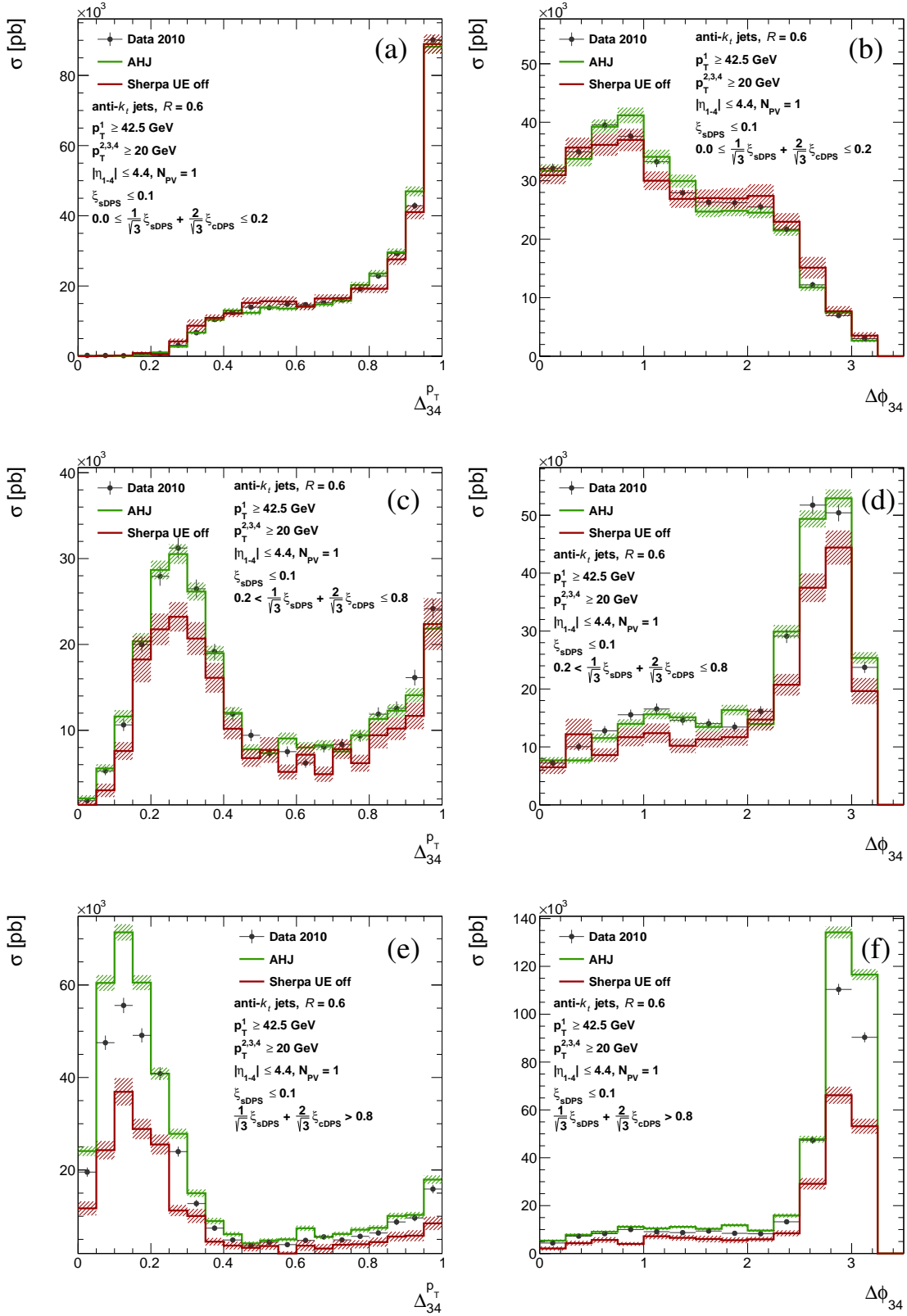


Figure 7.8: Distributions of the variables $\Delta_{34}^{p_T}$ ((a),(c) and(e)) and $\Delta\phi_{34}$ ((b), (d) and (f)), defined in Eq. (6.27), in four-jet events selected in the phase space defined in the figure, in data (dots), AHJ (green histogram) and SPS events generated with the SHERPA generator (burgundy histogram). The normalization factor of the distributions in MC is obtained from the ratio of the measured cross-sections in data and MC in the range defined in Eq. (7.4).

7 Methodology validation

- $\frac{1}{\sqrt{3}}\xi_{sDPS} + \frac{2}{\sqrt{3}}\xi_{cDPS} > 0.8$, $\xi_{sDPS} \leq 0.1$ in (e) and (f).

The normalization factor used for the distributions in MC in the range defined in Eq. (7.4) is used for the ranges defined above as well. A good agreement is observed between the data and AHJ in the distributions shown in Figs. 7.8(c) and (d), while SHERPA underestimates the effective number of events in data by about 20%, particularly in the regions where cDPS is expected to manifest itself ($\Delta_{34}^{PT} < 0.4$ and $\Delta\phi_{34} > 2.2$). In the range enriched with cDPS events ($\sim 25\%$), shown in Figs. 7.8(e) and (f), the distributions in data lie below the distributions in AHJ and above the distributions in SHERPA. The effective number of events in AHJ is 21% larger than in data in this range while in SHERPA it is smaller than in data by about 40%. The former is consistent with the observation that the fraction of DPS in AHJ is higher than in the data. The latter is expected since the SHERPA sample was generated with the module adding MPI turned off.

In conclusion, the excess of events with jets 3 and 4 at the back-to-back topology is traced back to an excess in DPS events in the AHJ sample compared to the data.

7.4 Validation of overlay method

The cDPS sample used in the determination of the fraction of cDPS events in data is constructed by overlaying two dijet events from data (see Section 6.7.4). In order to ascertain that the topology of cDPS events is reproducible by overlaying two dijet events, the dijet overlay sample is compared to the cDPS sample extracted from the AHJ MC. Distributions of the various input variables were studied. However, since the distributions are one or two-dimensional at most, they are incapable of representing the full four-jet event topology. Therefore, the most representative distribution of the event topology as a whole is the NN output distribution. As explained earlier, the NN is able to fold the N dimensions of the N input variables into two dimensions, while taking into account the correlations between the observables.

The NN is applied to the cDPS sample extracted from the AHJ MC and the output distribution is compared to the output distribution of the cDPS sample constructed from dijets in data. As before, the two-dimensional output distribution of the NN is divided into five one-dimensional distributions, making the comparison easier. Normalized distributions of the Dalitz plot in the range $0 \leq \xi_{sDPS} < 0.1$ are compared in Fig. 7.9(a). A good agreement is observed between the two distributions. In addition, a sharp peak is observed around $\frac{1}{\sqrt{3}}\xi_{sDPS} + \frac{2}{\sqrt{3}}\xi_{cDPS} = 1$, suggesting that most cDPS events are classified as such. About 64% of the cDPS events in the AHJ sample are assigned ξ_{sDPS} values in the range $0 \leq \xi_{sDPS} < 0.1$. Hence, this slice of the Dalitz plot is of the highest significance in classifying cDPS events and determining their fraction in an inclusive sample. A similar agreement is seen for the next slice of the triangle, $0.1 \leq \xi_{sDPS} < 0.3$, shown in Fig. 7.9(b), in which about 22% of the cDPS events in AHJ are classified.

The distributions of the remaining slices, $0.3 \leq \xi_{sDPS} < 0.5$, $0.5 \leq \xi_{sDPS} < 0.7$ and $0.7 \leq \xi_{sDPS} \leq 1.0$, are shown in Figs. 7.9(c), 7.9(d) and 7.9(e), respectively. A discrepancy between the distributions is seen in these slices. As the value of ξ_{sDPS} grows, the distributions of cDPS events from AHJ tend to have a larger contribution at lower values of $\frac{1}{\sqrt{3}}\xi_{sDPS} + \frac{2}{\sqrt{3}}\xi_{cDPS}$ compared to the distribution in the overlaid dijet events. Since a relatively small fraction ($\sim 14\%$) of the cDPS events are assigned values in the range $0.3 \leq \xi_{sDPS} \leq 1.0$, the effect of the discrepancy on the results of the fit is expected to be minimal (this is confirmed in Section 7.5). To demonstrate

the relative size of the discrepancy observed in the range $0.3 \leq \xi_{\text{sDPS}} \leq 1.0$, a projection of the full Dalitz plot on the horizontal axis is shown in Fig. 7.9(f). It can be seen that the discrepancy in the full distribution is of the order of 1%.

Based on these results, it is concluded that the topology of the overlaid dijet events is comparable to that of cDPS events extracted from AHJ. The advantage of using overlaid dijets from data to construct the cDPS sample is that the jets are at the same JES as the jets in four-jet events in data. This leads to a smaller systematic uncertainty. Moreover, a larger cDPS sample is obtained this way, leading to a smaller statistical uncertainty.

7.5 Validation of fit procedure

A final step of validation for the measurement methodology is of the fit procedure. The NN is applied to the inclusive AHJ sample and the resulting distribution is fitted with the NN output distributions of the SPS, cDPS and sDPS test samples. The fractions obtained from the fit, $f_{\text{cDPS}}^{(\text{MC})}$ and $f_{\text{sDPS}}^{(\text{MC})}$, are compared to the fractions at parton-level, $f_{\text{cDPS}}^{(\text{P})}$ and $f_{\text{sDPS}}^{(\text{P})}$, extracted in Section 7.1.

As explained in Section 6.11, a constrained fit is performed to the two-dimensional NN output distribution of the inclusive AHJ sample. Distributions of the three test samples, normalized to the measured four-jet cross-section, are the components used in the fit. The results are shown in five one-dimensional slices of the Dalitz plot in Fig. 7.10. In each slice, the distribution of four-jet events in AHJ is compared to a combination of the SPS, cDPS and sDPS fractional contributions, based on the results from the fit.

A comparison of the results obtained from the fit to the parton-level fractions is given below,

$$\begin{aligned} f_{\text{cDPS}}^{(\text{P})} &= 0.094 \pm 0.001 \text{ (stat.)}, & f_{\text{cDPS}}^{(\text{MC})} &= 0.094 \pm 0.003 \text{ (stat.)}, \\ f_{\text{sDPS}}^{(\text{P})} &= 0.048 \pm 0.001 \text{ (stat.)}, & f_{\text{sDPS}}^{(\text{MC})} &= 0.041 \pm 0.008 \text{ (stat.)}. \end{aligned} \tag{7.5}$$

A good agreement is observed, confirming the fit method to estimate the fractions and the overlay method to construct cDPS events. The larger statistical uncertainty on $f_{\text{cDPS}}^{(\text{MC})}$ and $f_{\text{sDPS}}^{(\text{MC})}$ compared to $f_{\text{cDPS}}^{(\text{P})}$ and $f_{\text{sDPS}}^{(\text{P})}$ reflect the loss of statistical power due to the use of a template fit to estimate the fractions and the fact that their uncertainties are fully correlated. The fit quality criteria, $\chi^2/\text{NDF} = 0.2$, indicates that the sum of the distributions is almost identical to the distribution of the four-jet AHJ sample. In the case of the SPS and sDPS test samples it is expected, since they were selected randomly from the full SPS and sDPS samples in AHJ. However, such an excellent result obtained with the cDPS sample constructed from overlaid dijet events from data confirms that the disagreement observed in the distributions in the range $0.3 \leq \xi_{\text{sDPS}} \leq 1.0$ (see Section 7.4) has a negligible effect on the fit. In conclusion, the comparison given in Eq. (7.5) indicates that the methodology is sound.

7 Methodology validation

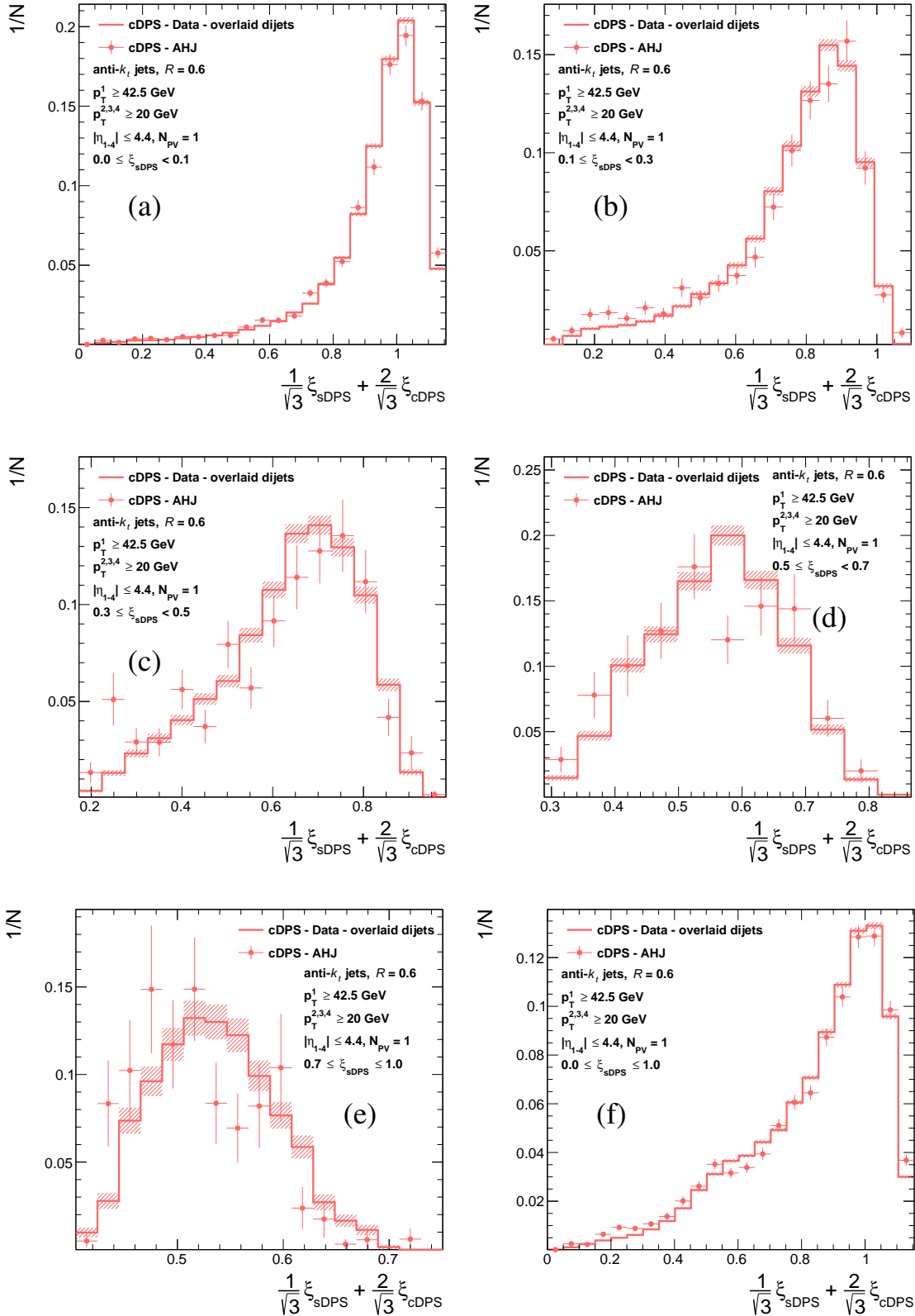


Figure 7.9: Normalized distributions of the NN outputs, $\frac{1}{\sqrt{3}} \xi_{\text{sDPS}} + \frac{2}{\sqrt{3}} \xi_{\text{cDPS}}$, in the ranges (a) $0.0 \leq \xi_{\text{sDPS}} < 0.1$, (b) $0.1 \leq \xi_{\text{sDPS}} < 0.3$, (c) $0.3 \leq \xi_{\text{sDPS}} < 0.5$, (d) $0.5 \leq \xi_{\text{sDPS}} < 0.7$, (e) $0.7 \leq \xi_{\text{sDPS}} \leq 1.0$ and (f) $0.0 \leq \xi_{\text{sDPS}} \leq 1.0$, in cDPS events extracted from AHJ (red dots), selected in the phase space defined in the figure, and in the cDPS sample constructed from dijet events in data (red histogram).

7.5 Validation of fit procedure

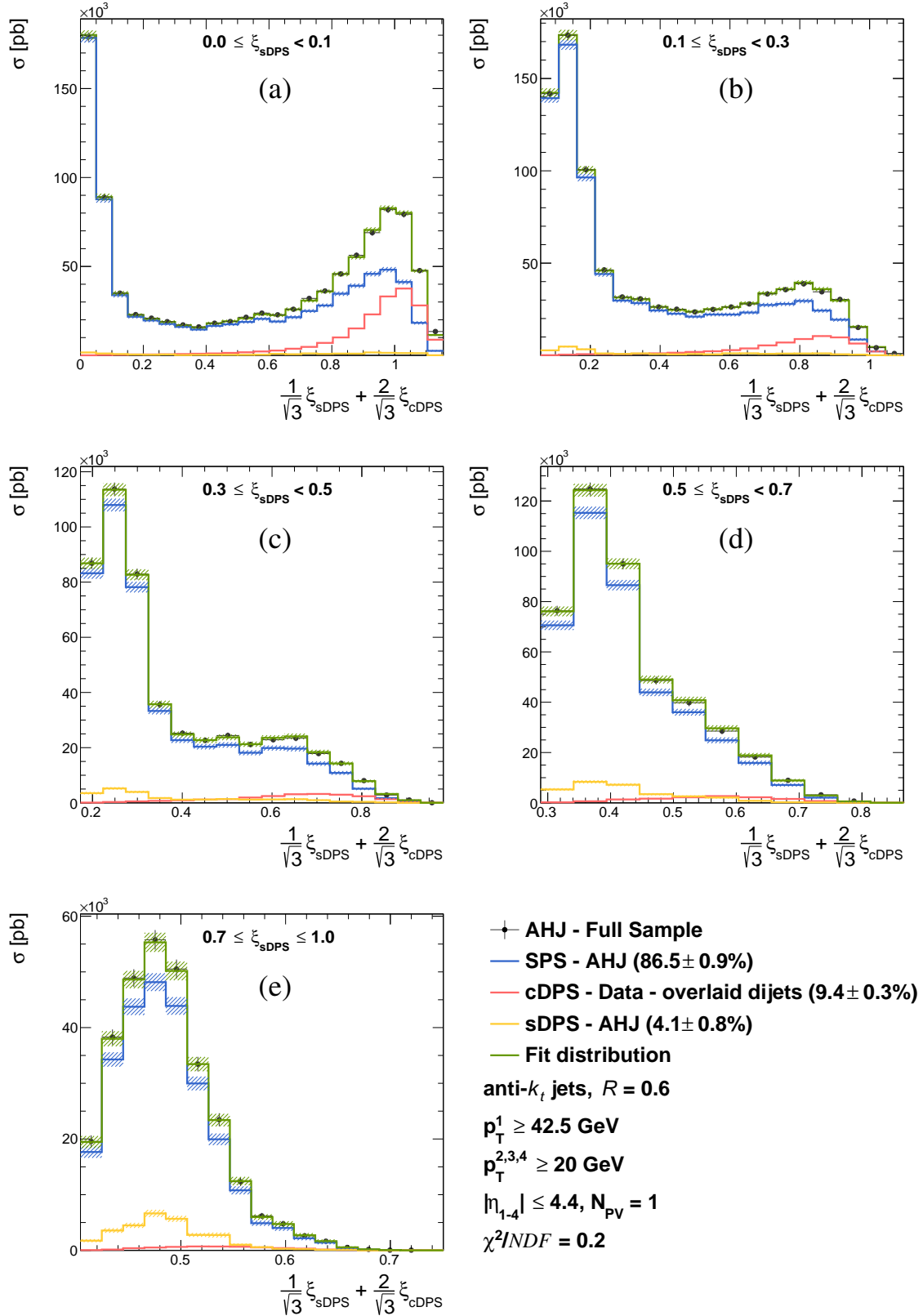


Figure 7.10: Distributions of the NN outputs, $\frac{1}{\sqrt{3}} \xi_{\text{sDPS}} + \frac{2}{\sqrt{3}} \xi_{\text{cDPS}}$, in the ξ_{sDPS} ranges indicated in the figures, for four-jet events in AHJ (dots), selected in the phase space defined in the legend, compared to the result of fitting a combination of the SPS (blue histogram), cDPS (red histogram) and sDPS (yellow histogram) contributions, the sum of which is shown as the green histogram. The fractions obtained and the quality criteria of the fit, χ^2/NDF , are indicated in the legend.

Uncertainties

The measurement of σ_{eff} is sensitive to various sources of uncertainty. Other than the statistical uncertainty, described below, uncertainties on the properties of the jets are taken into account and the uncertainty on the luminosity measurement is considered. The uncertainty on the properties of the jets is broken down into the JES uncertainty, mentioned in Section 3.8, and the jet energy and angular resolution. Apart from these uncertainties, various stability checks of the measurement are discussed in this section.

8.1 Statistical uncertainty

The statistical uncertainty on the four-jet data sample affects both the four-jet cross-section measurement and the fit process used to extract f_{DPS} in data. In addition, the dijet samples used to construct the cDPS input sample to the NN are the same samples used in the dijet cross-section measurements. Therefore, the statistical uncertainties on the double parton scattering fractions and on the measured cross-section are inherently correlated. Instead of calculating the correlation analytically, the combined uncertainty on σ_{eff} is estimated numerically by performing many pseudo-experiments.

The process of performing one pseudo-experiment is as follows. The value of each data point in the NN output Dalitz plot is smeared randomly within one standard deviation of the nominal value, where the standard deviation is derived from the respective statistical uncertainty. All the points in all four distributions, the four-jet data and the SPS, cDPS and sDPS distributions, are smeared simultaneously. The smeared distributions are then used to perform the fit and extract the “smeared” double parton scattering fractions, denoted as \tilde{f}_{cDPS} and \tilde{f}_{sDPS} . In addition, the “smeared” four-jet cross-section, $\tilde{\mathcal{S}}_{4j}$, is extracted from the smeared distribution in data. The measured dijet cross-sections are similarly treated, randomly varying each cross-section within one standard deviation as derived from the respective statistical uncertainty. The resulting “smeared” dijet cross-sections are denoted as $\tilde{\mathcal{S}}_{2j}$.

Rewriting Eq. (6.16) using the “smeared” values, one may define the quantity,

$$\tilde{\sigma}_{\text{eff}} = \left(1 - \frac{\gamma}{2}\right) \frac{\alpha_{2j}^{4j} \tilde{\mathcal{S}}_{2j}^A \tilde{\mathcal{S}}_{2j}^B}{\tilde{f}_{\text{cDPS}} + \tilde{f}_{\text{sDPS}} \tilde{\mathcal{S}}_{4j}}, \quad (8.1)$$

which represents the value of σ_{eff} , following the smearing procedure.

The pseudo-experiment described above is iterated many times, resulting in a distribution of values of $\tilde{\sigma}_{\text{eff}}$, shown in Fig. 8.1. The measured value of σ_{eff} is taken as the most probable value and the relative statistical uncertainty is obtained by finding the smallest interval $[\tilde{\sigma}_{\text{eff}}^{\text{up}}, \tilde{\sigma}_{\text{eff}}^{\text{down}}]$ containing 68% of the integral of the distribution [191],

$$\Delta\sigma_{\text{eff}} = {}_{-9.4}^{+12.2} \% \text{ (stat.)}.$$

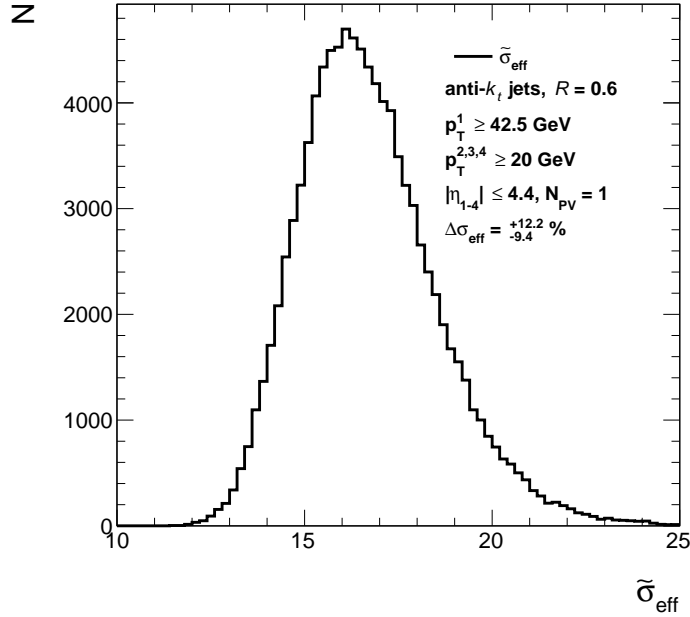


Figure 8.1: Distribution of $\tilde{\sigma}_{\text{eff}}$, defined in Eq. (8.1), representing the value of σ_{eff} obtained in each pseudo-experiment described in the text.

8.2 Systematic uncertainties

A systematic uncertainty of 3.5% due to the integrated luminosity measurement is added in quadrature to the uncertainty on σ_{eff} (see Section 3.3). As mentioned in Section 6.6.4, the statistical uncertainty on α_{2j}^{4j} (of $\sim 1\%$) is propagated as a systematic uncertainty and therefore added in quadrature to the uncertainty on σ_{eff} .

8.2.1 Uncertainty due to the re-weighting of AHJ

The systematic uncertainty associated with the re-weighting of AHJ is determined by performing many pseudo-experiments. The re-weighting of events in AHJ based on the kinematic properties of four-jet events in data (see Section 7.2.3) is performed using eight-dimensional p_T - y distributions. In one pseudo-experiment, each point in the latter distributions was smeared randomly within one standard deviation of the uncertainty of the corresponding bin. Subsequently, the re-weighting of events in AHJ was performed using the smeared distributions. The average relative change in the measured value of σ_{eff} due to the smeared weighting function is $\pm 5.9\%$, taken as a systematic uncertainty and added in quadrature to the uncertainty on σ_{eff} .

8.2.2 Uncertainty due to single-vertex events selection

To correct for events rejected due to the presence of additional pp collisions, a weight is given to each event based on μ (see Eq. (6.20)). The uncertainty associated with this correction is determined

8 Uncertainties

by increasing or decreasing the weight according to the systematic uncertainty on μ ($\pm 0.5\%$). The resulting systematic uncertainty on σ_{eff} is $\pm 0.1\%$.

8.2.3 Jet reconstruction efficiency uncertainty

The correction for the jet reconstruction efficiency is applied for each jet in an event (see [Section 3.7.1](#)). The uncertainty on the measured cross-section is then determined by increasing or decreasing the value of the correction applied according to the systematic uncertainty on the jet reconstruction efficiency. This results in the following fractional systematic uncertainties on the observed cross-sections:

$$\begin{aligned}\Delta S_{2j}^A &= {}^{+2.9}_{-3.1} \text{ (syst.) } \% , \\ \Delta S_{2j}^B &= {}^{+2.1}_{-2.2} \text{ (syst.) } \% , \\ \Delta S_{4j} &= {}^{+4.9}_{-5.3} \text{ (syst.) } \% .\end{aligned}\tag{8.2}$$

Propagated to the uncertainty on σ_{eff} , these cancel almost entirely,

$$\Delta\sigma_{\text{eff}} = \pm 0.1 \text{ (syst.) } \% .\tag{8.3}$$

This is well understood, considering that the cross-sections enter the calculation of σ_{eff} in the fraction

$$\sigma_{\text{eff}} \sim \frac{S_{2j}^A S_{2j}^B}{S_{4j}} .\tag{8.4}$$

Since the correction is applied for each jet separately, it is applied four times in the numerator (2×2) and four times in the denominator. The magnitude of the correction is similar since the p_T and y cuts applied to the jets in the two classes of dijet events were selected such that they correspond to the cuts in four-jet events. The systematic uncertainty quoted in [Eq. \(8.3\)](#) is added in quadrature to the uncertainty on σ_{eff} .

8.2.4 Uncertainty on the jet energy scale

Six sources of uncertainty on the JES, described in [Section 3.8](#), are considered; generator event modelling (AlpGen+Herwig+Jimmy), cluster thresholds, intercalibration, soft physics modelling (Perugia 2010), relative non-closure and single hadron response. The effects of the different components on the determination of the fraction of double parton scattering in data and on the calculation of the acceptances are determined by introducing positive and negative variations to the energy scale of jets in the MC.

For each JES uncertainty component, a variation of one standard deviation of the JES uncertainty for this component is introduced to the energy scale of the jets in the PYTHIA sample used to calculate the acceptance. As the JES uncertainty is dependent on the p_T and y of the jet, so is the variation. After the energy of jets is varied, they are re-sorted according to their p_T , and the event is either rejected or accepted. Accepted events are then re-classified as dijet events (of type A or B) and as four-jet events. The acceptances and their ratio, α_{2j}^{4j} , are subsequently calculated, as described in [Section 6.6](#).

The process of varying the energy scale of the jets is performed simultaneously in the AHJ sample used to extract the SPS and sDPS samples. Event selection is applied on the AHJ events after the variation and the re-weighting procedure described in [Section 7.2.3](#), using eight-dimensional p_T - y distributions, is performed. The latter is done in order to maintain an agreement with the data in the kinematic properties of four-jet events after varying the JES. Events are subsequently classified as either SPS or sDPS events. For each JES component, modified NN output distributions are obtained and used to extract f_{cDPS} and f_{sDPS} in data.

Since the cDPS sample is constructed from dijet events in data, no variation is applied to the energy scale of the jets in the cDPS sample used to extract f_{cDPS} and f_{sDPS} . This is considered one of the main advantages of using the data to construct the cDPS sample. The JES of jets in the data samples used in the cross-section measurements are not varied either.

Normalized distributions of five one-dimensional slices of the Dalitz plot for the SPS samples, extracted from AHJ after introducing positive and negative variations, are shown in [Figs. 8.2](#) and [8.3](#), respectively. The distributions obtained using the nominal JES are shown for comparison. The positive (negative) variation is denoted as “up” (“down”) in the figures. The differences observed between the distributions after varying the JES up or down are within 5% in most bins.

The values of the acceptance ratio and double parton scattering fractions obtained after each variation are used to calculate σ_{eff} for every component of the JES uncertainty. For all JES uncertainty components, the deviation from the nominal value of the sum $f_{\text{cDPS}} + f_{\text{sDPS}}$ is canceled somewhat in the ratio by the deviation of α_{2j}^{4j} from the nominal value. The contributions to the uncertainty on σ_{eff} from the different sources are considered uncorrelated, and so the total uncertainty is computed as the quadratic sum of all the components. The relative systematic uncertainties on σ_{eff} due to the different sources of uncertainty on the JES are listed in [Table 8.1](#). The JES uncertainty on σ_{eff} comes out asymmetric and amounts to $^{+35}_{-39}\%$.

JES source of uncertainty	$\Delta\sigma_{\text{eff}}$ [%]
Generator event modelling	+14 / -17
Cluster thresholds	+10 / -19
Intercalibration	+15 / -17
Soft physics modelling	+20 / -17
Relative non-closure	+7 / -14
Single hadron response	+16 / -12
Total relative JES systematic uncertainty	+35 / -39

Table 8.1: Summary of the relative systematic uncertainties on σ_{eff} due to the different sources of uncertainty on the jet energy scale. The total uncertainty is calculated as the quadratic sum of all components. The individual components of the uncertainty are described in [Section 3.8](#).

8 Uncertainties

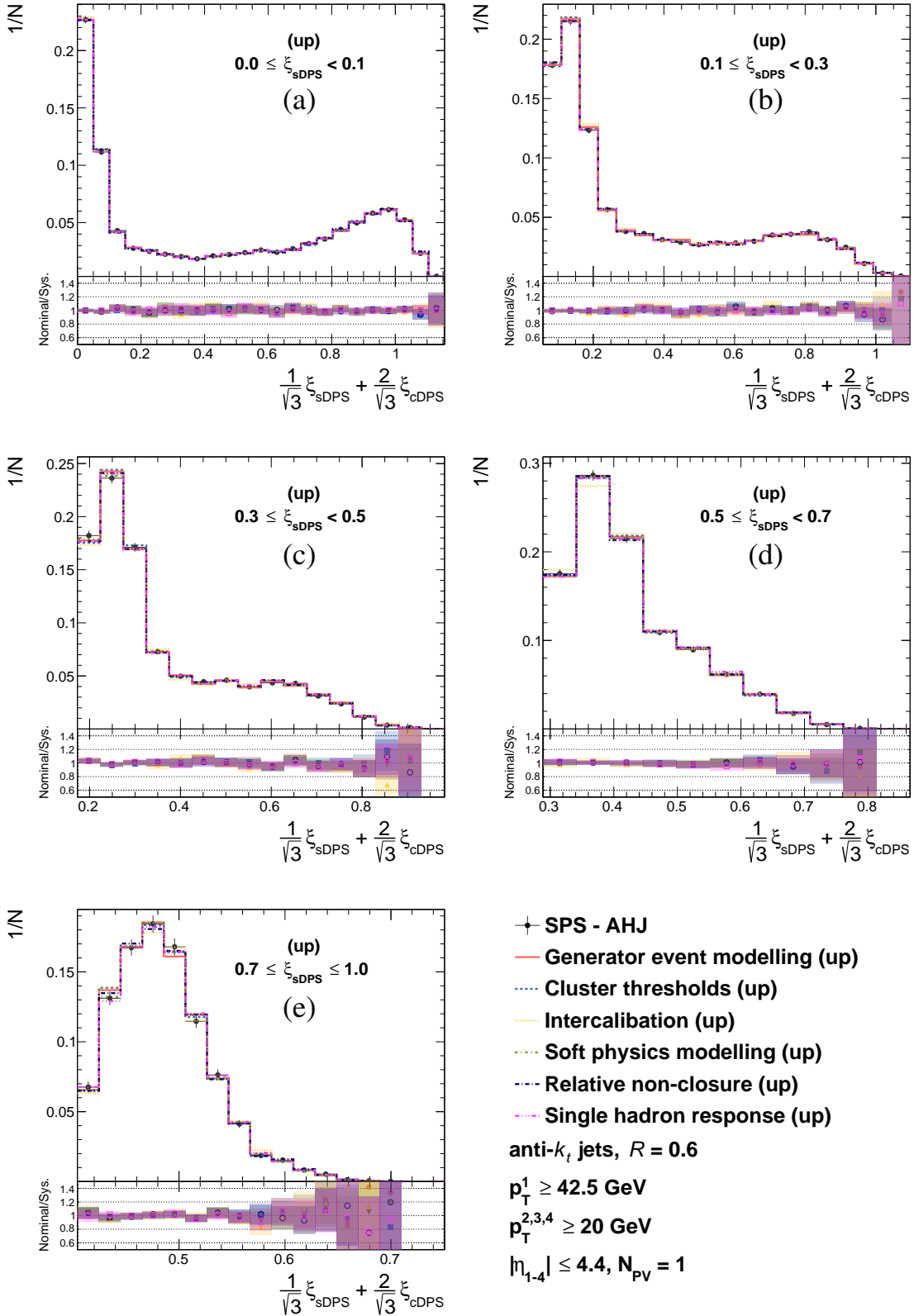


Figure 8.2: Normalized distributions of the NN outputs, $\frac{1}{\sqrt{3}} \xi_{\text{sDPS}} + \frac{2}{\sqrt{3}} \xi_{\text{cDPS}}$, in the ξ_{sDPS} ranges indicated in the figures, for SPS events extracted from the AHJ sample, selected in the phase space defined in the legend, using the nominal JES and after introducing a positive (up) variation to the energy scale of the jets, as indicated in the legend. The ratio between the nominal and modified JES distributions is shown in the bottom panels, where statistical uncertainties are shown as the shaded areas.

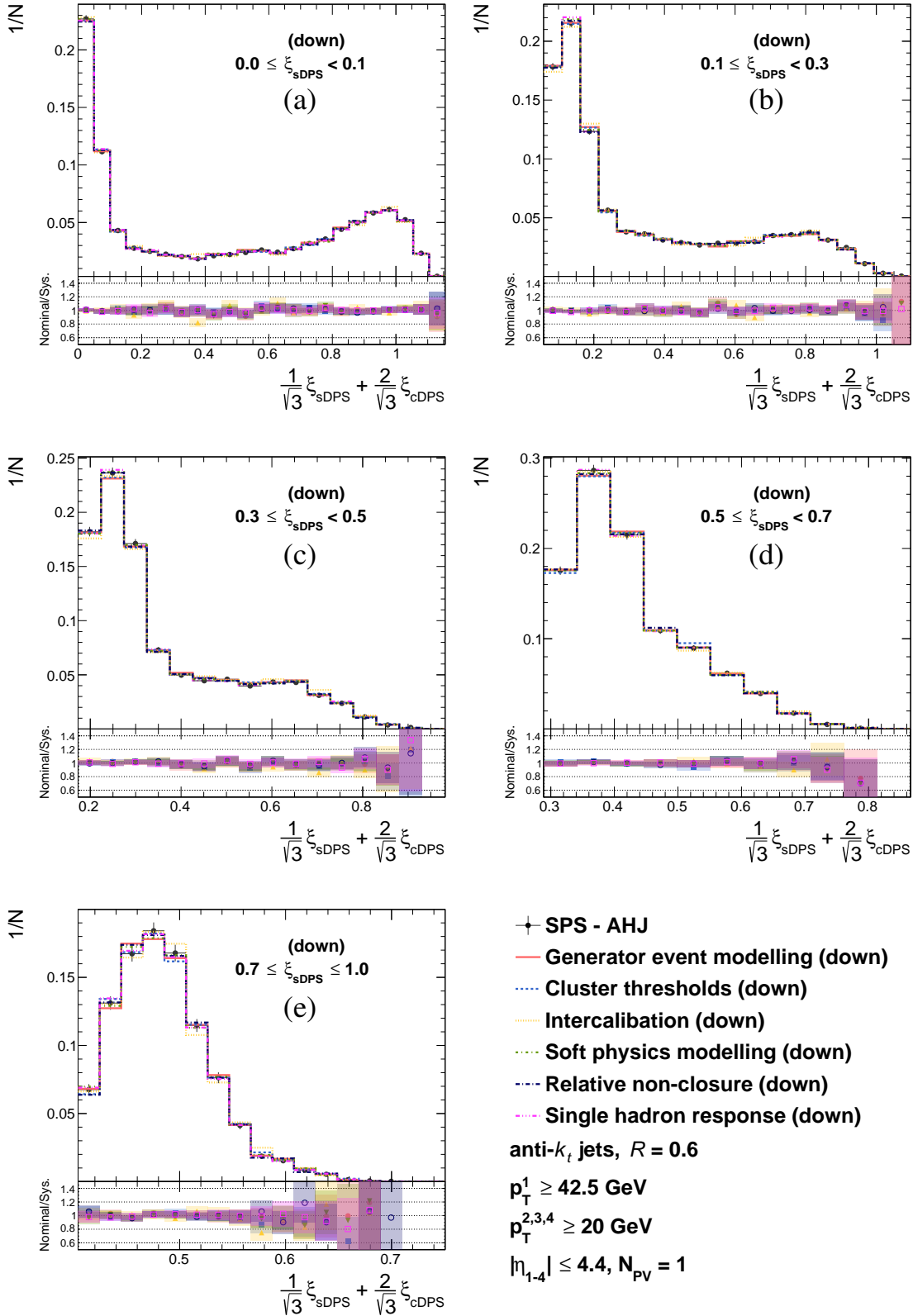


Figure 8.3: Normalized distributions of the NN outputs, $\frac{1}{\sqrt{3}}\xi_{\text{sDPS}} + \frac{2}{\sqrt{3}}\xi_{\text{cDPS}}$, in the ξ_{sDPS} ranges indicated in the figures, for SPS events extracted from the AHJ sample, selected in the phase space defined in the legend, using the nominal JES and after introducing a negative (down) variation to the energy scale of the jets, as indicated in the legend. The ratio between the nominal and modified JES distributions is shown in the bottom panels, where statistical uncertainties are shown as the shaded areas.

8.2.5 Jet energy and angular resolution uncertainty

The jet energy resolution (JER) is measured both using in-situ methods and by comparing to particle jets in the MC (closure test) [192]. Systematic uncertainties associated with the measured resolution are mostly dominated by data/MC disagreement when using in-situ methods and by the difference between results obtained with the closure test and with in-situ methods. The jet angular resolution is measured in MC using a derivative of the closure test, where the y and ϕ of calorimeter jets are compared to those of the corresponding particle jets. Systematic uncertainties on the angular resolution are estimated by varying the parameters used in the closure test.

In order to assess the effect of the jet energy and angular resolution uncertainties on the measurement of σ_{eff} , jets in the MC samples, PYTHIA and AHJ, are smeared according to the measured resolution uncertainties. To evaluate the JER systematic uncertainty, the energy of each jet is scaled by a random factor derived from the energy resolution uncertainty, based on its p_T and y . The random factor is pulled from a Gaussian distribution with a standard deviation set by the uncertainty. A similar approach is taken to estimate the jet angular resolution uncertainty, where jets are rotated in the rapidity and azimuthal planes based on a random smearing factor derived from the respective angular resolution uncertainty.

Similar to the process of evaluating the JES systematic uncertainties, for each source of resolution uncertainty, jets are smeared simultaneously in the PYTHIA and AHJ samples. Events selection is applied after the smearing and events in the AHJ sample are re-weighted based on the kinematic properties of four-jet events, as described in Section 7.2.3. For each source of resolution uncertainty, modified NN output distributions for SPS and sDPS events are used to extract f_{cDPS} and f_{sDPS} in data.

Normalized distributions of five one-dimensional slices of the Dalitz plot for the SPS samples, extracted from AHJ after smearing the jets, are shown in Fig. 8.4. The distributions obtained without smearing the jets are shown for comparison. An agreement within 5% is observed between the nominal distributions and the distributions obtained by smearing y or ϕ of the jets. A larger deviation of up to 10% is seen in the distributions due to the smearing of the energy of jets.

The relative systematic uncertainties on σ_{eff} are evaluated for the JER uncertainty and the jet angular uncertainties by extracting f_{cDPS} and f_{sDPS} using the modified distributions and calculating α_{2j}^{4j} using smeared jets. A summary of the corresponding uncertainties is listed in Table 8.2.

Source of uncertainty	$\Delta\sigma_{\text{eff}}$ [%]
Jet rapidity resolution	± 3
Jet azimuthal angle resolution	± 1
Jet energy resolution	± 12

Table 8.2: Summary of the relative systematic uncertainties on σ_{eff} due to the different sources of jet energy and angular resolution uncertainties.

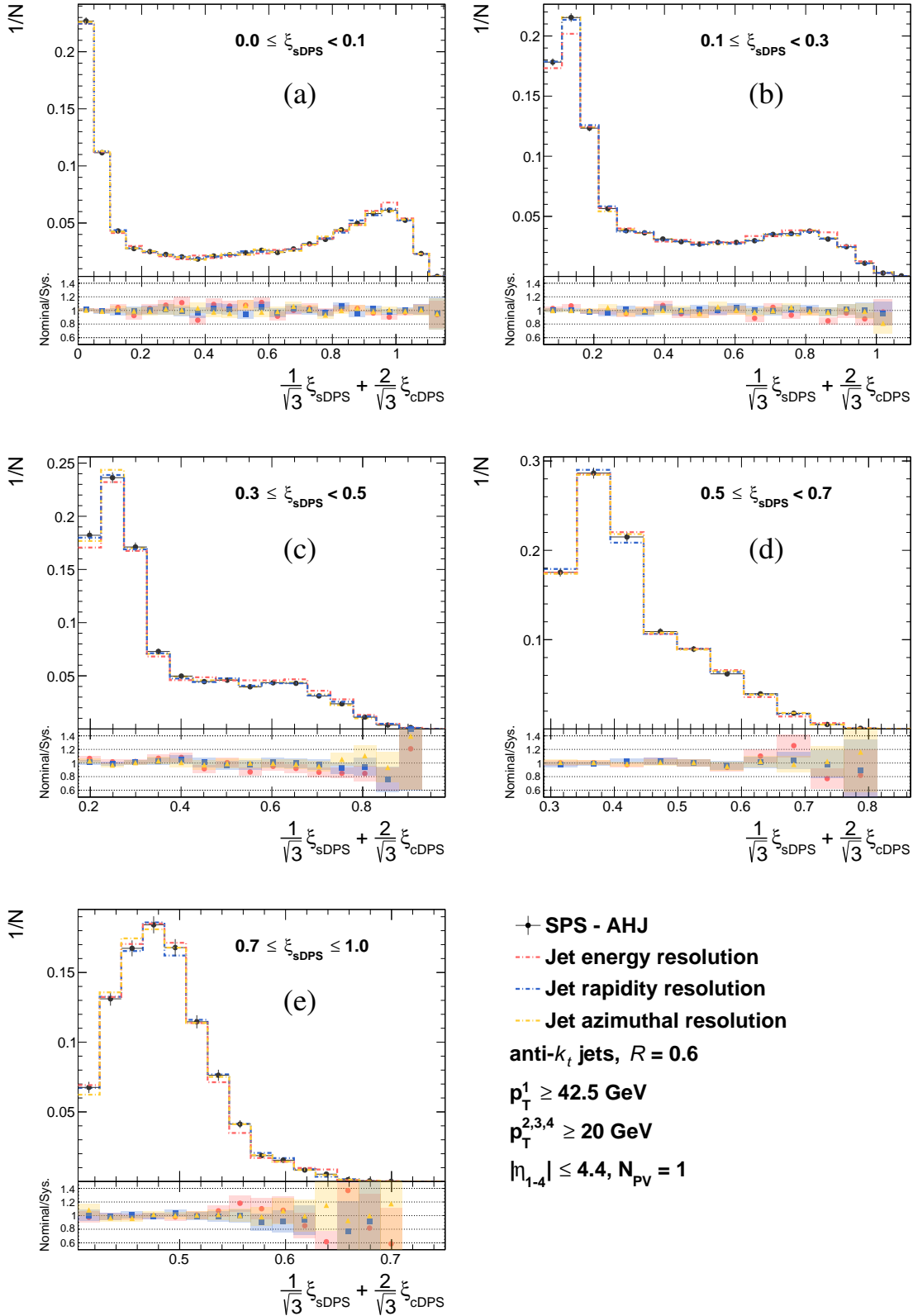


Figure 8.4: Normalized distributions of the NN outputs, $\frac{1}{\sqrt{3}}\xi_{\text{sDPS}} + \frac{2}{\sqrt{3}}\xi_{\text{cDPS}}$, in the ξ_{sDPS} ranges indicated in the figures, for SPS events extracted from the AHJ sample, selected in the phase space defined in the legend, using the nominal jets and after smearing the energy, rapidity or azimuthal angle of the jets, as indicated in the legend. The ratio between the nominal and smeared distributions is shown in the bottom panels, where statistical uncertainties are shown as the shaded areas.

8.3 Stability checks

The stability of the measured value of σ_{eff} with respect to the various parameter values used in the measurement was studied. Parameters such as p_T^{parton} and $\Delta R_{\text{jet-jet}}$ were varied and the requirement $\Delta R_{\text{parton-jet}} \leq 0.6$ was applied, leading to a relative change in σ_{eff} of the order of a few percent. A full study of the effects of these parameter values is not possible, as it would require repeating the measurement using a different set of observables, e.g., anti- k_t jets with a distance parameter of 0.4 or generating a new AHJ sample with a different matching scale. However, since the observed relative changes lie within the quoted statistical uncertainty on σ_{eff} , no systematic uncertainty is assigned due to these parameters.

Results

9.1 Determination of σ_{eff}

The results of the fit to the NN output distribution in four-jet events in data are shown in Fig. 9.1. The fractions of the cDPS and sDPS samples, as obtained by the fit, are

$$f_{\text{cDPS}} = 0.052 \pm 0.003 \text{ (stat.)}, \quad f_{\text{sDPS}} = 0.035 \pm 0.008 \text{ (stat.)}, \quad (9.1)$$

where the goodness-of-fit, χ^2 , divided by the number of degrees of freedom of the fit (NDF) yielded

$$\chi^2/\text{NDF} = 2.1.$$

A comparison of the fit distributions with the distributions in data in five one-dimensional slices of the Dalitz plot is shown in Fig. 9.1. The statistical uncertainty in each bin in the fit distribution is shown as the dark shaded area while the light shaded area represents their sum in quadrature with the systematic uncertainties. The distributions of the SPS, cDPS and sDPS contributions are also shown, normalized to their respective fraction in the data as obtained by the fit. The biggest disagreement with the data is seen for the left-most bin in the range $0.0 \leq \xi_{\text{sDPS}} < 0.1$ (Fig. 9.1(a)) and the three left-most bins in the range $0.1 \leq \xi_{\text{sDPS}} < 0.3$ (Fig. 9.1(b)) of the Dalitz plot. These bins contribute about 50% of the value of the χ^2 and are dominated by the SPS contribution and have negligible contribution from double parton scattering events. Thus, a discrepancy between the data and the fit result in these bins points to a mis-modelling in the MC of pQCD. It is expected to have a negligible effect on the measurement of the double parton scattering rate.

The quality of fit, $\chi^2/\text{NDF} = 2.1$, may indicate that the statistical uncertainties evaluated in the fit are underestimated. Therefore, in order to check whether this is the case, the distributions for f_{cDPS} and f_{sDPS} obtained when performing many pseudo-experiments (fits) were used (see Section 8.1). The most probable values for the fractions f_{cDPS} and f_{sDPS} as obtained from the \tilde{f}_{cDPS} and \tilde{f}_{sDPS} distributions are

$$f_{\text{cDPS}} = 0.052^{+0.002}_{-0.005} \text{ (stat.)}, \quad f_{\text{sDPS}} = 0.032^{+0.008}_{-0.01} \text{ (stat.)}, \quad (9.2)$$

where the uncertainties reflect the smallest interval containing 68% of the integral of the distribution. The fraction values and their statistical uncertainties obtained from the two approaches (Eqs. (9.1) and (9.2)) are in agreement.

Taking into account the systematic uncertainties for the calculation of χ^2 (without re-doing the fit), the value of χ^2 improves to

$$\chi^2/\text{NDF} = 0.7.$$

This value of χ^2/NDF suggests that the sum of the SPS, cDPS and sDPS contributions provides a good description of the data.

The distributions of the input variables in data are compared to a combination of the distributions in the three samples, SPS, cDPS and sDPS. The latter three distributions are normalized to their respective fraction in the data as obtained by the fit. The comparison is shown in Fig. 9.2 for the $\Delta_{34}^{p_T}$

9 Results

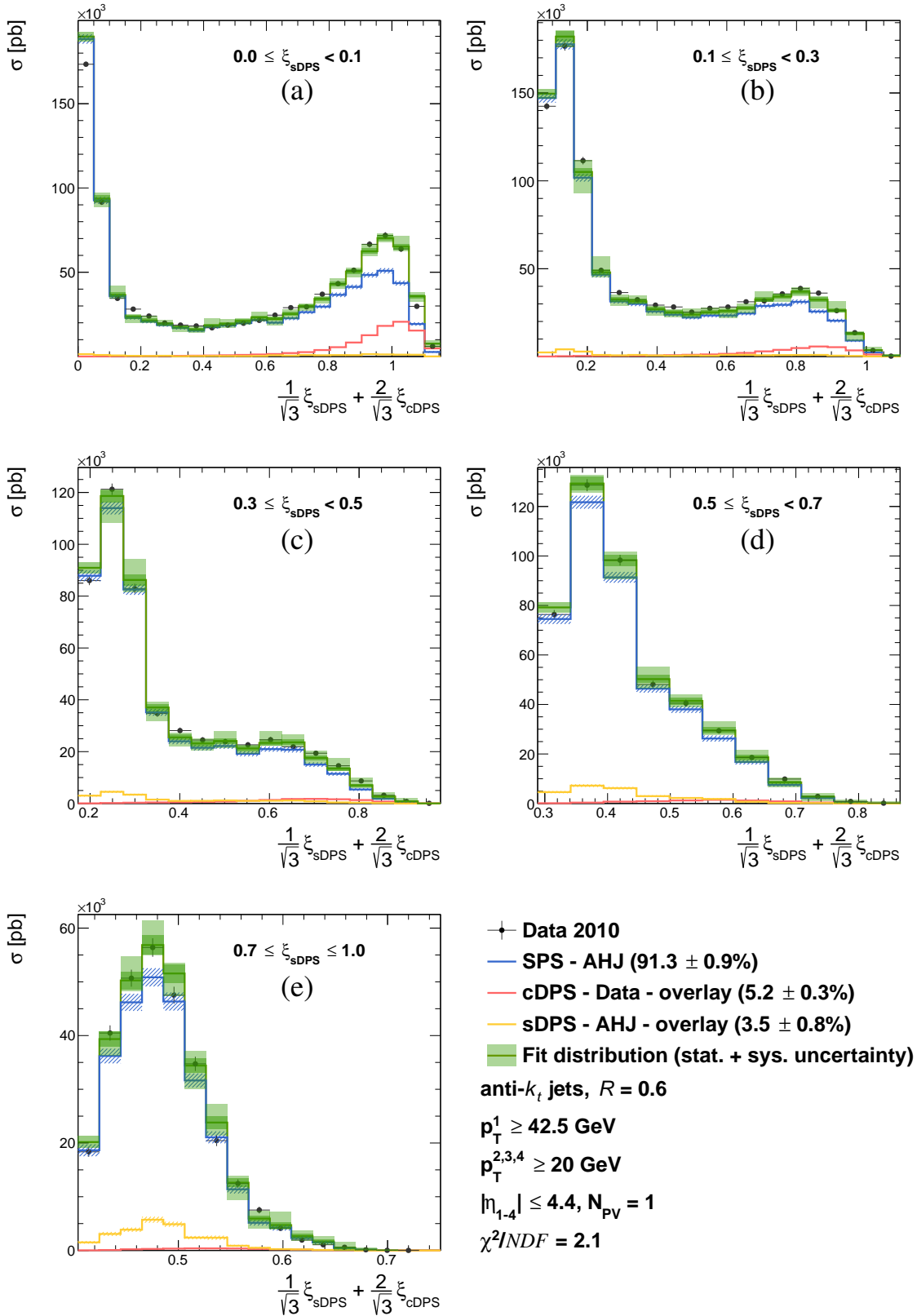


Figure 9.1: Distributions of the NN outputs, $\frac{1}{\sqrt{3}} \xi_{\text{sDPS}} + \frac{2}{\sqrt{3}} \xi_{\text{cDPS}}$, in the ξ_{sDPS} ranges indicated in the figures, for four-jet events in data (dots), selected in the phase space defined in the legend, compared to the result of fitting a combination of the SPS (blue histogram), cDPS (red histogram) and sDPS (yellow histogram) contributions, the sum of which is shown as the green histogram with statistical and systematic uncertainties added in quadrature. The fractions obtained and the quality criteria of the fit, χ^2/NDF , are indicated in the legend.

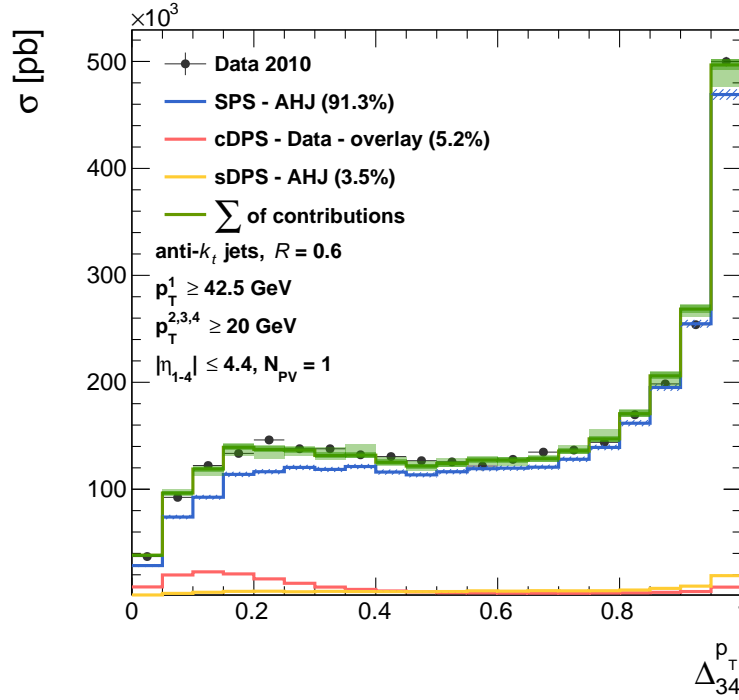


Figure 9.2: Comparison of the distribution of the variable $\Delta_{34}^{p_T}$, defined in Eq. (6.27), in four-jet events in data (dots), selected in the phase space defined in the figure, with the sum (green histogram) of the SPS (blue histogram), cDPS (red histogram) and sDPS (yellow histogram) contributions. The sum of the contributions is normalized to the cross-section measured in data and the various contributions are normalized to their respective fractions obtained from the fit, as indicated in the legend. The statistical uncertainty in each bin in the sum of contributions distribution is shown as the dark shaded area while the light shaded area represents their sum in quadrature with the systematic uncertainties.

variable and in Appendix A.2 for all other variables. A good description of the data in most regions of phase-space is achieved.

Once the fraction of double parton scattering in four-jet events in the data is estimated, the measurements of the dijet and four-jet cross-sections are used to calculate the effective overlap area between the interacting protons, σ_{eff} . For completeness, the measured cross-section values and the estimated acceptances ratio are repeated here,

$$\begin{aligned}
 S_{2j}^A &= 1.9534 \cdot 10^8 \pm 4.9 \cdot 10^5 \text{ (stat.) } {}^{+5.73}_{-6.01} \cdot 10^6 \text{ (syst.) pb,} \\
 S_{2j}^B &= 2.6206 \cdot 10^7 \pm 3.4 \cdot 10^4 \text{ (stat.) } {}^{+5.64}_{-5.84} \cdot 10^5 \text{ (syst.) pb,} \\
 S_{4j} &= 3.109 \cdot 10^6 \pm 1.1 \cdot 10^4 \text{ (stat.) } {}^{+1.53}_{-1.64} \cdot 10^5 \text{ (syst.) pb,} \\
 \alpha_{2j}^{4j} &= 0.94 \pm 0.01 \text{ (stat.) } {}^{+0.15}_{-0.14} \text{ (syst.) .}
 \end{aligned} \tag{9.3}$$

The statistical uncertainty on α_{2j}^{4j} is taken as a systematic uncertainty. The systematic uncertainties on the observed cross-sections and the acceptance ratio are partially canceled when propagated to

9 Results

σ_{eff} . The combination of these values together with the measured fractions given in Eq. (9.2) yields

$$\sigma_{\text{eff}} = 16.1^{+2.0}_{-1.5} \text{ (stat.) }^{+6.1}_{-6.8} \text{ (syst.) mb.} \quad (9.4)$$

This value is consistent within the quoted uncertainties with previous measurements at center-of-mass energies above 1 TeV, performed in ATLAS and in other experiments [71–75, 77, 78], some of which are summarized in Fig. 9.3.

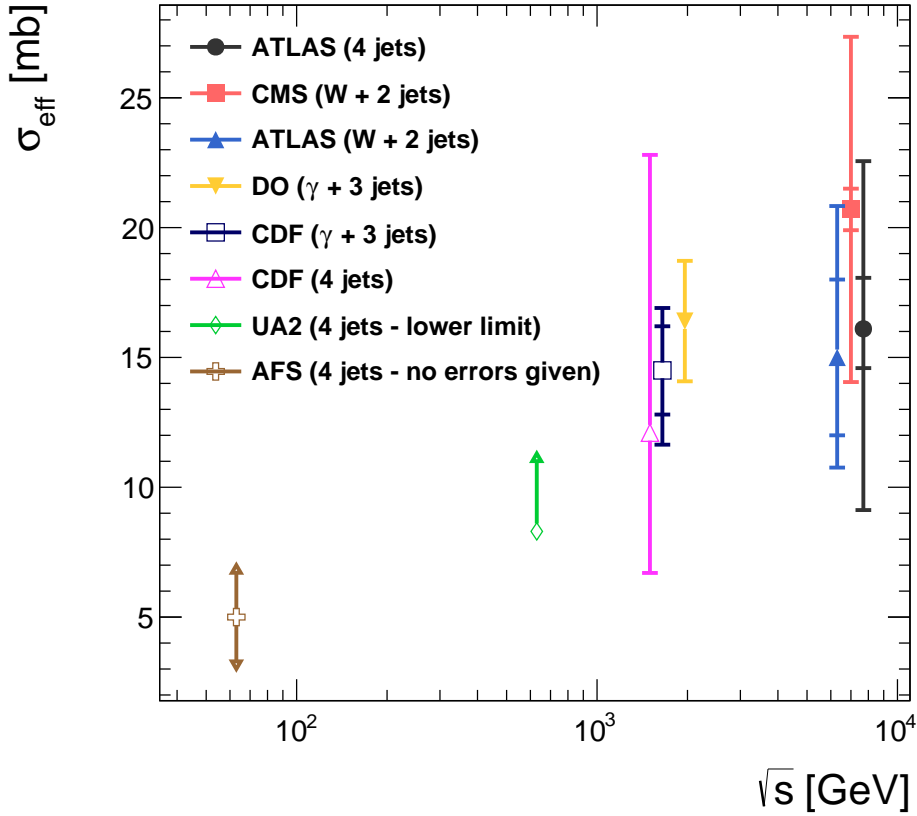


Figure 9.3: Dependence of the effective overlap area between the interacting protons, σ_{eff} , on center-of-mass energy, \sqrt{s} , in different processes and different experiments [71–75, 77, 78]. The inner error bars (where visible) correspond to the statistical uncertainties and the outer error bars represent their sum in quadrature with the systematic uncertainties. Arrows indicate the limited information on the quality of the measurement as stated in the legend. Measurements at identical \sqrt{s} are slightly shifted in center-of-mass energy for clarity.

Within the large uncertainties, the measurements are consistent with no \sqrt{s} dependence of σ_{eff} . The σ_{eff} value obtained is about a quarter of the measured value of σ_{inel} at $\sqrt{s} = 7$ TeV [131, 132]. An estimate for the fraction of the proton longitudinal momentum carried by the massless parton participating in the interaction, x , may be obtained from the jet kinematics (see Section 9.2.1). The typical value of x in the phase-space defined in this measurement is $x \sim 10^{-2}$, a region of the PDF dominated by the gluon (see Fig. 2.8). However, the measured value of σ_{eff} is a factor two less than what would be expected from the gluon form factor of the proton [133].

9.2 Characteristics of DPS events

A sample with a high fraction of DPS events, a DPS enriched sample (eDPS), may be selected from the data using the NN output,

$$\frac{1}{\sqrt{3}}\xi_{\text{sDPS}} + \frac{2}{\sqrt{3}}\xi_{\text{cDPS}} \geq 0.95, \quad \xi_{\text{sDPS}} \leq 0.1. \quad (9.5)$$

This cut provides a sample composed of $\sim 34\%$ DPS events, estimated from the two-dimensional fit. Similarly, a sample composed almost entirely of SPS events (99.7%), referred to in the following as an eSPS sample, may be selected with the following cut on the NN output:

$$\frac{1}{\sqrt{3}}\xi_{\text{sDPS}} + \frac{2}{\sqrt{3}}\xi_{\text{cDPS}} \leq 0.2, \quad \xi_{\text{sDPS}} \leq 0.1. \quad (9.6)$$

The cut $\xi_{\text{sDPS}} \leq 0.1$ renders the contribution of sDPS events in the eDPS and eSPS samples negligible. The characteristics of DPS events in data may then be compared to those of SPS events.

9.2.1 Parton kinematics

Under the assumption that the jets are massless, the estimate for x , x^{obs} , for a N-jet final state is obtained from

$$x_{\pm}^{\text{obs}} = \frac{1}{\sqrt{s}} \sum_i^N p_{T,i} e^{\pm y_i}, \quad (9.7)$$

where x_{\pm}^{obs} refers to the x^{obs} values of the parton x coming from the positive or negative z direction. The terms $p_{T,i}$ and y_i correspond to the p_T and y of the i^{th} jet. In the following, only x_+^{obs} distributions are shown (referred to as x^{obs}), since the distributions of x_+^{obs} and x_-^{obs} are expected to be identical for a fully symmetric detector.

Two x^{obs} values are calculated for each candidate DPS event, $x_{1,2}^{\text{obs}}$, corresponding to the two dijet pairs in the event. Up to this point, it was not necessary to pair the four jets in the event since the input to the NN included all possible pairings. However, it is required for the calculation of $x_{1,2}^{\text{obs}}$. One method for pairing the jets is based on p_T values such that x_1^{obs} corresponds to the leading two jets (1 and 2) and x_2^{obs} corresponds to jets 3 and 4. In DPS events extracted from AHJ it was found that this method leads to the right pairing in 85% of the events. Another method exploits the expected pair-wise p_T balance between the dijet pairs in DPS events [73]. The assignment of pairs of jets is performed by minimizing the quantity

$$S = \Delta_{ij}^{p_T} + \Delta_{kl}^{p_T}, \quad (9.8)$$

where all three possible pair combinations are considered $\{\langle i, j \rangle \langle k, l \rangle\}$ (see Section 6.8.2). This pairing was found to be correct in 92% of the DPS events extracted from AHJ. Therefore, in the following, the latter method is employed and x_1^{obs} corresponds to the primary interaction (associated with the leading jet) and x_2^{obs} corresponds to the secondary one.

The x_1^{obs} and x_2^{obs} distributions in the eDPS sample in data are compared in Fig. 9.4(a). As expected, the x_2^{obs} distribution of the secondary interaction is shifted towards lower x^{obs} values with respect to

9 Results

the x_1^{obs} distribution. The distribution of x_2^{obs} as a function of x_1^{obs} is shown in Fig. 9.4(b), where the number of events in each bin is proportional to the area of the box drawn. The dashed red line in Fig. 9.4(b) marks the case where $x_2^{\text{obs}} = x_1^{\text{obs}}$ and is drawn for visualization purposes. Two peaks are observed in the distribution, one below the red line for cases in which $x_1^{\text{obs}} > x_2^{\text{obs}}$ and one above the line ($x_1^{\text{obs}} < x_2^{\text{obs}}$). The former is more prominent, however events in which x_1^{obs} , associated with the leading jet, is smaller than x_2^{obs} are not rare. These are events in which the second pair of jets happens to be at higher y than the leading one. Within the two event types, no evident correlation between x_1^{obs} and x_2^{obs} is observed and the correlation coefficient is determined to be $r_{x_1^{\text{obs}} x_2^{\text{obs}}} = -0.07$.

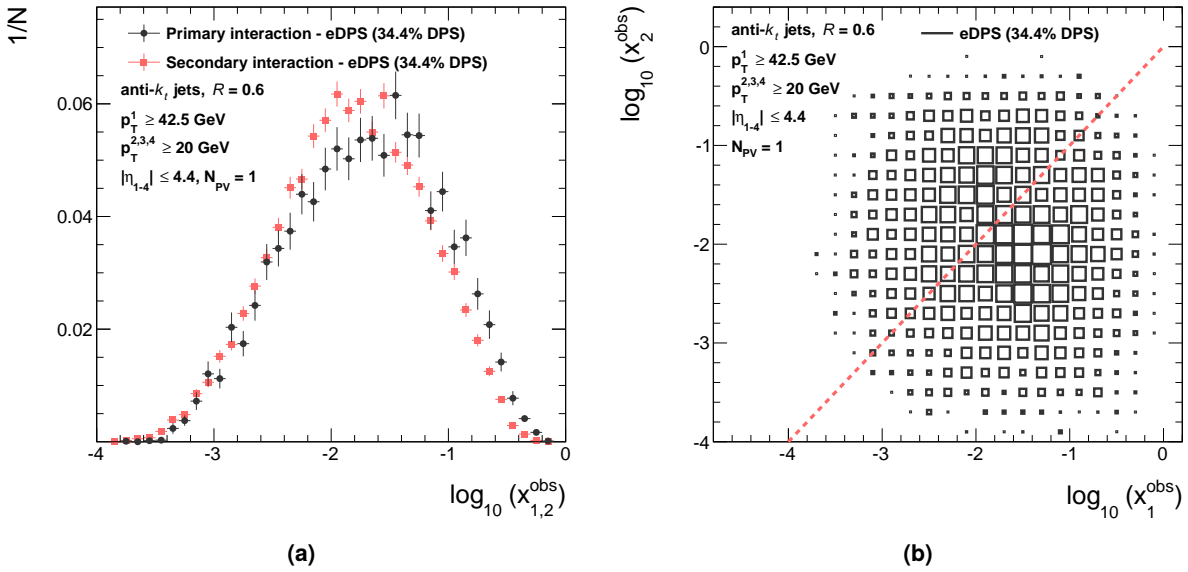


Figure 9.4: (a) Normalized distributions of the estimated fraction of the proton longitudinal momentum carried by the massless parton participating in the primary interaction, x_1^{obs} , and the secondary interaction, x_2^{obs} , in the eDPS sample selected using the cuts defined in Eq. (9.5), extracted from four-jet events in data selected in the phase-space defined in the figure. (b) Distribution of x_2^{obs} as a function of x_1^{obs} for the same sample. The estimate for $x_{1,2}^{\text{obs}}$ is obtained using Eq. (9.7).

Figure 9.5(a) shows a comparison of the x^{obs} distributions in the eDPS and eSPS samples extracted from data, obtained by summing over the four jets. For SPS events, x^{obs} is the estimate of x for the only hard scattering in the event, while for DPS events, it is the sum of the x values of the two hard interactions. A small shift towards lower x^{obs} values in the eDPS sample is observed. This may indicate that DPS events occur at lower x values, as expected.

In the following comparisons between data and AHJ, the original AHJ distributions are used (before any re-weighting, see Section 7.2.3). A comparison between the x^{obs} distributions in all four-jet events in data and in AHJ is shown in Fig. 9.5(b). The distribution in AHJ is shifted towards higher x^{obs} values, as expected from the harder jet p_T distribution observed in AHJ compared with the data (see Fig. 7.1(a)).

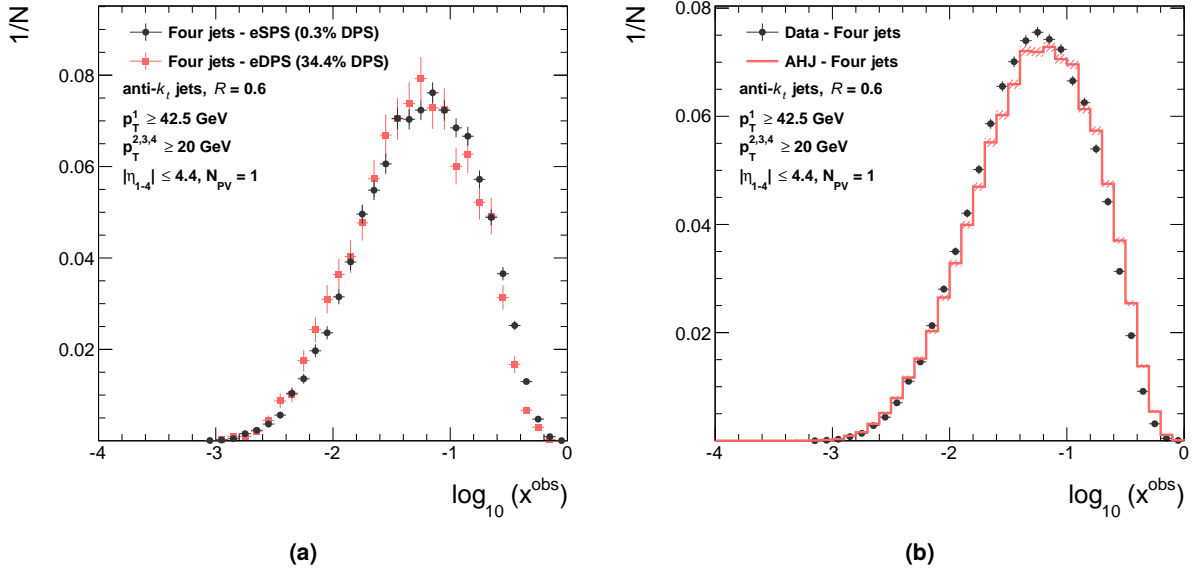


Figure 9.5: (a) Normalized distributions of the estimated fraction of the proton longitudinal momentum carried by the massless parton participating in the interaction, x^{obs} , in the eDPS and eSPS samples selected using the cuts defined in Eqs. (9.5) and (9.6), respectively, extracted from four-jet events in data selected in the phase-space defined in the figure. (b) Comparison between the normalized x^{obs} distributions in four-jet events in data (dots) and in AHJ (red histogram), selected in the phase-space defined in the figure. The estimate for x^{obs} is obtained from all four jets in the event using Eq. (9.7).

The distributions of x_1^{obs} in the eSPS samples in data and in AHJ are compared in Fig. 9.6(a). The x_1^{obs} distribution in AHJ is shifted towards higher values, similarly to the shift seen in Fig. 9.5(b), although a smaller shift is observed in the x_1^{obs} case. The same comparison is shown for the x_2^{obs} distribution in Fig. 9.6(b). In the case of the x_2^{obs} distribution, a good agreement between the data and AHJ is observed.

Figure 9.7 shows the same comparisons as in Fig. 9.6, but for the eDPS samples in data and in AHJ. An excess at high x_1^{obs} values is observed in the distribution in AHJ with respect to the distribution in the data (see Fig. 9.7(a)), as was seen for the eSPS sample. However, the excess is more pronounced in this case and it is observed also at low x_1^{obs} values. A disagreement is observed between the x_2^{obs} distributions in data and in AHJ (see Fig. 9.7(b)). The distribution in AHJ is wider and extends to lower x_2^{obs} values.

The x_1^{obs} and x_2^{obs} distributions in the eDPS sample in AHJ, shown in Fig. 9.7, may be separated into contributions of SPS and DPS events, directly extracted using the event record of AHJ. Normalized distributions of x_1^{obs} and x_2^{obs} in the eDPS sample in data are compared in Fig. 9.8 to the distributions in SPS and DPS events in the eDPS sample in AHJ. Interestingly, a good agreement is observed between the distributions in the eDPS sample in data and the SPS distributions in AHJ, for both variables. This indicates that in the data, there is not much difference in the x -distributions of SPS and DPS events. On the other hand, a discrepancy is observed between the distributions in the DPS sample in AHJ and the distributions in data. A wider x_1^{obs} distribution is observed in DPS events

9 Results

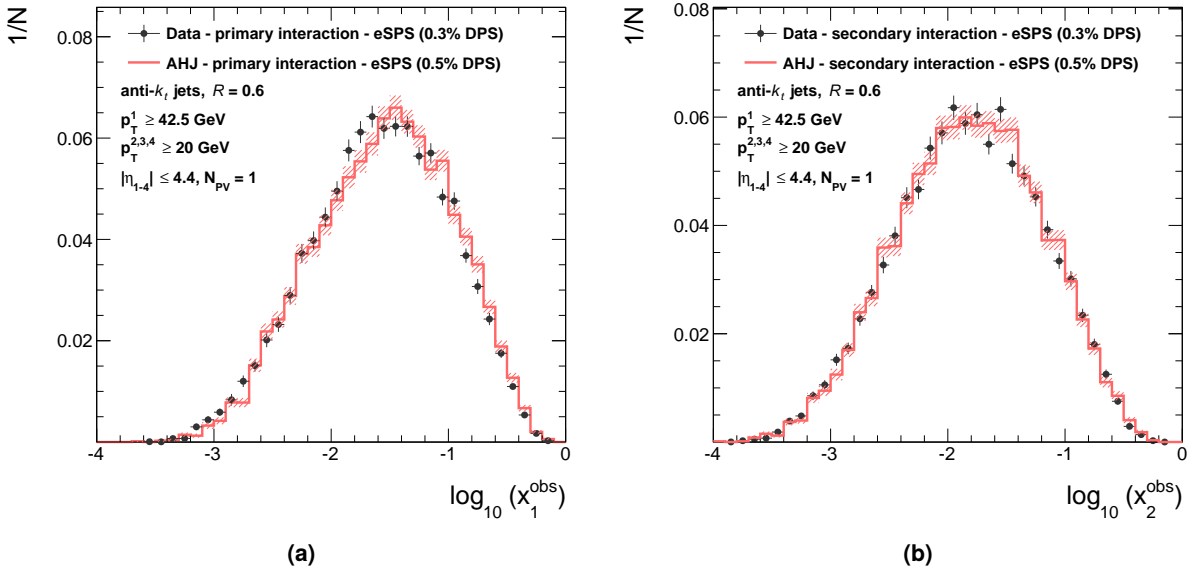


Figure 9.6: Normalized distributions of the estimated fraction of the proton longitudinal momentum carried by the massless parton participating in the (a) primary interaction, x_1^{obs} , and (b) secondary interaction, x_2^{obs} , in the eSPS sample selected using the cuts defined in Eq. (9.6), extracted from four-jet events in data (dots) and in AHJ (red histogram), selected in the phase-space defined in the figure. The estimate for $x_{1,2}^{\text{obs}}$ is obtained using Eq. (9.7).

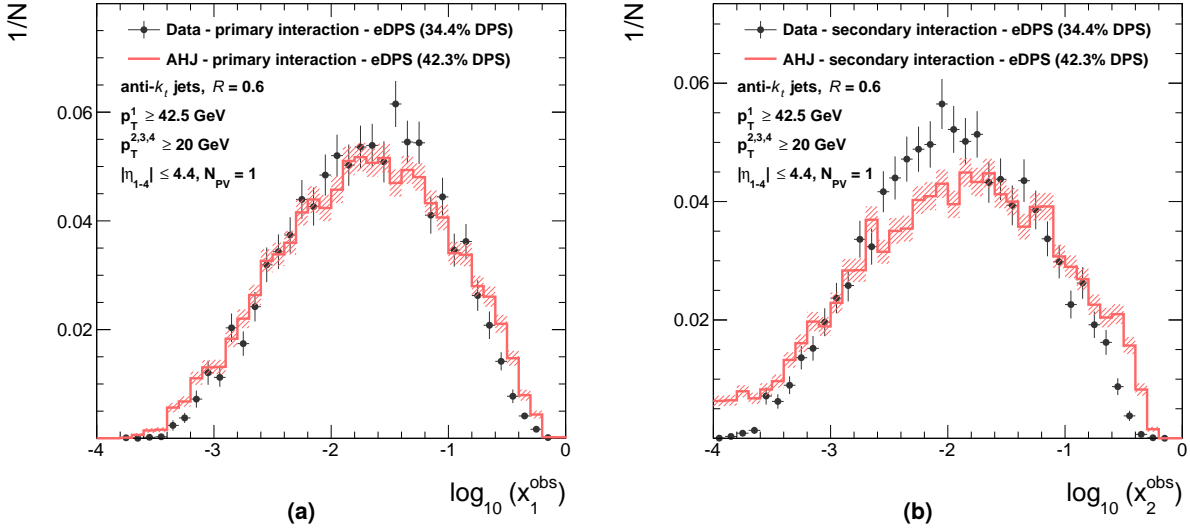


Figure 9.7: Normalized distributions of the estimated fraction of the proton longitudinal momentum carried by the massless parton participating in the (a) primary interaction, x_1^{obs} , and (b) secondary interaction, x_2^{obs} , in the eDPS sample selected using the cuts defined in Eq. (9.5), extracted from four-jet events in data (dots) and in AHJ (red histogram), selected in the phase-space defined in the figure. The estimate for $x_{1,2}^{\text{obs}}$ is obtained using Eq. (9.7).

in AHJ compared with the data. The x_2^{obs} distribution in DPS events in AHJ is flatter and does not have a clear peak as the distribution in data. These discrepancies may be attributed to the wider jet y distributions observed in AHJ compared with the data (see Fig. 7.1(b)). Interactions where both jets are in the forward (backward) region contribute to the excess at high (low) $x_{1,2}^{\text{obs}}$ values.

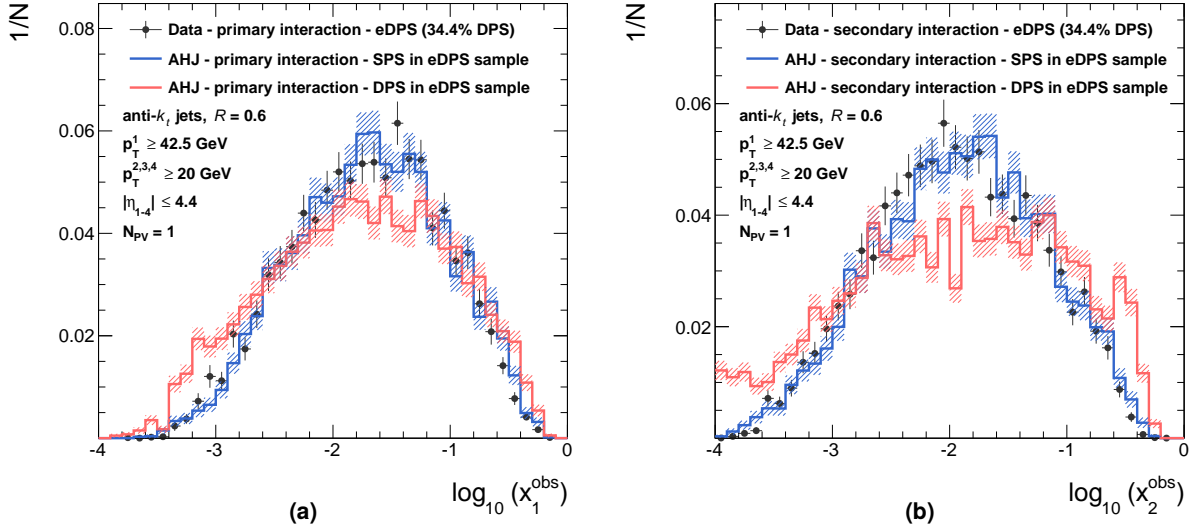


Figure 9.8: Normalized distributions of the estimated fraction of the proton longitudinal momentum carried by the massless parton participating in the (a) primary interaction, x_1^{obs} , and (b) secondary interaction, x_2^{obs} , in the eDPS sample selected using the cuts defined in Eq. (9.5), extracted from four-jet events in data (dots) selected in the phase-space defined in the figure, compared to the $x_{1,2}^{\text{obs}}$ distributions in SPS events (blue histogram) and DPS events (red histogram) directly extracted from AHJ. The estimate for $x_{1,2}^{\text{obs}}$ is obtained using Eq. (9.7).

The comparisons between data and AHJ in Figs. 9.5(b), 9.6, 9.7 and 9.8 are shown in Appendix A.3 after re-weighting the events in AHJ. As expected, after re-weighting, a better agreement between the distributions in data and in AHJ is observed, although some discrepancies remain.

9.2.2 Charged particle multiplicity

Naively, one might expect the particle multiplicity in DPS events to be higher than in SPS events. A test of this expectation may be performed by studying the distributions of charged particle multiplicity, where charged particles are measured as tracks in the detector. The distribution of the number of tracks in the event, N_{track} , associated with the primary vertex (see Chapter 5), is studied in the different samples. Normalized N_{track} distributions in the eDPS and eSPS samples extracted from data are compared in Fig. 9.9(a). The distribution in the eDPS sample is shifted towards higher N_{track} values with an average of 87.2 ± 0.5 tracks observed per event while an average of 81.2 ± 0.2 tracks is observed in the eSPS sample. The same comparison is shown in Fig. 9.9(b) for eDPS ($f_{\text{DPS}} \sim 42\%$) and eSPS ($f_{\text{DPS}} \sim 0.5\%$) samples extracted from AHJ. A larger shift is observed in AHJ, with the

9 Results

ratio

$$R_{N_{\text{track}}}^{\text{AHJ}} = \frac{\langle N_{\text{track}}^{\text{eDPS}} \rangle}{\langle N_{\text{track}}^{\text{eSPS}} \rangle} = 1.137 \pm 0.007, \quad (9.9)$$

while in data $R_{N_{\text{track}}}^{\text{data}} = 1.074 \pm 0.007$, where $\langle N_{\text{track}}^{\text{eDPS}} \rangle$ ($\langle N_{\text{track}}^{\text{eSPS}} \rangle$) refers to the average N_{track} in the eDPS (eSPS) sample. Only statistical uncertainties are estimated on the $\langle N_{\text{track}} \rangle$ values. The difference in the $R_{N_{\text{track}}}$ values between data and AHJ cannot be explained by the different f_{DPS} values in the two eDPS samples.

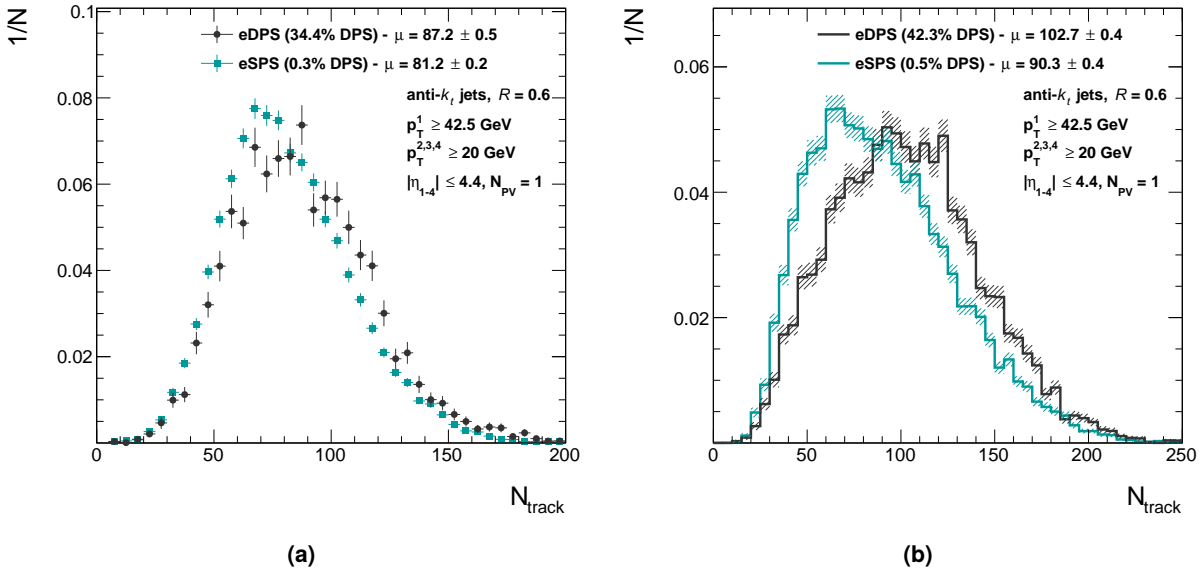


Figure 9.9: Normalized distributions of the number of tracks reconstructed in the event, N_{track} , in the eDPS and eSPS samples selected using the cuts defined in Eqs. (9.5) and (9.6), respectively, extracted from four-jet events in (a) data and in (b) AHJ, selected in the phase-space defined in the figure.

The N_{track} distribution in SPS and DPS events extracted from AHJ by matching jets to partons (see Section 6.7.2) is shown in Fig. 9.10(a). It can be seen that the distribution in SPS events extracted this way is shifted towards higher N_{track} values ($\langle N_{\text{track}}^{\text{SPS}} \rangle = 94.2 \pm 0.3$), compared to the distribution in the eSPS sample ($\langle N_{\text{track}}^{\text{eSPS}} \rangle = 90.3 \pm 0.4$). This suggests a dependence of the N_{track} distribution on the value of $\frac{1}{\sqrt{3}}\xi_{\text{sDPS}} + \frac{2}{\sqrt{3}}\xi_{\text{cDPS}}$, regardless of the event classification. Figure 9.10(b) confirms this observation, where the N_{track} distribution of events classified as coming from a SPS is shown for different values of $\frac{1}{\sqrt{3}}\xi_{\text{sDPS}} + \frac{2}{\sqrt{3}}\xi_{\text{cDPS}}$.

The dependence observed in AHJ of $\langle N_{\text{track}}^{\text{SPS}} \rangle$ on the value of $\frac{1}{\sqrt{3}}\xi_{\text{sDPS}} + \frac{2}{\sqrt{3}}\xi_{\text{cDPS}}$ may be used to extrapolate the value of $\langle N_{\text{track}}^{\text{SPS}} \rangle$ in data from the range used to select the eSPS sample to the range used to select the eDPS sample. The estimate

$$\langle N_{\text{track}}^{\text{SPS}} \rangle = 85 \pm 0.8, \quad (9.10)$$

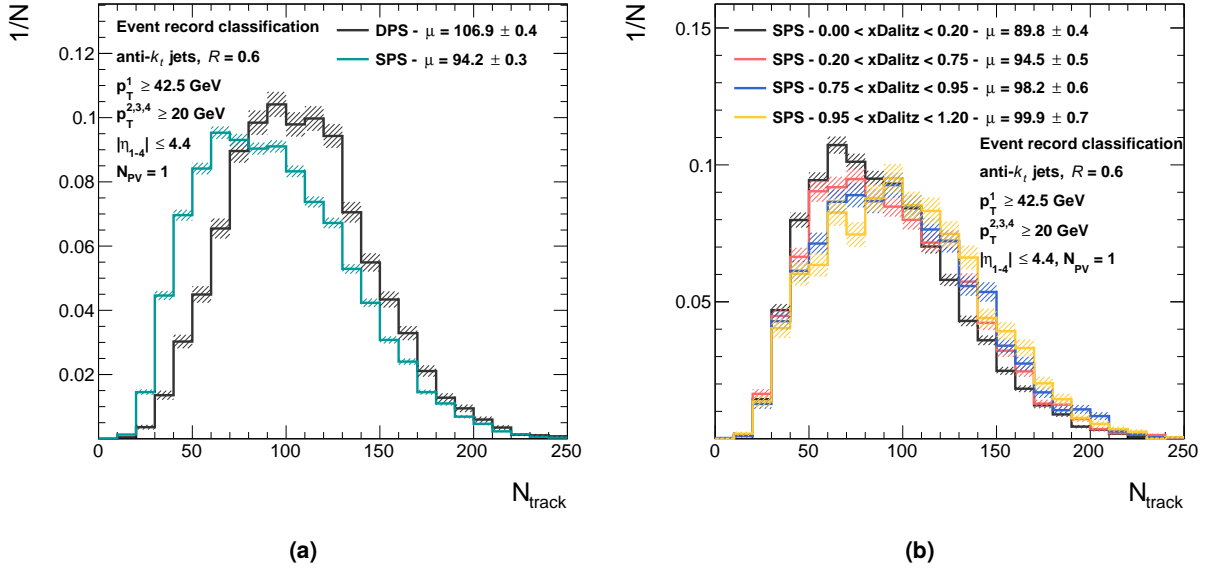


Figure 9.10: (a) Normalized distributions of the number of tracks reconstructed in the event, N_{track} , in the SPS and DPS samples extracted from four-jet events in AHJ, selected in the phase-space defined in the figure. (b) Normalized distributions of N_{track} in the SPS sample extracted from four-jet events in AHJ, selected in the phase-space defined in the figure, for various values of $\frac{1}{\sqrt{3}}\xi_{\text{SDPS}} + \frac{2}{\sqrt{3}}\xi_{\text{cDPS}}$ (x_{Dalitz}), as indicated in the legend.

in the eDPS sample in data is obtained in this manner, where the uncertainty is only statistical and does not reflect the validity of the assumption used in the extrapolation. Considering that the eDPS sample is composed of approximately 34% DPS events and using Eq. (9.10), an estimate for the average charged particle multiplicity in DPS events in data is obtained, $\langle N_{\text{track}}^{\text{DPS}} \rangle = 92 \pm 0.9$. This implies that DPS events in data have about 8% more tracks than SPS events. This effect was expected and it is observed also in MC, though the effect in MC is larger (13%).

It is worth noting that the input to the NN consists of variables pertaining only to the topology of the jets. However, events classified as DPS events by the NN exhibit a different N_{track} distribution, a property of the events not included in the classification process.

Summary and conclusions

A measurement of the rate of hard double parton scattering in four-jet events was performed using a sub-sample of data collected with the ATLAS experiment in 2010, with an average number of interactions per bunch crossing, $\langle\mu\rangle = 0.41$, corresponding to an integrated luminosity of $(37.3 \pm 1.3) \text{ pb}^{-1}$. Three different sub-samples were selected, all consisting of single-vertex events of proton–proton collisions at a center-of-mass energy, $\sqrt{s} = 7 \text{ TeV}$. Four-jet events are defined as those in which at least four jets with transverse momentum, $p_T \geq 20 \text{ GeV}$, and pseudo-rapidity, $|\eta| \leq 4.4$, are reconstructed. Events are further constrained such that the highest- p_T jet has $p_T \geq 42.5 \text{ GeV}$. Two additional dijet samples were selected with the requirement of having at least two jets with transverse momentum, $p_T \geq 20 \text{ GeV}$, and pseudo-rapidity, $|\eta| \leq 4.4$. One of the dijet samples was further constrained such that it contains at least one jet with $p_T \geq 42.5 \text{ GeV}$.

The fraction of events arising from double parton scattering has been measured using an artificial neural network, where the four-jet topology originating from double parton scattering is represented by a random combination of dijet events selected in data. The topology of four-jet events in which three jets originate from one interaction and the fourth jet originates from a secondary interaction was extracted from MC. The rate of the latter class of double parton scattering events is directly estimated in data.

The fraction of double parton scattering in four-jet events was estimated to be,

$$f_{\text{DPS}} = 0.084^{+0.009}_{-0.012} \text{ (stat.) }^{+0.062}_{-0.031} \text{ (syst.)} . \quad (10.1)$$

Combining this with measurements of the dijet and four-jet cross-sections in the appropriate phase-space regions, the effective overlap area between the interacting protons, σ_{eff} , yields

$$\sigma_{\text{eff}} = 16.1^{+2.0}_{-1.5} \text{ (stat.) }^{+6.1}_{-6.8} \text{ (syst.) mb} .$$

This value is about a quarter of the measured value of σ_{inel} at $\sqrt{s} = 7 \text{ TeV}$ and about half of what would be expected from the gluon form factor of the proton. The σ_{eff} value obtained is consistent with previous measurements performed at center-of-mass energies above 1 TeV and in various final states. This suggests that σ_{eff} is a universal parameter, process and phase-space independent.

Some of the characteristics of DPS events were studied by selecting a sample enriched with DPS events (34%) and comparing it to a sample of SPS events (with purity above 99%). Comparisons of the distributions of the fraction of the proton longitudinal momentum carried by the massless parton participating in the interaction, x , indicate that in DPS events the x values of the two interactions taking place are uncorrelated. The average charged particle multiplicity in DPS events in data was estimated to be $\sim 8\%$ higher than in SPS events.

Additional figures

Auxiliary figures, pertaining to different sections in the thesis, are presented in the following.

A.1 Distributions of the input variables in the three samples

Normalized distributions of all the variables defined in Eq. (6.27), in the SPS, cDPS and sDPS samples, are presented in the following:

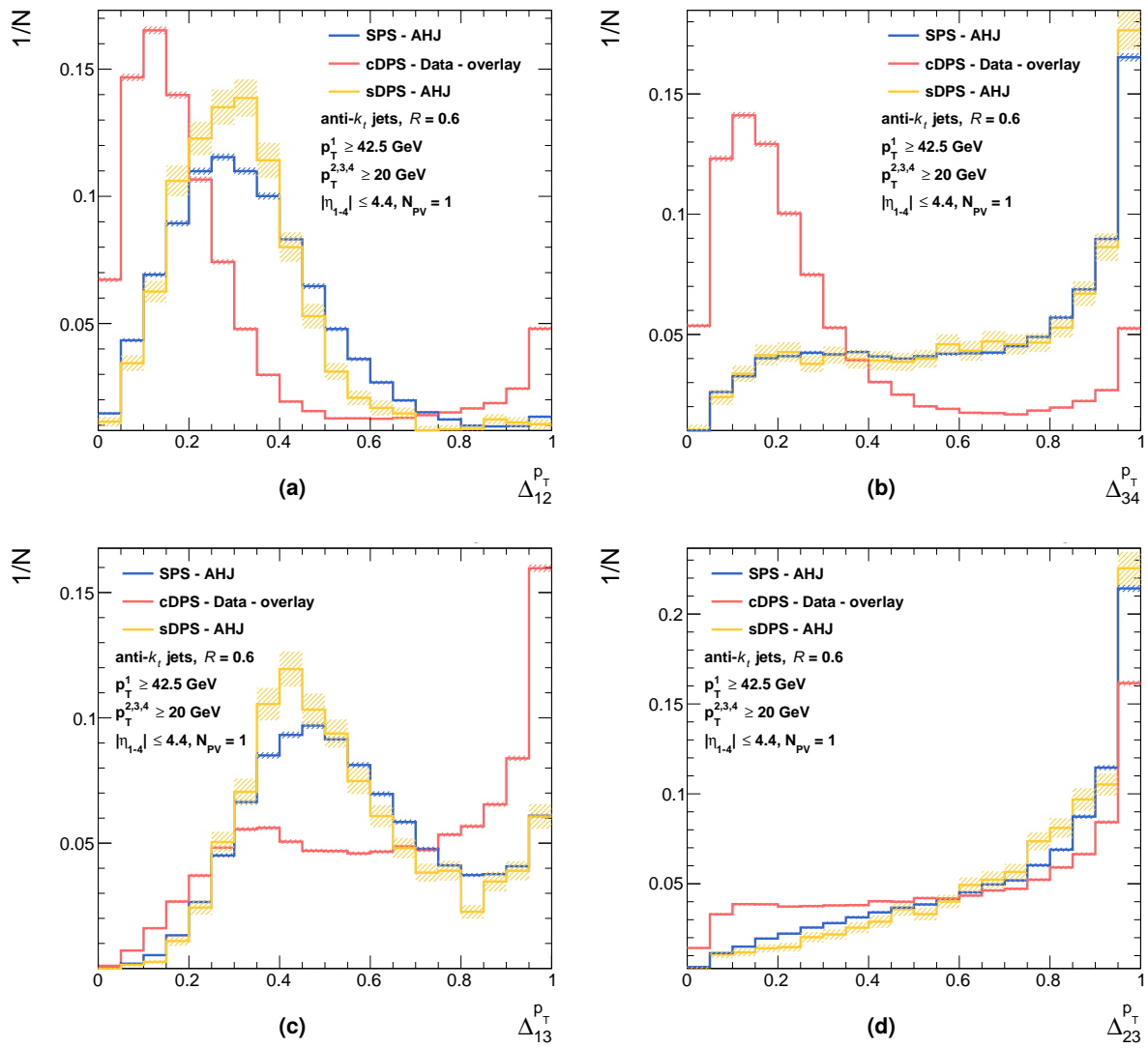


Figure A.1: Normalized distributions of the variables, (a) $\Delta_{12}^{p_T}$, (b) $\Delta_{34}^{p_T}$, (c) $\Delta_{13}^{p_T}$ and (d) $\Delta_{23}^{p_T}$, defined in Eq. (6.27), in the SPS (blue histogram, AHJ), cDPS (red histogram, overlaid dijets from data) and sDPS (yellow histogram, AHJ) samples, selected in the phase-space defined in the legend.

A Additional figures

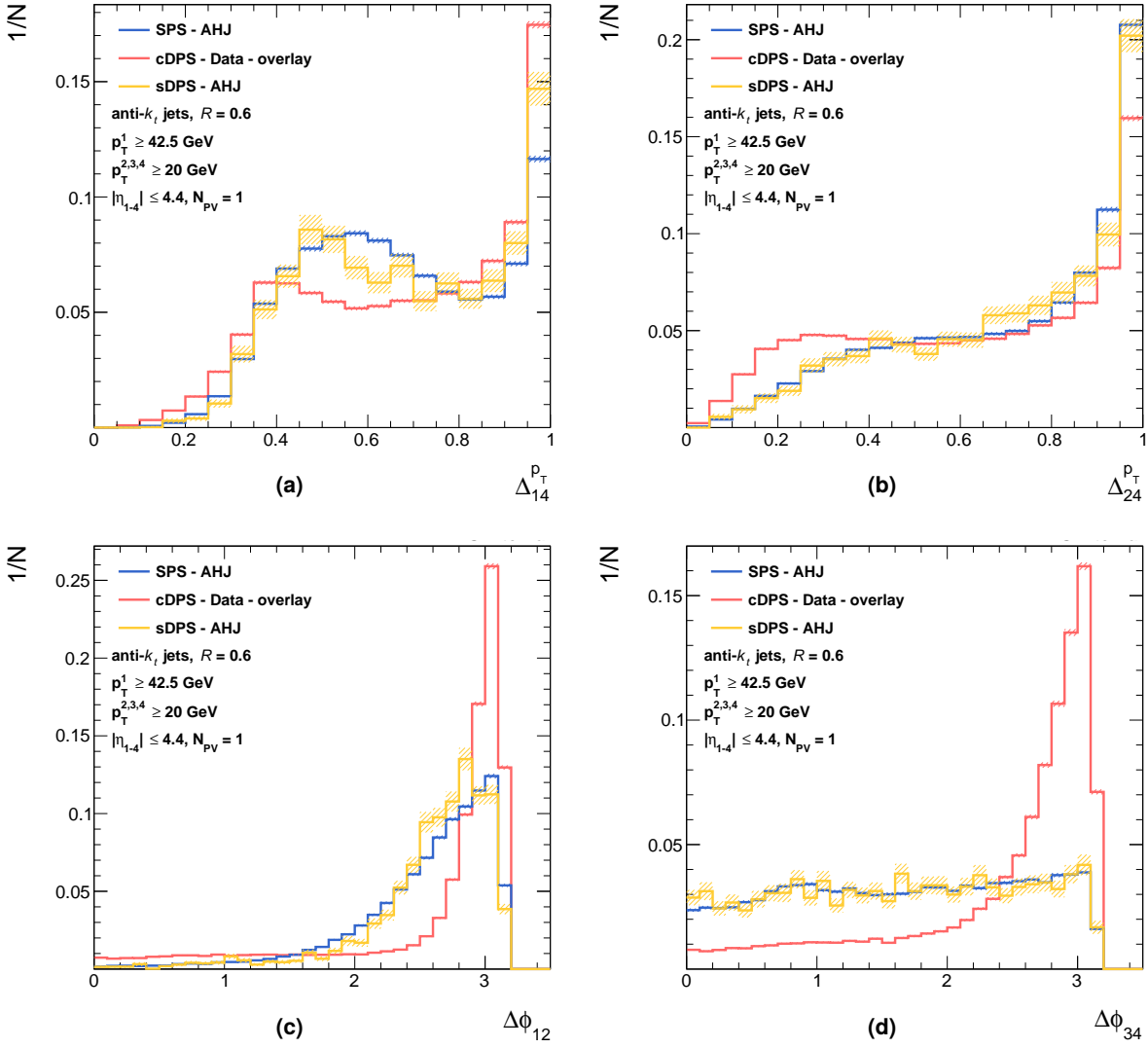


Figure A.2: Normalized distributions of the variables, (a) $\Delta_{14}^{P_T}$, (b) $\Delta_{24}^{P_T}$, (c) $\Delta\phi_{12}$ and (d) $\Delta\phi_{34}$, defined in Eq. (6.27), in the SPS (blue histogram, AHJ), cDPS (red histogram, overlaid dijets from data) and sDPS (yellow histogram, AHJ) samples, selected in the phase-space defined in the legend.

A.1 Distributions of the input variables in the three samples

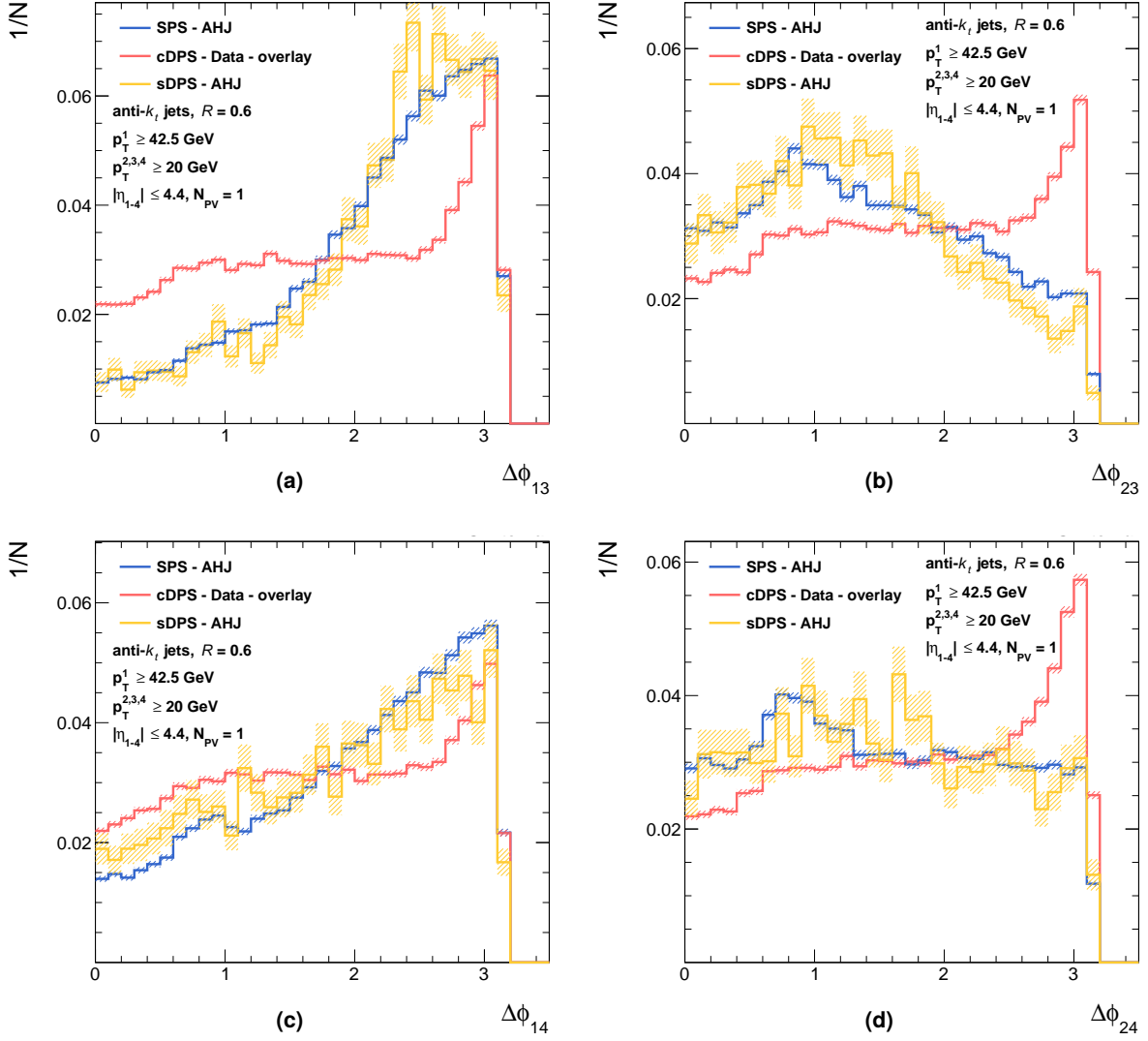


Figure A.3: Normalized distributions of the variables, (a) $\Delta\phi_{13}$, (b) $\Delta\phi_{23}$, (c) $\Delta\phi_{14}$ and (d) $\Delta\phi_{24}$, defined in Eq. (6.27), in the SPS (blue histogram, AHJ), cDPS (red histogram, overlaid dijets from data) and sDPS (yellow histogram, AHJ) samples, selected in the phase-space defined in the legend.

A Additional figures

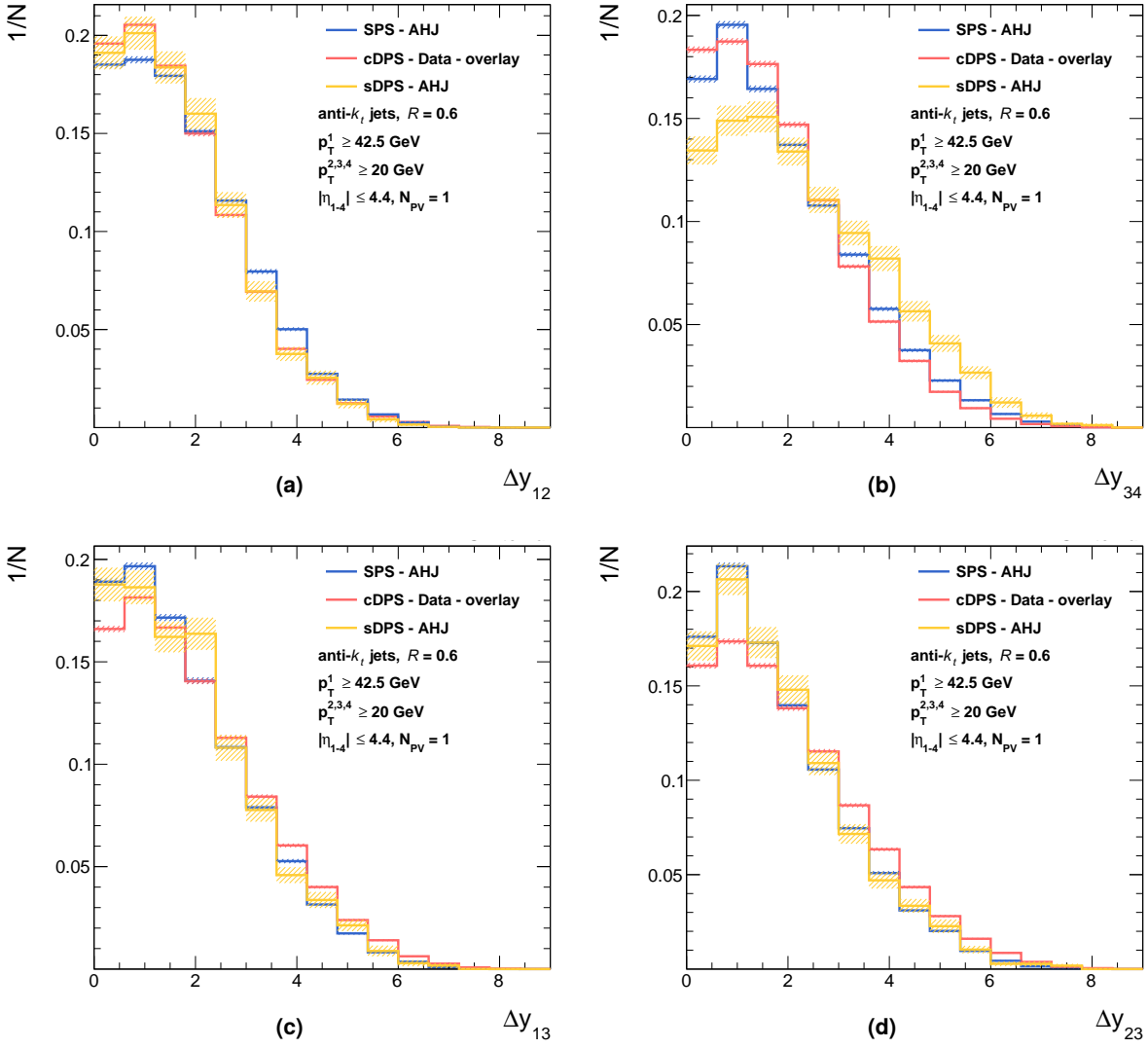


Figure A.4: Normalized distributions of the variables, (a) Δy_{12} , (b) Δy_{34} , (c) Δy_{13} and (d) Δy_{23} , defined in Eq. (6.27), in the SPS (blue histogram, AHJ), cDPS (red histogram, overlaid dijets from data) and sDPS (yellow histogram, AHJ) samples, selected in the phase-space defined in the legend.

A.1 Distributions of the input variables in the three samples

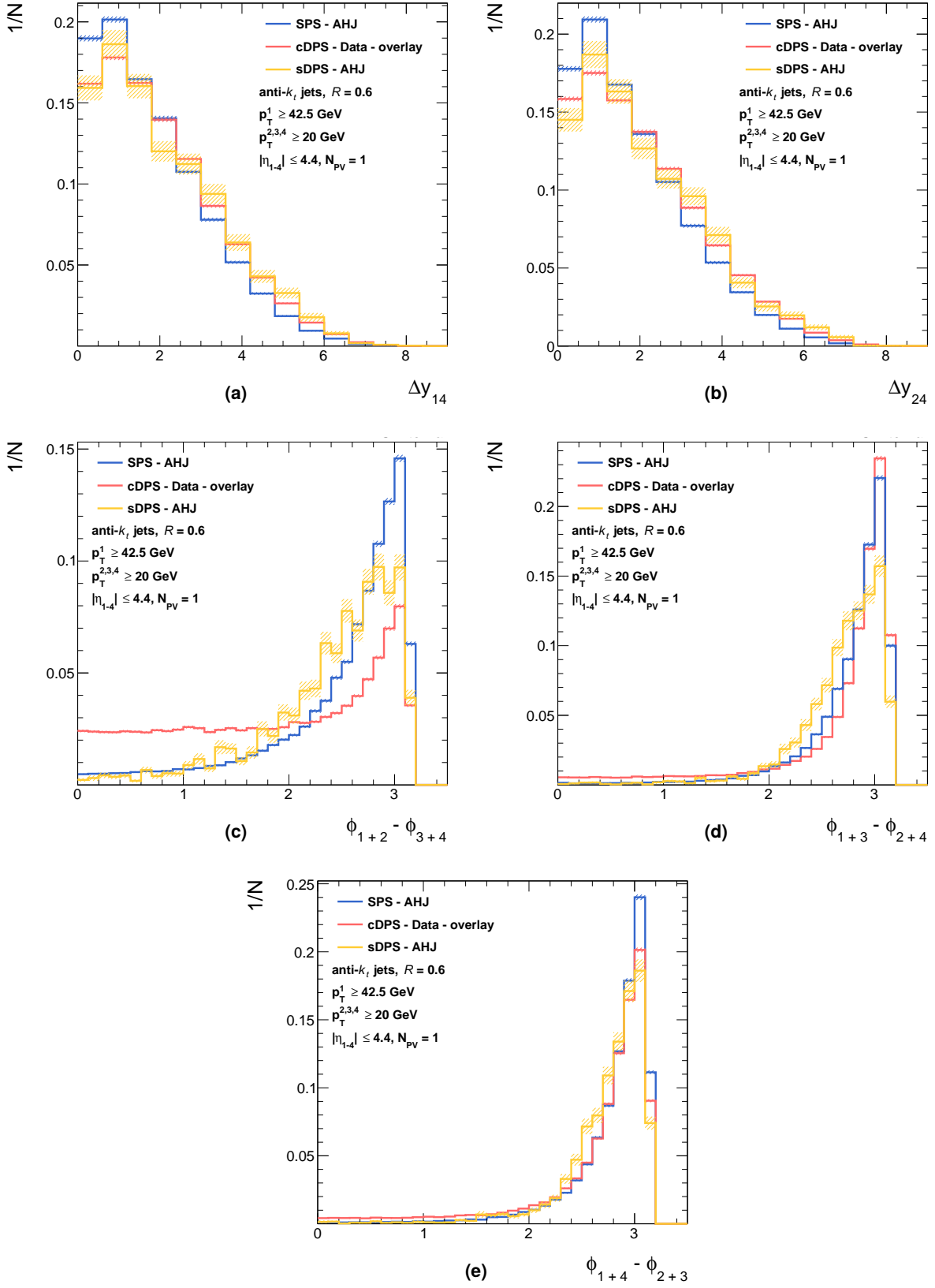


Figure A.5: Normalized distributions of the variables, (a) Δy_{14} , (b) Δy_{24} , (c) $\phi_{1+2} - \phi_{3+4}$, (d) $\phi_{1+3} - \phi_{2+4}$ and (e) $\phi_{1+4} - \phi_{2+3}$, defined in Eq. (6.27), in the SPS (blue histogram, AHJ), cDPS (red histogram, overlaid dijets from data) and sDPS (yellow histogram, AHJ) samples, selected in the phase-space defined in the legend.

A.2 Variables distributions in data compared to fit results

In the following, the distributions of the input variables in data are compared to a combination of the distributions in the three samples, SPS, cDPS and sDPS, where latter three distributions are normalized to their respective fraction of the data as obtained by the fit:

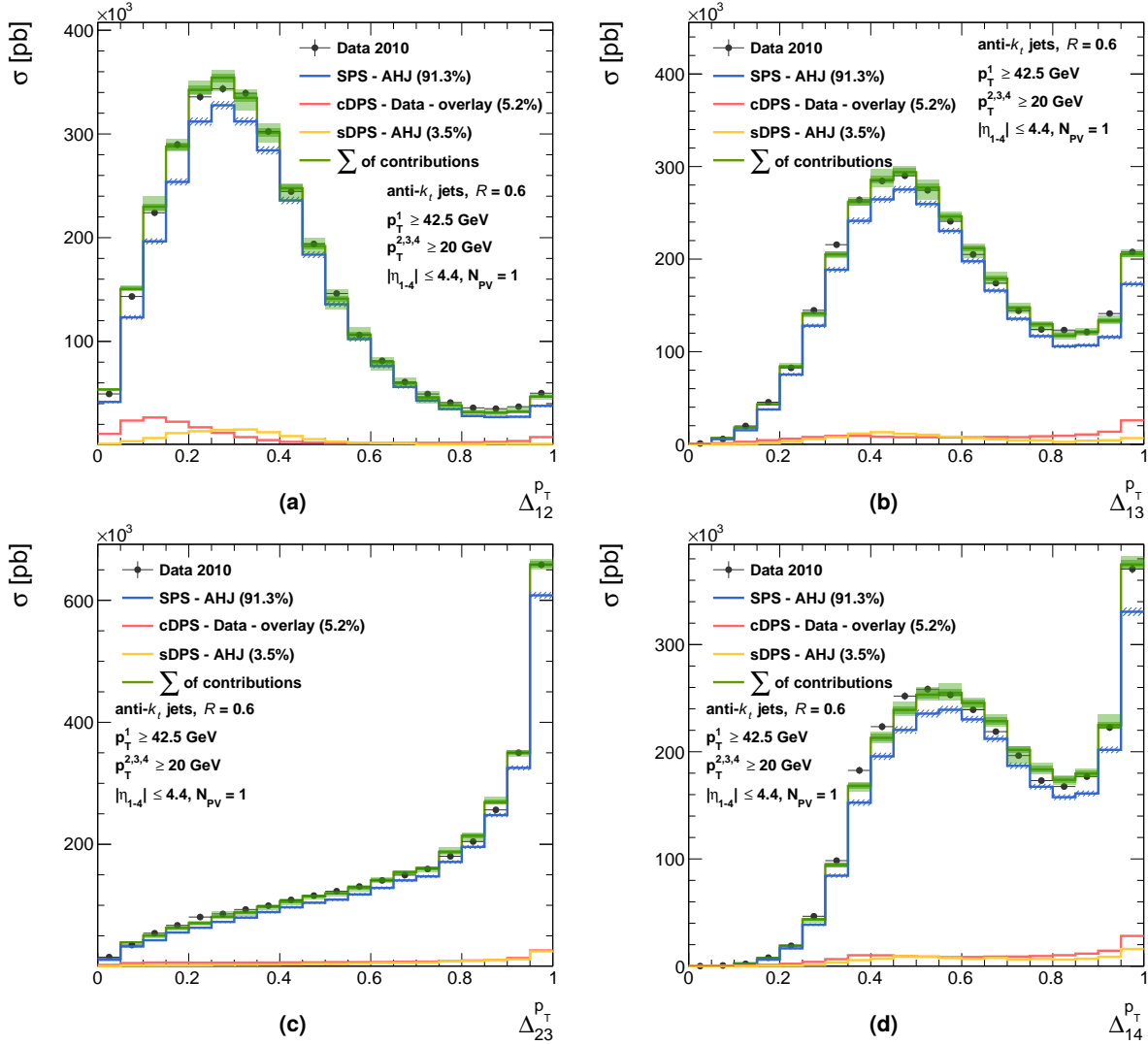


Figure A.6: Comparison of the distribution of the variables (a) $\Delta_{12}^{p_T}$, (b) $\Delta_{13}^{p_T}$, (c) $\Delta_{23}^{p_T}$ and (d) $\Delta_{14}^{p_T}$, defined in Eq. (6.27), in four-jet events in data (dots), selected in the phase space defined in the figure, with the sum (green histogram) of the SPS (blue histogram), cDPS (red histogram) and sDPS (yellow histogram) contributions. The sum of the contributions is normalized to the cross-section measured in data and the various contributions are normalized to their respective fractions obtained from the fit, as indicated in the legend. The statistical uncertainty in each bin in the sum of contributions distribution is shown as the dark shaded area while the light shaded area represents their sum in quadrature with the systematic uncertainties.

A.2 Variables distributions in data compared to fit results

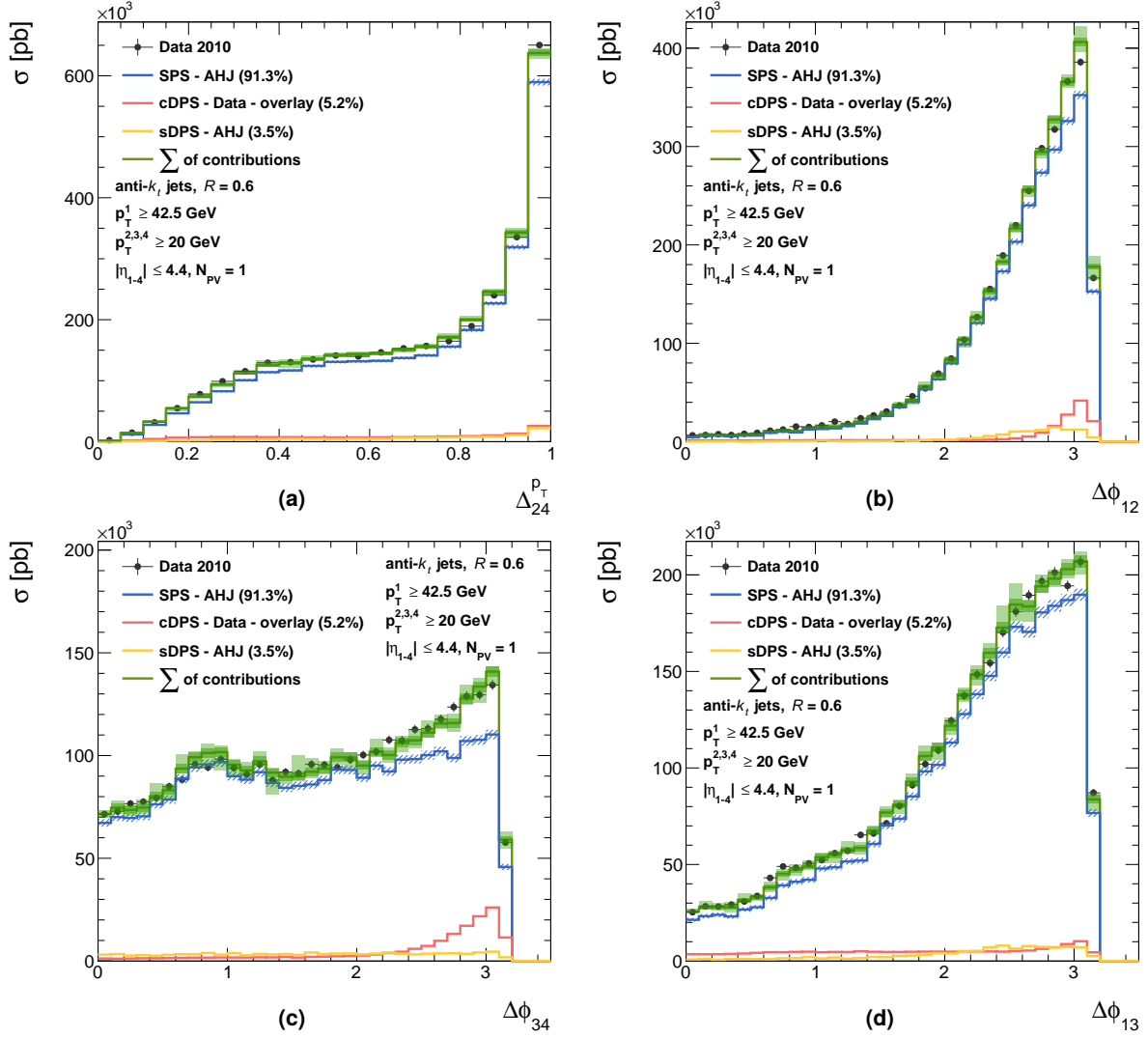


Figure A.7: Comparison of the distribution of the variables (a) $\Delta_{24}^{P_T}$, (b) $\Delta\phi_{12}$, (c) $\Delta\phi_{34}$ and (d) $\Delta\phi_{13}$, defined in Eq. (6.27), in four-jet events in data (dots), selected in the phase space defined in the figure, with the sum (green histogram) of the SPS (blue histogram), cDPS (red histogram) and sDPS (yellow histogram) contributions. The sum of the contributions is normalized to the cross-section measured in data and the various contributions are normalized to their respective fractions obtained from the fit, as indicated in the legend. The statistical uncertainty in each bin in the sum of contributions distribution is shown as the dark shaded area while the light shaded area represents their sum in quadrature with the systematic uncertainties.

A Additional figures

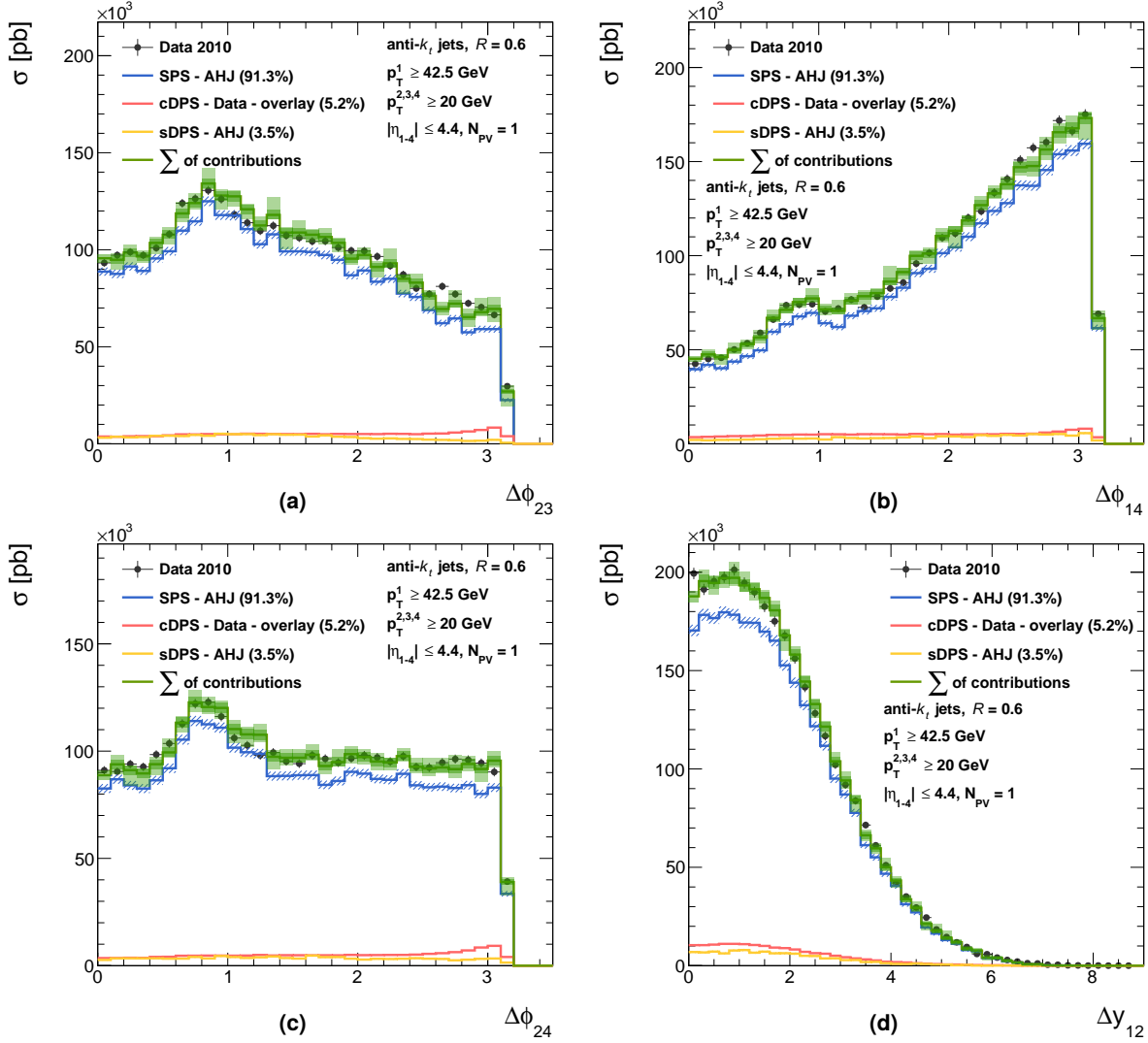


Figure A.8: Comparison of the distribution of the variables (a) $\Delta\phi_{23}$, (b) $\Delta\phi_{14}$, (c) $\Delta\phi_{24}$ and (d) Δy_{12} , defined in Eq. (6.27), in four-jet events in data (dots), selected in the phase space defined in the figure, with the sum (green histogram) of the SPS (blue histogram), cDPS (red histogram) and sDPS (yellow histogram) contributions. The sum of the contributions is normalized to the cross-section measured in data and the various contributions are normalized to their respective fractions obtained from the fit, as indicated in the legend. The statistical uncertainty in each bin in the sum of contributions distribution is shown as the dark shaded area while the light shaded area represents their sum in quadrature with the systematic uncertainties.

A.2 Variables distributions in data compared to fit results

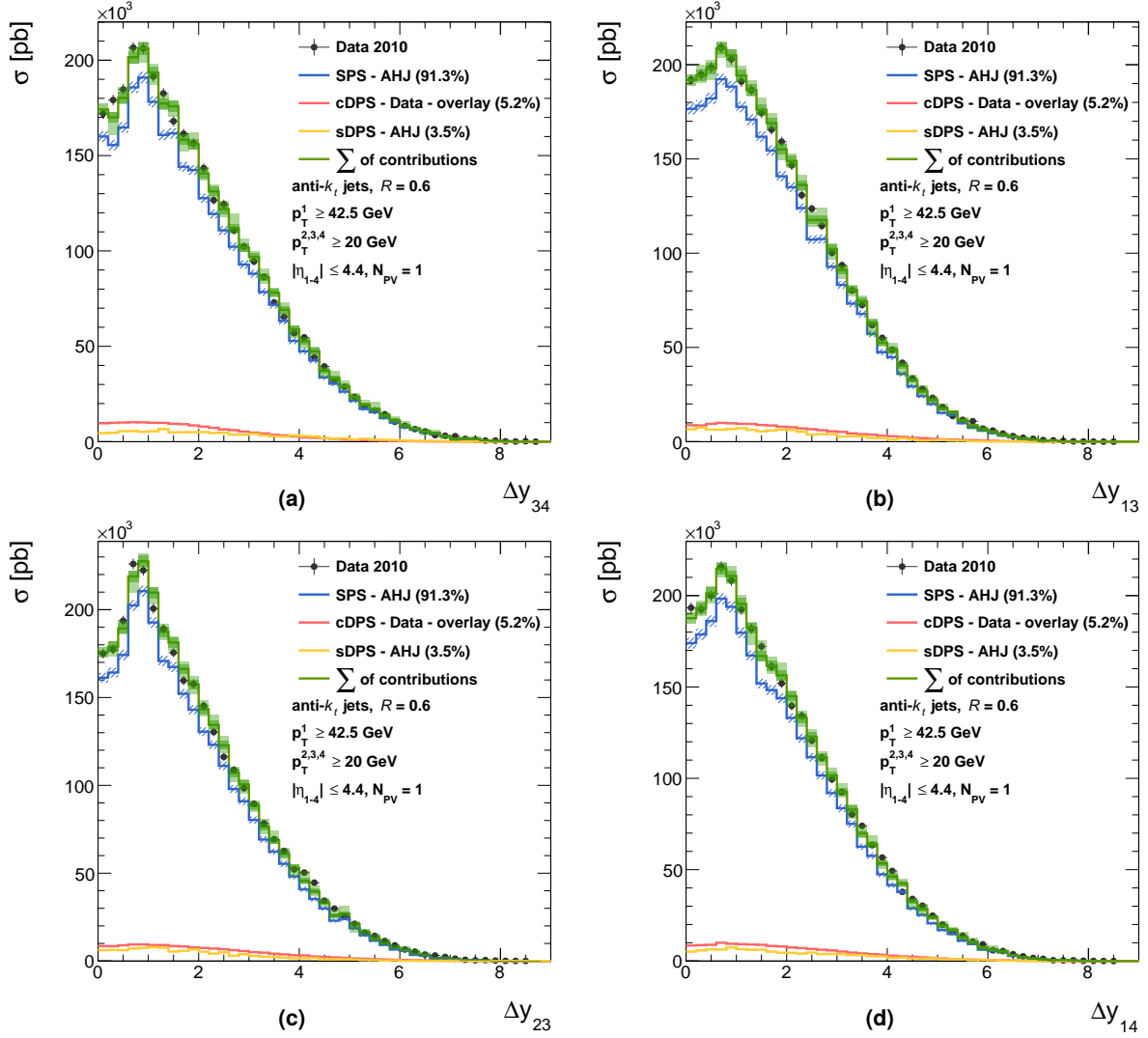


Figure A.9: Comparison of the distribution of the variables (a) Δy_{34} , (b) Δy_{13} , (c) Δy_{23} and (d) Δy_{14} , defined in Eq. (6.27), in four-jet events in data (dots), selected in the phase space defined in the figure, with the sum (green histogram) of the SPS (blue histogram), cDPS (red histogram) and sDPS (yellow histogram) contributions. The sum of the contributions is normalized to the cross-section measured in data and the various contributions are normalized to their respective fractions obtained from the fit, as indicated in the legend. The statistical uncertainty in each bin in the sum of contributions distribution is shown as the dark shaded area while the light shaded area represents their sum in quadrature with the systematic uncertainties.

A Additional figures

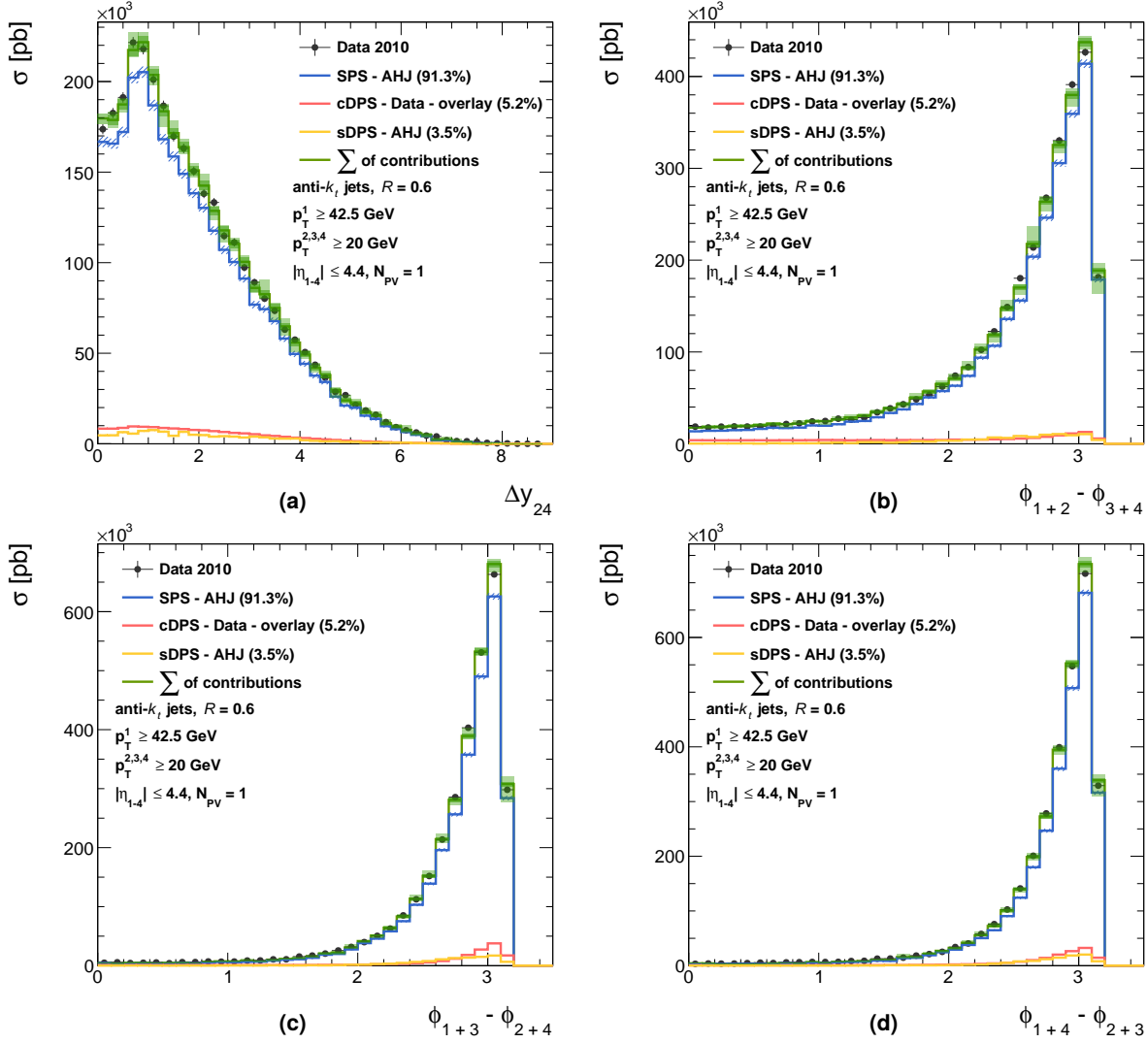


Figure A.10: Comparison of the distribution of the variables (a) Δy_{24} , (b) $\phi_{1+2} - \phi_{3+4}$, (c) $\phi_{1+3} - \phi_{2+4}$ and (d) $\phi_{1+4} - \phi_{2+3}$, defined in Eq. (6.27), in four-jet events in data (dots), selected in the phase space defined in the figure, with the sum (green histogram) of the SPS (blue histogram), cDPS (red histogram) and sDPS (yellow histogram) contributions. The sum of the contributions is normalized to the cross-section measured in data and the various contributions are normalized to their respective fractions obtained from the fit, as indicated in the legend. The statistical uncertainty in each bin in the sum of contributions distribution is shown as the dark shaded area while the light shaded area represents their sum in quadrature with the systematic uncertainties.

A.3 Distributions of x^{obs} in data and AHJ

In the following, distributions of x^{obs} are compared between the data and AHJ after applying the re-weighting procedure discussed in Section 7.2.3.

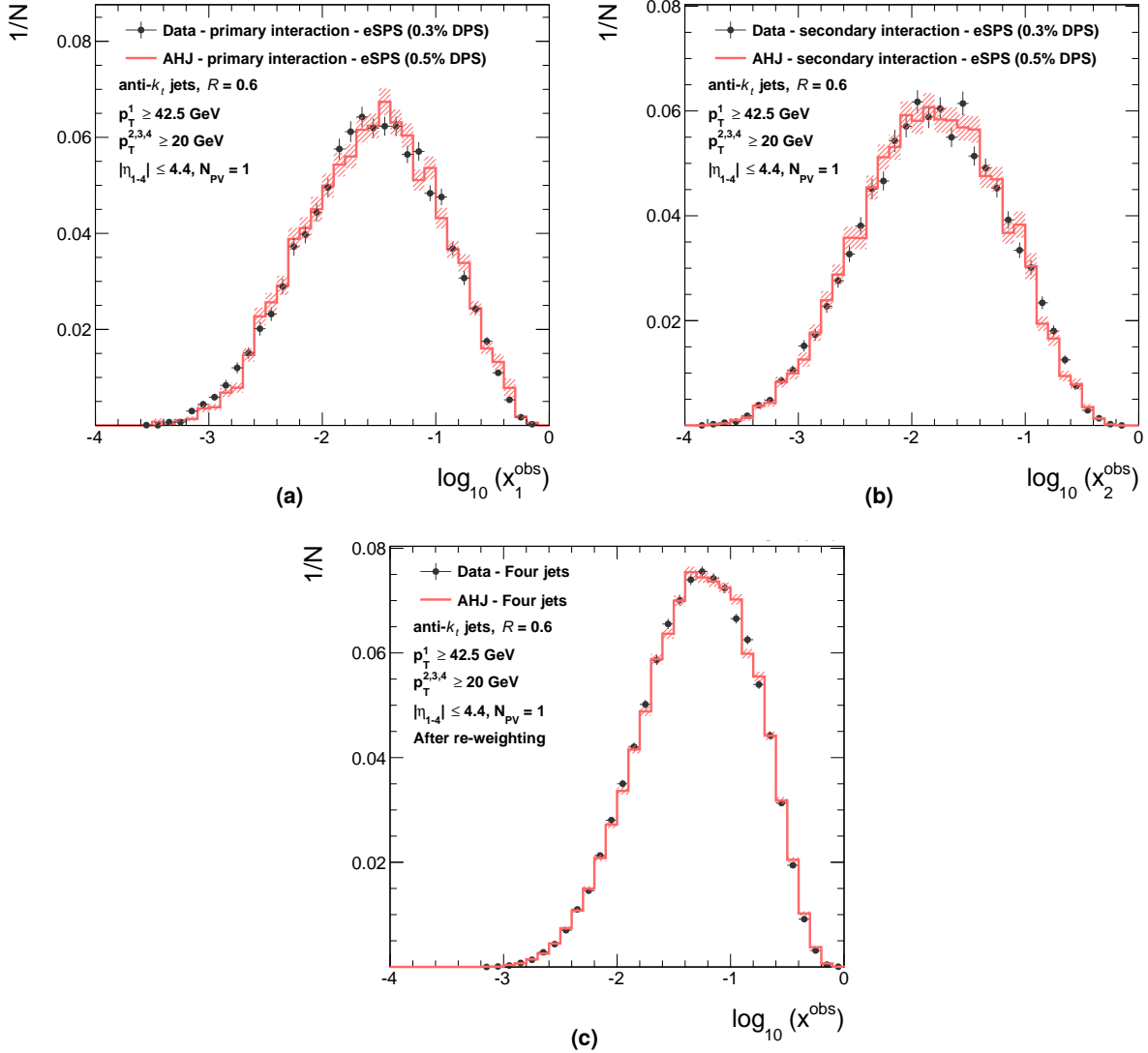


Figure A.11: Normalized distributions of the estimated fraction of the proton longitudinal momentum carried by the massless parton participating in the (a) primary interaction, x_1^{obs} , and (b) secondary interaction, x_2^{obs} , in the eSPS sample selected using the cuts defined in Eq. (9.6), extracted from four-jet events in data (dots) and in AHJ after re-weighting (red histogram), selected in the phase-space defined in the figure. (c) Comparison between the normalized x^{obs} distributions in four-jet events in data (dots) and in AHJ after re-weighting (red histogram), selected in the phase-space defined in the figure. The estimate for x^{obs} and $x_{1,2}^{\text{obs}}$ are obtained using Eq. (9.7).

A Additional figures

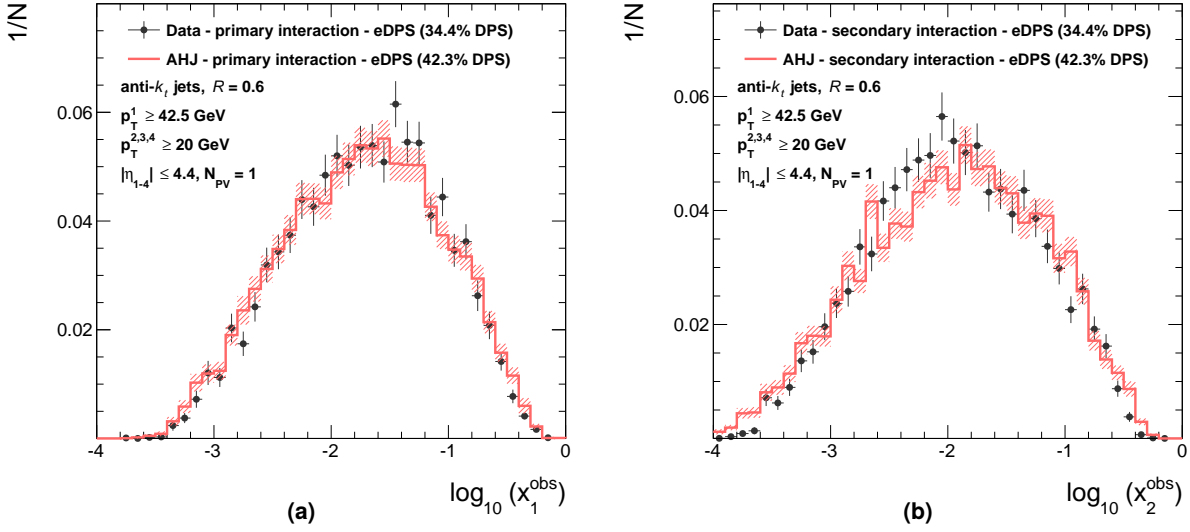


Figure A.12: Normalized distributions of the estimated fraction of the proton longitudinal momentum carried by the massless parton participating in the (a) primary interaction, x_1^{obs} , and (b) secondary interaction, x_2^{obs} , in the eDPS sample selected using the cuts defined in Eq. (9.5), extracted from four-jet events in data (dots) and in AHJ after re-weighting (red histogram), selected in the phase-space defined in the figure. The estimate for $x_{1,2}^{\text{obs}}$ is obtained using Eq. (9.7).

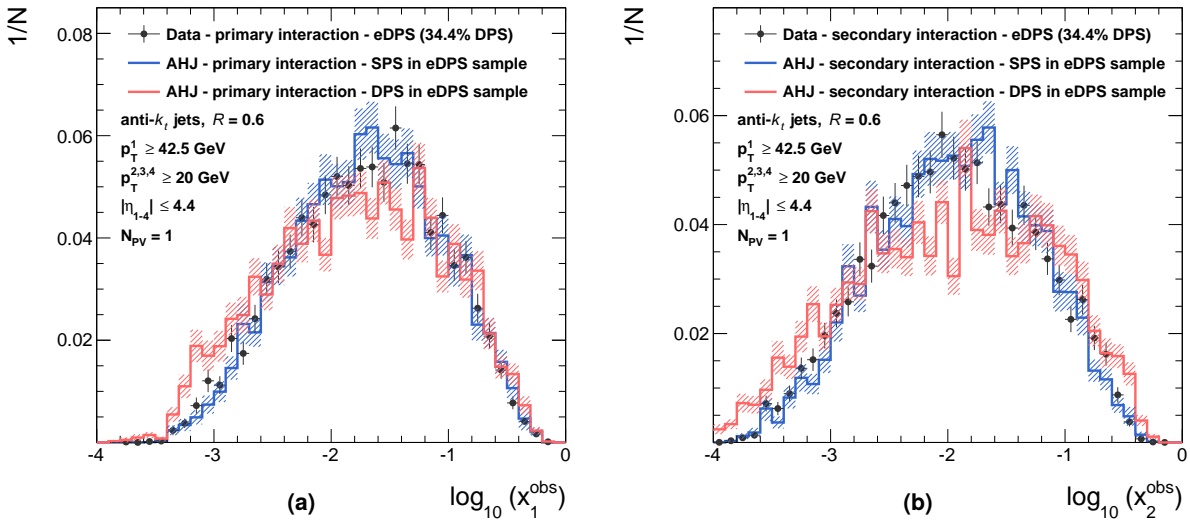


Figure A.13: Normalized distributions of the estimated fraction of the proton longitudinal momentum carried by the massless parton participating in the (a) primary interaction, x_1^{obs} , and (b) secondary interaction, x_2^{obs} , in the eDPS sample selected using the cuts defined in Eq. (9.5), extracted from four-jet events in data (dots) selected in the phase-space defined in the figure, compared to the $x_{1,2}^{\text{obs}}$ distributions in SPS events (blue histogram) and DPS events (red histogram) directly extracted from AHJ after re-weighting. The estimate for $x_{1,2}^{\text{obs}}$ is obtained using Eq. (9.7).

Bibliography

- [1] S. L. Glashow, *Partial Symmetries of Weak Interactions*, *Nucl. Phys.* **22** (1961) 579.
- [2] S. Weinberg, *A Model of Leptons*, *Phys. Rev. Lett.* **19** (1967) 1264.
- [3] A. Salam, *Weak and Electromagnetic Interactions*, Conf. Proc. **C680519** (1968) 367.
- [4] G. 't Hooft and M. J. G. Veltman, *Regularization and Renormalization of Gauge Fields*, *Nucl. Phys. B* **44** (1972) 189.
- [5] ATLAS Collaboration, *Observation of a new particle in the search for the Standard Model Higgs boson with the ATLAS detector at the LHC*, *Phys. Lett.* **B716** (2012) 1, [arXiv:1207.7214 \[hep-ex\]](#).
- [6] CMS Collaboration, *Observation of a new boson at a mass of 125 GeV with the CMS experiment at the LHC*, *Phys. Lett.* **B716** (2012) 30, [arXiv:1207.7235 \[hep-ex\]](#).
- [7] ATLAS Collaboration, *Evidence for the spin-0 nature of the Higgs boson using ATLAS data*, *Phys. Lett.* **B726** (2013) 120, [arXiv:1307.1432 \[hep-ex\]](#).
- [8] ATLAS Collaboration, *Measurements of Higgs boson production and couplings in diboson final states with the ATLAS detector at the LHC*, *Phys. Lett.* **B726** (2013) 88, [arXiv:1307.1427 \[hep-ex\]](#).
- [9] CMS Collaboration, *Measurement of Higgs boson production and properties in the WW decay channel with leptonic final states*, *JHEP* **01** (2014) 096, [arXiv:1312.1129 \[hep-ex\]](#).
- [10] CMS Collaboration, *Measurement of the properties of a Higgs boson in the four-lepton final state*, *Phys. Rev.* **D89** (2014) 092007, [arXiv:1312.5353 \[hep-ex\]](#).
- [11] CMS Collaboration, *Observation of the diphoton decay of the Higgs boson and measurement of its properties*, *Eur. Phys. J.* **C74** (2014) 3076, [arXiv:1407.0558 \[hep-ex\]](#).
- [12] The ALEPH, DELPHI, L3, OPAL and SLD Collaborations, *Precision electroweak measurements on the Z resonance*, *Phys. Rept.* **427** (2006) 257, [arXiv:hep-ex/0509008 \[hep-ex\]](#).
- [13] Gfitter Group, M. Baak et al., *The global electroweak fit at NNLO and prospects for the LHC and ILC*, *Eur. Phys. J.* **C 74** (2014) 3046, [arXiv:1407.3792 \[hep-ph\]](#).
- [14] D. Stump et al., *Inclusive jet production, parton distributions, and the search for new physics*, *JHEP* **10** (2003) 046, [arXiv:hep-ph/0303013](#).
- [15] A. Sherstnev and R. Thorne, *Parton Distributions for LO Generators*, *Eur. Phys. J.* **C55** (2008) 553, [arXiv:0711.2473 \[hep-ph\]](#).
- [16] J. Pumplin et al., *New generation of parton distributions with uncertainties from global QCD analysis*, *JHEP* **07** (2002) 012, [arXiv:0201195 \[hep-ph\]](#).
- [17] HERMES Collaboration, A. Airapetian et al., *Single-spin asymmetries in semi-inclusive deep-inelastic scattering on a transversely polarized hydrogen target*, *Phys. Rev. Lett.* **94** (2005) 012002, [arXiv:hep-ex/0408013 \[hep-ex\]](#).

Bibliography

- [18] COMPASS Collaboration, E. S. Ageev et al., *A New measurement of the Collins and Sivers asymmetries on a transversely polarised deuteron target*, *Nucl. Phys. B* **765** (2007) 31, [arXiv:hep-ex/0610068](#) [hep-ex].
- [19] CLAS Collaboration, M. Osipenko et al., *Measurement of unpolarized semi-inclusive π^+ electroproduction off the proton*, *Phys. Rev. D* **80** (2009) 032004, [arXiv:0809.1153](#) [hep-ex].
- [20] HERMES Collaboration, A. Airapetian et al., *Observation of the Naive-T-odd Sivers Effect in Deep-Inelastic Scattering*, *Phys. Rev. Lett.* **103** (2009) 152002, [arXiv:0906.3918](#) [hep-ex].
- [21] COMPASS Collaboration, M. G. Alekseev et al., *Measurement of the Collins and Sivers asymmetries on transversely polarised protons*, *Phys. Lett. B* **692** (2010) 240, [arXiv:1005.5609](#) [hep-ex].
- [22] CLAS Collaboration, H. Avakian et al., *Measurement of Single and Double Spin Asymmetries in Deep Inelastic Pion Electroproduction with a Longitudinally Polarized Target*, *Phys. Rev. Lett.* **105** (2010) 262002, [arXiv:1003.4549](#) [hep-ex].
- [23] R. Asaturyan et al., *Semi-Inclusive Charged-Pion Electroproduction off Protons and Deuterons: Cross Sections, Ratios and Access to the Quark-Parton Model at Low Energies*, *Phys. Rev. C* **85** (2012) 015202, [arXiv:1103.1649](#) [nucl-ex].
- [24] Jefferson Lab Hall A Collaboration, X. Qian et al., *Single Spin Asymmetries in Charged Pion Production from Semi-Inclusive Deep Inelastic Scattering on a Transversely Polarized ^3He Target*, *Phys. Rev. Lett.* **107** (2011) 072003, [arXiv:1106.0363](#) [nucl-ex].
- [25] J. Katich et al., *Measurement of the Target-Normal Single-Spin Asymmetry in Deep-Inelastic Scattering from the Reaction $^3\text{He}^\uparrow(e, e')X$* , *Phys. Rev. Lett.* **113** (2014) 022502, [arXiv:1311.0197](#) [nucl-ex].
- [26] CLAS Collaboration, W. Gohn et al., *Beam-spin asymmetries from semi-inclusive pion electroproduction*, *Phys. Rev. D* **89** (2014) 072011, [arXiv:1402.4097](#) [hep-ex].
- [27] Jefferson Lab Hall A Collaboration, Y. X. Zhao et al., *Single spin asymmetries in charged kaon production from semi-inclusive deep inelastic scattering on a transversely polarized ^3He target*, *Phys. Rev. C* **90** (2014) 055201, [arXiv:1404.7204](#) [nucl-ex].
- [28] P. V. Landshoff, J. C. Polkinghorne, and D. M. Scott, *Production of baryons with large transverse momentum*, *Phys. Rev. D* **12** (1975) 3738.
- [29] P. V. Landshoff and J. C. Polkinghorne, *Calorimeter triggers for hard collisions*, *Phys. Rev. D* **18** (1978) 3344.
- [30] M. Strikman, *Transverse Nucleon Structure and Multiparton Interactions*, *Acta Phys. Polon. B* **42** (2011) 2607, [arXiv:1112.3834](#) [hep-ph].
- [31] E. L. Berger, C. Jackson, and G. Shaughnessy, *Characteristics and Estimates of Double Parton Scattering at the Large Hadron Collider*, *Phys. Rev. D* **81** (2010) 014014, [arXiv:0911.5348](#) [hep-ph].

- [32] B. Humpert and R. Odorico, *Multiparton scattering and QCD radiation as sources of four jet events*, *Phys. Lett.* **B154** (1985) 211.
- [33] L. Ametller, N. Paver, and D. Treleani, *Possible signature of multiple parton interactions in collider four jet events*, *Phys. Lett.* **B169** (1986) 289.
- [34] B. Blok, Yu. Dokshitzer, L. Frankfurt, and M. Strikman, *pQCD physics of multiparton interactions*, *Eur. Phys. J.* **C72** (2012) 1963, [arXiv:1106.5533 \[hep-ph\]](#).
- [35] B. Blok, Y. Dokshitzer, L. Frankfurt, and M. Strikman, *The Four jet production at LHC and Tevatron in QCD*, *Phys. Rev.* **D83** (2011) 071501, [arXiv:1009.2714 \[hep-ph\]](#).
- [36] S. Domdey, H.-J. Pirner, and U. A. Wiedemann, *Testing the Scale Dependence of the Scale Factor δ_{eff} in Double Dijet Production at the LHC*, *Eur. Phys. J.* **C65** (2010) 153, [arXiv:0906.4335 \[hep-ph\]](#).
- [37] M. Luszczak, R. Maciula, and A. Szczurek, *Production of two $c\bar{c}$ pairs in double-parton scattering*, [arXiv:1111.3255 \[hep-ph\]](#).
- [38] M. Mangano, *Four jet production at the Tevatron Collider*, *Z. Phys. C* **42** (1989) 331.
- [39] F. Takagi, *Multiple Production of Quark Jets off Nuclei*, *Phys. Rev. Lett.* **43** (1979) 1296.
- [40] A. Del Fabbro and D. Treleani, *Double parton scatterings in b quark pairs production at the CERN LHC*, *Phys. Rev.* **D66** (2002) 074012, [arXiv:hep-ph/0207311 \[hep-ph\]](#).
- [41] M. Hussein, *Double parton scattering in associate Higgs boson production with bottom quarks at hadron colliders*, [arXiv:0710.0203 \[hep-ph\]](#).
- [42] M. Drees and T. Han, *Signals for double parton scattering at the Fermilab Tevatron*, *Phys. Rev. Lett.* **77** (1996) 4142, [arXiv:hep-ph/9605430 \[hep-ph\]](#).
- [43] C. Goebel, D. M. Scott, and F. Halzen, *Double Drell-Yan annihilations in hadron collisions: Novel tests of the constituent picture*, *Phys. Rev.* **D22** (1980) 2789.
- [44] E. Maina, *Multiple Parton Interactions in $Z + 4j$, $W^\pm W^\pm + 0/2j$ and $W^+ W^- + 2j$ production at the LHC*, *JHEP* **0909** (2009) 081, [arXiv:0909.1586 \[hep-ph\]](#).
- [45] J. R. Gaunt, C.-H. Kom, A. Kulesza, and W. J. Stirling, *Same-sign W pair production as a probe of double parton scattering at the LHC*, *Eur. Phys. J.* **C69** (2010) 53, [arXiv:1003.3953 \[hep-ph\]](#).
- [46] C. Kom, A. Kulesza, and W. Stirling, *Prospects for observation of double parton scattering with four-muon final states at LHCb*, *Eur. Phys. J.* **C71** (2011) 1802, [arXiv:1109.0309 \[hep-ph\]](#).
- [47] C. Kom, A. Kulesza, and W. Stirling, *Pair production of J/ψ as a probe of double parton scattering at LHCb*, *Phys. Rev. Lett.* **107** (2011) 082002, [arXiv:1105.4186 \[hep-ph\]](#).
- [48] E. L. Berger, C. Jackson, S. Quackenbush, and G. Shaughnessy, *Calculation of $W b \bar{b}$ Production via Double Parton Scattering at the LHC*, *Phys. Rev.* **D84** (2011) 074021, [arXiv:1107.3150 \[hep-ph\]](#).

Bibliography

- [49] A. Del Fabbro and D. Treleani, *A Double parton scattering background to Higgs boson production at the LHC*, *Phys. Rev.* **D61** (2000) 077502, [arXiv:hep-ph/9911358 \[hep-ph\]](#).
- [50] E. Maina, *Multiple Parton Interactions, top-antitop and $W + 4j$ production at the LHC*, *JHEP* **0904** (2009) 098, [arXiv:0904.2682 \[hep-ph\]](#).
- [51] G. Calucci and D. Treleani, *Double parton scatterings in high-energy hadronic collisions*, *Nucl. Phys. Proc. Suppl.* **71** (1999) 392, [arXiv:hep-ph/9711225 \[hep-ph\]](#).
- [52] A. M. Snigirev, *QCD status of factorization ansatz for double parton distributions*, *Phys. Rev.* **D68** (2003) 114012.
- [53] J. R. Gaunt and W. J. Stirling, *Double Parton Distributions Incorporating Perturbative QCD Evolution and Momentum and Quark Number Sum Rules*, *JHEP* **03** (2010) 005, [arXiv:0910.4347 \[hep-ph\]](#).
- [54] G. Calucci and D. Treleani, *Proton structure in transverse space and the effective cross-section*, *Phys. Rev.* **D60** (1999) 054023, [arXiv:hep-ph/9902479 \[hep-ph\]](#).
- [55] T. Rogers and M. Strikman, *Multiple Hard Partonic Collisions with Correlations in Proton-Proton Scattering*, *Phys. Rev.* **D81** (2010) 016013, [arXiv:0908.0251 \[hep-ph\]](#).
- [56] J. R. Gaunt, *The GS09 double parton distribution functions*, *PoS DIS2010* (2010) 030, [arXiv:1006.1118 \[hep-ph\]](#).
- [57] F. A. Ceccopieri, *An update on the evolution of double parton distributions*, *Phys. Lett.* **B697** (2011) 482, [arXiv:1011.6586 \[hep-ph\]](#).
- [58] M. Ryskin and A. Snigirev, *A Fresh look at double parton scattering*, *Phys. Rev.* **D83** (2011) 114047, [arXiv:1103.3495 \[hep-ph\]](#).
- [59] J. R. Gaunt and W. J. Stirling, *Single and Double Perturbative Splitting Diagrams in Double Parton Scattering*, [arXiv:1202.3056 \[hep-ph\]](#).
- [60] J. R. Gaunt, *Single Perturbative Splitting Diagrams in Double Parton Scattering*, *JHEP* **1301** (2013) 042, [arXiv:1207.0480 \[hep-ph\]](#).
- [61] C. Flensburg, G. Gustafson, L. Lonnblad, and A. Ster, *Correlations in double parton distributions at small x* , *JHEP* **1106** (2011) 066, [arXiv:1103.4320 \[hep-ph\]](#).
- [62] A. V. Manohar and W. J. Waalewijn, *What is Double Parton Scattering?*, *Phys. Lett.* **B713** (2012) 196, [arXiv:1202.5034 \[hep-ph\]](#).
- [63] A. V. Manohar and W. J. Waalewijn, *A QCD Analysis of Double Parton Scattering: Color Correlations, Interference Effects and Evolution*, *Phys. Rev.* **D85** (2012) 114009, [arXiv:1202.3794 \[hep-ph\]](#).
- [64] H.-M. Chang, A. V. Manohar, and W. J. Waalewijn, *Double Parton Correlations in the Bag Model*, *Phys. Rev.* **D87** (2013) 034009, [arXiv:1211.3132 \[hep-ph\]](#).
- [65] B. Blok, Yu. Dokshitzer, L. Frankfurt, and M. Strikman, *Perturbative QCD correlations in multi-parton collisions*, *Eur. Phys. J.* **C74** (2014) 2926, [arXiv:1306.3763 \[hep-ph\]](#).

- [66] M. Diehl and T. Kasemets, *Positivity bounds on double parton distributions*, *JHEP* **1305** (2013) 150, [arXiv:1303.0842 \[hep-ph\]](#).
- [67] M. Diehl, T. Kasemets, and S. Keane, *Correlations in double parton distributions: effects of evolution*, *JHEP* **1405** (2014) 118, [arXiv:1401.1233 \[hep-ph\]](#).
- [68] A. Snigirev, N. Snigireva, and G. Zinovjev, *Perturbative and nonperturbative correlations in double parton distributions*, *Phys. Rev.* **D90** (2014) 014015, [arXiv:1403.6947 \[hep-ph\]](#).
- [69] F. A. Ceccopieri, *A second update on double parton distributions*, *Phys. Lett.* **B734** (2014) 79, [arXiv:1403.2167 \[hep-ph\]](#).
- [70] K. Golec-Biernat and E. Lewandowska, *How to impose initial conditions for QCD evolution of double parton distributions?*, *Phys. Rev.* **D90** (2014) 014032, [arXiv:1402.4079 \[hep-ph\]](#).
- [71] T. Akesson et al., *Double parton scattering in pp collisions at $\sqrt{s} = 63$ GeV*, *Z. Phys. C* **34** (1986) 163.
- [72] J. Alitti et al., *A study of multi-jet events at the CERN pp collider and a search for double parton scattering*, *Phys. Lett.* **B268** (1991) 145.
- [73] CDF Collaboration, F. Abe et al., *Study of four-jet events and evidence for double parton interactions in $p\bar{p}$ collisions at $\sqrt{s} = 1.8$ TeV*, *Phys. Rev.* **D47** (1993) 4857.
- [74] CDF Collaboration, F. Abe et al., *Double parton scattering in $\bar{p}p$ collisions at $\sqrt{s} = 1.8$ TeV*, *Phys. Rev.* **D56** (1997) 3811.
- [75] D0 Collaboration, V. Abazov et al., *Double parton interactions in photon+3 jet events in p - \bar{p} collisions $\sqrt{s} = 1.96$ TeV*, *Phys. Rev.* **D81** (2010) 052012, [arXiv:0912.5104 \[hep-ex\]](#).
- [76] D0 Collaboration, V. M. Abazov et al., *Double parton interactions in photon + 3 jet and photon + b/c jet + 2 jet events in $ppbar$ collisions at $\sqrt{s}=1.96$ TeV*, *Phys. Rev.* **D89** (2014) 072006, [arXiv:1402.1550 \[hep-ex\]](#).
- [77] ATLAS Collaboration, *Measurement of hard double-parton interactions in $W(\rightarrow l\nu)+2$ jet events at $\sqrt{s}=7$ TeV with the ATLAS detector*, *New J. Phys.* **15** (2013) 033038, [arXiv:1301.6872 \[hep-ex\]](#).
- [78] CMS Collaboration, *Study of double parton scattering using $W+2$ -jet events in proton-proton collisions at $\sqrt{s} = 7$ TeV*, *JHEP* **1403** (2014) 032, [arXiv:1312.5729 \[hep-ex\]](#).
- [79] LHCb Collaboration, *Observation of double charm production involving open charm in pp collisions at $\sqrt{s} = 7$ TeV*, *JHEP* **1206** (2012) 141, [arXiv:1205.0975 \[hep-ex\]](#).
- [80] CMS Collaboration, *Measurement of four-jet production in proton-proton collisions at $\sqrt{s} = 7$ TeV*, *Phys. Rev.* **D89** (2014) 092010, [arXiv:1312.6440 \[hep-ex\]](#).
- [81] R. B. Mann, *An introduction to particle physics and the standard model*. CRC press, 2010.
- [82] F. Englert and R. Brout, *Broken Symmetry and the Mass of Gauge Vector Mesons*, *Phys. Rev. Lett.* **13** (1964) 321.

Bibliography

- [83] P. W. Higgs, *Broken symmetries, massless particles and gauge fields*, *Phys. Lett.* **12** (1964) 132.
- [84] P. W. Higgs, *Broken Symmetries and the Masses of Gauge Bosons*, *Phys. Rev. Lett.* **13** (1964) 508.
- [85] G. S. Guralnik, C. R. Hagen, and T. W. B. Kibble, *Global Conservation Laws and Massless Particles*, *Phys. Rev. Lett.* **13** (1964) 585.
- [86] P. W. Higgs, *Spontaneous Symmetry Breakdown without Massless Bosons*, *Phys. Rev.* **145** (1966) 1156.
- [87] T. W. B. Kibble, *Symmetry breaking in nonAbelian gauge theories*, *Phys. Rev.* **155** (1967) 1554.
- [88] W. Greiner, S. Schramm, and E. Stein, *Quantum Chromodynamics*. Springer-Verlag Berlin Heidelberg, 2007.
- [89] M. Gell-Mann, *Symmetries of Baryons and Mesons*, *Phys. Rev.* **125** (1962) 1067.
- [90] Y. Ne'eman, *Higher symmetries and current conservation*, *Phys. Lett.* **4** (1963) 81.
- [91] M. Gell-Mann and Y. Ne'eman, *The Eight Fold Way*. Benjamin, New York, 1964.
- [92] M. Gell-Mann, *A schematic model of baryons and mesons*, *Phys. Lett.* **8** (1964) 214.
- [93] G. Zweig, *An SU_3 model for strong interaction symmetry and its breaking*, <https://cds.cern.ch/record/570209>.
- [94] E. D. Bloom et al., *High-Energy Inelastic $e^- p$ Scattering at 6° and 10°* , *Phys. Rev. Lett.* **23** (1969) 930.
- [95] J. D. Bjorken and E. A. Paschos, *Inelastic Electron-Proton and γ -Proton Scattering and the Structure of the Nucleon*, *Phys. Rev.* **185** (1969) 1975.
- [96] R. P. Feynman, *Very High-Energy Collisions of Hadrons*, *Phys. Rev. Lett.* **23** (1969) 1415.
- [97] O. W. Greenberg, *Spin and Unitary-Spin Independence in a Paraquark Model of Baryons and Mesons*, *Phys. Rev. Lett.* **13** (1964) 598.
- [98] M. Y. Han and Y. Nambu, *Three-Triplet Model with Double $SU(3)$ Symmetry*, *Phys. Rev.* **139** (1965) B1006.
- [99] TASSO Collaboration, R. Brandelik et al., *Evidence for a Spin One Gluon in Three Jet Events*, *Phys. Lett. B* **97** (1980) 453.
- [100] PLUTO Collaboration, C. Berger et al., *A Study of Multi-Jet Events in $e^+ e^-$ Annihilation*, *Phys. Lett. B* **97** (1980) 459.
- [101] D. J. Gross and F. Wilczek, *Ultraviolet Behavior of Non-Abelian Gauge Theories*, *Phys. Rev. Lett.* **30** (1973) 1343.
- [102] H. D. Politzer, *Reliable Perturbative Results for Strong Interactions?*, *Phys. Rev. Lett.* **30** (1973) 1346.

- [103] Particle Data Group Collaboration, K. A. Olive et al., *Review of Particle Physics*, [Chin. Phys. C **38** \(2014\) 090001](#).
- [104] C. G. Callan, Jr. and D. J. Gross, *High-energy electroproduction and the constitution of the electric current*, [Phys. Rev. Lett. **22** \(1969\) 156](#).
- [105] ZEUS and H1 Collaboration, H. Abramowicz et al., *Combination of Measurements of Inclusive Deep Inelastic $e^\pm p$ Scattering Cross Sections and QCD Analysis of HERA Data*, [arXiv:1506.06042 \[hep-ex\]](#).
- [106] V. N. Gribov and L. N. Lipatov, *Deep inelastic $e p$ scattering in perturbation theory*, *Sov. J. Nucl. Phys.* **15** (1972) 438, [*Yad. Fiz.*15,781(1972)].
- [107] Y. L. Dokshitzer, *Calculation of the Structure Functions for Deep Inelastic Scattering and $e^+ e^-$ Annihilation by Perturbation Theory in Quantum Chromodynamics.*, *Sov. Phys. JETP* **46** (1977) 641, [*Zh. Eksp. Teor. Fiz.*73,1216(1977)].
- [108] G. Altarelli and G. Parisi, *Asymptotic Freedom in Parton Language*, [Nucl. Phys. B **126** \(1977\) 298](#).
- [109] A. Bacchetta, M. Diehl, K. Goeke, A. Metz, P. J. Mulders, and M. Schlegel, *Semi-inclusive deep inelastic scattering at small transverse momentum*, [JHEP **02** \(2007\) 093](#), [arXiv:hep-ph/0611265 \[hep-ph\]](#).
- [110] M. Anselmino, M. Boglione, U. D'Alesio, A. Kotzinian, F. Murgia, A. Prokudin, and C. Turk, *Transversity and Collins functions from SIDIS and $e^+ e^-$ data*, [Phys. Rev. D **75** \(2007\) 054032](#), [arXiv:hep-ph/0701006 \[hep-ph\]](#).
- [111] M. Anselmino, M. Boglione, U. D'Alesio, A. Kotzinian, S. Melis, F. Murgia, A. Prokudin, and C. Turk, *Sivers Effect for Pion and Kaon Production in Semi-Inclusive Deep Inelastic Scattering*, [Eur. Phys. J. A **39** \(2009\) 89](#), [arXiv:0805.2677 \[hep-ph\]](#).
- [112] J. Collins and T. Rogers, *Understanding the large-distance behavior of transverse-momentum-dependent parton densities and the Collins-Soper evolution kernel*, [Phys. Rev. D **91** \(2015\) 074020](#), [arXiv:1412.3820 \[hep-ph\]](#).
- [113] J. C. Collins and D. E. Soper, *The Theorems of Perturbative QCD*, [Ann. Rev. Nucl. Part. Sci. **37** \(1987\) 383](#).
- [114] A. Datta et al., *Physics at the Large Hadron Collider*. Springer India, 2009.
- [115] M. L. Mangano, M. Moretti, F. Piccinini, R. Pittau, and A. D. Polosa, *ALPGEN, a generator for hard multiparton processes in hadronic collisions*, [JHEP **07** \(2003\) 001](#), [arXiv:hep-ph/0206293](#).
- [116] V. Sudakov, *Vertex parts at very high-energies in quantum electrodynamics*, *Sov. Phys. JETP* **3** (1956) 65.
- [117] M. L. Mangano, M. Moretti, and R. Pittau, *Multijet matrix elements and shower evolution in hadronic collisions: $Wb\bar{b} + n$ jets as a case study*, [Nucl. Phys. B **632** \(2002\) 343](#), [arXiv:hep-ph/0108069 \[hep-ph\]](#).

Bibliography

- [118] S. Catani, F. Krauss, R. Kuhn, and B. Webber, *QCD matrix elements + parton showers*, JHEP **0111** (2001) 063, [arXiv:hep-ph/0109231](#) [hep-ph].
- [119] F. Krauss, *Matrix elements and parton showers in hadronic interactions*, JHEP **0208** (2002) 015, [arXiv:hep-ph/0205283](#) [hep-ph].
- [120] Y. L. Dokshitzer, V. A. Khoze, A. H. Mueller, and S. I. Troian, *Basics of perturbative QCD*. 1991.
- [121] B. Andersson, G. Gustafson, G. Ingelman, and T. Sjostrand, *Parton Fragmentation and String Dynamics*, Phys. Rept. **97** (1983) 31.
- [122] B. Webber, *A QCD Model for Jet Fragmentation Including Soft Gluon Interference*, Nucl. Phys. B **238** (1984) 492.
- [123] J.-C. Winter, F. Krauss, and G. Soff, *A Modified cluster hadronization model*, Eur. Phys. J. C **36** (2004) 381, [arXiv:hep-ph/0311085](#) [hep-ph].
- [124] D. Amati and G. Veneziano, *Preconfinement as a Property of Perturbative QCD*, Phys. Lett. B **83** (1979) 87.
- [125] CDF Collaboration, R. D. Field, *The Underlying event in hard scattering processes*, eConf C010630 (2001) P501, [arXiv:hep-ph/0201192](#) [hep-ph].
- [126] J. M. Butterworth, J. R. Forshaw, and M. H. Seymour, *JIMMY Generator, Multiparton Interactions in HERWIG*, <http://jimmy.hepforge.org/>.
- [127] J. Butterworth, J. R. Forshaw, and M. Seymour, *Multiparton interactions in photoproduction at HERA*, Z. Phys. C **72** (1996) 637, [arXiv:hep-ph/9601371](#) [hep-ph].
- [128] ATLAS Collaboration, *Measurement of distributions sensitive to the underlying event in inclusive Z-boson production in pp collisions at $\sqrt{s} = 7$ TeV with the ATLAS detector*, Eur. Phys. J. C **74** (2014) 3195, [arXiv:1409.3433](#) [hep-ex].
- [129] T. Sjostrand and P. Z. Skands, *Multiple interactions and the structure of beam remnants*, JHEP **03** (2004) 053, [arXiv:hep-ph/0402078](#).
- [130] M. Bahr, S. Gieseke, and M. H. Seymour, *Simulation of multiple partonic interactions in Herwig++*, JHEP **0807** (2008) 076, [arXiv:0803.3633](#) [hep-ph].
- [131] ATLAS Collaboration, *Measurement of the total cross section from elastic scattering in pp collisions at $\sqrt{s} = 7$ TeV with the ATLAS detector*, Nucl. Phys. B **889** (2014) 486, [arXiv:1408.5778](#) [hep-ex].
- [132] TOTEM Collaboration, G. Antchev, P. Aspell, I. Atanassov, V. Avati, J. Baechler, et al., *First measurement of the total proton-proton cross section at the LHC energy of $\sqrt{s} = 7$ TeV*, Europhys. Lett. **96** (2011) 21002, [arXiv:1110.1395](#) [hep-ex].
- [133] L. Frankfurt, M. Strikman, and C. Weiss, *Dijet production as a centrality trigger for pp collisions at CERN LHC*, Phys. Rev. D **69** (2004) 114010, [arXiv:hep-ph/0311231](#) [hep-ph].
- [134] M. H. Seymour and A. Siodmok, *Constraining MPI models using σ_{eff} and recent Tevatron and LHC Underlying Event data*, JHEP **1310** (2013) 113, [arXiv:1307.5015](#) [hep-ph].

- [135] CMS Collaboration, *Underlying Event Tunes and Double Parton Scattering*, Tech. Rep. CMS-PAS-GEN-14-001, CERN, Geneva, 2014.
<https://cds.cern.ch/record/1697700>.
- [136] B. Blok and P. Gunnellini, *Dynamical approach to MPI four-jet production in Pythia*, *Eur. Phys. J. C* **75** (2015) 282, [arXiv:1503.08246](https://arxiv.org/abs/1503.08246) [[hep-ph](#)].
- [137] D. Treleani, *Double parton scattering, diffraction and effective cross section*, *Phys. Rev. D* **76** (2007) 076006, [arXiv:0708.2603](https://arxiv.org/abs/0708.2603) [[hep-ph](#)].
- [138] M. Bahr, M. Myska, M. H. Seymour, and A. Siodmok, *Extracting $\sigma_{\text{effective}}$ from the CDF $\gamma+3\text{jets}$ measurement*, *JHEP* **1303** (2013) 129, [arXiv:1302.4325](https://arxiv.org/abs/1302.4325) [[hep-ph](#)].
- [139] ATLAS Collaboration, *Luminosity determination in ATLAS*, <https://twiki.cern.ch/twiki/bin/view/AtlasPublic/LuminosityPublicResults>.
- [140] ATLAS Collaboration, *The ATLAS Experiment at the CERN Large Hadron Collider*, *JINST* **3** (2008) S08003.
- [141] ATLAS Collaboration, *Performance of the ATLAS Trigger System in 2010*, *Eur. Phys. J. C* **72** (2012) 1849, [arXiv:1110.1530](https://arxiv.org/abs/1110.1530) [[hep-ex](#)].
- [142] ATLAS Collaboration, *Luminosity Determination in pp Collisions at $\sqrt{s} = 7$ TeV Using the ATLAS Detector at the LHC*, *Eur. Phys. J. C* **71** (2011) 1630, [arXiv:1101.2185](https://arxiv.org/abs/1101.2185) [[hep-ex](#)].
- [143] S. van der Meer, *Calibration of the effective beam height in the ISR*, Tech. Rep. CERN-ISR-PO-68-31. ISR-PO-68-31, CERN, Geneva, 1968.
<https://cds.cern.ch/record/296752>.
- [144] ATLAS Collaboration, *Improved luminosity determination in pp collisions at $\sqrt{s} = 7$ TeV using the ATLAS detector at the LHC*, *Eur. Phys. J. C* **73** (2013) 2518, [arXiv:1302.4393](https://arxiv.org/abs/1302.4393) [[hep-ex](#)].
- [145] J. E. Huth et al., *Toward a standardization of jet definitions*, in *1990 DPF Summer Study on High-energy Physics: Research Directions for the Decade (Snowmass 90) Snowmass, Colorado, June 25-July 13*. 1990.
- [146] C. Buttar, J. D'Hondt, M. Kramer, G. Salam, M. Wobisch, et al., *Standard Model Handles and Candles Working Group: Tools and Jets Summary Report*, [arXiv:0803.0678](https://arxiv.org/abs/0803.0678) [[hep-ph](#)].
- [147] M. Cacciari, G. P. Salam, and G. Soyez, *The Anti- $k(t)$ jet clustering algorithm*, *JHEP* **0804** (2008) 063, [arXiv:0802.1189](https://arxiv.org/abs/0802.1189) [[hep-ph](#)].
- [148] S. D. Ellis and D. E. Soper, *Successive combination jet algorithm for hadron collisions*, *Phys. Rev. D* **48** (1993) 3160, [hep-ph/9305266](https://arxiv.org/abs/hep-ph/9305266).
- [149] Y. L. Dokshitzer, G. D. Leder, S. Moretti, and B. R. Webber, *Better jet clustering algorithms*, *JHEP* **08** (1997) 001, [hep-ph/9707323](https://arxiv.org/abs/hep-ph/9707323).
- [150] M. Wobisch and T. Wengler, *Hadronization corrections to jet cross sections in deep-inelastic scattering*, [hep-ph/9907280](https://arxiv.org/abs/hep-ph/9907280).

Bibliography

- [151] M. Cacciari and G. P. Salam, *Dispelling the N^3 myth for the k_t jet-finder*, *Phys. Lett. B* **641** (2006) 57, [arXiv:hep-ph/0512210](#).
- [152] C. Cojocaru et al., *Hadronic calibration of the ATLAS liquid argon end-cap calorimeter in the pseudorapidity region $1.6 < |\eta| < 1.8$ in beam tests*, *Nucl. Instrum. Meth.A* **531** (2004) 481.
- [153] W. Lampl et al., *Calorimeter clustering algorithms: description and performance*, Tech. Rep. [ATL-LARG-PUB-2008-002](#), April, 2008.
- [154] ATLAS Collaboration, *Jet energy measurement with the ATLAS detector in proton-proton collisions at $\sqrt{s} = 7$ TeV*, *Eur. Phys. J. C* **73** (2013) 2304, [arXiv:1112.6426 \[hep-ex\]](#).
- [155] ATLAS Collaboration, *Measurement of inclusive jet and dijet production in pp collisions at $\sqrt{s} = 7$ TeV using the ATLAS detector*, *Phys. Rev. D* **86** (2012) 014022, [arXiv:1112.6297 \[hep-ex\]](#).
- [156] ATLAS Collaboration, *Properties of jets measured from tracks in proton-proton collisions at center-of-mass energy $\sqrt{s} = 7$ TeV with the ATLAS detector*, *Phys. Rev. D* **84** (2011) 054001, [arXiv:1107.3311 \[hep-ex\]](#).
- [157] ATLAS Collaboration, *Charged-particle multiplicities in pp interactions at $\sqrt{s} = 900$ GeV measured with the ATLAS detector at the LHC*, *Phys. Lett. B* **688** (2010) 21, [arXiv:1003.3124 \[hep-ex\]](#).
- [158] I. Sadeh, *Double parton scattering in four-jet events in pp collisions at 7 TeV with the ATLAS experiment at the LHC*, [arXiv:1308.0587 \[hep-ex\]](#).
- [159] ATLAS Collaboration, *Measurement of inclusive jet and dijet production in pp collisions at $\sqrt{s}=7$ TeV using the ATLAS detector*, Tech. Rep. [ATL-COM-PHYS-2011-738](#), CERN, 2011. <https://cds.cern.ch/record/1360174>.
- [160] V. Lendermann, J. Haller, M. Herbst, K. Kruger, H.-C. Schultz-Coulon, et al., *Combining Triggers in HEP Data Analysis*, *Nucl. Instrum. Meth.A* **604** (2009) 707, [arXiv:0901.4118 \[hep-ex\]](#).
- [161] A. Buckley, J. Butterworth, S. Gieseke, D. Grellscheid, S. Hoche, et al., *General-purpose event generators for LHC physics*, *Phys. Rept.* **504** (2011) 145, [arXiv:1101.2599 \[hep-ph\]](#).
- [162] T. Sjostrand and M. van Zijl, *A Multiple Interaction Model for the Event Structure in Hadron Collisions*, *Phys. Rev. D* **36** (1987) 2019.
- [163] G. Marchesini, B. Webber, G. Abbiendi, I. Knowles, M. Seymour, et al., *HERWIG: A Monte Carlo event generator for simulating hadron emission reactions with interfering gluons. Version 5.1 - April 1991*, *Comput. Phys. Commun.* **67** (1992) 465.
- [164] G. Corcella et al., *HERWIG 6.5: an event generator for Hadron Emission Reactions With Interfering Gluons (including supersymmetric processes)*, *JHEP* **01** (2001) 010, [arXiv:hep-ph/0011363](#).
- [165] ATLAS Collaboration, *New ATLAS event generator tunes to 2010 data*, Tech. Rep. [ATL-PHYS-PUB-2011-008](#), CERN, 2011. <https://cds.cern.ch/record/1345343>.

- [166] J. M. Butterworth and M. H. Seymour, *Multi-parton interactions in Herwig for the LHC*, 2005. <http://jimmy.hepforge.org/draft20051116.ps>.
- [167] T. Sjostrand, S. Mrenna, and P. Z. Skands, *PYTHIA 6.4 Physics and Manual*, **JHEP** **0605** (2006) 026, [arXiv:hep-ph/0603175](https://arxiv.org/abs/hep-ph/0603175) [[hep-ph](#)].
- [168] T. Sjostrand and P. Z. Skands, *Transverse-momentum-ordered showers and interleaved multiple interactions*, *Eur. Phys. J.* **C39** (2005) 129, [arXiv:0408302](https://arxiv.org/abs/hep-ph/0408302) [[hep-ph](#)].
- [169] J. R. Forshaw and J. K. Storrow, *Mini - jets and the total inelastic photoproduction cross-section*, *Phys. Lett.* **B268** (1991) 116, [Erratum: *Phys. Lett.* **B276** (1992) 565].
- [170] ATLAS Collaboration, *Charged-particle multiplicities in pp interactions measured with the ATLAS detector at the LHC*, *New J. Phys* **13** (2011) 053033, [arXiv:1012.5104](https://arxiv.org/abs/1012.5104) [[hep-ex](#)].
- [171] F. Krauss, R. Kuhn, and G. Soff, *AMEGIC++ 1.0: A Matrix element generator in C++*, **JHEP** **02** (2002) 044, [arXiv:hep-ph/0109036](https://arxiv.org/abs/hep-ph/0109036) [[hep-ph](#)].
- [172] T. Gleisberg, S. Hoeche, F. Krauss, M. Schonherr, S. Schumann, et al., *Event generation with SHERPA 1.1*, **JHEP** **0902** (2009) 007, [arXiv:0811.4622](https://arxiv.org/abs/0811.4622) [[hep-ph](#)].
- [173] S. Hoeche, F. Krauss, S. Schumann, and F. Siegert, *QCD matrix elements and truncated showers*, **JHEP** **05** (2009) 053, [arXiv:0903.1219](https://arxiv.org/abs/0903.1219) [[hep-ph](#)].
- [174] GEANT4 Collaboration, S. , Agostinelli, et al., *GEANT4: A Simulation toolkit*, *Nucl. Instrum. Meth.A* **506** (2003) 250.
- [175] ATLAS Collaboration, *The ATLAS Simulation Infrastructure*, *Eur. Phys. J.* **C70** (2010) 823, [arXiv:1005.4568](https://arxiv.org/abs/1005.4568) [[physics.ins-det](#)].
- [176] Y. I. Azimov, Y. L. Dokshitzer, V. A. Khoze, and S. I. Troyan, *Similarity of Parton and Hadron Spectra in QCD Jets*, *Z. Phys. C* **27** (1985) 65.
- [177] Y. I. Azimov, Y. L. Dokshitzer, V. A. Khoze, and S. I. Troyan, *Humpbacked QCD Plateau in Hadron Spectra*, *Z. Phys. C* **31** (1986) 213.
- [178] Y. L. Dokshitzer, V. A. Khoze, and S. I. Troian, *On the concept of local parton hadron duality*, *J. Phys. G* **17** (1991) 1585.
- [179] I. T. Jolliffe, *Principal Component Analysis*. Springer Series in Statistics. Springer-Verlag, 2 ed., 2002.
- [180] C. M. Bishop, *Neural Networks for Pattern Recognition*. Oxford University Press, USA, 1 ed., Jan., 1996.
- [181] W. S. Sarle, *Neural Networks and Statistical Models*. SAS Institute, 1994.
- [182] D. Michie, D. J. Spiegelhalter, and C. C. Taylor, *Machine Learning, Neural and Statistical Classification*. Ellis Horwood, New York, NY, 1994.
- [183] R. Brun and F. Rademakers, *ROOT: An object oriented data analysis framework*, *Nucl. Instrum. Meth.A* **389** (1997) 81.
- [184] C. G. BROYDEN, *The Convergence of a Class of Double-rank Minimization Algorithms I. General Considerations*, *IMA. J. Appl. Math.* **6** (1970) 76.

Bibliography

- [185] R. Fletcher, *A new approach to variable metric algorithms*, *Comp. J.* **13** (1970) 317.
- [186] D. Goldfarb, *A Family of Variable-Metric Methods Derived by Variational Means*, *Math. Comp.* **24** (1970) 23.
- [187] D. F. Shanno, *Conditioning of Quasi-Newton Methods for Function Minimization*, *Math. Comp.* **24** (1970) 647.
- [188] G. Cybenko, *Approximation by superpositions of a sigmoidal function*, *Math. Control Signals System* **2** (1989) 303.
- [189] K. Hornik, M. Stinchcombe, and H. White, *Multilayer feedforward networks are universal approximators*, *Neural Networks* **2** (1989) 359.
- [190] W. Hsieh, *Machine Learning Methods in the Environmental Sciences: Neural Networks and Kernels*. Cambridge University Press, 2009.
- [191] A. Caldwell, D. Kollár, and K. Kröninger, *BAT - The Bayesian analysis toolkit*, *Comput. Phys. Commun.* **180** (2009) 2197, [arXiv:0808.2552](#).
- [192] ATLAS Collaboration, *Jet energy resolution in proton-proton collisions at $\sqrt{s} = 7$ TeV recorded in 2010 with the ATLAS detector*, *Eur. Phys. J.* **C73** (2013) 2306, [arXiv:1210.6210 \[hep-ex\]](#).

תקציר

אירועי ארבעה ג'טים בהתנגשויות פרוטון-פרוטון, באנרגיית מרכז מסה של $\sqrt{s}=7\text{ TeV}$, נותחו על מנת לזהות הימצאותם של אירועי פיזור כפול של פרטונים, בעזרת נתונים התואמים ללומינוסיטי של $(37\pm 1.3)\text{ pb}^{-1}$ שנאספו בגלאי ATLAS ב-LHC. החלק היחסי של אירועי פיזור כפול חולץ באמצעות רשת נוירונים מלאכותית, תחת ההנחה שהטופולוגיה של ארבעה ג'טים הנוצרים מפיזור כפול יכולה להיות מיוצגת על ידי שילוב אקראי של אירועי זוגות ג'טים. החלק היחסי הוערך להיות $f_{\text{DPS}}=0.084^{+0.009}_{-0.012}(\text{stat.})^{+0.062}_{-0.031}(\text{syst.})$ באירועי ארבעה ג'טים, בהם כל אירוע מכיל לפחות ארבעה ג'טים עם תנע רוחבי, $p_T \geq 20\text{ GeV}$, פסואודו-רפידיתי, $|\eta| \leq 4.4$, ולג'ט עם התנע הרוחבי הגבוה ביותר יש $p_T \geq 42.5\text{ GeV}$. בשילוב עם מדידות של חתך הפעולה של אירועים עם זוגות ג'טים ואירועים עם ארבעה ג'טים, במרחב הפאזות המתאים, שטח החפיפה האפקטיבי בין הפרוטונים המבצעים אינטרקציה, σ_{eff} , נמצא להיות $\sigma_{\text{eff}}=16.1^{+2.0}_{-1.5}(\text{stat.})^{+6.1}_{-6.8}(\text{syst.})\text{ mb}$. תוצאה זו קונסיסטנטית, בתוך השגיאות, עם מדידות עבר של σ_{eff} באנרגיות מרכז מסה מעל 1 TeV עם תוצרי אינטרקציות שונים והיא בערך רבע מחתך הפעולה האיאלסטי באנרגיות אלה. מדגם מועשר באירועי פיזור כפול חולץ ומספר מאפיינים של אירועים אלה נחקרו.

העבודה הוכנה בחוג לפיזיקת החלקיקים של אוניברסיטת תל-אביב,
בהדרכתם של פרופ' הלינה אברמוביץ ופרופ' אהרן לוי.



אוניברסיטת תל-אביב
הפקולטה למדעים מדויקים ע"ש ריימונד וברלי סאקלר

**חקר של פיזור כפול של פרטונים
באירועי ארבעה ג'טים בהתנגשויות pp
באנרגיית מרכז מסה $\sqrt{s} = 7 \text{ TeV}$
עם ניסוי LHC-ב-ATLAS**

חיבור זה הוגש לסנאט של אוניברסיטת תל-אביב,
כחלק מהדרישות לקבלת תואר "דוקטור לפילוסופיה"

ביה"ס לפיזיקה ולאסטרונומיה
החוג לחלקיקים

על-ידי

אוראל גואטה

ספטמבר 2015

העבודה הוכנה בהדרכתם של
פרופ' הלינה אברמוביץ ופרופ' אהרן לוי.